AD-A248 429

ITATION PAGE

Form Approved
OMB No. 0704-0188

ed to average 1 hour per response, including the time for reviewing instructions, searching existing data sour viewing the collection of information. Send comments regarding this burden estimate or any other aspect of rden, to Washington Headquarters Services, Directorate for Information Operations and Reports, 1215 Jeffe ffice of Management and Budget, Paperwork Reduction Project (0704-0188), Washington, DC 20503

1. AGENCY USE ONLY (Leave blank)	2. REPORT DATE	3. REPORT TYPE AND DATES COVERED
	January 1992	Final, SEP 1987 - MAR 1991

4. TITLE AND SUBTITLE

A Numerical Wind Tunnel Study of Viscous-Inviscid Interaction

5. FUNDING NUMBERS

6. AUTHOR(S)

David C. Wilcox

7. PERFORMING ORGANIZATION NAME(S) AND ADDRESS(ES)

DCW Industries, Inc.
5354 Palm Drive
La Cañada, California 91011

8. PERFORMING ORGANIZATION REPORT NUMBER

DCW-R-33-01

9. SPONSORING/MONITORING AGENCY NAME(S) AND ADDRESS(ES)

U. S. Army Research Office
P. O. Box 12211
Research Triangle Park, NC 27709-2211

10. SPONSORING/MONITORING AGENCY REPORT NUMBER

DTIC ELECTE APR 13 1992 S D

11. SUPPLEMENTARY NOTES

The view, opinions and/or findings contained in this report are those of the author(s) and should not be construed as an official Department of the Army position, policy, or decision, unless so designated by other documentation.

12a. DISTRIBUTION/AVAILABILITY STATEMENT

Approved for public release; distribution unlimited.

12b. DISTRIBUTION CODE

13. ABSTRACT *(Maximum 200 words)*

Research results based on the Wilcox k-ω and multiscale turbulence models aimed at analyzing viscous-inviscid interaction are presented. Surface boundary conditions for rough surfaces and for surface mass injection are developed and tested for the multiscale model. The multiscale model is also applied to three-dimensional ship-hull flows, flow over convex surfaces, and free shear flows. Both the k-ω and multiscale models are applied to a variety of two-dimensional shock-separated flows using an extremely fast numerical algorithm. Results show that such computations can be routinely done on a fast desktop computer. Using perturbation methods, an alternative to wall functions is devised to circumvent integration through the viscous sublayer without significant loss of accuracy. Partially successful attempts at implementing the k-ω and multiscale models in a three-dimensional time-averaged Navier-Stokes program are also described.

14. SUBJECT TERMS

TURBULENCE MODELING, COMPUTATIONAL FLUID DYNAMICS

15. NUMBER OF PAGES

90

16. PRICE CODE

17. SECURITY CLASSIFICATION OF REPORT	18. SECURITY CLASSIFICATION OF THIS PAGE	19. SECURITY CLASSIFICATION OF ABSTRACT	20. LIMITATION OF ABSTRACT
UNCLASSIFIED	UNCLASSIFIED	UNCLASSIFIED	UL

DISCLAIMER NOTICE

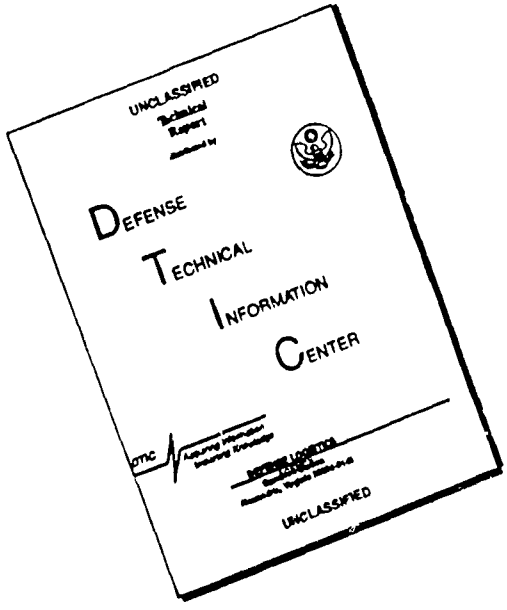

THIS DOCUMENT IS BEST QUALITY AVAILABLE. THE COPY FURNISHED TO DTIC CONTAINED A SIGNIFICANT NUMBER OF PAGES WHICH DO NOT REPRODUCE LEGIBLY.

A NUMERICAL WIND TUNNEL STUDY OF VISCOUS-INVISCID INTERACTION

Final Report DCW-R-33-01

by

David C. Wilcox

January 1992

Prepared for

U. S. ARMY RESEARCH OFFICE

Research Triangle Park. North Carolina

Contract DAAL-87-C-0004

DCW INDUSTRIES, INC.
5354 Palm Drive, La Cañada, CA 91011
818/790-3844

Approved for Public Release

Distribution Unlimited

The views, opinions, and/or findings contained in this report are those of the author and should not be construed as an official Department of the Army position, policy, or decision, unless so designated by other documentation.

92-09261

92 4 10 030

CONTENTS

SECTION		PAGE
1.	INTRODUCTION	1
2.	RESEARCH OVERVIEW	3
	2.1 Multiscale Model Development	3
	2.2 Free Shear Flows	3
	2.3 Three-Dimensional Boundary Layers	4
	2.4 An Alternative to Wall Functions	4
	2.5 Two-Dimensional Shock-Separated Flows	4
	2.6 Three-Dimensional Program Modification	5
	2.6.1 Computer-Program Overview	5
	2.6.2 Portable-Subroutine Overview	5
3.	SUMMARY AND CONCLUSIONS	9
	APPENDIX A: k-ω MODEL BASELINE PAPER	10
	APPENDIX B: MULTISCALE MODEL BASELINE PAPER	23
	APPENDIX C: 3-D BOUNDARY-LAYER APPLICATIONS	34
	APPENDIX D: MULTISCALE MODEL BOUNDARY CONDITIONS	48
	APPENDIX E: AN ALTERNATIVE TO WALL FUNCTIONS	61
	APPENDIX F: SEPARATED FLOW APPLICATIONS	72
	APPENDIX G: HISTORICAL OVERVIEW OF k-ω MODELS	78
	REFERENCES	89

Accesion For
NTIS CRA&I
DTIC TAB
Unannounced
Justification
By
Distribution/
Availability Codes
Dist | Avail and/or Special
A-1

1. INTRODUCTION

Under sponsorship of the Army Research Office (Contracts DAAG29-83-C-0003 and DAAL-87-C-0004), DCW Industries, Inc. engineers have developed and tested state-of-the-art computational fluid dynamics (CFD) tools. Our research efforts have produced several publications[1-9] detailing our progress in making numerical simulation of shock-separated flows both realistic and computationally efficient. While our primary focus has been upon two-dimensional flows, part of the objective in this contract was to extend our CFD capability to three-dimensions. This report summarizes research accomplished in Contract DAAL-87-C-0004 between September, 1987, and March, 1991.

Our personal assessment of the work accomplished versus the work proposed for Contract DAAL-87-C-0004 is that five of the six proposed tasks have been successfully completed while the sixth task has been only partially successful. In ***Task 1*** we devised surface boundary conditions for the multiscale model including effects of roughness and blowing. This work tied up some loose ends of the model's development. We focused upon free shear flows in ***Task 2***. While our results were excellent for the mixing layer, numerical difficulties initially precluded obtaining satisfactory solutions for wakes and jets. An improved numerical algorithm ultimately produced accurate solutions that illustrated a sensitivity to boundary conditions that has not been fully appreciated in the past. We have made major improvements to our three-dimensional boundary-layer program in ***Task 3***. We have done several computations with the program and no model deficiencies have appeared for three-dimensional boundary layers. ***Task 4*** proved to be a bit more difficult than anticipated, and the results won't be fully appreciated until we perform three-dimensional Navier-Stokes computations. Using a combination of perturbation and numerical analysis, we devised compressible wall-function-type surface boundary conditions consistent with the k-ω and multiscale models. In ***Task 5***, the MacCormack[10] flux-splitting/Gauss-Seidel-based algorithm has been optimized for both the k-ω and multiscale models. The optimized algorithm has been exercised extensively for two-dimensional separated turbulent flows and has proven to be incredibly fast. The algorithm is so fast that, using as many as 4000 grid points, no wall functions, and the multiscale model, two-dimensional separated turbulent flow computations can now be routinely done on a fast (80386- or 80486-based) desktop personal computer. ***Task 6*** proved to far more difficult than anticipated. The object was to perform three-dimensional Navier-Stokes computations. However, the three-dimensional version of MacCormack's new algorithm was not be available to us and we opted to use a NASA Langley program known as CFL3DE. Having far less familiarity with the numerical algorithm and code structure in CFL3DE, we have been unsuccessful in developing a fully operational program.

Section 2 presents an overview of research accomplished. Section 3 presents a summary and conclusions based on the overall work accomplished. Because research conducted in an earlier ARO Contract (DAAG29-83-C-0003) forms the foundation of the present research, Appendices A and B include the two key publications from Contract DAAG29-83-C-0003. Appendices C, D, E, F and G include reprints of the papers published under this Contract.

2. RESEARCH OVERVIEW

2.1 Multiscale Model Development

The earliest efforts in this Contract were directed at cleaning up some loose ends in developing the Wilcox multiscale model (see Appendix B). The most significant issue was the development of boundary conditions suitable for flow over rough surfaces and for surfaces with mass injection. While we devised such boundary conditions for the k-ω model (see Appendix A), the multiscale model had proven to be a bit more difficult to integrate through the viscous sublayer. In this Contract, we improved the numerical algorithm implemented in our viscous sublayer program and successfully developed the boundary conditions. Complete details are given in Subsections 3.1 through 3.3 of the reprint in Appendix D.

A full Reynolds stress closure must be used to obtain accurate results for flows with significant streamline curvature. To test the multiscale model's ability to predict properties of such flows, two applications were done for flows with convex curvature. Results are summarized in Subsection 3.4 of the reprint in Appendix D. As expected, excellent agreement between computed and measured boundary layer properties has been obtained.

2.2 Free Shear Flows

Free shear flows provide an interesting test of the range of applicability of both models, which have been developed mainly for wall-bounded flows. Subsection 3.5 of the reprint in Appendix D shows that both the k-ω and multiscale models yield a reasonable solution for the incompressible mixing layer. However, both models display a disconcerting sensitivity to the freestream value of the specific dissipation rate, ω. Initial attempts at obtaining solutions for the jet and wake proved to be extremely difficult. A better numerical algorithm was implemented and solutions for the k-ω model were obtained for the mixing layer, plane jet, round jet, radial jet and plane wake. Again computational results display a sensitivity to the freestream value of ω. However, we also found that realistic spreading rates can be obtained for all five of these free shear flows, provided an optimum freestream value of ω is chosen. By contrast, the popular k-ϵ model predicts a reasonable spreading rate only for the plane jet, and has no sensitivity to freestream conditions. Consequently, the k-ϵ model is unreliable for four of the five cases considered. Section V of the reprint in Appendix G summarizes these results.

2.3 Three-Dimensional Boundary Layers

The only successful three-dimensional applications in this Contract were for two ship-hulls. Section 3.3 of the reprint in Appendix C shows that: (a) k-ω and multiscale results are very similar and (b) either model predicts flow properties much closer to measurements than the mixing-length model for both cases.

2.4 An Alternative to Wall Functions

In preparation for three-dimensional applications, we devised a perturbation-method based strategy for obviating integration through the viscous sublayer. The methodology, termed ***wall matching***, is an alternative to the use of wall functions. Most importantly, solutions display far less sensitivity to the point of application of the grid point nearest the surface than do conventional wall functions. The reprint in Appendix E gives a complete description of the procedure.

2.5 Two-Dimensional Shock-Separated Flows

Turning to boundary-layer separation, early in the Contract we attempted a Mach 3 shock-wave/boundary-layer interaction computation. The numerical algorithm was a semi-implicit method developed by MacCormack.[11] The flow considered was the reflection of an oblique shock wave from a planar surface. The computations were done on a relatively coarse grid. Although a bit crude, the computations suggested that the multiscale model would predict a somewhat lower pressure plateau over the separation bubble and a larger separated region. Both differences would put computed results in closer agreement with measurements. Additionally, the computations suggested an inherent unsteadiness, similar to that observed experimentally. While the latter feature ultimately proved to be spurious numerical error, the other predictions were borne out in subsequent applications. These results are summarized in Section 4 of the reprint in Appendix C.

The highlight of research conducted in this Contract is the two-dimensional compression corner applications reported in the reprint in Appendix F. While the computations, again using MacCormack's semi-implicit algorithm,[11] required significant computing time on a Cray X/MP computer, they clearly illustrate the superiority of the multiscale model over a two-equation model for separated flows. As Contract research progressed, we incorporated the k-ω and multiscale models in a program based on MacCormack's[10] Gauss-Seidel line-relaxation method. The program reduced execution time by nearly a factor of 100, and made two-dimensional shock-separated flow computations practical on a fast (80386- or 80486-based) desktop microcomputer. The reprint in Appendix E includes examples of how fast the new program is.

2.6 Three-Dimensional Program Modification

In this task, the k-ω and multiscale models have been incorporated in a three-dimensional compressible fluid flow program known as CFL3DE. The model equations have been added to CFL3DE in the form of a "portable subroutine" which, in principle, can be added to any three-dimensional Navier-Stokes program with very little modification. The subroutine is undergoing careful testing but remains inoperable due to coding errors.

2.6.1 Computer-Program Overview

CFL3DE is a very general, fully-vectorized, computer program which implements upwind-biased spatial differencing.[12] This program can be used to compute a wide range of problems ranging from inviscid to separated turbulent flows with either perfect gas or equilibrium air equation-of-state options. Compressibility effects are accounted for in the program by using Favre[13] mass averaging.

The program has a multiple-zone grid capability and has options to use either Roe's[14] flux-difference splitting (FDS) technique or Van Leer's[15] flux-vector splitting (FVS) method. The program implements a hybrid streamwise-relaxation/crossflow-approximately-factored algorithm and can be run in several different modes, viz,

- Space-marching, Euler
- Space-marching, parabolized Navier-Stokes
- Time-marching, steady Euler
- Time-marching, steady thin-layer Navier-Stokes

2.6.2 Portable-Subroutine Overview

To help expedite program development, the new subroutine implementing the k-ω and multiscale models is restricted to: (a) a single grid; (b) Roe's FDS procedure; and, (c) time-marching solution of the thin-layer Navier-Stokes equations. If desired, the other options can be added later once the program has been fully validated.

The subroutine has been written with an input parameter, NEQNS, that is 2 for the k-ω model and 8 for the multiscale model. The approximate amount of memory, in bytes, required for the primary program arrays is given by the following formulas for the unmodified program and the modified program with each of the turbulence models.

$$N_{Baseline} = 140\,(I_{max} + 10)\,J_{max}\,K_{max} \quad (1)$$

$$N_{2\text{-}Equation} = 156\,(I_{max} + 10)\,J_{max}\,K_{max} \quad (2)$$

$$N_{Multiscale} = 204\,(I_{max} + 10)\,J_{max}\,K_{max} \quad (3)$$

The quantities I_{max}, J_{max} and K_{max} are the maximum number of grid points in the streamwise direction, crossflow direction and direction normal to the surface. Thus, the k-ω model requires an 11% increase in memory while the multiscale model requires a 46% increase. Table 1 summarizes the memory required, in megabytes, for a grid with $I_{max} = J_{max} = K_{max}$. For example, on an 80386 or 80486 based microcomputer using MS-DOS and the Phar Lap DOS Extender, 2 megabytes of memory must be set aside for the operating system, program instructions and stack space. Thus, based on Table 1, the multiscale model version of CFL3DE will run on a 16-megabyte-memory, 80386 or 80486 microcomputer with a 38x38x38 grid (approximately 55,000 points). A k-ω model computation can be done on such a computer with a 42x42x42 grid (approximately 74,000 points).

Table 1. Megabytes of Computer Memory Required for $I_{max} = J_{max} = K_{max}$

I_{max}	$N_{Baseline}$	$N_{2\text{-}Equation}$	$N_{Multiscale}$
35	7.7	8.6	11.2
40	11.2	12.5	16.3
45	15.6	17.4	22.7
50	21.0	23.4	30.6

Symbolically, we write the equations of motion as follows.

$$\frac{\partial Q}{\partial t} + \frac{\partial}{\partial \xi}(F - F_v) + \frac{\partial}{\partial \eta}(G - G_v) + \frac{\partial}{\partial \zeta}(H - H_v) = 0 \quad (4)$$

$$\frac{\partial q}{\partial t} + \frac{\partial}{\partial \xi}(f - f_v) + \frac{\partial}{\partial \eta}(g - g_v) + \frac{\partial}{\partial \zeta}(h - h_v) = s \quad (5)$$

where ξ, η and ζ are general streamwise, crossflow and normal coordinates. In Equation (4): Q is the vector of mean-flow properties; F, G, and H are the mean-flow inviscid-flux vectors; and, F_v, G_v and H_v are the mean-flow viscous-flux vectors. Similarly, in Equation (5): q is the vector of mean-flow properties; f, g, and h are the turbulence inviscid-flux vectors; f_v, g_v and h_v are the turbulence viscous-flux vectors; and s is the source-term vector. For example, the vector Q is as follows.

$$Q = J^{-1}[\rho \;\; \rho u \;\; \rho v \;\; \rho w \;\; \rho E]^T \tag{6}$$

where J is the Jacobian of the coordinate transformation, ρ is fluid density, u, v, and w are the Cartesian velocity components, $E = \hat{e} + \frac{1}{2}(u^2+v^2+w^2)$ is total energy, and $\hat{e}$ is internal energy. The form of the vector q depends upon which turbulence model is implemented.

k-ω model

$$q = J^{-1}[\rho k \;\; \rho\omega]^T \tag{7}$$

Multiscale model

$$q = J^{-1}[\rho k \;\; \rho\omega \;\; \rho(k\text{-}e) \;\; \rho\delta T_{xx} \;\; \rho\delta T_{xy} \;\; \rho\delta T_{xz} \;\; \rho\delta T_{yy} \;\; \rho\delta T_{yz}]^T \tag{8}$$

where $\rho(k\text{-}e)$ is the energy of the upper partition eddies and $\rho\delta T_{ij}$ is the deviatoric part of the upper partition contribution to the Reynolds-stress tensor. That is, we define

$$\rho\delta T_{ij} = \rho T_{ij} + \frac{2}{3}\rho(k\text{-}e)\delta_{ij} = \tau_{ij} + \frac{2}{3}\rho k\delta_{ij} \tag{9}$$

Details of the flux vectors, F, G, H, f, g, h, and their viscous counterparts are omitted for the sake of brevity. Their form is given, for example, by Walters and Thomas[12] and, more recently, by Morrison.[16] One noteworthy subtle feature of the multiscale model is that the viscous-flux terms for $\rho\delta T_{ij}$ are all zero.

The basic flowfield solver contained in CFL3DE is used without modification for Equation (4). The solution involves inverting a 5x5-block-tridiagonal matrix. At this stage of development, we are deliberately omitting the turbulence kinetic energy from the mean energy Equation. The advantage of doing this is the original CFL3DE source code remains unaltered. We will eventually assess the importance of this omission by performing the same k-ω computations as Morrison[16] who has included k in his mean-energy equation.

The new subroutine solves the turbulence-model equations separate from the main program. Thus, the overall computational procedure consists of a sequential solution first of Equation (4) followed by solution of Equation (5). The only way turbulence properties appear in Equation (4) is through the diffusion terms. More specifically, it is through the eddy viscosity. Our experience has shown that this coupling is rather weak for Navier-Stokes solvers. Hence, solving Equations (4) and (5) sequentially should not cause any significant computing time penalty compared to a coupled solution.

The way the source term vector s is treated guarantees that the discretized version of Equation (5) requires inversion of standard tridiagonal matrices for each component of q. For example, the vector s for the k-ω model is

$$s = [\,(P_k - D_k)\;\;(P_w - D_w)\,]^T \tag{10}$$

where P_k, D_k, P_w and D_w are given by

$$P_k = \tau_{ij}\frac{\partial u_i}{\partial x_j} \quad , \quad D_k = \beta^* \rho\, \omega\, k \tag{11}$$

$$P_w = \alpha\frac{\omega}{k}\tau_{ij}\frac{\partial u_i}{\partial x_j} \quad , \quad D_w = \beta\, \rho\, \omega^2 \tag{12}$$

Part of the discretization procedure involves computing the Jacobian $\partial s_i / \partial q_j$. To compute this Jacobian for the k-ω model, we rewrite the vector s as follows.

$$s = [\,(P_k - \beta^* q_1^2/\mu_t)\;\;(\alpha\rho P_k/\mu_t - \beta\, q_2^2/\rho)\,]^T \tag{13}$$

where μ_t is the eddy viscosity. Then, the Jacobian assumes the following diagonal form.

$$\frac{\partial s_i}{\partial q_j} = \begin{bmatrix} -2\beta^*\omega & 0 \\ 0 & -2\beta\,\omega \end{bmatrix} \tag{14}$$

Since none of the flux vectors contributes off diagonal terms, treating the source terms in this manner yields uncoupled tridiagonal matrix equations for both ρk and ρω. The multiscale model's source vector Jacobian is treated in the same manner resulting in 8 uncoupled tridiagonal matrix equations for ρk, ρω, ρ(k-e), and the five pertinent components of $\rho\delta T_{ij}$.

Treating the turbulence equations in this manner has proven very successful in our two-dimensional Navier-Stokes computations using MacCormack's[10] method with Gauss-Seidel line relaxation. The rapid convergence and short computing times for our two-dimensional Navier-Stokes computations of Appendix F attest to the efficiency of our procedure. We expect the method will work just as well with CFL3DE.

Unfortunately, our unfamiliarity with the numerical algorithm and, much more importantly, the structure of this 18,000 line program has severely impeded our progress. The program remains inoperable due to an undiscovered coding error. Although we are confident we will eventually develop a functioning program, Contract funds are now exhausted.

3. SUMMARY AND CONCLUSIONS

Using our established expertise and computational tools, the future appears bright especially when we complete development of the three-dimensional program. Research accomplished in this Contract shows that, using MacCormack's[10] algorithm, two-dimensional shock-separated turbulent flows can be routinely done on an 80386/IBM-PC-class computer in a matter of hours.[9] Even crude-mesh three-dimensional computations can be done on such a machine, although a Cray-class computer is needed for adequate resolution of fine details in a complicated flow.

It appears that we have developed the most complete and accurate turbulence model available at this time. The Wilcox multiscale model[6] has been tested for more than 50 well-documented flows including isotropic turbulence, free shear flows, compressible and incompressible boundary layers (including surface roughness, blowing and curvature), unsteady boundary layers, and shock-separated flows from transonic to supersonic speeds. None of the applications attempted to date has yielded major discrepancies between computed and measured flow properties.

While more work may be needed to arrive at a truly universal turbulence model, the success achieved thus far with the multiscale model suggests that we are in a position to begin studying fine details of viscous-inviscid interactions at supersonic speeds, particularly those details which elude experimenters. Such an end is indeed one of the ultimate goals of CFD, viz, to augment the physical wind tunnel. Detailed studies could be made for some of the flows we have already computed (e.g., flow structure near separation and reattachment) and the results certainly would be interesting. However, convincing the engineering community that the "physics" predicted by a turbulence model is believable nevertheless remains unlikely without even stronger evidence that the model has captured key details of turbulence structure.

APPENDIX A: k-ω MODEL BASELINE PAPER

The paper reproduced in this appendix appears in the November, 1988 issue of the AIAA Journal. The formal reference to this paper is as follows.

> Wilcox, D. C., "Reassessment of the Scale Determining Equation for Advanced Turbulence Models," *AIAA Journal*, Vol. 26, No. 11, Nov. 1988, pp. 1299-1310.

This paper defines the Wilcox k-ω two-equation model of turbulence. The primary contribution in this paper is a perturbation analysis of the defect layer including effects of pressure gradient. The paper also develops surface boundary conditions appropriate for rough surface and for surface mass injection. Applications include both incompressible and compressible boundary layers and the incompressible mixing layer.

Reassessment of the Scale-Determining Equation for Advanced Turbulence Models

David C. Wilcox*
DCW Industries, Inc., La Cañada, California

A comprehensive and critical review of closure approximations for two-equation turbulence models has been made. Particular attention has focused on the scale-determining equation in an attempt to find the optimum choice of dependent variable and closure approximations. Using a combination of singular perturbation methods and numerical computations, this paper demonstrates that: 1) conventional k-ϵ and k-ω^2 formulations generally are inaccurate for boundary layers in adverse pressure gradient; 2) using "wall functions" tends to mask the shortcomings of such models; and 3) a more suitable choice of dependent variables exists that is much more accurate for adverse pressure gradient. Based on the analysis, a two-equation turbulence model is postulated that is shown to be quite accurate for attached boundary layers in adverse pressure gradient, compressible boundary layers, and free shear flows. With no viscous damping of the model's closure coefficients and without the aid of wall functions, the model equations can be integrated through the viscous sublayer. Surface boundary conditions are presented that permit accurate predictions for flow over rough surfaces and for flows with surface mass addition.

I. Introduction

DURING the past 20 years, a great deal of research has focused on the task of devising closure approximations for the long-time-averaged Navier-Stokes equations suitable for predicting properties of turbulent flows. Prior to 1968, virtually all turbulence closure schemes were "incomplete," i.e., their implementation required some advance knowledge about the flowfield under consideration in order to obtain a solution. The best-known incomplete turbulence model is the mixing-length model.[1] This model is incomplete because the appropriate form of the mixing length must be determined empirically for each new application, in general, it cannot be specified a priori.

In 1968, the first Stanford conference[2] on turbulent flows was held to test existing turbulence models against the best experimental data available. The data base was confined to incompressible two-dimensional boundary layers. The competition was won, more or less, by the "incomplete" model of Bradshaw et al.[3]

The trend in turbulence modeling since the first Stanford conference has been toward development of complete models. For clarity, note that the terminology "complete model of turbulence," as used in this paper, means a set of equations that can be used to predict a given turbulent flow with no advance information other than boundary conditions required in order to achieve a solution. The terminology is not intended to imply anything with regard to the range of applicability of the theory.

Over the past 15 years, the most vigorous modeling efforts have been conducted by Donaldson et al.,[4] Launder et al.,[5,6] and Wilcox et al.[7-10] Recognizing the substantial progress the various researchers seemed to be making, the second Stanford conference on turbulent flows was held in 1980 and 1981.[11] This time, however, the scope of the experimental data was expanded tremendously to include complicating effects of compressibility, streamline curvature, surface mass transfer, boundary-layer separation, secondary motions, etc., that is, virtually every complicating effect known to man was included if experimental data of reliable quality existed.

From this researcher's viewpoint, results of the second of the two Stanford conferences were at once very encouraging and disappointing. On the one hand, the state-of-the-art has been shown to have advanced dramatically since the first Stanford conference. It was hard to imagine in 1968 that separated flowfields could be routinely predicted with any degree of accuracy just 13 short years later. (Of course, turbulence modelers should receive only part of the credit; magnificent advances in numerical methods, such as those of MacCormack,[12] have played a very important role, to say the least!) On the other hand, although such predictions can be routinely made, obtaining results consistent with measurements is not nearly as routine. Far worse, it was not even clear from the results presented at the second Stanford conference that effects of an adverse pressure gradient on the turbulent boundary layer could be predicted any more accurately than in 1968. Clearly, progress in turbulence modeling has been a bit uneven.

In light of this situation, this study was initiated by taking a modest step backward to review and assess the original closure approximations for the class of turbulence models known as two-equation models, that is, closure being accomplished using the long time averaged Navier-Stokes equations and two additional differential equations. The rationale for starting at what would seem to be a very elementary level stems from a key observation made at the second Stanford conference: the greatest amount of uncertainty and controversy over two-equation and higher-order models lies in the scale-determining equation. It is even unclear what the optimum choice of dependent variables is for a two-equation model. As a result of this study, we feel we have found the optimum choice and, based on this choice, we have postulated a new two-equation turbulence model.

Section II summarizes the new model, including arguments that set values of all but two of the closure coefficients appearing in the postulated equations. Section III presents results of a perturbation analysis of the incompressible defect layer, including effects of pressure gradient. Predictions of the new model are compared with those of the Jones-Launder[5] and the Wilcox-Rubesin[10] models. Section IV uses perturbation methods to analyze the viscous sublayer, including effects of surface roughness and surface mass injection. Section V

Presented as Paper 84-0176 at the AIAA 22nd Aerospace Sciences Meeting, Reno, NV, Jan 9-12, 1984, received Jan. 26, 1987, revision received Nov. 2, 1987. Copyright © American Institute of Aeronautics and Astronautics, Inc., 1987. All rights reserved.

*President. Associate Fellow AIAA.

includes results of attached boundary-layer computations for boundary layers subjected to adverse pressure gradient, surface mass injection and compressibility, and free shear flows.

II. Equations of Motion

This section states the postulated equations of motion, including established values of all closure coefficients. Physical interpretations of turbulence field properties are given and, additionally, arguments are presented that have been used in setting values of several of the closure coefficients.

A. Postulated Equations

For general compressible turbulent fluid flows, the turbulence model equations are written in terms of Favre[13] mass-averaged quantities as follows.

Mass conservation:

$$\frac{\partial \rho}{\partial t} + \frac{\partial}{\partial x_j}(\rho u_j) = 0 \tag{1}$$

Momentum conservation:

$$\frac{\partial}{\partial t}(\rho u_i) + \frac{\partial}{\partial x_j}(\rho u_i u_j) = -\frac{\partial p}{\partial x_i} + \frac{\partial \hat{\tau}_{ij}}{\partial x_j} \tag{2}$$

Mean energy conservation:

$$\frac{\partial}{\partial t}(\rho E) + \frac{\partial}{\partial x_j}(\rho u_j H) = \frac{\partial}{\partial x_j}\left[u_i \hat{\tau}_{ij} + (\mu + \sigma^* \mu_T)\frac{\partial k}{\partial x_j} - q_j\right] \tag{3}$$

Turbulent mixing energy:

$$\frac{\partial}{\partial t}(\rho k) + \frac{\partial}{\partial x_j}(\rho u_j k) = \tau_{ij}\frac{\partial u_i}{\partial x_j} - \beta^* \rho \omega k + \frac{\partial}{\partial x_j}\left[(\mu + \sigma^* \mu_T)\frac{\partial k}{\partial x_j}\right] \tag{4}$$

Specific dissipation rate:

$$\frac{\partial}{\partial t}(\rho \omega) + \frac{\partial}{\partial x_j}(\rho u_j \omega) = (\gamma \omega / k)\tau_{ij}\frac{\partial u_i}{\partial x_j} - \beta \rho \omega^2 + \frac{\partial}{\partial x_j}\left[(\mu + \sigma \mu_T)\frac{\partial \omega}{\partial x_j}\right] \tag{5}$$

where t is time, x_i position vector, u_i velocity vector, ρ density, p pressure, μ molecular viscosity, $\hat{\tau}_{ij}$ the sum of the molecular and Reynolds stress tensors, and q_j the sum of the molecular and turbulent heat flux vectors. In Eq. (3), the quantities $E = e + k + u_i u_i/2$ and $H = h + k + u_i u_i/2$ are total energy and enthalpy, respectively, with $h = e + p/\rho$; e and h denote internal energy and enthalpy. Additionally, τ_{ij} is the Reynolds stress tensor. The turbulent mixing energy k and the specific dissipation rate ω are needed to define the eddy viscosity μ_T, which is given by

$$\mu_T = \gamma^* \frac{\rho k}{\omega} \tag{6}$$

The total viscous stress tensor is given by

$$\hat{\tau}_{ij} = 2\mu\left[S_{ij} - \frac{1}{3}\frac{\partial u_k}{\partial x_k}\delta_{ij}\right] + \tau_{ij} \tag{7}$$

where, by definition, the mean strain-rate tensor S_{ij} is

$$S_{ij} = \frac{1}{2}\left[\frac{\partial u_i}{\partial x_j} + \frac{\partial u_j}{\partial x_i}\right] \tag{8}$$

We invoke the Boussinesq approximation that the Reynolds stress tensor is proportional to the mean strain-rate tensor, that is,

$$\tau_{ij} = 2\mu_T\left[S_{ij} - \frac{1}{3}\frac{\partial u_k}{\partial x_k}\delta_{ij}\right] - \tfrac{2}{3}\rho k \delta_{ij} \tag{9}$$

Finally, the heat flux vector q_j is approximated as

$$q_j = -\left(\frac{\mu}{Pr_L} + \frac{\mu_T}{Pr_T}\right)\frac{\partial h}{\partial x_j} \tag{10}$$

where Pr_L and Pr_T are the laminar and turbulent Prandtl numbers, respectively.

Several closure coefficients, namely, β, β^*, γ, γ^*, σ, and σ^*, appear in Eqs. (1-10). A key objective of this study has been to review typical arguments used in establishing values of such coefficients in a model of this type. In the next subsection and in later sections, the arguments are presented. The values are summarized in the following equations:

$$\beta = 3/40, \quad \beta^* = 9/100, \quad \gamma = 5/9, \quad \gamma^* = 1,$$
$$\sigma = 1/2, \quad \sigma^* = 1/2 \tag{11}$$

Before proceeding to further discussion of the closure coefficients, it is worthwhile to pause and discuss the form of the model equations and the physical meanings of the quantities k and ω. As in other two-equation models of turbulence, the quantity k represents a measure of the kinetic energy of the turbulence. Whether k is specifically identified as being the exact kinetic energy of the turbulence or, alternatively, the kinetic energy of the fluctuations in the direction of shear[9] is not critically important. All we require on physical grounds is that k be proportional to the square of the velocity at which local turbulent mixing occurs. The second quantity introduced in the model, ω, is referred to as the specific dissipation rate. Its dimensions are inversely proportional to time, and it is, in fact, the same variable used by this author in all prior turbulence modeling studies. Perhaps the simplest physical interpretation of ω is that it is the ratio of the turbulent dissipation rate ϵ to the turbulent mixing energy. Alternatively, ω is the rate of dissipation of turbulence per unit energy.

As is obvious from inspection of Eq. (4), the equation for k is modeled directly after the exact, long-time-averaged equation for the turbulent kinetic energy. On this point, the model is consistent with virtually all other two-equation models. The second of the two model equations is similar in form to the equation for k. Although it adds no rigor to the approach, the equation for ω can be regarded as the modeled form of the equation that would result from 1) writing the exact equations for turbulent kinetic energy and dissipation rate and 2) making the formal change of dependent variables defined by

$$\omega = \frac{\epsilon}{(\beta^* k)} \tag{12}$$

The primary difference between the model postulated in this study and the models in this author's prior research is the form of the equation for ω. Most notably, past studies have written the equation in terms of the square of ω. Interestingly, the first two-equation model in which the variables k and ω were used was postulated by Kolmogorov,[14] and his equation for ω was written in terms of ω rather than ω^2. The reason for our choice will become quite clear in Sec. III, where we analyze model-predicted structure of the defect layer.

B. Establishing Closure Coefficient Values

In this subsection, we present straightforward arguments from which values of the four closure coefficients β, β^*, γ, and γ^* can be established. A review of the arguments generally presented by turbulence model researchers indicates that the following are as physically sound as possible within the context of two-equation turbulence models.

Considering first the coefficient γ^*, we rewrite Eqs. (1-10) in terms of the quantity ω/γ^*. Inspection of the resulting equations shows that this rescaling of ω is equivalent to setting $\gamma^* = 1$. Hence with no loss of generality, we conclude that the value of γ^* is indeed unity.

Next, we turn to the ratio of β to β^*. For decaying homogeneous, isotropic turbulence, Eqs. (4) and (5) simplify to

$$\frac{dk}{dt} = -\beta^*\omega k \qquad \text{and} \qquad \frac{d\omega}{dt} = -\beta\omega^2 \tag{13}$$

from which the asymptotic solution for k is readily found to be

$$k \sim t^{-\beta^*/\beta} \tag{14}$$

Experimental observations indicate that $k \sim t^{-6/5}$ for decaying, homogeneous, isotropic turbulence, which implies that $\beta^*/\beta = 6/5$.

Values for the coefficients γ and β^* can be established by examining the so-called "wall layer." The wall layer is defined as the portion of the boundary layer far enough from the surface to render molecular viscosity negligible relative to eddy viscosity, yet close enough for convective effects to be negligible relative to the rate at which the turbulence is being created and destroyed. In the limiting case of an incompressible constant-pressure boundary layer, defining $\nu_T = \mu_T/\rho$, Eqs. (1-10) simplify to

$$0 = \frac{\partial}{\partial y}\left[\nu_T \frac{\partial u}{\partial y}\right]$$

$$0 = \nu_T\left[\frac{\partial u}{\partial y}\right]^2 - \beta^*\omega k + \sigma^*\frac{\partial}{\partial y}\left[\nu_T\frac{\partial k}{\partial y}\right]$$

$$0 = \gamma\left[\frac{\partial u}{\partial y}\right]^2 - \beta\omega^2 + \sigma\frac{\partial}{\partial y}\left[\nu_T\frac{\partial \omega}{\partial y}\right] \tag{15}$$

We seek the conditions under which these simplified equations yield a solution consistent with the law of the wall, i.e., velocity varying linearly with the logarithm of distance from the surface. As can easily be verified, Eqs. (15) possess a solution consistent with the law of the wall, namely,

$$u = \frac{u_\tau}{\kappa}\ln\left[\frac{u_\tau y}{\nu}\right], \quad k = \frac{u_\tau^2}{\sqrt{\beta^*}}, \quad \omega = \frac{u_\tau}{(\sqrt{\beta^*}\kappa y)} \tag{16}$$

where u_τ is the conventional friction velocity and κ is von Kármán's constant. There is one constraint imposed in the solution to Eqs. (15): a unique relation exists between the implied value of von Kármán's constant and the various closure coefficients. Specifically, the following equation must hold.

$$\gamma = \frac{\beta}{\beta^*} - \frac{\sigma\kappa^2}{\sqrt{\beta^*}} \tag{17}$$

Additionally, note that the Reynolds shear stress τ is constant in the wall layer and is equal to u_τ^2. Inspection of Eq. (16) shows that this implies $\tau = k\sqrt{\beta^*}$ in the wall layer. A variety of experimental measurements[14] indicate that the ratio of τ to k is about 3/10 in the wall layer. Thus, the predicted wall-layer solution is consistent with experimental observations, provided $\beta^* = 9/100$.

In summary, the arguments presented in this subsection are sufficient to uniquely set the values of γ^*, β^*, and β. Also, Eq. (17) determines γ in terms of the as-yet undetermined value of σ. As a by-product of analysis in the next section, the values of σ and σ^* will be established.

III. Defect-Layer Analysis

In this section, we use singular perturbation methods to analyze model-predicted structure of the classical defect layer. The analysis presented is a generalization of that done by Wilcox and Traci.[9] In contrast to the Wilcox and Traci analysis, effects of pressure gradient have been included. Additionally, the analysis has been done for three turbulence models: the model postulated in Eqs. (1-10), the Wilcox-Rubesin[10] model, and the Jones-Launder[5] model. First, we review details of the perturbation solution procedure. Next, we compare solutions for the three models in the absence of pressure gradient. Then, effects of pressure gradient are studied for the three models. Finally, we justify the values chosen for σ and σ^*.

A. Perturbation Solution

In the past, the only detailed analyses of the defect layer for any turbulence model have been those of Bush and Fendell[16] (for the mixing-lenth model) and Wilcox and Traci (for a k-ω^2 model). In neither case were effects of pressure gradient delineated. In this section, we extend the Wilcox-Traci analysis to include presssure gradient.

To study the defect layer, we confine our analysis to incompressible flow and we seek a perturbation solution. The expansion proceeds in terms of the ratio of friction velocity to the boundary-layer-edge velocity u_τ/U_e and the dimensionless vertical coordinate η, defined by

$$\eta = \frac{u_\tau y}{U_e\delta^*} \tag{18}$$

where δ^* is displacement thickness. For the sake of brevity, we confine details of the expansion procedure to the Appendix. It is instructive to note that the velocity is given by

$$\frac{u}{U_e} = 1 - \left(\frac{u_\tau}{U_e}\right)U_1(\eta) + \cdots \tag{19}$$

which, to order u_τ/U_e, can be rewritten as

$$\frac{(U_e - u)}{u_\tau} = f\left(\frac{y}{\Delta}\right), \qquad \Delta = \frac{U_e\delta^*}{u_\tau} \tag{20}$$

The coordinates appearing in Eq. (20) are the classical defect-layer coordinates. Additionally, it is important to note that pressure gradient appears in the equations of motion in dimensionless form as

$$\beta_T = \delta^*(dp/dx)/\tau_w \tag{21}$$

where τ_w is the surface shear stress. Coles and Hirst[2] refer to β_T as the equilibrium parameter.

In order to solve the defect-layer equations, we have used an improved version of the implicit time-marching program developed by Wilcox and Traci. That is, we add unsteady terms to each of the equations of motion, make an educated guess at the solution, and integrate over time until the solution displays negligible temporal variation.

B. Flat-Plate Boundary Layer

Figure 1a compares numerical predictions of the three models with corresponding experimental data of Wieghardt as tabulated by Coles and Hirst.[2] (Note that, in the new-model computation, we use $\sigma = \sigma^* = \cdots$; we defer any further discussion of the appropriate values to Sec. IIID.) The experi-

mental data presented are those at the highest Reynolds number for which data are reported. This is consistent with the defect-layer solution that is formally valid for very large Reynolds number. Numerical results are shown for three models: the new (k-ω) model, the Wilcox-Rubesin (k-ω^2) model, and the Jones-Launder (k-ϵ) model.

As shown, all three models predict velocity profiles that differ from measured values by no more than about 3% of scale. Interestingly, the new model shows the smallest differences from the Wieghardt data. Additionally, skin friction C_f can be inferred from the defect-layer solution (see Appendix). Corresponding computed and measured values are summarized in the insert on Fig. 1a, the largest difference is less than 3%. Thus, based on analysis of the constant-pressure defect layer, there is little difference among the three models.

C. Effects of Pressure Gradient

Turning now to the effect of pressure gradient, we have computed defect-layer solutions for the equilibrium parameter β_T, ranging from -0.5 to $+9.0$, where positive β_T corresponds to an adverse pressure gradient. The choice of this range of β_T has been dictated by the requirement of the perturbation solution that β_T be constant. This is as wide a range as we have been able to find for which experimental data have been taken with β_T more or less constant.

Figure 1c compares computed wake strength $\bar{\pi}$ with values inferred by Coles and Hirst[2] from experimental data. For the sake of clarity, note that the wake strength appears in Coles' composite law-of-the-wall/wake profile,

$$\frac{u}{u_\tau} = \frac{1}{\kappa}\ln\left|\frac{u_\tau y}{\nu}\right| + B + \frac{2\pi}{\kappa}\sin^2\left|\frac{\pi}{2}\frac{y}{\delta}\right| \qquad (22)$$

Inspection of Fig. 1c reveals provocative differences among the three models. Most notably, the new model yields wake strengths closest to values inferred from data over the complete range considered. Consistent with predictions of Chambers and Wilcox,[17] the Jones-Launder model exhibits the largest differences, with predicted wake strength 50–100% lower than inferred values when β_T is as small as 2!

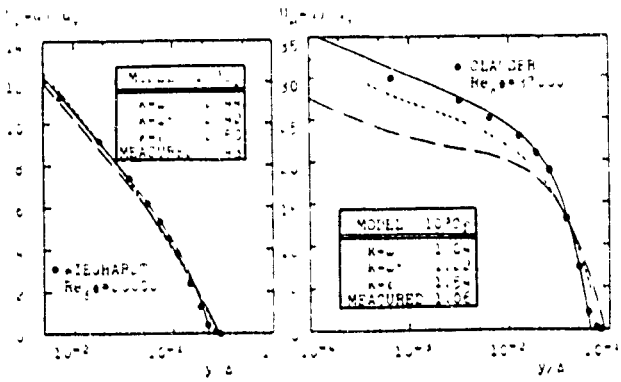

a) Velocity profiles, $B_T = 0$ b) Velocity profiles, $B_T = 9$

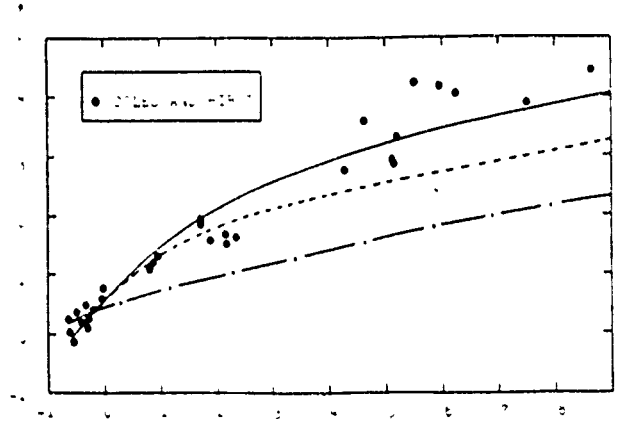

c) Variation of wake strength with pressure gradient

Fig. 1 Comparison of computed and measured defect-layer properties: —— k-ω model; ----- k-ω^2 model; — — k-ϵ model.

Figure 1b compares computed velocity profiles with experimental data of Clauser[2] for $\beta_T = 8.7$. As with the constant-pressure case, computed and measured skin friction are included in the insert. Consistent with the wake-strength predictions, the new model yields a velocity profile and skin friction closest to measurements, whereas the Jones-Launder model shows the greatest differences. The Wilcox-Rubesin profile and skin friction lie about midway between those of the other two models.

The explanation of the Jones-Launder model's poor performance for adverse pressure gradient can be developed from inspection of the asymptotic behavior of solutions as $\eta \to 0$. For the three models tested, the velocity behaves as

$$(U_e - u)/u_\tau \sim -\kappa^{-1}\ell n\eta + A - \beta_T C\eta\ell n\eta + \ldots \quad \text{as } \eta \to 0 \qquad (23)$$

where Table 1 summarizes the constants A and C. Note that while the coefficient A is determined as part of the solution (from the integral constraint that mass be conserved), the coefficient C follows directly from the limiting form of the solution as $\eta \to 0$. As seen from Table 1, C is largest for the Jones-Launder model and smallest for the new model. The presence of the $\eta\ell n\eta$ term gives rise to the inflection in the velocity profile as $\eta \to 0$ that is most pronounced for the Jones-Launder model. In terms of turbulence properties, the turbulence length scale, $\ell = k^{1/2}/\omega$, behaves according to

$$\ell \sim \beta^{*-1/2}\kappa\eta[1 + \beta_T L\eta\ell n\eta + \ldots] \qquad \text{as } \eta \to 0 \qquad (24)$$

Table 1 also includes the coefficient L for each model. Again, we see that the $\eta\ell n\eta$ term is largest for the Jones-Launder model and smallest for the new model. Thus, in the presence of adverse pressure gradient, the Jones-Launder turbulence length scale tends to be too large in the near-wall region. Note, of course, that this shortcoming is not evident in the constant-pressure case, which has $\beta_T = 0$.

The manner in which the new model achieves smaller values of ℓ than the Jones-Launder model can be seen by changing dependent variables. That is, starting with the k-ω formulation, defining $\epsilon \equiv \beta^*\omega k$ and $\nu_T \equiv k/\omega$, we can deduce the following incompressible equation for ϵ implied by the new model:

$$\frac{d\epsilon}{dt} = (1+\gamma)k\left|\frac{\partial u}{\partial y}\right|^2 - \left(1 + \frac{\beta}{\beta^*}\right)\frac{\epsilon^2}{k} + \frac{\partial}{\partial y}\left[\sigma\nu_T\frac{\partial \epsilon}{\partial y}\right] - 2\sigma\nu_T\frac{\partial k}{\partial y}\left[\frac{\partial(\epsilon/k)}{\partial y}\right] \qquad (25)$$

All terms except the last one on the right-hand side of Eq. (25) are identical in form to those of the Jones-Launder model (see Appendix). The last term is negligibly small as $\eta \to 0$ for constant-pressure boundary layers because $k \to$ constant as $\eta \to 0$. However, $\partial k/\partial y$ is nonvanishing when $\beta_T \neq 0$ and $\partial(\epsilon/k)/\partial y$ generally is quite large as $\eta \to 0$. The net effect of this additional term is to suppress the rate of increase of ℓ close to the surface.

Table 1 Summary of coefficients A, C, and L in Eqs. (23) and (24) for $\beta_T = 9$

Model	A	C	L
New	13.1	10.6	−19.8
Wilcox-Rubesin	9.8	23.4	−32.6
Jones-Launder	5.4	54.8	−61.1

As a final comment, note that all of the computations have used the model-predicted behavior [e.g., Eqs. (23) and (24)] as "wall-function" type of boundary conditions for $\eta \to 0$. Using other empirical wall functions presumably would improve the Jones-Launder predictions. However, the asymptotic behavior (e.g., inflected velocity profile) inherent in the model ultimately must prevail at high Reynolds number if the point of application of the wall functions remains constant at, say, $y^+ = 80$. To understand this point, one need only note that, by definition, η is related to y^+ by

$$\eta = \frac{y^+}{(U_e \delta^*/\nu)} \tag{26}$$

Hence, suppressing the asymptotic behavior inherent in the model requires using wall functions to increasingly larger values of y^+ as Reynolds number increases.

D. Establishing Closure Coefficient Values

Unlike the four closure coefficients discussed in Sec. IIB, we have been unable to find satisfactory arguments to establish the values of σ and σ^* before performing any numerical computations. However, we have found from numerical experimentation that the computed variation of $\tilde{\pi}$ with β_T (Fig. 1c) seems to match experimental results most faithfully when we use $\sigma = \sigma^* = \frac{1}{2}$. Effects of departures from this pair of values are so pronounced, in fact, that our computations seem to indicate that $\sigma = \sigma^* = \frac{1}{2}$ represents a saddle point in closure-coefficient space! Thus, we conclude that σ and σ^* are equal and that the most appropriate value is $\frac{1}{2}$.

IV. Sublayer Analysis

In order to facilitate integration of the model equations through the viscous sublayer, we must, at a minimum, have molecular diffusion terms in the equations of motion. Potentially, we might also have to allow the various closure coefficients to be functions of viscosity as well. In this section, we use perturbation methods to analyze viscous sublayer structure predicted by the new model, including effects of surface roughness and surface mass injection. Note that we confine our analysis to the new model because results of Sec III indicate that it is superior to the other models considered.

A. Perturbation Solution

Considering the incompressible constant-pressure case, convective terms are negligible in the sublayer; thus, the equations of motion for the new model (with molecular diffusion included) simplify to

$$u_\tau^2 = (\nu + \nu_T)\frac{du}{dy} \tag{27}$$

$$0 = \nu_T\left[\frac{du}{dy}\right]^2 - \beta^*\omega k + \frac{d}{dy}\left[(\nu + \sigma^*\nu_T)\frac{dk}{dy}\right] \tag{28}$$

$$0 = \gamma\left[\frac{du}{dy}\right]^2 - \beta\omega^2 + \frac{d}{dy}\left[(\nu + \sigma\nu_T)\frac{d\omega}{dy}\right] \tag{29}$$

Five boundary conditions are needed for this fifth-order system, two of which follow from matching to the law of the wall as $y^+ \to \infty$:

$$k \to \frac{u_\tau^2}{\sqrt{\beta^*}} \quad \text{and} \quad \omega \to \frac{u_\tau}{(\sqrt{\beta^*}\kappa y)} \text{ as } y^+ \to \infty \tag{30}$$

where $y^+ \equiv u_\tau y/\nu$. Two more boundary conditions follow from "no slip" at the surface, which implies that u and k vanish at $y = 0$. Thus,

$$u = k = 0 \quad \text{at} \quad y^+ = 0 \tag{31}$$

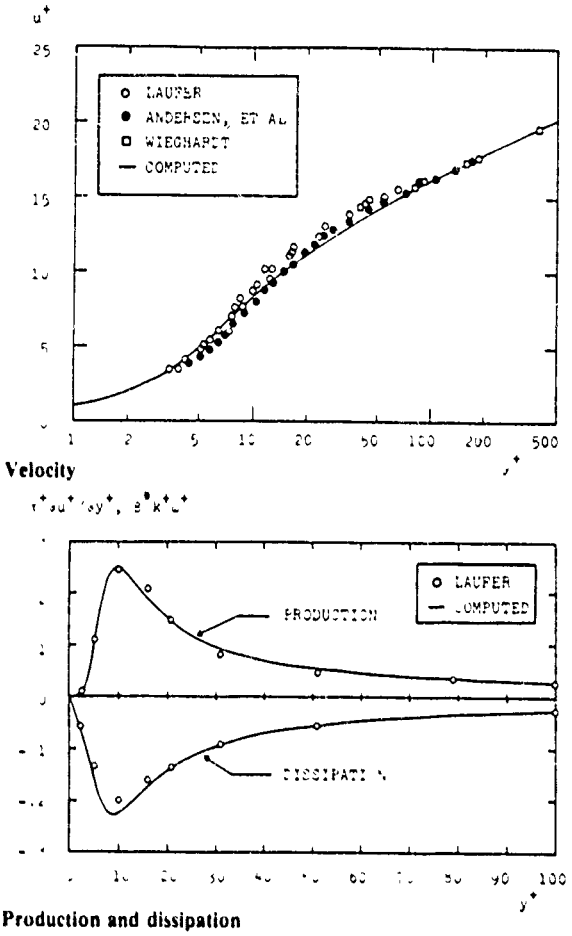

a) Velocity

b) Production and dissipation

Fig. 2 Comparison of computed and measured sublayer properties for a perfectly smooth surface.

The final condition is similar to that deduced in earlier studies,[8-10] where we have found that, for perfectly smooth surfaces, molecular diffusion and dissipation balance in Eq. (29), and this leads to

$$\omega \to \frac{6\nu}{(\beta y^2)} \quad \text{as} \quad y^+ \to 0 \tag{32}$$

More general boundary conditions for rough surfaces and for surfaces with mass injection will be devised in Secs. IVB and IVC. For now, we focus on the perfectly smooth surface.

As part of the solution to Eqs. (27-32), we obtain the constant in the law of the wall, B, where the velocity, $u^+ \equiv u/u_\tau$, asymptotes to

$$u^+ \to \frac{1}{\kappa}\ell n y^+ + B \quad \text{as} \quad y^+ \to \infty \tag{33}$$

As with the defect layer, we solve the sublayer equations by 1) adding unsteady terms to the left-hand sides of Eqs. (28) and (29), 2) making an initial guess at the solution, and 3) using an implicit, time-marching, second-order-accurate program to generate the long-time solution in which the unsteady terms tend to zero. The velocity is computed at each time step using the fourth-order Runge-Kutta method. The program used is an improved version of that developed in the study by Wilcox and Traci.[9]

Using this program, we find that Eqs. (27-32) predict the smooth-wall value of B as

$$B = \lim_{y^+ \to \infty}\left[u^+ - \frac{1}{\kappa}\ell n y^+\right] = 5.1 \tag{34}$$

That this value is well within the scatter of measured values of B strongly suggests that no further viscous modifications are needed.

Figure 2a compares computed and measured[2,18,19] sublayer velocity profiles. As shown, computed velocities generally fall within experimental data scatter. In Fig. 2b, we compare computed and measured[18] turbulence production and dissipation terms. Again, predictions fall well within experimental error bounds.

Perhaps the only deficiency of predicted smooth-surface sublayer structure is that, very near the surface, the model predicts

$$k \sim y^{3.23} \quad \text{as} \quad y \to 0 \tag{35}$$

By contrast, the Wilcox-Rubesin model predicts that $k \sim y^4$, which suggests that $k \sim \langle v'^2 \rangle$, a point this researcher has made[9] as a more plausible interpretation than saying that k is the kinetic energy of the turbulence. By letting the closure coefficient β^* increase as a function of turbulent Reynolds number, $Re_T \equiv k/(\omega\nu)$, it is possible to force either $k \sim y^4$ or $k \sim y^2$, but then we find that to recover $B \doteq 5$, at least two other closure coefficients must vary with Re_T. Such additional complexity is pointless in light of Fig. 2.

B. Rough-Wall Analysis

A key advantage of the k-ω^2 and k-ω formulations over the k-ϵ formulation is the fact that ω-oriented equations possess solutions in which the value of ω may be arbitrarily specified at the surface.[17] This is an advantage because it provides a natural way to incorporate effects of surface roughness through surface boundary conditions. This feature of the equations was originally recognized by Saffman.[20]

If we now rewrite the surface boundary condition [Eq. (32)] on ω as

$$\omega = \frac{u_\tau^2}{\nu} S_R \quad \text{at} \quad y = 0 \tag{36}$$

we can generate sublayer solutions for arbitrary S_R, including the limiting cases $S_R \to 0$ and $S_R \to \infty$.

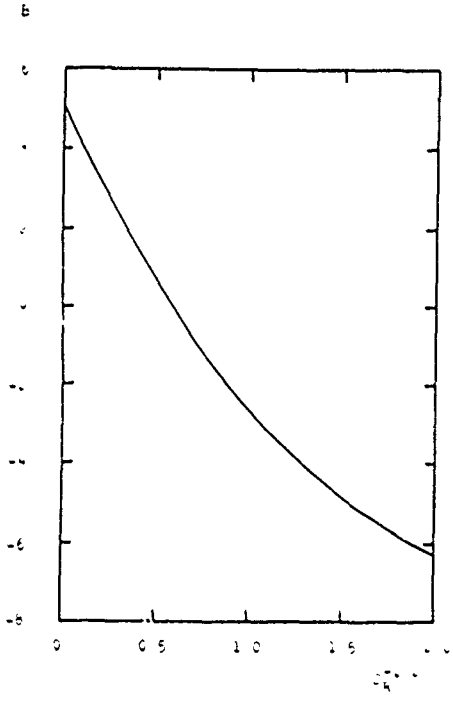

Fig. 3 Computed variation of the constant in the law of the wall, B, with the surface value of the specific dissipation rate.

Figure 3 shows the computed value of B for a wide range of values of S_R. As shown, in the limit $S_R \to \infty$, B tends to 5.1. In the limit $S_R \to 0$, an excellent correlation of the numerical predictions is given by

$$B \to 8.4 + \frac{1}{\kappa} \ln \frac{S_R}{100} \quad \text{as} \quad S_R \to 0 \tag{37}$$

By experimental means, as summarized by Schlichting,[21] Nikuradse found that for flow over very rough surfaces,

$$B \to 8.5 + \frac{1}{\kappa} \ln \frac{1}{k_R^+}, \qquad k_R^+ = \frac{u_\tau k_R}{\nu} \tag{38}$$

where k_R is the average height of sand-grain roughness elements. (Note that, in our computations, we use $\kappa = 0.41$, whereas Nikuradse used $\kappa = 0.40$.) Thus, if we make the correlation

$$S_R = \frac{100}{k_R^+} \quad \text{for } k_R^+ >> 1 \tag{39}$$

then Eqs. (37) and (38) are nearly identical. Figure 4 compares computed velocity profiles with the analytical fit obtained by using Eqs. (37) and (38) in the law of the wall, that is,

$$u^+ = \frac{1}{\kappa} \ln \frac{y}{k_R} + 8.4 \tag{40}$$

for three of the computations. The correlation is nearly exact. The most remarkable fact about this correlation is that Eq. (40) is the form the law of the wall assumes for flow over "completely rough" surfaces, including the value of the additive constant (8.4 and 8.5 differ by 1%).

By making a qualitative argument based on flow over a wavy wall, Wilcox and Chambers[22] have shown that, for small roughness heights, we should expect to have

$$S_R \sim \left(\frac{1}{k_R^+}\right)^2 \quad \text{as} \quad k_R^+ \to 0 \tag{41}$$

Comparison with Nikuradse's data shows that the following correlation between S_R and k_R^+ will reproduce measured effects of sand-grain roughness for values of k_R^+ up to about 400.

$$S_R = \begin{cases} \left(\dfrac{50}{k_R^+}\right)^2, & k_R^+ < 25 \\ \dfrac{100}{k_R^+}, & k_R^+ \geq 25 \end{cases} \tag{42}$$

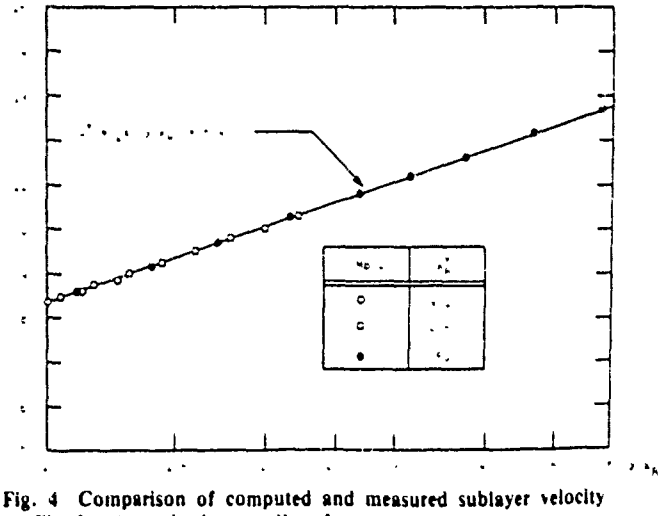

Fig. 4 Comparison of computed and measured sublayer velocity profiles for "completely rough" surfaces

C. Effects of Surface Mass Injection

For boundary layers with surface mass injection, the introduction of an additional velocity scale (v_w = normal flow velocity at the surface) suggests that the scaling for ω at the surface may differ from Eq. (36). Andersen et al.[19] provide further evidence that the specific-dissipation-rate boundary condition must be revised when mass injection is present by showing, from correlation of their experimental data, that both κ and B are functions of $v_w^+ = v_w/u_\tau$. Because our rough-surface computations of the preceding subsection show that the value of B is strongly affected by the surface value of the specific dissipation rate, this suggests that the surface value of ω will depend in some manner on v_w. Examination of the limiting form of the model equations for $y^+ \to \infty$ (i.e., the "wall-layer" in Sec. IIB) shows immediately that the effective von Kármán "constant" varies with v_w^+ according to

$$\tilde{\kappa} = \frac{\kappa}{1 + \Xi v_w^+} \tag{43}$$

where Ξ is given by

$$\Xi = 3.11 + 0.61 \ln y^+ \tag{44}$$

The variation of $\tilde{\kappa}$ predicted in Eqs. (43) and (44) is consistent with the data of Andersen et al. Including appropriate convective terms in Eqs. (27-29), we have performed sublayer computations for the cases experimentally documented by Andersen et al. In each case, the surface value of ω has been given by

$$\omega = \frac{u_\tau^2}{\nu} S_B \qquad \text{at} \qquad y = 0 \tag{45}$$

and the value of S_B has been varied until optimum agreement between measured and computed velocity profiles is achieved. The final correlation between S_B and v_w^+ is given in analytical form as

$$S_B = \frac{20}{v_w^+ (1 + 5 v_w^+)} \tag{46}$$

Figure 5 displays the level of agreement between theory and experiment using Eqs. (45) and (46). This concludes our formulation of the new turbulence model and attending surface boundary conditions.

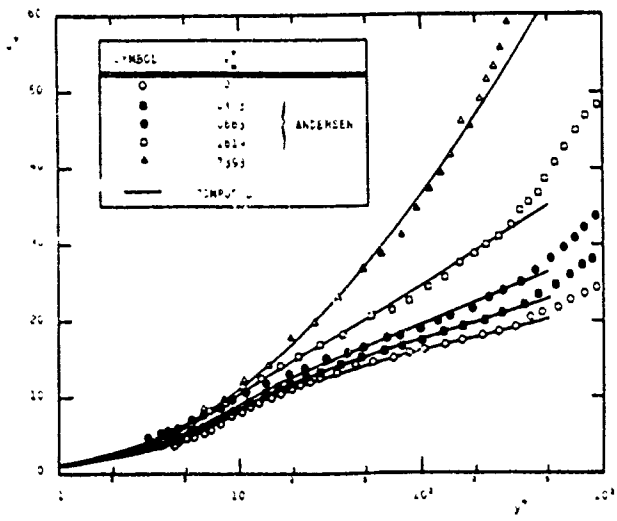

Fig. 5 Comparison of computed and measured sublayer velocity profiles for boundary layers with surface mass injection.

V. Numerical Applications

The purpose of this section is to apply the new model to several well-documented turbulent boundary layers, including effects of adverse pressure gradient, surface mass injection, and compressibility, and to free shear flows. All boundary-layer computations have been done with a second-order-accurate boundary-layer program, EDDYBL,[23] based on the Blottner[24] variable-grid method and the algoarithm developed by Wilcox[25] to permit large streamwise steps. The free shear flow computations have been done with the same numerical procedure implemented to solve the sublayer equations in Sec. IV.

A. Boundary Conditions

For boundary-layer computations, we must specify boundary conditions at the surface ($y = 0$) and at the edge of the layer ($y = \delta$). At the surface, we impose the no-slip condition, which gives the following:

$$u = k = 0 \qquad \text{at} \qquad y = 0 \tag{47}$$

For compressible flows, we specify either surface temperature T_w or surface heat flux q_w, so that the enthalpy boundary condition for a calorically perfect gas becomes

$$h = \frac{T_w}{C_p} \quad \text{or} \quad \frac{\partial h}{\partial y} = \frac{-Pr_L C_p q_w}{\mu_w} \qquad \text{at} \qquad y = 0 \tag{48}$$

where C_p is specific heat at constant pressure and subscript w denotes surface ($y = 0$) value. For the compressible flow

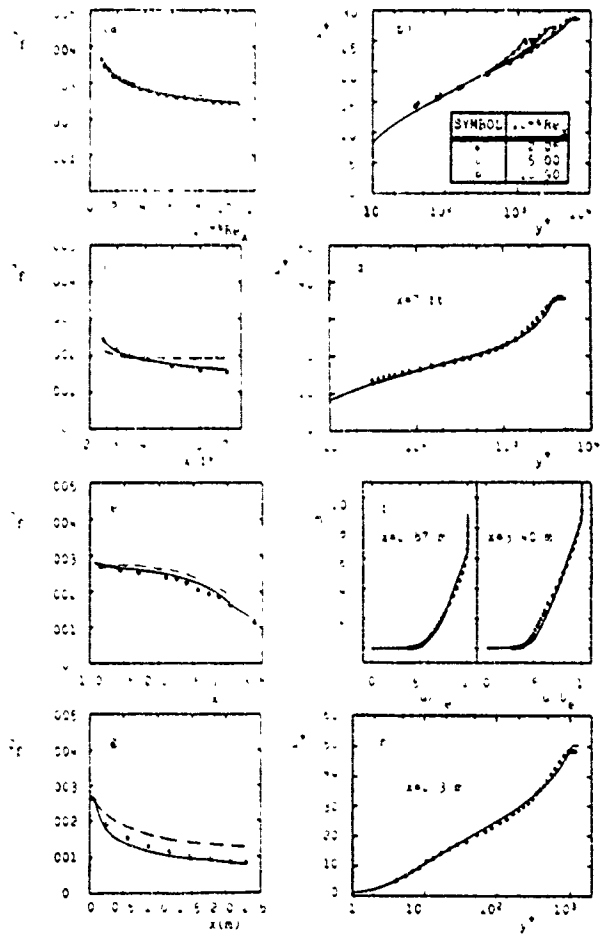

Fig. 6 Comparison of computed and measured skin-friction and velocity profiles for incompressible boundary layers: —— k-ω model; —·— k-ϵ model; ○ measured.

computations of Sec. VB, we assume that our fluid is air so that $Pr_L = 0.72$, and the value used for Pr_T is 8/9. Finally, for perfectly smooth surfaces with no surface mass injection, we require that

$$v = 0 \quad \text{and} \quad \omega \to \frac{6\nu_w}{\beta y^2} \quad \text{as} \quad y \to 0 \quad \text{(no mass injection)} \tag{49}$$

For the computation with surface mass injection (Sec. VB), the surface conditions satisfied by v and ω are given by

$$v = v_w \quad \text{and} \quad \omega = \frac{u_\tau^2}{\nu_w} S_B \quad \text{at} \quad y = 0 \quad \text{(with mass injection)} \tag{50}$$

where the dimensionless coefficient S_B is defined in terms of the blowing rate parameter $v_w^+ = v_w/u_\tau$ by Eq. (46).

The manner in which the surface boundary condition on ω is implemented when mass addition is present is straightforward. For the perfectly smooth surface, the method used is less obvious and requires special care. As indicated in Eq. (49), we must make sure ω approaches the correct asymptotic form as $y \to 0$. If proper care is not taken, the near-wall velocity profile is distorted which, in turn, distorts the entire boundary layer. Note that the singular behavior of ω is consistent with the physics of turbulence, which dictates that there are rapidly decaying small eddies close to solid boundaries. This means that the time scale for decay, proportional to the reciprocal of ω, must approach 0 as $y \to 0$.

In order to achieve the proper limiting form, the boundary-layer program uses Eq. (49) for all points up to $y^+ = u_\tau y/\nu_w = 2.5$ rather than attempting to solve the differential equation for ω directly. This procedure is very accurate, provided the mesh point closest to the surface lies below $y^+ = 1$ and that at least 5 mesh points lie between $y^+ = 0$ and $y^+ = 2.5$. Note that Eq. (49) is the *exact solution* to Eq. (5) in the limit $y^+ \to 0$, and using it to define ω for the mesh points closest to the surface is done to guarantee numerical accuracy. The procedure should not be confused with the use of wall functions.

In addition to specifying surface boundary conditions, values of the dependent variables must also be specified at the edge of the boundary layer. Ideally, we would like to implement "zero-gradient" boundary conditions at the boundary-layer edge. Although such conditions are "clean" from a theoretical point of view, they are undesirable from a numerical point of view. That is, the conditions we have used in past applications are of the Neumann type, whereas "zero-gradient" conditions are of the Dirichlet type. Almost universally, convergence of iterative numerical schemes (EDDYBL uses an iterative scheme) is much slower with Dirichlet conditions than with Neumann conditions.

In order to resolve this apparent dilemma, we appeal directly to the equations of motion. Beyond the boundary-layer edge, we have vanishing normal gradients, so that the equations for k and ω simplify to the following:

$$U_e \frac{dk_e}{dx} = -\beta^* \omega_e k_e \tag{51}$$

$$U_e \frac{d\omega_e}{dx} = -\beta \omega_e^2 \tag{52}$$

where subscript e denotes the value at the boundary-layer edge. The solution to Eqs. (51) and (52) can be obtained by simple quadrature, independently of integrating the equations of motion through the boundary layer. Once k_e and ω_e are determined from Eqs. (51) and (52), it is then possible to specify Neumann-type boundary conditions that guarantee zero normal gradients.

B. Boundary-Layer Applications

We turn now to application of the new model equations to a total of four incompressible boundary layers and to the compressible constant-pressure (flat-plate) boundary layer. First, we apply the model to the incompressible flat-plate case. The next two applications are to boundary layers in an adverse pressure gradient. The final incompressible application is for a boundary layer with surface mass injection. We conclude with application of the model to the compressible flat-plate boundary layer with and without heat transfer for Mach numbers 0-5. Numerical details of the computations are given by Wilcox.[26]

Incompressible Flat-Plate Boundary Layer

The first application is for the constant-pressure incompressible boundary layer. Although this application does not provide a severe test of the new model, it is nevertheless necessary to be sure the boundary-layer program has been coded properly. Also, the new model would be of little use as a predictive tool if it were inaccurate for the simplest of all boundary layers.

The computation begins at a plate-length Reynolds number Re_x of $1 \cdot 10^6$ and continues to an Re_x of $10.9 \cdot 10^6$. Figures 6a and 6b compare computed and measured[2] skin-friction and velocity profiles, respectively. As shown in Fig. 6a, computed skin friction virtually duplicates corresponding measurements for the entire range of Reynolds numbers considered. Figure 6b shows that differences between computed and measured velocity profiles are no more than 3% of scale for the three Reynolds numbers indicated. Thus, it comes as no great surprise that the new model is quite accurate for the flat-plate boundary layer. Skin-friction results[17] for the k-ϵ model are included in Fig. 6a. Note that, as predicted in the defect-layer analysis of Sec. III, computed C_f is about 3% higher than measured.

Incompressible Boundary Layers with Adverse Pressure Gradient

We consider two boundary layers with adverse pressure gradient. The first case has a moderate adverse pressure gradient, the experimental data being those of Bradshaw[2] (case 3300). The second case has increasingly adverse pressure gradient, the experimental data being those of Samuel and Joubert[11] (flow 0141).

For the Bradshaw case, streamwise distance extends from $x = 2.5$ to 7.0 ft, corresponding to an increase in Re_x from about $2 \cdot 10^6$ to about $4 \cdot 10^6$. Figures 6c and 6d compare computed and measured skin friction and a velocity profile. Inspection of both graphs shows that differences between theory and experiment nowhere exceed 5% for this flow. Figure 6c includes k-ϵ results obtained by Chambers and Wilcox;[17] computed C_f exceeds measured values by as much as 20%. Because the equilibrium parameter $\beta_T \doteq 2$ for this flow, the poor results for the k-ϵ model are unsurprising.

In the Samuel-Joubert case, we integrate from $x = 1$ to 3.40 m, corresponding to an Re_x range of about $2 \cdot 10^6$-$4 \cdot 10^6$. Figures 6e and 6f compare computed and measured skin-friction and two velocity profiles for this flow. Computed and measured skin friction differ by less than 5% of scale. Velocity profiles at $x = 2.87$ m are within 5% whereas those at $x = 3.40$ m differ by no more than 9%. Since β_T exceeds 9 toward the end of the computation, the poor performance[27] of the k-ϵ model shown in Fig. 6e (computed C_f exceeds measured values by as much as 35%) is again consistent with the defect-layer analysis of Sec. III.

Incompressible Boundary Layer with Surface Mass Injection

As the final incompressible application of the model, we consider a boundary layer with surface mass injection. The case considered was included in the second Stanford conference[12] (flow 0241), and data for the flow were taken by Andersen et al.[19] The surface mass injection rate v_w is 0.00375 U_e, where U_e is the constant boundary-layer-edge velocity, i.e., the flow has constant pressure. Figures 6g and 6h compare computed and measured skin-friction and velocity profiles, respectively. As shown, computed and measured skin

friction differ by less than 4% of scale whereas computed and measured velocity profiles are within 3% of each other. Although this flow has zero pressure gradient, corresponding skin friction predicted[11] by the k-ϵ model is as much as 50% higher than measured, probably because the wall functions used by Rodi in this computation are inadequate for flows with mass injection.

Compressible Flat-Plate Boundary Layers

In order to test the k-ω model for effects of compressibility, we consider flows 8101 and 8201 of the second Stanford conference.[11] We first consider the adiabatic-wall case with freestream Mach number 0-5. For each Mach number, computation begins at an Re_x of $1.0 \cdot 10^6$ and continues to the point where momentum-thickness Reynolds number Re_θ is 10,000. Figure 7a compares the computed ratio of skin friction C_f to the incompressible value C_{fo}, with the correlation developed by Rubesin. As shown, differences between computed ratios and correlated values are barely noticeable.

Next, we turn to effects to surface temperature on flat-plate skin friction. For this round of computations, the freestream Mach number is 5; the ratio of surface temperature to the adiabatic-wall value ranges from 0.2 to 1.0. Again, computation begins at $Re_x = 1.0 \cdot 10^6$ and terminates when $Re_\theta = 10{,}000$. Figure 7b compares the predicted ratio of C_f to the incompressible value with Rubesin's correlation for the range of surface temperatures considered. Differences between predicted and correlated values nowhere exceed 4%.

C. Incompressible Free Shear Flows

The final application is to an incompressible free shear flow, specifically, to the mixing layer. The model equations admit a similarity solution in which the independent variable is $\eta = y/x$. To solve the resulting equations, we have used the same time-marching procedure implemented in the defect-layer and sublayer analyses of Secs. III and IV. Complete analytical and numerical details are given by Wilcox.[26]

To compare computed and measured spreading rates, we use the definition given by Birch in the second Stanford conference.[11] Predicted spreading rate is sensitive to the freestream values of k and ω, so that a range of spreading rates between 0.100 and 0.141 is possible. This range brackets the measured value of 0.115.

VI. Summary and Conclusions

The primary objectives of this study have been accomplished: we have made a critical review of closure approximations used in two-equation turbulence models and determined what appears to be an optimum choice of dependent variables. As a result, we have developed a new two-equation model that promises more accuracy for boundary layers in an adverse pressure gradient than any similar model.

As in our prior turbulence modeling efforts, we have made extensive use of perturbation methods (Secs. III and IV). In contrast to prior studies, our analysis of the defect layer includes pressure gradient. As discussed in Sec. III, limiting the defect-layer analysis to the constant-pressure case displays little difference among the various two-equation models in general usage. However, as soon as an adverse pressure gradient is included, the models exhibit large differences. As a general observation, the second Stanford conference demonstrated that modern turbulence models are not much more accurate than those in use in 1968 if the flow of concern is a boundary layer in adverse pressure gradient. The analysis of Sec. III indicates why this is true and, with the introduction of the new model, offers the basis for development of new models that are accurate for such flows.

The model thus far has been tested for the mixing layer, four incompressible boundary layers, and effects of compressibility on flat-plate boundary layers. These numerical applications complement the perturbation analysis predictions of this paper and further validate the claim that the k-ω model is much more accurate than comparable two-equation models. More testing is needed and will be done in future research efforts.

Additional development of the model will be needed, however, before such tests can or should be done. Most importantly, the constitutive relation between Reynolds stress and mean-flow properties must be revised. Use of the Boussinesq approximation that stress is proportional to strain rate fails both to predict anisotropy of the normal stresses and to account for streamline curvature effects. Additionally, it is not at all clear that model predictions will bear any relation to physical reality for flows that are unsteady and/or include boundary-layer separation.

Although important development work remains to be done, the primary intent of this work has been to settle the issue of the correct scale-determining equation, and the effort has been

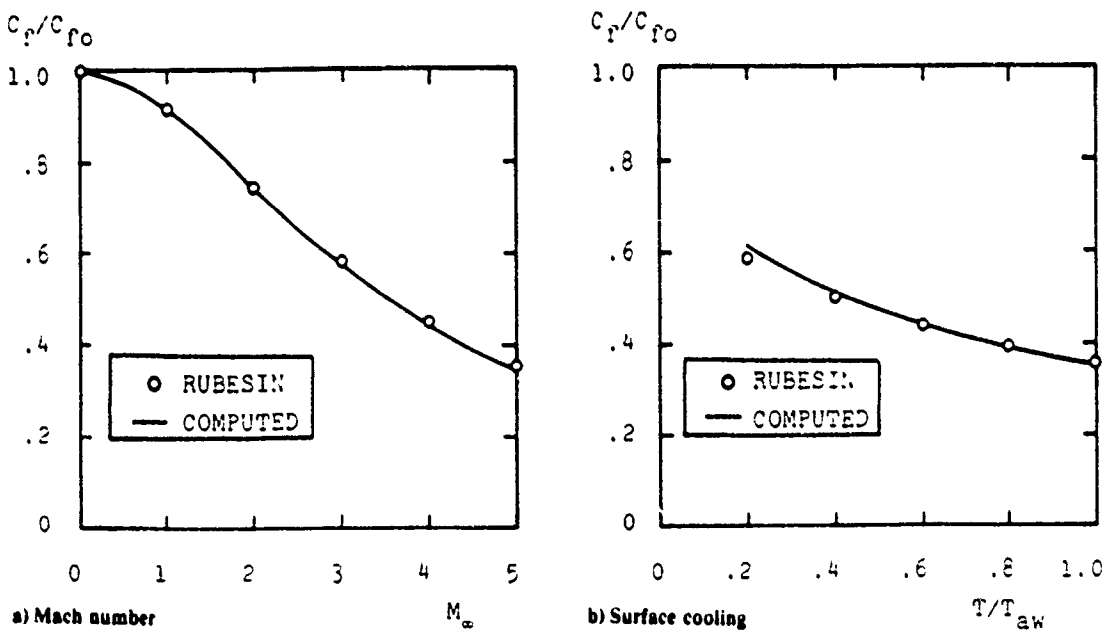

Fig. 7 Comparison of computed and measured effects of freestream Mach number and surface cooling on flat-plate boundary-layer skin friction.

successful. Now that this step has been accomplished, complicating effects such as anisotropic shear, streamline curvature, unsteadiness, and separation can be addressed by building on the solid foundation offered by the k-ω model introduced in this paper.

Appendix: Defect-Layer Equations

In this Appendix, we present details of the formal perturbation expansion solution to the defect-layer equations. First, we summarize the three turbulence models under consideration. Next, we outline the form of the perturbation expansions and state the equations for the leading-order terms in the expansions. Then, we present boundary conditions used in solving the defect-layer equations. Finally, we indicate the manner in which skin friction and wake strength can be extracted from the defect-layer solution.

Turbulence Models Under Consideration

In analyzing the defect layer, we focus on three turbulence models: the new model postulated in Sec. II, the Wilcox-Rubesin[10] model, and the Jones-Launder[3] model. For all three of the models, we must solve the equations for mean mass and momentum conservation, an equation for turbulent energy, and an equation for a turbulence dissipation scale. For all three models, the first three equations assume the following form:

$$\frac{\partial u}{\partial x}+\frac{\partial v}{\partial y}=0 \tag{A1}$$

$$\frac{du}{dt}=U_e\frac{dU_e}{dx}+\frac{\partial}{\partial y}\left[\nu_T\frac{\partial u}{\partial y}\right] \tag{A2}$$

$$\frac{dk}{dt}=\nu_T\left[\frac{\partial u}{\partial y}\right]^2-\epsilon+\frac{\partial}{\partial y}\left[\sigma^*\nu_T\frac{\partial k}{\partial y}\right] \tag{A3}$$

where $d/dt=u\partial/\partial x+v\partial/\partial y$. Note that Eqs. (A1-A3) do not include molecular viscosity. This is a valid approximation in the defect layer as the eddy viscosity is proportional to $U_e\delta^*$, where U_e is the boundary-layer-edge velocity and δ^* is displacement thickness. Hence, the ratio of molecular to eddy viscosity varies inversely with displacement-thickness Reynolds number and is thus very small. The difference among the three models is in the way the dissipation ϵ and the kinematic eddy viscosity ν_T are computed.

For the new model, in addition to Eqs. (A1-A3), we have

$$\epsilon=\beta^*\omega k \tag{A4a}$$

$$\nu_T=k/\omega \tag{A5a}$$

$$\frac{d\omega}{dt}=\gamma\left[\frac{\partial u}{\partial y}\right]^2-\beta\omega^2+\frac{\partial}{\partial y}\left[\sigma\nu_T\frac{\partial\omega}{\partial y}\right] \tag{A6a}$$

$$\gamma=5/9,\quad \beta=3/40,\quad \beta^*=9/100,\quad \sigma=1/2,\quad \sigma^*=1/2 \tag{A7a}$$

In the Wilcox-Rubesin model, the additional equations are as follows:

$$\epsilon=\beta^*\omega k \tag{A4b}$$

$$\nu_T=k/\omega \tag{A5b}$$

$$\frac{d\omega^2}{dt}=\gamma\omega\left[\frac{\partial u}{\partial y}\right]^2-\left[\beta+2\sigma\left(\frac{\partial\ell}{\partial y}\right)^2\right]\omega^3+\frac{\partial}{\partial y}\left[\sigma\nu_T\frac{\partial\omega^2}{\partial y}\right] \tag{A6b}$$

$$\gamma=10/9,\quad \beta=3/20,\quad \beta^*=9/100,\quad \sigma=1/2,\quad \sigma^*=1/2 \tag{A7b}$$

where $\ell=\sqrt{k}/\omega$.

In the Jones-Launder model, we compute dissipation ϵ directly, so that additional equations are

$$\nu_T=\beta^*k^2/\epsilon \tag{A5c}$$

$$\frac{d\epsilon}{dt}=\beta^*C_1k\left[\frac{\partial u}{\partial y}\right]^2-C_2\frac{\epsilon^2}{k}+\frac{\partial}{\partial y}\left[\sigma\nu_T\frac{\partial\epsilon}{\partial y}\right] \tag{A6c}$$

$$\beta^*=9/100,\quad C_1=31/20,\quad C_2=2,\quad \sigma=10/13,\quad \sigma^*=1 \tag{A7c}$$

Expansion Procedure

Following the formulation of Wilcox and Traci,[9] we introduce a stream function ψ and seek a perturbation solution of the form

$$\psi=U_e\Delta\left[\eta-\frac{u_\tau}{U_e}F_1(\eta)+\ldots\right] \tag{A8}$$

$$k=\frac{u_\tau^2}{\sqrt{\beta^*}}\left[K_0(\eta)+\ldots\right] \tag{A9}$$

$$\omega=\frac{u_\tau}{\sqrt{\beta^*}\Delta}\left[W_0(\eta)+\ldots\right] \tag{A10}$$

$$\epsilon=\frac{u_\tau^3}{\Delta}\left[E_0(\eta)+\ldots\right] \tag{A11}$$

where

$$\eta=\frac{y}{\Delta},\qquad \Delta=\frac{U_e\delta^*}{u_\tau} \tag{A12}$$

Inserting Eqs. (A8-A12) into Eqs. (A1-A7), neglecting higher-order terms, letting $N_0(\eta)$ denote dimensionless eddy viscosity, and defining

$$U_1(\eta)=\frac{\partial F_1}{\partial\eta},\qquad L_0(\eta)=\frac{\sqrt{K_0}}{W_0} \tag{A13}$$

we obtain the following equations:

$$\frac{\partial}{\partial\eta}\left[N_0\frac{\partial U_1}{\partial\eta}\right]+(\alpha_T-2\beta_T-2\omega_T)\eta\frac{\partial U_1}{\partial\eta}+(\beta_T-2\omega_T)U_1=2\sigma_T x\frac{\partial U_1}{\partial x} \tag{A14}$$

$$\sigma^*\frac{\partial}{\partial\eta}\left[N_0\frac{\partial K_0}{\partial\eta}\right]+(\alpha_T-2\beta_T-2\omega_T)\eta\frac{\partial K_0}{\partial\eta}-4\omega_TK_0+\sqrt{\beta^*}\left[N_0\left(\frac{\partial U_1}{\partial\eta}\right)^2-E_0\right]=2\sigma_T x\frac{\partial K_0}{\partial x} \tag{A15}$$

where

$$E_0=K_0W_0\qquad\text{and}\qquad N_0=\frac{K_0}{W_0}=\frac{K_0^2}{E_0} \tag{A16}$$

The final equation for each model is different; the equations are:

New model:

$$\sigma\frac{\partial}{\partial\eta}\left[N_0\frac{\partial W_0}{\partial\eta}\right]+(\alpha_T-2\beta_T-2\omega_T)\eta\frac{\partial W_0}{\partial\eta}+(\alpha_T-\beta_T-4\omega_T)W_0+\sqrt{\beta^*}\left[\gamma\left(\frac{\partial U_1}{\partial\eta}\right)^2-\left(\frac{\beta}{\beta^*}\right)W_0^2\right]=2\sigma_T x\frac{\partial W_0}{\partial x} \tag{A17a}$$

Wilcox-Rubesin model:

$$\sigma\frac{\partial}{\partial\eta}\left[N_0\frac{\partial W_0^2}{\partial\eta}\right]+(\alpha_T-2\beta_T-2\omega_T)\eta\frac{\partial W_0^2}{\partial\eta}+2(\alpha_T-\beta_T-4\omega_T)W_0^2+\sqrt{\beta^*}\left\{\gamma W_0\left(\frac{\partial U_1}{\partial\eta}\right)^2-\left[\frac{\beta}{\beta^*}+2\sigma\left(\frac{\partial L_0}{\partial\eta}\right)^2\right]W_0^3\right\}=2\sigma_T x\frac{\partial W_0^2}{\partial x} \tag{A17b}$$

Jones-Launder model:

$$\sigma\frac{\partial}{\partial\eta}\left[N_0\frac{\partial E_0}{\partial\eta}\right]+(\alpha_T-2\beta_T-2\omega_T)\eta\frac{\partial E_0}{\partial\eta}+(\alpha_T-\beta_T-8\omega_T)E_0+\sqrt{\beta^*}\left[\frac{C_1}{\beta^*}K_0\left(\frac{\partial U_1}{\partial\eta}\right)^2-C_2\frac{E_0^2}{K_0}\right]=2\sigma_T x\frac{\partial E_0}{\partial x} \tag{A17c}$$

where the parameters α_T, β_T, σ_T, and ω_T are defined in terms of δ^*, u_τ, and skin friction, $C_f=2(u_\tau/U_e)^2$, i.e.,

$$\alpha_T=\frac{2}{C_f}\frac{d\delta^*}{dx}$$

$$\beta_T=\frac{\delta^*}{\tau_w}\frac{dp}{dx}$$

$$\sigma_T=\frac{\delta^*}{C_f x}$$

$$\omega_T=\frac{\delta^*}{C_f u_\tau}\frac{du_\tau}{dx} \tag{A18}$$

Equations (A14-A17) will have self-similar solutions only if α_T, β_T, and ω_T are independent of x. As noted by Bush and Fendell,[16] for $(U_e\delta^*/\nu)>>1$, u_τ varies sufficiently slowly that we have

$$\omega_T=o(1) \quad \text{as} \quad U_e\delta^*/\nu\to\infty \tag{A19}$$

and, in addition, the shape factor to leading order approaches 1, which (from inspection of the momentum-integral equation) implies

$$\alpha_T\to 1+3\beta_T \quad \text{as} \quad U_e\delta^*/\nu\to\infty \tag{A20}$$

Thus, self-similar solutions exist, provided only that β_T is independent of x.

In summary, the defect-layer equations for the leading-order terms in the perturbation expansions become

All models:

$$\frac{d}{d\eta}\left[N_0\frac{dU_1}{d\eta}\right]+(1+\beta_T)\eta\frac{dU_1}{d\eta}+\beta_T U_1=0 \tag{A21}$$

$$\sigma^*\frac{d}{d\eta}\left[N_0\frac{dK_0}{d\eta}\right]+(1+\beta_T)\eta\frac{dK_0}{d\eta}+\sqrt{\beta^*}\left[N_0\left(\frac{dU_1}{d\eta}\right)^2-E_0\right]=0 \tag{A22}$$

New model:

$$\sigma\frac{d}{d\eta}\left[N_0\frac{dW_0}{d\eta}\right]+(1+\beta_T)\eta\frac{dW_0}{d\eta}+(1+2\beta_T)W_0+\sqrt{\beta^*}\left[\gamma\left(\frac{dU_1}{d\eta}\right)^2-\frac{\beta}{\beta^*}W_0^2\right]=0 \tag{A23a}$$

Wilcox-Rubesin model:

$$\sigma\frac{d}{d\eta}\left[N_0\frac{dW_0^2}{d\eta}\right]+(1+\beta_T)\eta\frac{dW_0^2}{d\eta}+2(1+2\beta_T)W_0^2+\sqrt{\beta^*}\left\{\gamma W_0\left(\frac{dU_1}{d\eta}\right)^2-\left[\frac{\beta}{\beta^*}+2\sigma\left(\frac{dL_0}{d\eta}\right)^2\right]W_0^3\right\}=0 \tag{A23b}$$

Jones-Launder model:

$$\sigma\frac{d}{d\eta}\left[N_0\frac{dE_0}{d\eta}\right]+(1+\beta_T)\eta\frac{dE_0}{d\eta}+(1+2\beta_T)E_0+\sqrt{\beta^*}\left[\frac{C_1}{\beta^*}K_0\left(\frac{dU_1}{d\eta}\right)^2-C_2\frac{E_0^2}{K_0}\right]=0 \tag{A23c}$$

Boundary Conditions

At the outer edge of the defect layer, we require that the velocity equal the freestream velocity. Additionally, we let the turbulent energy assume a small value and insist that the turbulent length scale have zero slope at the boundary-layer edge. In their defect-layer analysis, Wilcox and Traci used these boundary conditions, as well as explicitly prescribing both K_0 and W_0. Thus,

$$U_1=\frac{dL_0}{d\eta}=0 \quad \text{and} \quad K_0=\text{small value} \quad \text{at} \quad \eta=\eta_e \tag{A24}$$

Approaching the surface, we must formally match to the law of the wall. Matching is a bit different for each model but is nevertheless straightforward; details of the algebra will thus be omitted in the interest of brevity. The limiting forms used for $\eta\to 0$ follow.

$$\left.\begin{aligned}U_1&\sim\frac{1}{\kappa}\left[-\ell n\eta+u_0-u_1\eta\ell n\eta\right]\\K_0&\sim\left[1+k_1\eta\ell n\eta\right]\\W_0&\sim\frac{1}{\kappa\eta}\left[1+w_1\eta\ell n\eta\right]\\E_0&\sim\frac{1}{\kappa\eta}\left[1+e_1\eta\ell n\eta\right]\end{aligned}\right\}\quad\text{as}\quad\eta\to 0 \tag{A25}$$

The coefficients u_1, k_1, w_1, and e_1 are as follows:

All models:

$$k_1=\frac{\beta_T/\kappa}{\sigma^*\kappa^2/(2\sqrt{\beta^*})-1} \tag{A26}$$

New model:

$$u_1=\frac{[\beta/(\gamma\beta^*)]\,\sigma^*\kappa^2/(2\sqrt{\beta^*})}{1-\beta/(\gamma\beta^*)}k_1 \tag{A27a}$$

$$w_1=\frac{\sigma^*\kappa^2/(2\sqrt{\beta^*})}{1-\beta/(\gamma\beta^*)}k_1 \tag{A28a}$$

Wilcox-Rubesin model:

$$u_1 = \frac{[\beta/\sqrt{\beta^*} + \sigma\kappa^2]\,\sigma^*\kappa^2/(2\sqrt{\beta^*})}{2\gamma\sqrt{\beta^*}\,[1 - \beta/(\gamma\beta^*)] + 2\sigma\kappa^2}\,k_1 \qquad \text{(A27b)}$$

$$w_1 = \frac{\gamma\sqrt{\beta^*}\,[\sigma^*\kappa^2/(2\sqrt{\beta^*})] + \sigma\kappa^2}{2\gamma\sqrt{\beta^*}\,[1 - \beta/(\gamma\beta^*)] + 2\sigma\kappa^2}\,k_1 \qquad \text{(A28b)}$$

Jones-Launder model:

$$u_1 = \frac{(1 + \sigma^*\kappa^2/\sqrt{\beta^*})C_2 - C_1}{2(C_1 - C_2)}\,k_1 \qquad \text{(A27c)}$$

$$e_1 = \frac{(1 + \sigma^*\kappa^2/\sqrt{\beta^*})C_1 - C_2}{2(C_1 - C_2)}\,k_1 \qquad \text{(A28c)}$$

Additionally, the coefficient u_0 is determined from the integral constraint for mass conservation, that is,

$$\int_0^{\eta_e} U_1(\eta)\,d\eta = 1 \qquad \text{(A29)}$$

To implement Eq. (A29) in the numerical solution of the defect-layer equations, we proceed as follows. Because the velocity is singular at $\eta = 0$, we integrate the numerical velocity profile from a point above the surface, which we denote by η_L (typically of order 0.001-0.01), to the edge of the boundary layer η_e. Then, we integrate the asymptotic profile for $U_0(\eta)$ given in Eqs. (A25) from $\eta = 0$ to $\eta = \eta_L$. The latter integration involves the unknown coefficient u_0. Finally, the sum of these two integrals must be unity by virtue of Eq. (A29).

Skin Friction and Wake Strength

It is possible to determine the skin friction implied by the solution to the defect-layer equations by formal matching to the sublayer asymptotic velocity profile. Considering only leading-order terms, we say:

$$\lim_{y^+ \to \infty}\left[\frac{1}{\kappa}\ln y^+ + B\right] = \lim_{\eta \to 0}\left[\frac{U_e}{u_\tau} + \frac{1}{\kappa}\ln\eta - \frac{1}{\kappa}u_0\right] \qquad \text{(A30)}$$

We note that $y^+ = \eta/(U_e\delta^*/\nu)$ and $u_\tau/U_e = \sqrt{C_f/2}$, there follows immediately:

$$\sqrt{\frac{C_f}{2}} = B + \frac{1}{\kappa}u_0 + \frac{1}{\kappa}\ln\left(\frac{U_e\delta^*}{\nu}\right) \qquad \text{(A31)}$$

Finally, combining Coles' composite profile [Eq. (22)] with Eq. (A31) and evaluating the resulting equation at the boundary-layer edge, we arrive at the following expression for wake strength $\tilde{\pi}$.

$$\tilde{\pi} = \tfrac{1}{2}(u_0 - \ln\eta_e) \qquad \text{(A32)}$$

Acknowledgment

This research was sponsored by the U.S. Army Research Office under Contract DAAG-29-83-C-0003 with Dr. Robert E. Singleton as technical monitor.

References

[1]Cebeci, T. and Smith, A. M. O., *Analysis of Turbulent Boundary Layers*, Series in Applied Mathematics and Mechanics, Vol XV, Academic Press, Orlando, FL, 1974

[2]Coles, D. E. and Hirst, E. A., *Computation of Turbulent Boundary Layers—1968 AFOSR-IFP-Stanford Conference*, Vol. II, Stanford Univ. Press, Stanford, CA, 1969.

[3]Bradshaw, P., Ferriss, D. H., and Atwell, N. P., "Calculation of Boundary Layer Development Using the Turbulent Energy Equation," *Journal of Fluid Mechanics*, Vol. 28, Pt. 3, 1967, pp. 593-616.

[4]Donaldson, C. duP., "Calculation of Turbulent Shear Flows for Atmospheric and Vortex Motions," *AIAA Journal*, Vol. 10, Jan 1972, pp. 4-12.

[5]Jones, W. P. and Launder, B. E., "The Prediction of Laminarization with a Two-Equation Model of Turbulence," *International Journal of Heat and Mass Transfer*, Vol. 15, 1972, pp. 301-314.

[6]Rodi, W., "Progress in Turbulence Modeling for Incompressible Flows," AIAA Paper 81-0045, Jan. 1981.

[7]Wilcox, D. C. and Alber, I. E., "A Turbulence Model for High Speed Flows," *Proceedings of the 1972 Heat Transfer and Fluid Mechanics Institute*, Stanford Univ. Press, Stanford, CA, 1972, pp. 231-252

[8]Saffman, P. G. and Wilcox, D. C., "Turbulence-Model Predictions for Turbulent Boundary Layers," *AIAA Journal*, Vol. 12, April 1974, pp. 541-546.

[9]Wilcox, D. C. and Traci, R. M., "A Complete Model of Turbulence," AIAA Paper 76-351, July 1976.

[10]Wilcox, D. C. and Rubesin M. W., "Progress in Turbulence Modeling for Complex Flow Fields Including Effects of Compressibility," NASA TP-1517, April 1980.

[11]Kline, S. J., Cantwell, B. J., and Lilley, G. M. (eds.), *Proceedings of the 1980-81 AFOSR-HTTM-Stanford Conference on Complex Turbulent Flows*, Stanford Univ. Press, Stanford, CA, 1981.

[12]MacCormack, R. W., "A Numerical Method for Solving the Equations of Compressible Viscous Flow," AIAA Paper 81-0110, Jan. 1981.

[13]Favre, A., "Equations des Gaz Turbulents Compressibles," *Journal de Mecanique*, Vol. 4, No. 3, 1965, pp. 361-390.

[14]Kolmogorov, A. N., "Equations of Turbulent Motion of an Incompressible Fluid," *Izvestia Academy of Sciences, USSR; Physics*, Vol. 6, Nos. 1 and 2, 1942, pp. 56-58.

[15]Townsend, A. A., *The Structure of Turbulent Shear Flow*, 2nd ed., Cambridge University Press, Cambridge, England, 1976, pp. 107-108.

[16]Bush, W. B. and Fendell, F. E., "Asymptotic Analysis of Turbulent Channel and Boundary-Layer Flow," *Journal of Fluid Mechanics*, Vol. 56, Pt. 4, 1972, pp. 657-681

[17]Chambers, T. L. and Wilcox, D. C., "Critical Examination of Two-Equation Turbulence Closure Models for Boundary Layers," *AIAA Journal*, Vol 15, July 1977, pp. 821-828.

[18]Laufer, J., "The Structure of Turbulence in Fully Developed Pipe Flow," NACA 1174, 1952.

[19]Andersen, P. S., Kays, W. M., and Moffat, R. J., "The Turbulent Boundary Layer on a Porous Plate: An Experimental Study of the Fluid Mechanics for Adverse Free-Stream Pressure Gradients," Dept. of Mechanical Engineering, Stanford University, Stanford, CA, Rept. HMT-15, May 1972.

[20]Saffman, P. G., "A Model for Inhomogeneous Turbulent Flow," *Proceedings of the Royal Society, London*, Vol. A317, 1970, pp. 417-433.

[21]Schlichting, H., *Boundary Layer Theory*, 4th ed., McGraw-Hill, New York, 1960, pp. 519-527.

[22]Wilcox, D. C. and Chambers, T. L., "Further Refinement of the Turbulence Model Transition-Prediction Technique," DCW Industries, Sherman Oaks, CA, Rept. DCW-R-03-02, 1975.

[23]Wilcox, D. C., "Program EDDYBL User's Guide," DCW Industries, La Cañada, CA, Rept. DCW-R-NC-04 1988.

[24]Blottner, F. G., "Variable Grid Scheme Applied to Turbulent Boundary Layers," *Computational Methods for Applied Mechanics and Engineering*, Vol. 4, No. 2, 1974, pp. 179-194.

[25]Wilcox, D. C., "Algorithm for Rapid Integration of Turbulence Model Equations on Parabolic Regions," *AIAA Journal*, Vol. 19, Feb. 1981, pp. 248-251.

[26]Wilcox, D. C., "A Complete Model of Turbulence Revisited," AIAA Paper 84-0176, Jan. 1984.

[27]Rodi, W. and Scheuerer, G., "Scrutinizing the k-ϵ Turbulence Model Under Adverse Pressure Gradient Conditions," *Transactions of the ASME*, Vol 108, June 1986, pp. 174-179.

[28]Wilcox, D. C., "More Advanced Applications of the Multiscale Model for Turbulent Flows," AIAA Paper 88-0220, Jan. 1988.

APPENDIX B: MULTISCALE MODEL BASELINE PAPER

The paper reproduced in this appendix appears in the November, 1988 issue of the AIAA Journal. The formal reference to this paper is as follows.

> Wilcox, D. C., "Multiscale Model for Turbulent Flows," *AIAA Journal*, Vol. 26, No. 11, Nov. 1988, pp. 1311-1320.

This paper defines the Wilcox multiscale model of turbulence. The primary contribution is development of a model that does not require use of the Boussinesq approximation. The model has most of the generality of a full second-order closure model while being nearly as simple to implement as an algebraic stress model. Applications include homogeneous turbulent flows, incompressible and compressible boundary layers and unsteady boundary layers.

Multiscale Model for Turbulent Flows

David C. Wilcox*
DCW Industries, Inc., La Cañada, California

A model is devised for computing general turbulent flows. The model is an improvement over two-equation turbulence models in a critically important manner, that is, the new model accounts for disalignment of the Reynolds-stress-tensor and the mean-strain-rate-tensor principal axes. The improved representation of the Reynolds-stress tensor has been accomplished through the introduction of a multiscale description of the turbulence, i.e., two energy scales are used corresponding to upper and lower partitions of the turbulence energy spectrum. A novel feature of the formulation is that the differential equation for the Reynolds-stress tensor is of first order, which in effect corresponds to what can be termed an "algebraic stress model" with convective terms. As a consequence of its mathematical simplicity, the model is very efficient and easy to implement computationally. The model is applied to a wide range of turbulent flows including homogeneous turbulence, compressible and incompressible two-dimensional boundary layers, and unsteady boundary layers including periodic separation and reattachment. Comparisons with corresponding experimental data show that the model reproduces all salient features of the flows considered. Perturbation analysis of the viscous sublayer shows that integration through the sublayer can be accomplished with no special viscous modifications to the closure coefficients appearing in the model.

I. Introduction

THIS paper presents results of the second phase of a continuing turbulence-modeling effort initiated after the second Stanford conference[1] on turbulent flows. The first phase led to development of a new two-equation turbulence model[2] that is much more accurate than any existing model for boundary layers in an adverse pressure gradient. In this phase, the primary goal is to focus on the constitutive relation between Reynolds stress and mean-flow properties.

An important shortcoming of two-equation turbulence models is their inability to adjust at physically realistic rates to a change in the mean-strain-rate tensor field. This shortcoming is most easily seen by examining two-equation model predictions for homogeneous turbulence in uniform shear, such as the flow considered by Champagne et al.[3] Wilcox and Rubesin[4] have shown that a two-equation model predicts an asymptotic approach to the experimentally measured asymptotic structure to within experimental accuracy. However, the predicted time to reach the asymptote is an order of magnitude longer than measured. This shortcoming is a direct consequence of the two-equation model's assumption that Reynolds stress is proportional to mean-strain rate.

Another straightforward example of this shortcoming is provided by a homogeneous turbulence that has been subjected to some time to a uniform rate of strain, followed by sudden removal of the strain rate. As shown in many experiments, the turbulence approaches isotropy asymptotically with time. However, if we postulate that Reynolds stress is proportional to mean-strain rate, the model will predict an instantaneous return to isotropy. Note that the same conclusion holds for nonlinear stress/strain-rate constitutive relationships, such as the so-called algebraic stress model.

To overcome this shortcoming, some researchers have attempted to develop a model for the Reynolds-stress tensor equation obtained by taking moments of the Navier-Stokes equation. The drastic surgery performed in such attempts often leaves rigor far behind and, in effect, appears more as an attempt to model the differential equations rather than the physics of turbulent flow processes. In this study, a deliberate attempt has been made to avoid the conventional approach. Thus, although the final set of equations formulated in this paper shares many features of models devised by others, the approach taken differs both in detail and in spirit.

There have been two key developments that have stimulated the approach taken in this paper. The first is the development of the algebraic stress model by Rodi[5] and subsequently exercised in many applications by Lakshminarayana.[6] Using the algebraic stress model yields an accurate method for describing effects of streamline curvature and secondary motions, for example, two effects that cannot be directly represented with a standard two-equation turbulence model. The second development is the elegant Johnson-King[7] model. This model implements a simple first-order differential equation for shear-stress magnitude to be used in conjunction with the mixing-length model in order to circumvent shortcomings of the mixing-length model in separated flows. The goals of this study are to 1) create a model similar to the algebraic stress model, which also accounts for sudden changes in mean-strain rate, and 2) create a complete tensor-invariant analog of the Johnson-King model in the context of advanced turbulence models.

In this paper, we begin with the premise that turbulence can be described by representing the turbulence energy spectrum in terms of an upper and a lower partition with the upper partition corresponding to lowest frequency, energy-bearing eddies. This notion is used in large-eddy simulation work[8] where small eddies (corresponding to the lower partition of the spectrum) are modeled and large eddies (corresponding to the upper partition of the spectrum) are numerically simulated. By contrast, we model both the small and the large eddies. We use the general observations[9] that eddies in the lower partition are expected to contain most of the vorticity, to be isotropic, and to dissipate rapidly into heat. A key feature of eddies in the upper partition is that they are more or less inviscid. As shown in Sec. III, in terms of model equations these facts yield 1) two

Presented as Paper 86-0029 at the AIAA 24th Aerospace Sciences Meeting, Reno, NV, Jan. 6-9, 1986, and Paper 87-0290 at the AIAA 25th Aerospace Sciences Meeting, Reno, NV, Jan. 12-15, 1987; received Jan. 29, 1987; revision received Dec. 21, 1987. Copyright © American Institute of Aeronautics and Astronautics, Inc., 1988. All rights reserved.

*President. Associate Fellow AIAA

equations that are essentially the two-equation model devised by Wilcox,[2] and 2) an inviscid tensor equation for the upper partition contribution to the Reynolds-stress tensor.

After stating the complete multiscale model equations in Sec. II, closure approximations are discussed in detail in Sec. III. In special limiting cases, some of the approximations are similar to those introduced by Launder et al.[10] All closure coefficients that the multiscale model has in common with the Wilcox k-ω model[2] assume the same values used in the two-equation model. Values for all additional closure coefficients are selected based on general observations of turbulent flow behavior, perturbation analysis of the viscous sublayer, and a modest amount of computer optimization. Section IV presents results of numerical applications to homogeneous turbulent flows. Section V summarizes results of a perturbation analysis of model-predicted viscous sublayer structure. Section VI presents three types of numerical applications including steady incompressible turbulent boundary layers, steady compressible turbulent boundary layers, and unsteady incompressible turbulent boundary layers. In all cases, comparisons with experimental data are presented.

II. Equations of Motion

Before proceeding to develop the multiscale model, it is instructive to first summarize the complete set of equations that constitute the model. For general compressible turbulent fluid flows, the turbulence model equations are written in terms of Favre[11] mass-averaged quantities as follows:

Mass conservation:

$$\frac{\partial \rho}{\partial t} + \frac{\partial}{\partial x_j}(\rho u_j) = 0 \tag{1}$$

Momentum conservation:

$$\frac{\partial}{\partial t}(\rho u_i) + \frac{\partial}{\partial x_j}(\rho u_j u_i) = -\frac{\partial p}{\partial x_i} + \frac{\partial \hat{\tau}_{ij}}{\partial x_j} \tag{2}$$

Mean energy Conservation:

$$\frac{\partial}{\partial t}(\rho E) + \frac{\partial}{\partial x_j}(\rho u_j H) = \frac{\partial}{\partial x_j}\left[u_i \hat{\tau}_{ij} + (\mu + \sigma^* \mu_T)\frac{\partial k}{\partial x_j} - q_j\right] \tag{3}$$

Turbulent kinetic energy:

$$\frac{\partial}{\partial t}(\rho k) + \frac{\partial}{\partial x_j}(\rho u_j k) = \tau_{ij}\frac{\partial u_i}{\partial x_j} - \beta^* \rho \omega k + \frac{\partial}{\partial x_j}\left[(\mu + \sigma^* \mu_T)\frac{\partial k}{\partial x_j}\right] \tag{4}$$

Specific dissipation rate:

$$\frac{\partial}{\partial t}(\rho \omega) + \frac{\partial}{\partial x_j}(\rho u_j \omega) = \left(\frac{\gamma \omega}{k}\right)\tau_{ij}\frac{\partial u_i}{\partial x_j} - \beta \rho \omega^2 - \xi \beta \rho \omega \sqrt{2\Omega_{mn}\Omega_{nm}} + \frac{\partial}{\partial x_j}\left[(\mu + \sigma \mu_T)\frac{\partial \omega}{\partial x_j}\right] \tag{5}$$

Upper partition stress tensor:

$$\frac{\partial}{\partial t}(\rho T_{ij}) + \frac{\partial}{\partial x_k}(\rho u_k T_{ij}) = -P_{ij} + E_{ij} \tag{6}$$

where t is time, x_i is position vector, u_i is velocity vector, ρ is density, p is pressure, μ is molecular viscosity, $\hat{\tau}_{ij}$ is the sum of the molecular and Reynolds stress tensors, and q_j is the sum of the molecular and turbulent heat flux vectors. In Eq. (3), the quantities $E = \epsilon + k + u_i u_i/2$ and $H = h + k + u_i u_i/2$ are total energy and enthalpy, respectively, with $h = \epsilon + p/\rho$; ϵ and h denote internal energy and enthalpy. Additionally, τ_{ij} is the Reynolds-stress tensor. The turbulent kinetic energy k and the specific dissipation rate ω are needed to define the eddy viscosity μ_T, which is given by

$$\mu_T = \rho k/\omega \tag{7}$$

The total viscous stress tensor is given by

$$\hat{\tau}_{ij} = 2\mu\left[S_{ij} - \left(\frac{1}{3}\right)\left(\frac{\partial u_k}{\partial x_k}\right)\delta_{ij}\right] + \tau_{ij} \tag{8}$$

where, by definition, the mean-strain-rate tensor S_{ij} and the mean-rotation tensor Ω_{ij} [appearing in Eq. (5)] are given by

$$S_{ij} = \frac{1}{2}\left(\frac{\partial u_i}{\partial x_j} + \frac{\partial u_j}{\partial x_i}\right) \tag{9a}$$

$$\Omega_{ij} = \frac{1}{2}\left(\frac{\partial u_i}{\partial x_j} - \frac{\partial u_j}{\partial x_i}\right) \tag{9b}$$

The heat flux vector q_j is approximated as

$$q_j = -\left(\frac{\mu}{Pr_L} + \frac{\mu_T}{Pr_T}\right)\frac{\partial h}{\partial x_j} \tag{10}$$

where Pr_L and Pr_T are the laminar and turbulent Prandtl numbers, respectively.

In order to close this system of equations, we must postulate a relation between the Reynolds stress tensor τ_{ij} and mass-averaged flow properties. The multiscale model computes τ_{ij} according to

$$\tau_{ij} = \rho T_{ij} - \tfrac{2}{3}\rho e \delta_{ij} \tag{11}$$

where ρT_{ij} is the upper partition contribution to the Reynolds-stress tensor and ρe is the energy of the eddies in the lower partition. The tensor E_{ij} in Eq. (6) represents the exchange of energy among the mean, upper, and lower partition energies and is given by

$$E_{ij} = -C_1 \beta^* \omega\left(\tau_{ij} + \frac{2}{3}\rho k \delta_{ij}\right) + \hat{\alpha} P_{ij} + \hat{\beta} D_{ij} + \hat{\gamma}\rho k\left(S_{ij} - \frac{1}{3}\frac{\partial u_k}{\partial x_k}\delta_{ij}\right) + \frac{2}{3}\rho \omega k (1 - e/k)^{3/2}\delta_{ij} \tag{12}$$

The tensors P_{ij} and D_{ij} are the conventional production tensors defined by

$$P_{ij} = \tau_{im}\frac{\partial u_j}{\partial x_m} + \tau_{jm}\frac{\partial u_i}{\partial x_m} \tag{13a}$$

$$D_{ij} = \tau_{im}\frac{\partial u_m}{\partial x_j} + \tau_{jm}\frac{\partial u_m}{\partial x_i} \tag{13b}$$

Finally, the 10 closure coefficients appearing in Eqs. (1-12) are as follows.

$$\hat{\alpha} = 42/55, \quad \hat{\beta} = 6/55, \quad \hat{\gamma} = 1/4$$

$$\beta = 3/40, \quad \gamma = 4/5, \quad \sigma = 1/2$$

$$\beta^* = 9/100, \quad \xi = 1, \quad \sigma^* = 1/2$$

$$C_1 = 1 + 4(1 - e/k)^{3/2} \tag{14}$$

III. Theoretical Formulation of the Model

For the sake of clarity, formulation of the multiscale model is done for incompressible flow. The most noteworthy feature of the multiscale model is the idea that we must keep track of energy in two separate partitions of the turbulence energy spectrum. In this spirit, the lower partition of the spectrum is postulated to be responsible for the equilibrium value of the Reynolds-stress tensor, whereas the upper partition gives rise to departure from equilibrium. In formulating the model, special care has been taken in 1) tracing energy transfer between the mean, upper, and lower partition energies, 2) modeling as much of the physics of turbulence as possible within a phenomenological point of view, 3) achieving consistency with conventional closure approximations in special limiting cases, and 4) devising a set of equations that are numerically tractable.

A. Basic Postulates

We begin with the premise that turbulence can be described in terms of the energies of two separate partitions of the turbulence energy spectrum. We also make use of the general observations that eddies in the lower partition are expected to contain most of the vorticity, to be isotropic, and to dissipate rapidly into heat, whereas the eddies in the upper partition are inviscid. In terms of model equations, these facts are stated as follows.

B. Mathematical Decomposition

For incompressible flows, the Reynolds-stress tensor $\tau_{ij} = -\rho \overline{u_i' u_j'}$, where the overbar denotes mass average, is represented as the sum of two contributions,

$$\tau_{ij} = \rho T_{ij} + \rho t_{ij} \tag{15}$$

where T_{ij} and t_{ij} are attributed to the upper and lower partitions, respectively. Assuming the eddies in the upper partition are inviscid, the tensor T_{ij} will change as a result of work done against the mean-velocity gradient field and energy exchange with the eddies in the lower partition. Mathematically, we state these facts by writing

$$\rho \frac{\mathrm{d}T_{ij}}{\mathrm{d}t} = -P_{ij} + E_{ij} \tag{16}$$

where $\mathrm{d}/\mathrm{d}t = \partial/\partial t + u_k \partial/\partial x_k$. The tensor P_{ij} is the production tensor defined in Eq. (13a), and E_{ij} is the energy exchange tensor. Assuming the eddies in the lower partition are isotropic, we can say

$$t_{ij} = -\tfrac{2}{3} e \delta_{ij} \tag{17}$$

where the quantity e represents the energy of the eddies in the lower partition. The equation for e can be written as

$$\rho \frac{\mathrm{d}e}{\mathrm{d}t} = E - D + F \tag{18}$$

where F is diffusion, D is dissipation, and E is the trace of E_{ij}, i.e.,

$$E = \tfrac{1}{2} E_{mm} \tag{19}$$

The total kinetic energy of the turbulent fluctuations k is expressed by contracting the Reynolds-stress tensor so that, in terms of e and T_{ij},

$$k = e - \tfrac{1}{2} T_{mm} \tag{20}$$

Hence, contracting Eq. (16) and combining with Eqs. (18-20), we obtain the following equation for k:

$$\rho \frac{\mathrm{d}k}{\mathrm{d}t} = P - D + F \tag{21}$$

where the "production" term P is the trace of the production tensor, i.e.,

$$P = \tfrac{1}{2} P_{mm} \tag{22}$$

C. Closure Approximation

In order to close the system, we must establish mathematical approximations for the dissipation D, diffusion F, and the energy exchange tensor E_{ij}. To maintain consistency with the Wilcox[2] k-ω model formulation, we express the dissipation and diffusion terms according to

$$D = \beta^* \rho \omega k \tag{23a}$$

$$F = \frac{\partial}{\partial x_j}\left[(\mu + \sigma^* \mu_T)\frac{\partial k}{\partial x_j}\right] \tag{23b}$$

where σ^* is a closure coefficient.

Thus, the remaining task is to establish a rational representation for the energy transfer tensor. We do this in two steps. First, we examine the decay of homogeneous turbulence in the absence of mean velocity gradients. Then, we examine the limiting case of a constant-pressure boundary layer.

In the first step of this procedure, we thus focus on homogeneous turbulence with all mean-velocity gradients set to zero. For such turbulence, the equations for total turbulence kinetic energy and for the energy of the upper partition eddies (k-e) are given by

$$\rho \frac{\mathrm{d}k}{\mathrm{d}t} = -D \tag{24a}$$

$$\rho \frac{\mathrm{d}(k\text{-}e)}{\mathrm{d}t} = -E \tag{24b}$$

Now, if we define the characteristic length scale of the turbulence b·

$$\ell = \frac{k^{1/2}}{\omega} \tag{25}$$

then we can rewrite the equation for k as follows:

$$\frac{\mathrm{d}k}{\mathrm{d}t} = -\frac{\beta^* k^{3/2}}{\ell} \tag{26}$$

We now postulate that the large eddies decay on the same scale as the overall turbulence, so that we expect to have

$$\frac{\mathrm{d}(k\text{-}e)}{\mathrm{d}t} = -\frac{\beta^*(k\text{-}e)^{3/2}}{\ell} = -\beta^* \omega k \left(1 - \frac{e}{k}\right)^{3/2} \tag{27}$$

Thus, in the absence of mean velocity gradients, we postulate that the limiting form of E is given by

$$E = \beta^* \rho \omega k \left(1 - \frac{e}{k}\right)^{3/2} \qquad \text{for } S_{ij} = 0 \tag{28}$$

In the second step of the procedure, note that we can combine the lower and upper partition equations to derive an equation for the Reynolds-stress tensor. The equation assumes the following form:

$$\frac{\mathrm{d}\tau_{ij}}{\mathrm{d}t} = -P_{ij} + \tfrac{2}{3}\beta^* \rho \omega k \delta_{ij} + \left(E_{ij} - \tfrac{2}{3} E \delta_{ij}\right) + (\text{diffusion terms}) \tag{29}$$

Equation (29) matches the Launder et al.[10] closure approximation and is consistent with Eq. (28), provided we select

$$E_{ij} = -C_1\beta^*\omega(\tau_{ij} + \tfrac{2}{3}\rho k\delta_{ij}) + \hat{\alpha}P_{ij} + \hat{\beta}D_{ij} + \hat{\gamma}\rho kS_{ij} + \tfrac{2}{3}\beta^*\rho\omega k\left(1 - \frac{e}{k}\right)^{3/2}\delta_{ij} \tag{30}$$

where C_1, $\hat{\alpha}$, $\hat{\beta}$, and $\hat{\gamma}$ are additional closure coefficients, and D_{ij} is defined in Eq. (13b).

D. Specific Dissipation-Rate Equation

One additional equation is needed to close the system, namely, an equation for the specific dissipation rate ω. Again, we draw from the earlier work on the two-equation model[2] and an interesting development extracted from the large-eddy simulation work of Bardina et al.[8] The postulated equation for ω is

$$\rho\frac{d\omega}{dt} = \left(\frac{\gamma\omega}{k}\right)P - \beta\rho\omega^2 - \xi\beta\rho\omega\sqrt{2\Omega_{mn}\Omega_{nm}} + \frac{\partial}{\partial x_j}\left[(\mu + \sigma\mu_T)\frac{\partial\omega}{\partial x_j}\right] \tag{31}$$

where β, γ, ξ, and σ are closure coefficients.

The term proportional to ξ follows the work of Bardina et al.[8] In the context of homogeneous turbulence, it is required in order to accurately simulate effects of system rotation. The term also introduces subtle differences between model-predicted effects of plane strain and uniform shear on homogeneous turbulence.

E. Closure Coefficients

The model contains a total of 10 closure coefficients: β, β^*, γ, σ, σ^*, ξ, C_1, $\hat{\alpha}$, $\hat{\beta}$, and $\hat{\gamma}$. We use arguments similar to those presented by Wilcox[2] and in addition we have gone through a very careful series of computations to establish the value of each. Note that, consistent with the notions that most of the vorticity is contained in the lower partition eddies, and that ω is closely related to the fluctuating vorticity, we expect that the four coefficients appearing in Eq. (31) must be independent of the ratio of e to k. After more than 30 applications of this model, we find that only C_1 needs to depend on e/k, and it does so in a straightforward manner. To complete the formulation, a relationship between C_1 and the ratio of e to k must be established. That C_1 should depend upon this ratio seems logical for the following reasons. The mathematical representation of turbulence adopted for this model includes two distinct energy scales. Additionally, inspection of Eqs. (29) and (30) shows that the term proportional to C_1 represents the rate at which anisotropic turbulence returns to isotropy. The process of returning to isotropy should involve interaction of the turbulence with itself, with no net change in total energy of the turbulence. Thus, the only energy scales relevant in such a process would be e and k. Assuming no other dimensional parameters are pertinent (e.g., viscosity), then the only dimensionless grouping available is e/k.

Experimental observations[12] indicate that large eddies tend toward isotropy more rapidly than small eddies. Then, if we rewrite the return-to-isotropy term as

$$C_1\beta^*\omega[\tau_{ij}/\rho + \tfrac{2}{3}k\delta_{ij}] = C_1\epsilon_{tot}[\tau_{ij}/(\rho k) + \tfrac{2}{3}\delta_{ij}] \tag{32}$$

where $\epsilon_{tot} = \beta^*\omega k$ appears in the turbulent energy equation, a plausible approximation is to say

$$C_1\epsilon_{tot} = C_{1L}\epsilon_L + C_{1S}\epsilon_S \tag{33}$$

where ϵ_L and ϵ_S are the dissipation terms appearing in the equations for the upper partition energy (k-e) and the lower partition energy e, respectively. Straightforward manipulation of Eqs. (26), (27), and (33) yields

$$C_1 = C_{1L}\left(1 - \frac{e}{k}\right)^{3/2} + C_{1S}\left[1 - \left(1 - \frac{e}{k}\right)^{3/2}\right] \tag{34}$$

In the limiting case where only small eddies are present, i.e., the limiting case $e \to k$, we expect C_1 to asymptotically approach its smallest physically acceptable value of unity. (If C_1 were smaller than one, anisotropic turbulence would depart further from isotropy.) Thus,

$$C_{1S} = 1 \tag{35}$$

In order to establish the value of C_{1L}, we turn now to analysis of the so-called wall layer. The wall layer is the region of a constant-pressure boundary layer sufficiently close to the surface that convective terms are negligible, yet sufficiently distant from the surface that effects of molecular viscosity are negligible. In the wall layer, the velocity follows the classical law of the wall. Perturbation analysis of the multiscale model shows that convective terms are negligible and, to leading order, the diffusion term in the turbulent energy equation is negligible. From these observations there follows immediately

$$e/k = 1 - (1 - \hat{\alpha} - \hat{\beta})^{3/2} \doteq \tfrac{1}{4} \tag{36}$$

in the wall layer. Then, insisting that the value of C_1 for the wall layer match the value used by Launder et al.,[10] namely, 3/2, there follows

$$C_{1L} = 5 \tag{37}$$

Thus, the final form for C_1 postulated for the multiscale model is given by

$$C_1 = 1 + 4\left(1 - \frac{e}{k}\right)^{3/2} \tag{38}$$

In summary, the closure coefficients for the multiscale model are given in Eqs. (14). All applications in the following sections have been done using these values for the closure coefficients.

F. Discussion

Before proceeding to the applications, it is worthwhile to pause and discuss some of the premises underlying formulation of the multiscale model. A novel feature of the model is that it uses a single turbulence-length-scale determining equation. This is a direct consequence of the assumption that upper partition eddies decay on the same scale as the overall turbulence, as reflected in Eq. (27). This approximation has been, to some extent, substantiated by large-eddy simulation studies.[8] Given the uncertainties surrounding proper modeling of the length-scale-determining equation, introducing this approximation is neither more nor less rigorous than adding a second length-scale determining equation. Note that this means the model equations implicitly (and automatically) determine the boundary between the lower and upper partitions of the energy spectrum.

The most controversial approximation made is that the lower partition eddies are isotropic. To explain why, we first contract Eq. (6) to form the following equation for the upper partition turbulent energy:

$$\rho\frac{d(k-e)}{dt} = (1 - \hat{\alpha} - \hat{\beta})P - \beta^*\rho\omega k\left(1 - \frac{e}{k}\right)^{3/2} \tag{39}$$

Because we have used the Launder-Reece-Rodi values for $\hat{\alpha}$ and $\hat{\beta}$, the value of $(1 - \hat{\alpha} - \hat{\beta})$ is approximately 0.13. Consequently, only 13% of the total turbulence energy production goes into the upper partition. Thus, we should expect that the lower partition energy will often be a significant fraction of

the total. In the wall layer, for example, the ratio e/k is 0.75. This means that the boundary between energy partitions will often lie above the inertial subrange, encroaching on the energy-containing eddies, which are certainly not isotropic. Although postulating that eddies this far up the spectrum are isotropic may be physically unrealistic, the mathematical simplification attending the approximation is tremendous. The simplification is most evident if we form the equation for the Reynolds-stress deviator $(\tau_{ij} + \frac{2}{3}\rho k\delta_{ij})$ implied by the model, that is,

$$\frac{d}{dt}(\tau_{ij} + \tfrac{2}{3}\rho k\delta_{ij}) = -(P_{ij} - \tfrac{2}{3}P\delta_{ij}) + (E_{ij} - \tfrac{2}{3}E\delta_{ij}) \tag{40}$$

This equation is of first order due to the absence of diffusion terms. We should thus expect its implementation to be less difficult than that of a full Reynolds-stress transport model. This has indeed proven to be the case. As the entire formulation is empirical in its essence, the usefulness of and justification for any such approximation ultimately lies in how well the model performs in applications, and we defer to the applications of the following sections as our justification.

A few additional words regarding the absence of diffusion terms are in order. One guiding premise of this modeling effort has been to include the minimum amount of complexity while capturing the maximum amount of the physics of turbulence, with the central goal being to remove limitations imposed by the Boussinesq approximation. Most turbulence modeling researchers accept without question the commonly used approximation that triple correlation terms in the exact equation for τ_{ij} can be modeled with a gradient-diffusion approximation. Aside from the fact that using gradient-diffusion approximations to describe any aspect of turbulent mixing requires stretching the imagination a bit, it seems pointless to include such terms at the expense of elegance and mathematical complexity. This is especially true since, in most applications, the standard diffusion terms used are negligible. Ideally, the closure approximations chosen for the multiscale model implicitly include all salient effects of the triple correlation terms. To carry this discussion any further, however, violates a basic objective of this study, viz., to model the physics of turbulence rather than the differential equations.

IV. Homogeneous Turbulence

The first round of applications is to homogeneous turbulent flows. The cases selected are most of those considered in the second Stanford conference[1] and are as listed in Table 1. Most of the results submitted to the Stanford conference for the homogeneous turbulence cases could not be considered acceptable for general engineering applications. As will be shown in this section, the multiscale model performs exceptionally well for homogeneous turbulent flows. Note that in all of the homogeneous turbulence computations performed, the initial value of the specific dissipation rate ω_o has been chosen to insure a match between computed and measured turbulent kinetic energy k at the end of the computation. The average difference between the value of ω_o determined in this manner and the values recommended for use in the conference is 17%.

A. Decay of Isotropic Turbulence

Decay of isotropic turbulence is the simplest of all homogeneous turbulent flows. The case considered here is flow 0371 of the Stanford conference. The initial value of e/k has no effect on this computation. As shown in Fig. 1a, computed and measured values of k are virtually identical. This is no major surprise, however, as the ratio of β to β^* has been chosen to insure accurate simulation of this flow.

B. Effects of System Rotation

Turning now to effects of system rotation, the term in Eq. (5) proportional to ξ plays a central role. As noted earlier, this term is borrowed from the work of Bardina et al.[8] Consistent with their work, optimum agreement between model-predicted and measured turbulent energy is obtained using $\xi = 1$. Figures 1b-1d compare computed and measured turbulent energy for rotation rates of $\Omega = 0$, 20, and 80 s^{-1}. In all three cases, the initial value of the dissipation $\epsilon_o = \beta^*\omega k$ has been assumed to be 262 m^2/s^3, which corresponds to the three different dissipation rate values quoted. Again, the ratio $(e/k)_o$ has no effect on the predicted value for k. As shown, computed turbulent energies are well within the scatter of the experimental data.

C. Return to Isotropy

The least satisfactory of all the homogeneous turbulence applications in the Stanford conference were those for the return of initially anisotropic turbulence to isotropy. Figures 1e-1h compare computed and measured k, u'^2, and v'^2 variation with time for cases 0373A-D. Table 1 summarizes initial values used for dissipation rate $(e/k)_o$ and Re_T. As shown, model predictions differ from corresponding measured values by less than 10% for all four cases. The predicted results are sensitive to the initial value of e/k, but, as will be discussed in the next subsection, the values used are sensible.

D. Plane Strain

The two plane strain cases included in the Stanford conference differ in the value of the strain rate. Flow 0374A, corresponding to the experiment performed by Townsend,[13] has $\dot{\epsilon} = \partial w/\partial z = -\partial v/\partial y = 9.44\ s^{-1}$. Flow 0374B, corresponding to the Tucker-Reynolds[14] experiment, has approximately half of this value, $\dot{\epsilon} = 4.45\ s^{-1}$. In the Stanford conference, the portion of the Tucker-Reynolds experiment for which the strain rate is removed and the turbulence allowed to approach isotropy ($t > 0.4$s) was included as a return to

Table 1 Summary of homogeneous turbulence test cases

Flow ID	Description	Figure	$\omega_o(s^{-1})$	Re_T	$(e/k)_o$
0371	Decay of isotropic turbulence	1 a	512	53.5	–
0372A	System rotation; $\Omega = 0$	1 b	2980	2.0	–
0372B	System rotation; $\Omega = 20\ s^{-1}$	1 c	2950	2.0	–
0372C	System rotation; $\Omega = 80\ s^{-1}$	1 d	2610	2.6	–
0373A	Return to isotropy	1 e	17	6 6	0.66
0373B	Return to isotropy	1 f	47	5.0	0.86
0373C	Return to isotropy	1 g	70	9.5	0.71
0373D	Return to isotropy	1 h	72	24.2	0.64
0374A	Plane strain; $\dot{\epsilon} = 9.44\ s^{-1}$	1 i	165	14.8	0.75
0374B	Plane strain; $\dot{\epsilon} = 4.45\ s^{-1}$	1 j	100	32.7	0.75
0376A	Uniform shear; $\partial U/\partial y = 12.9\ s^{-1}$	1 k	84	67.0	0 80
0376B	Uniform shear; $\partial U/\partial y = 48.0\ s^{-1}$	1 l	86	138.0	0 80

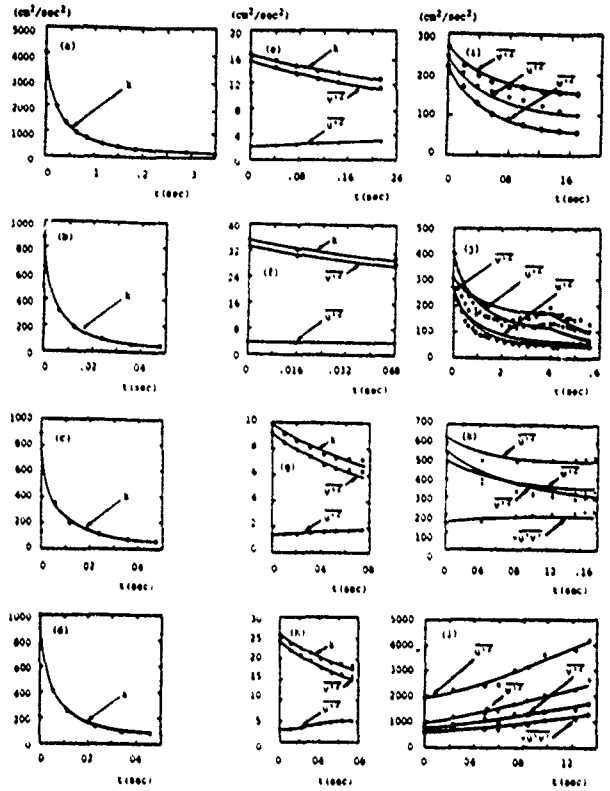

Fig. 1 Comparison of computed and measured turbulent energy and Reynolds stresses for homogeneous turbulence (——— computed, ○ ● □ △ ▽ measured).

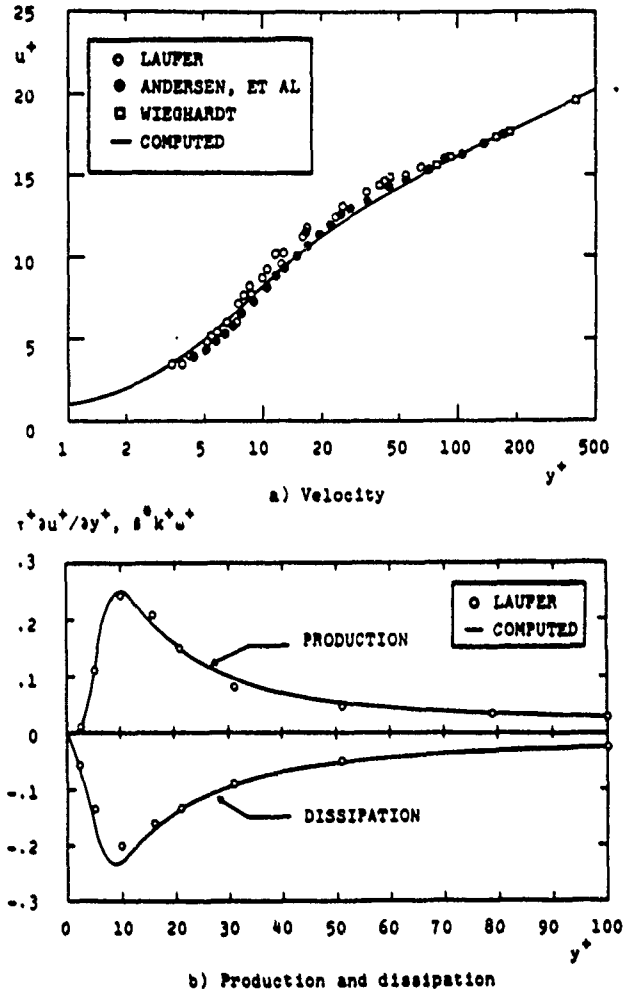

Fig. 2 Comparison of computed and measured sublayer properties for a perfectly smooth surface.

isotropy case, flow 0373E. In the computation done in this study, flows 0374B and 0373E have been combined into a single computation.

Figures 1i and 1j compare computed and measured variations of k, $\overline{u'^2}$, and $\overline{v'^2}$ for the two cases. Just as with the wall layer, an asymptotic analysis shows that for very long times the ratio of e to k approaches a constant value of approximately 3/4 for plane strain. The Townsend case was done using an initial ratio $e/k = 3/4$. Varying the initial ratio between 1/2 and 9/10 produces less than a 15% change overall in the Reynolds stress components. Figure 1j shows the results obtained for the Tucker-Reynolds case using initial e/k ratios of 3/4 (solid curves) and 9/10 (dashed curves). As shown, the primary difference appears in $\overline{w'^2}$. Using the larger value produces closer agreement between theory and experiment. Consistent with the asymptotic analysis, by the end of the computation e/k is almost exactly 3/4, regardless of the value used for $(e/k)_o$.

Although the model has not been applied to any of the axisymmetric strain cases included in the Stanford conference, we have numerically investigated the asymptitic solution for large time. This analysis is pertinent to the return to isotropy cases discussed in the preceeding subsection because the experimental setup used by Uberoi[15] in collecting the data of cases 0373A-D first subjected the turbulence to axisymmetric strain, followed by a return to isotropy. Interestingly, the asymptotic ratio of e to k depends on the ratio of the strain rate to the initial value of ω. The asymptotic value of e/k can range from 1/2 to almost 9/10. As noted earlier, the values used in the computations for flows 0373A-D fall within this range.

E. Uniform Shear

The final applications for homogeneous turbulence are for uniform shear. The Stanford conference included two cases, flow 0376A that corresponds to the experiment by Champagne et al.[3] in which the mean shear is $\partial U/\partial y = 12.9\ s^{-1}$, and flow 0376B that corresponds to the experiment by Harris et al.[16] in which the mean shear is $\partial U/\partial y = 48.0\ s^{-1}$. Figures 1k and 1l compare computed and measured Reynolds stresses. For uniform shear, the asymptotic value of e/k for large time is 4/5. Both computations use $(e/k)_o = 4/5$.

V. Viscous Sublayer

To prepare the multiscale model for application to flows with solid boundaries, we now examine the limiting form of the model-predicted solution for the viscous sublayer. The solution exactly parallels the perturbation analysis given by Wilcox.[2] For a perfectly smooth surface, the constant in the law of the wall B is defined by

$$\frac{u}{u_\tau} = \frac{1}{\kappa}\log\frac{u_\tau y}{\nu} + B \tag{41}$$

where u_τ is friction velocity and κ is von Kármán's constant. Using the perturbation analysis procedure described by Wilcox,[2] the value of B predicted by the model depends on the value selected for the closure coefficients σ and σ^*. Using $\sigma = \sigma^* = \frac{1}{2}$ yields

$$B = 5.2 \tag{42}$$

for a perfectly smooth surface. Since this value falls well within the scatter of experimental data, this computation serves as the basis for selecting the values quoted for σ and σ^*. In addition, these results indicate that no special viscous

damping terms are needed for any of the multiscale model's closure coefficients to accommodate integration through the viscous sublayer. Figure 2 compares computed and measured[17-19] sublayer properties. As shown, differences between theory and experiment are insignificant.

VI. Boundary-Layer Applications

A. Incompressible Boundary Layers

The first case selected is the boundary layer on a flat plate for which the pressure is constant. This, and all of the steady boundary-layer computations reported in this paper, have been done with a two-dimensional or axisymmetric boundary-layer program named EDDYBL.[20] The computation extends from a plate-length Reynolds number Re_x of 1.0×10^6 to 10.9×10^6. Figures 3a and 3b compare computed and measured skin friction C_f and velocity profiles. As expected, differences between theory and experiment are almost insignificant, with the largest differences being less than 3%.

The next two cases focus on effects of adverse pressure gradient. Two cases are selected: the moderate adverse gradient case of Bradshaw[19] (case 3300) and the increasingly adverse gradient case of Samuel and Joubert[1] (flow 0141). For the Bradshaw case, Figs. 3c and 3d compare computed and measured skin friction and a velocity profile at the final station. Differences between theory and experiment are almost undetectable. For the Samuel-Joubert case, Figs. 3e-3g compare computed and measured flow properties. As shown, computed and measured skin friction differ by less than 3%, velocity profiles are nearly identical, and Reynolds shear-stress profiles differ by less than 7%.

B. Compressible Boundary Layers

As a first test of the multiscale model for compressible flows, we consider flows 8101 and 8201 of the second Stanford conference.[1] Flow 8101 addresses the adiabatic wall case with freestream Mach numbers ranging from 0 to 5. For each Mach number, computation begins at $Re_x = 1.0 \times 10^6$ and continues to the point where momentum-thickness Reynolds number is 10,000. Figure 4a compares computed ratio of skin friction to the incompressible value C_{fo} with the correlation developed by Rubesin for the second Stanford conference. Differences between computed ratios and correlated values are trivial.

Flow 8201 focuses on effects of surface temperature on flat-plate skin friction. For this round of computations the freestream Mach number is 5; the ratio of surface temperature to the adiabatic wall value ranges from 0.2 to 1.0. Again, computation begins at $Re_x = 1.0 \times 10^6$ and terminates when momentum-thickness Reynolds number is 10,000. Figure 4b compares the predicted ratio of C_f to the incompressible value with Rubesin's correlation for the range of surface temperatures considered. Differences between predicted values and correlated values nowhere exceed 4%.

The final compressible boundary-layer application is for a Mach 4, adiabatic-wall boundary layer subjected to an adverse pressure gradient. The data are attributed to Zwarts and correspond to flow 0842 of the second Stanford conference. Figure 5 presents results of the computation. As shown, computed and measured skin friction C_f, shape factor H, and momentum thickness θ differ by less than 8%.

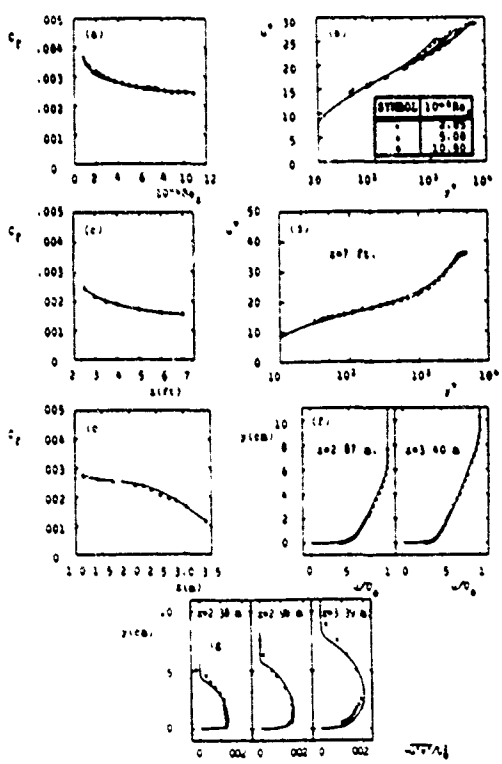

Fig. 3 Comparison of computed and measured skin friction and profiles for incompressible boundary layers (——— computed, ○ ● □ measured).

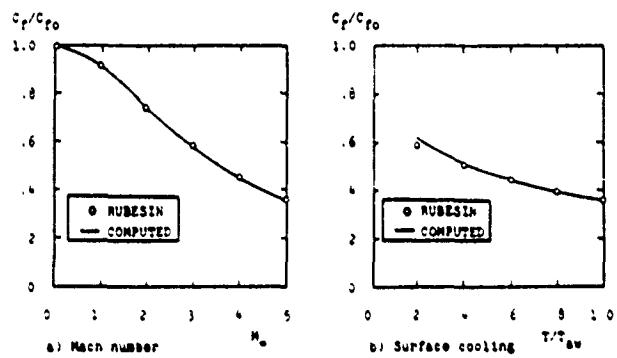

Fig. 4 Comparison of computed and measured effect of freestream Mach number and surface cooling on flat-plate boundary-layer skin friction.

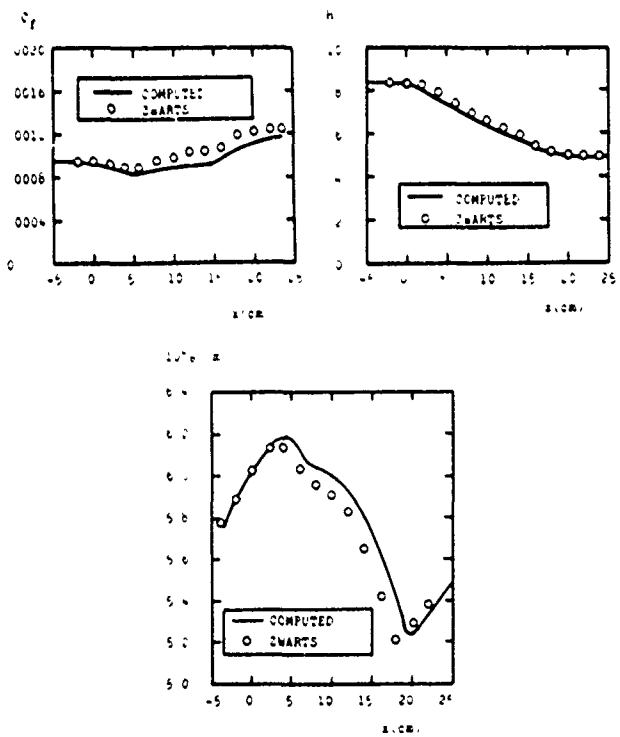

Fig. 5 Comparison of computed and measured properties for a Mach 4 boundary layer with adverse pressure gradient.

C. Unsteady Boundary Layers

The final round of applications is for incompressible, unsteady turbulent boundary layers. These flows pose a difficult challenge to the model because many complicated frequency-dependent phenomena are generally present, including periodic separation and reattachment.

1. Cases Analyzed

To test the model equations for unsteady boundary layers, we have simulated the experiments performed by Jayaraman et al.[21] In these experiments, a well-developed steady turbulent boundary layer enters a test section that has been designed to have freestream velocity that varies according to

$$U_e = U_o[1 - ax'[1 - \cos(2\pi ft)]]$$

$$x' = (x - x_0)/(x_1 - x_0) \tag{43}$$

The quantity x' is the fractional distance through the test section where x_0 and x_1 are the values of streamwise distance x at the beginning and end of the test section, respectively.

Thus, an initially steady equilibrium turbulent boundary layer is subjected to a sinusoidally varying adverse pressure gradient. The experiments were performed for low and high amplitude unsteadiness characterized by having a $a = 0.05$ and 0.25, respectively. For both amplitudes, experiments were conducted for five frequencies ranging from $f = 0.1$ to 2.0 Hz. The computations simulate nine of the experiments, including all five of the low-amplitude cases and all but the lowest frequency case for high amplitude. Complete details about the numerical method, finite-difference grids, and other pertinent computational details are given by Wilcox.[22]

2. Numerical Considerations

a) Numerical algorithm. The numerical algorithm used for the computations is an unconditionally stable implicit marching method. The scheme is second-order accurate in the direction normal to the surface. For stability, particularly through separation, the computational procedure uses upwind differencing for the streamwise convection terms. Although the algorithm is unconditionally stable, the presence of source terms in the turbulence model equations makes the equations sufficiently stiff to preclude using a streamwise Courant number $C_x = U\Delta t/\Delta x$ in excess of approximately 0.6. By contrast, the boundary-layer computations are stable with a viscous Courant number $C_y = 2\nu\Delta t/(\Delta y)^2$ in excess of 600.

Integration through separation is accomplished by computing the streamwise convective term in the momentum equation according to

$$u\frac{\partial u}{\partial x} = \max[0,u]\cdot\frac{\Delta u}{\Delta x} \tag{44}$$

where $\Delta u/\Delta x$ is the finite-difference approximation to $\partial u/\partial x$. In other words, on regions of reverse flow we set the streamwise convective term to zero. This is the procedure first implemented by Reyhner and Flugge-Lotz.[23]

b) Data reduction. In order to compare computed and measured flow properties, we must decompose any flow property $y(x,t)$ in terms of three components, that is,

$$y(x,t) = \bar{y}(x) + \tilde{y}(x,t) + y'(x,t) \tag{45}$$

where $\bar{y}(x)$ is the long-time averaged value of $y(x,t)$, $\tilde{y}(x,y)$ is the organized response component due to the imposed unsteadiness, and $y'(x,t)$ is the turbulent fluctuation. In order to extract the quantities presented in graphical form by Jayaraman et al., we first note that what the program computes is the phase-averaged component $\langle y(x,t)\rangle$ defined by

$$\langle y(x,t)\rangle = \bar{y}(x) + \tilde{y}(x,t) \tag{46}$$

Jayaraman et al. expand $\langle y(x,t)\rangle$ in a Fourier series according to

$$\langle y(x,t)\rangle = \bar{y}(x) + \sum_{n=1}^{\infty} A_{n,y}(x)\cos[2n\pi ft + \phi_{n,y}(x)] \tag{47}$$

Velocity profile data, for example, are presented by Jayaraman et al. in terms of $\bar{u}(x)$, $A_{1,u}(x)$, and $\phi_{1,u}(x)$. These quantities have been extracted from the boundary-layer solution by the normal Fourier decomposition by computing the following integrals:

$$\bar{u}(x) = f\int_0^{1/f}\langle u(x,t)\rangle dt \tag{48}$$

$$A_{1,u}(x)\cos\phi_{1,u} = f\int_0^{1/f}\langle u(x,t)\rangle\cos(2\pi ft)\,dt \tag{49}$$

$$A_{1,u}(x)\sin\phi_{1,u} = -f\int_0^{1/f}\langle u(x,t)\rangle\sin(2\pi ft)\,dt \tag{50}$$

3. Results

a) Zero frequency limit. Before proceeding to the unsteady computations, we first test for consistency with a key observation made by Jayaraman et al. for the limit of zero frequency. On the one hand, they find that for the mean velocity given by Eq. (43) with $f = 0$ and $a = 0.25$, massive separation occurs in the test section. On the other hand, even at the smallest frequency for which experiments were done, when f is not zero the observed flow is much more well behaved. On the average, the boundary layer remains attached, although at some frequencies for the high-amplitude cases periodic separation and reattachment occurs.

Part of the reason for this behavior is explained by Jayaraman et al. When we set $f = 0$, the pressure gradient is given by

$$\frac{dp}{dx'} = \rho U_o^2 a(1 - ax') \qquad \text{for } f = 0 \tag{51}$$

However, because of the nonlinearity of the convective terms in the momentum equation, for any nonzero f, the mean (long-time average) pressure gradient is

$$\frac{d\bar{p}}{dx'} = \rho U_o^2 a\left(1 - \frac{3}{2}ax'\right) \qquad \text{for } f \neq 0 \tag{52}$$

The gradient for $f \neq 0$ is thus reduced (for adverse gradient, i.e., for $a > 0$) and is less likely to cause separation.

To test the model's consistency with this observation, two steady computations have been done, the first using the pressure gradient for $f = 0$ [Eq. (51)] and the second for the gradient given in Eq. (52). The computations have been performed with the steady boundary-layer program EDDYBL and with the new unsteady program. Using a value for a of 0.25, our predictions match those described by Jayaraman et al. For the pressure gradient in Eq. (51), the boundary layer separates at $x' = 0.87$. By contrast, when the pressure gradient of Eq. (52) is used, the boundary layer remains attached throughout the test section.

b) Low-amplitude cases. For each of the low-amplitude cases, computation continues for at least five and has as many as ten periods. This proves sufficient to achieve a periodic solution as determined by monitoring skin friction. Figure 6 compares computed and measured velocity profiles at $x' = 0.88$ for the five low-amplitude cases. As shown, computed mean-velocity profiles differ from corresponding measured profiles by no more than 5% of scale. Comparison of computed and measured $A_{1,u}$ profiles shows that, consistent with measurements, unsteady effects are confined to the near-wall Stokes layer at the higher frequencies ($f > 0.5$ Hz). By contrast, at the two lowest frequencies, the entire boundary

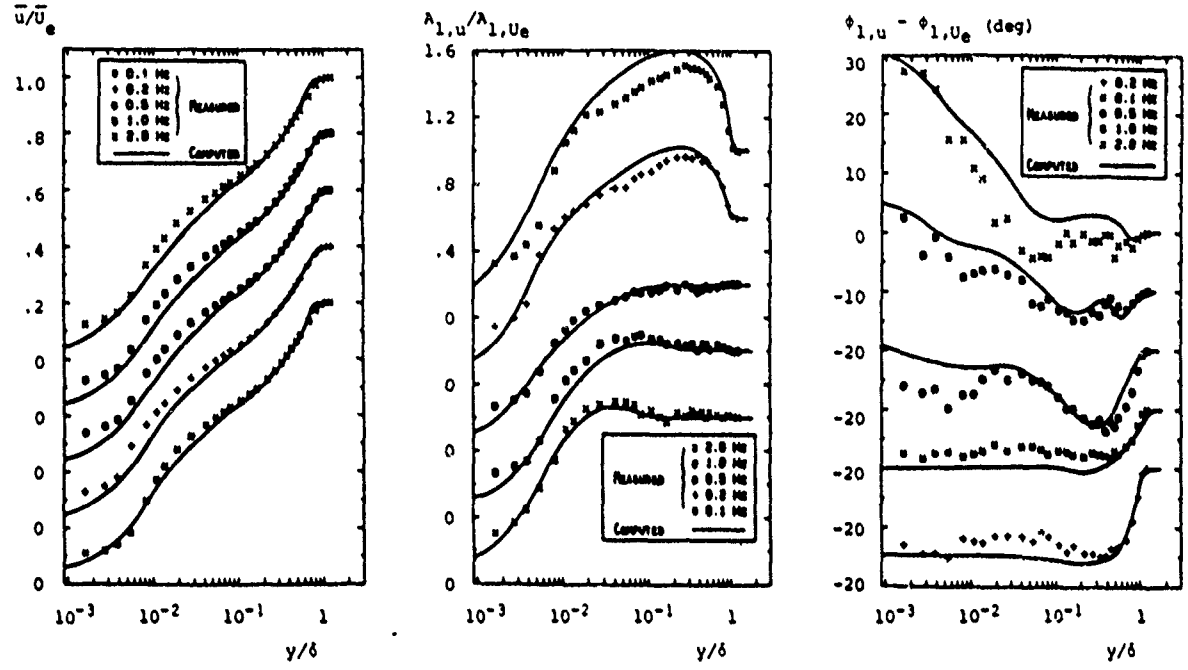

Fig. 6 Comparison of computed and measured mean velocity, $A_{1,u}$ and phase profiles; low amplitude.

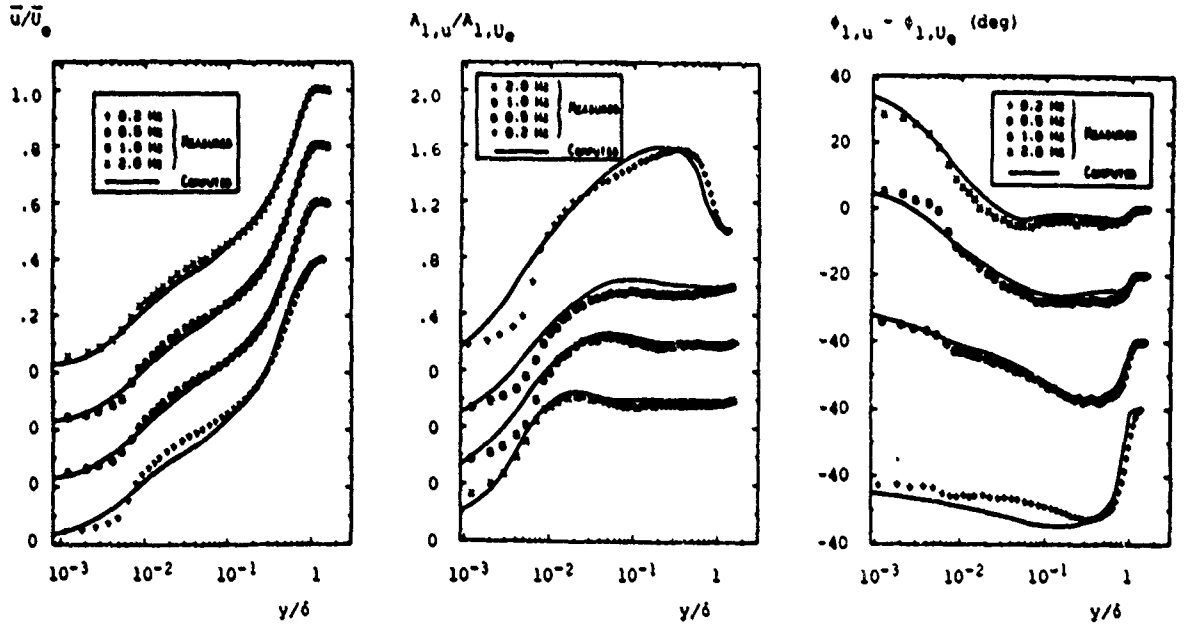

Fig. 7 Comparison of computed and measured mean velocity, $A_{1,u}$ and phase profiles; high amplitude.

layer is affected with significant amplification of the organized component occuring away from the surface. Differences between the numerical and experimental $A_{1,u}$ profiles are less than 10%. Computed and measured phase $\phi_{1,u}$ profiles are very similar with differences nowhere exceeding 5 deg.

c) High-amplitude cases. Figure 7 compares computed and measured velocity profiles at $x' = 0.94$. As with the low-amplitude cases, computed and measured $\bar{u}(x)$ profiles lie within 5% of scale of each other. Similarly, the computed $A_{1,u}$ and $\phi_{1,u}$ profiles differ from the corresponding measured profiles by less than 10%. To provide a measure of how accurately temporal variations have been predicted, Fig. 8 compares computed and measured shape factor through a complete cycle for all four frequencies. Differences between computed and measured shape factors are less than 5%.

d) k-ω model predictions. The high-amplitude cases have also been computed using the k-ω model. Results are included in Fig. 8, which shows that the k-ω and multiscale model predicitons differ by only a few percent. Although it is possible that the test cases are not as difficult as we expected, this seems unlikely in view of the wide Strouhal number range and the fact that periodic separation and reattachment are present. More likely, the k-ω model fares well because all of the cases have attached boundary layers through most of each cycle and in the mean.

VII. Summary and Conclusions

A new turbulence model has been devised that describes turbulence in terms of two energy scales. The two scales correspond to a lower and an upper partition of the turbulence

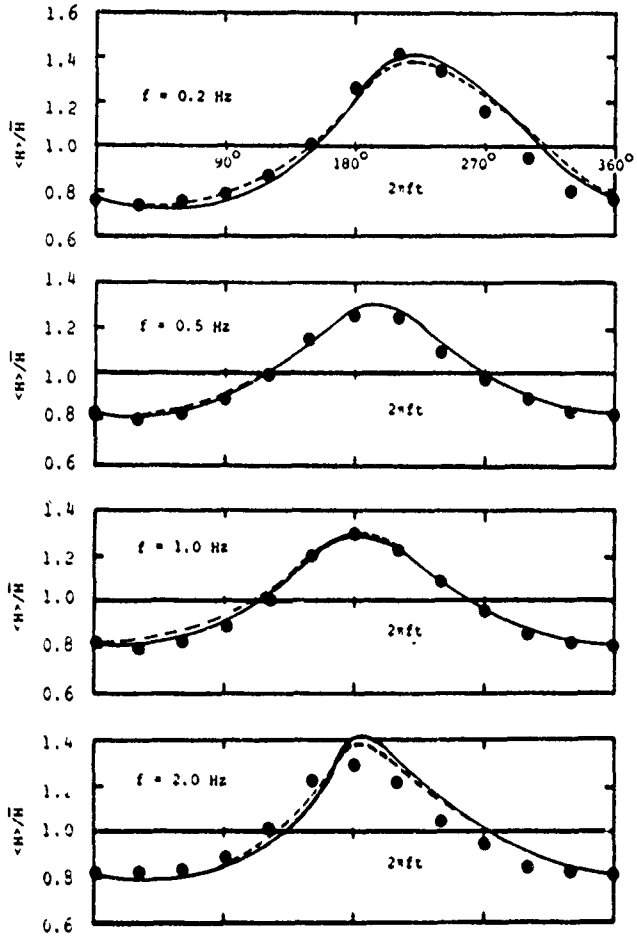

Fig. 8 Comparison of computed and measured temporal variation of shape factor for the high-amplitude cases (– – – – k-ω model, ——— multiscale model, • measured).

energy spectrum, with the upper partition corresponding to the lowest frequency eddies. Closure approximations have been designed to reflect as much as possible the physics of turbulent flow processes and to obviate limitations attending the Boussinesq approximation.

Results of the theory's application to homogeneous turbulence are very satisfactory. Virtually all of the second Stanford conference test cases have been predicted to within experimental error. Applications to the viscous sublayer indicate that, similar to the k-ω model that serves as the foundation on which the multiscale model rests, no special modifications to the closure coefficients are needed to accommodate integration through the sublayer. Results of the steady boundary-layer computations indicate the model is even more accurate than the Wilcox k-ω model for adverse pressure gradient.

From a numerical viewpoint, the new model is quite efficient, especially for the steady cases. Typically, there is only a 50% increase in computing time relative to the k-ω model for steady boundary-layer computations; the increase is typically 70% for unsteady computations.

The unsteady boundary-layer computations offer the first definitive measure of how accurately the multiscale model simulates the physics of turbulent boundary layers. For a wide range of Strouhal numbers, the multiscale model more or less duplicates the structure of a turbulent boundary layer subjected to a sinusoidally varying adverse pressure gradient. As somewhat of a surprise, the two-equation model is just as accurate for these flows.

Acknowledgment

This research has been supported by the U.S. Army Research Office under Contract DAAG-29-83-C-0003, with Dr. Robert E. Singleton as technical monitor. The original idea of developing a model based on partitioning the turbulence energy spectrum was suggested to me by Prof. John Laufer.

References

[1]Kline, S. J., Cantwell, B. J., and Lilley, G. M. (eds.), *Proceedings of the 1980-81 AFOSR-HTTM-Stanford Conference on Complex Turbulent Flows*, Vol. 1, Stanford Univ. Press, Stanford, CA, 1981.

[2]Wilcox, D. C., "Reassessment of the Scale Determining Equation for Advanced Turbulence Models," *AIAA Journal* (to be published).

[3]Champagne, F. H., Harris, V. G., and Corrsin, S., "Experiments on Nearly Homogeneous Turbulent Shear Flow," *Journal of Fluid Mechanics*, Vol. 41, Pt. 1, 1970, pp. 81-139.

[4]Wilcox, D. C. and Rubesin, M. W., "Progress in Turbulence Modeling for Complex Flow Fields Including Effects of Compressibility," NASA TP 1517, April 1980.

[5]Rodi, W., "A New Algebraic Relation for Calculating Reynolds Stresses," *Zeitschrift fuer Angewandte Mathematik und Mechanik*, Vol. 56, 1976, p. 219.

[6]Lakshminarayana, B., "Turbulence Modeling for Complex Shear Flows," *AIAA Journal*, Vol. 24, Dec. 1986, pp. 1900-1917.

[7]Johnson, D. A. and King, L. S., "A Mathematically Simple Turbulence Closure Model for Attached and Separated Turbulent Boundary Layers," *AIAA Journal*, Vol. 23, Nov. 1985, pp. 1684-1692.

[8]Bardina, J., Ferziger, J. H., and Reynolds, W. C., "Improved Turbulence Models Based on Large Eddy Simulation of Homogeneous, Incompressible Turbulent Flows," Dept. of Mechanical Engineering, Stanford Univ., Stanford, CA, Rept. TF-19, May 1983.

[9]Tennekes, H. and Lumley, J. L., *A First Course in Turbulence*, MIT Press, Cambridge, MA, 1972.

[10]Launder, B. E., Reece, G. J., and Rodi, W., "Progress in the Development of a Reynolds-Stress Turbulence Closure," *Journal of Fluid Mechanics*, Vol. 68, Pt. 3, 1975, pp. 537-566.

[11]Favre, A., "Equations des Gaz Turbulents Compressibles," *Journal de Mechanique*, Vol. 4, No. 3, 1965, pp. 361-390.

[12]Townsend, A. A., *The Structure of Turbulent Shear Flow*, 2nd ed., Cambridge University Press, Cambridge, England, 1976, pp. 66-71.

[13]Townsend, A. A., "The Uniform Distortion of Homogeneous Turbulence," *Quarterly Journal of Mechanics and Applied Mathematics*, Vol. 7, 1956, p. 104.

[14]Tucker, H. J. and Reynolds, A. J., "The Distortion of Turbulence by Irrotational Plane Strain," *Quarterly Journal of Mechanics and Applied Mathematics*; Vol. 7, 1968, p. 104.

[15]Uberoi, M. S., "Effect of Wind Tunnel Contraction of Free Stream Turbulence," *Journal of the Aeronautical Sciences*, 1956, p. 754.

[16]Harris, V. G., Graham, J. A. H., and Corrsin, S., "Further Experiments in Nearly Homogeneous Turbulent Shear Flow," *Journal of Fluid Mechanics*, Vol. 81, 1977, p. 657.

[17]Laufer, J., "The Structure of Turbulence in Fully Developed Pipe Flow," NACA TR-1174, 1952.

[18]Andersen, P. S., Kays, W. M., and Moffat, R. J., "The Turbulent Boundary Layer on a Porous Plate: An Experimental Study of the Fluid Mechanics for Adverse Free-Stream Pressure Gradients," Dept. of Mechanical Engineering, Stanford Univ., Stanford, CA, Rept. HMT-15, May 1972.

[19]Coles, D. E. and Hirst, E. A., *Computation of Turbulent Boundary Layers-1968 AFOSR-IFP-Stanford Conference*, Vol. II, Stanford Univ. Press, Stanford, CA, 1969.

[20]Wilcox, D. C., "Program EDDYBL User's Guide," DCW Industries, La Cañada, CA, Rept. DCW-R-NC-04, 1988.

[21]Jayaraman, R., Parikh, P., and Reynolds, W. C., "An Experimental Study of the Dynamics of an Unsteady Turbulent Boundary Layer," Dept. of Mechanical Engineering, Stanford Univ., Stanford, CA, TR TF-18, Dec. 1982.

[22]Wilcox, D. C., "Advanced Applications of the Multiscale Model for Turbulent Flows," AIAA Paper 87-0290, Jan. 1987.

[23]Reyhner, T. A. and Flugge-Lotz, I., "The Interaction of a Shock Wave With a Laminar Boundary Layer," *International Journal of Non-Linear Mechanics*, Vol. 3, 1968, pp. 173-199.

APPENDIX C: 3-D BOUNDARY-LAYER APPLICATIONS

The paper reproduced in this appendix was presented at the AIAA 25th Aerospace Sciences Meeting, held in Reno, Nevada, January 12-15, 1987. The formal reference to this paper is as follows.

> Wilcox, D. C., "Advanced Applications of the Multiscale Model for Turbulent Flows," AIAA Paper 87-0290, Jan. 1987.

While the unsteady boundary layer results in this paper were ultimately included in the paper reproduced in Appendix B, the paper includes three-dimensional boundary layer applications that were not published. There is also a shock-induced separation computation that suggested the multiscale model would prove superior to the k-ω model for such flows. While this indeed proved to be true, the unsteadiness observed in the computation reported proved to be numerical in origin.

AIAA'87

AIAA-87-0290

Advanced Applications of the Multiscale Model for Turbulent Flows

D.C. Wilcox, DCW INDUSTRIES, Inc.
La Canada, CA

AIAA 25th Aerospace Sciences Meeting
January 12-15, 1987/Reno, Nevada

For permission to copy or republish, contact the American Institute of Aeronautics and Astronautics 1633 Broadway, New York, NY 10019

ADVANCED APPLICATIONS OF THE MULTISCALE MODEL FOR TURBULENT FLOWS

David C. Wilcox†
DCW Industries, Inc.
La Cañada, California

Abstract

The new "multiscale" model for turbulent flows developed by the author has been subjected to a series of rigorous applications to test its accuracy in simulating complex phenomena. The applications include three-dimensional boundary layers, shock-induced boundary layer separation, and unsteady boundary layers. Results of the applications indicate the multiscale model's predictive accuracy is comparable to that of two-equation turbulence models for attached boundary layers and may be profoundly superior for separated flows.

1. Introduction

This work is the result of the third phase of a continuing turbulence-modeling effort initiated after the Second Stanford Olympics[1]. The first phase led to development of a new two-equation turbulence model which is far more accurate than any existing model for boundary layers in an adverse pressure gradient[2]. Additionally, the two-equation model analysis laid the foundation for making even more significant improvements in the closure scheme for an improved engineering model of turbulence. The second phase led to development of a new turbulence model, viz, the "multiscale" model, which describes the turbulence in terms of two energy scales[3]. Most importantly, the multiscale model is not inhibited by the Boussinesq approximation in which mean-strain-rate and Reynolds-stress tensors have parallel principal axes.

The first two phases of this study have focused upon theoretical development of the new models, and applications have been limited to attached, two-dimensional boundary-layers. The primary purpose of the third phase is to address much more complex flows in testing the multiscale model. This paper presents three types of advanced applications including: three-dimensional boundary layers; shock-separated turbulent boundary layers; and unsteady turbulent boundary layers. In all cases, comparisons with experimental data are presented.

A novel feature of this phase of the research project is the fact that all of the numerical computations, including the Navier-Stokes cases, have been done on a desk top microcomputer. The computer used is an AT&T PC 6300 equipped with the Definicon[4] Motorola 68020/68881 based DSI-020 coprocessor board. The machine has been found to have the computing power of a VAX 11-780.

Section 2 presents the multiscale model equations, including values of all closure coefficients. Sections 3, 4 and 5 include results of the applications. The concluding section summarizes research findings.

2. Equations of Motion

Before proceeding to the applications, it is instructive to state the equations of motion used for the various applications. First of all, we must solve the mass-averaged[5] equations for conservation of mass, momentum and energy, viz,

$$\partial\rho/\partial t + \partial/\partial x_j(\rho u_j) = 0 \qquad (1)$$

$$\partial/\partial t(\rho u_i) + \partial/\partial x_j[\rho u_i u_j + p\delta_{ij} - \tau_{ij}] = 0 \qquad (2)$$

$$\partial/\partial t(\rho E) + \partial/\partial x_j[\rho u_j H - u_i \tau_{ij} + q_j - (\mu+\sigma^*\mu_T)\partial k/\partial x_j] = 0 \qquad (3)$$

where t is time, x_i is position vector, u_i is velocity vector, ρ is density, p is pressure, τ_{ij} is stress tensor and q_j is heat-flux vector. In Equation (3), the quantities $E=e+k+u_i u_i/2$ and $H=h+k+u_i u_i/2$ are total energy and total enthalpy, respectively, with $h=e+p/\rho$. Additionally, μ and μ_T are molecular and eddy viscosity, k is turbulent energy and σ^* is a closure coefficient. The heat flux vector is computed according to

$$q_j = -(\mu/Pr_L + \mu_T/Pr_T)\partial h/\partial x_j \qquad (4)$$

In order to close this system of equations, we must postulate a relation between the stress tensor, τ_{ij}, and mass-averaged flow properties. The multiscale model computes τ_{ij} according to

$$\tau_{ij} = 2\mu[S_{ij} - 1/3(\partial u_k/\partial x_k)\delta_{ij}] + \rho T_{ij} - 2/3\rho e\delta_{ij} \qquad (5)$$

where $S_{ij}=1/2(\partial u_i/\partial x_j + \partial u_j/\partial x_i)$ is the mean strain rate tensor, ρT_{ij} is the "large eddy" contribution to the Reynolds-stress tensor and ρe is the energy of the "small" eddies.

†President
Associate Fellow AIAA

Copyright © American Institute of Aeronautics and Astronautics, Inc., 1987. All rights reserved.

The energy of the "large" eddies, $\rho(k-e)$, and the energy of the "small" eddies, ρe, are computed from the following equations.

$$\partial/\partial t(\rho k) + \partial/\partial x_j[\rho u_j k-(\mu+\sigma^*\mu_T)\partial k/\partial x_j] = \tau_{ij}\partial u_i/\partial x_j - \beta^*\rho\omega k \quad (6)$$

$$\partial/\partial t[\rho(k-e)] + \partial/\partial x_j[\rho u_j(k-e)] = (1-\hat{\alpha}-\beta)\tau_{ij}\partial u_i/\partial x_j - \beta^*\rho\omega k(1-e/k)^{3/2} \quad (7)$$

where $\hat{\alpha}$, β and β^* are closure coefficients, and $\tau_{ij}=\rho T_{ij}-{}^2/_3\rho e\delta_{ij}$ is the Reynolds stress tensor. Also, the quantity ω is the dissipation rate which satisfies

$$\partial/\partial t(\rho\omega) + \partial/\partial x_j[\rho u_j\omega-(\mu+\sigma\mu_T)\partial\omega/\partial x_j)] = (\gamma\omega/k)\tau_{ij}\partial u_i/\partial x_j - \beta\rho\omega^2 - \zeta\beta\rho\omega/2\Omega_{mn}\Omega_{mn} \quad (8)$$

where $\Omega_{mn}={}^1/_2(\partial u_m/\partial x_n-\partial u_n/\partial x_m)$ is the mean rotation tensor. The quantities β, γ, ζ and σ are additional closure coefficients. Note also that the eddy viscosity, μ_T, appearing in Equations (3, 4, 6 and 8) is defined by

$$\mu_T = \rho k/\omega \quad (9)$$

Finally, the "large" eddy Reynolds stress equation is

$$\partial/\partial t(\rho T_{ij}) + \partial/\partial x_k(\rho u_k T_{ij}) = -P_{ij} + E_{ij} \quad (10)$$

where E_{ij} represents the exchange of energy amongst the mean, large-eddy and small-eddy energies. With the multiscale model, we postulate that

$$E_{ij} = -C_1\beta^*\omega(\tau_{ij}+{}^2/_3\rho k\delta_{ij}) + \hat{\alpha}P_{ij} + \beta D_{ij} + \gamma\rho k(S_{ij}-{}^1/_3\partial u_k/\partial x_k\delta_{ij}) + {}^2/_3\rho\omega k(1-e/k)^{3/2}\delta_{ij} \quad (11)$$

where C_1 and γ are closure coefficients. The tensors P_{ij} and D_{ij} are the conventional production tensors defined by

$$P_{ij} = \tau_{im}\partial u_j/\partial x_m+\tau_{jm}\partial u_i/\partial x_m \quad (12)$$

$$D_{ij} = \tau_{im}\partial u_m/\partial x_j+\tau_{jm}\partial u_m/\partial x_i \quad (13)$$

Finally, the ten closure coefficients appearing in Equations (1-11) have been established in the prior study by Wilcox[3]. No changes in those coefficients have been made for any of the applications in this study. The values of the closure coefficients are as follows.

$$\left.\begin{array}{l}\hat{\alpha} = 42/55,\quad \beta = 6/55,\quad \gamma = 1/4\\ \beta = 3/40,\quad \gamma = 4/5,\quad \sigma = 1/2\\ \beta^* = 9/100,\quad \zeta = 1\ ,\quad \sigma^* = 1/2\\ C_1 = 1 + 4(1-e/k)^{3/2}\end{array}\right\} \quad (14)$$

3. Three-Dimensional Boundary Layers

The first set of applications is for three-dimensional (3-D) boundary layers. These flows present challenging tests because the possibility of anisotropic shear arises in three dimensions, i.e., the effective eddy diffusivity can be different depending upon direction. Consequently, any turbulence model such as the multiscale model which avoids using the Boussinesq approximation has the potential for more accurate predictions than those made with a model in which stress is proportional to strain rate.

3.1 Cases Analyzed

Two cases have been analyzed, both corresponding to flow over a ship hull, viz, the SSPA Model 720 and the HSVA Tanker. The two cases are from the 1980 SSPA-ITTC Workshop on ship boundary layers[6]. In addition to comparing multiscale-model predictions with experimental data, results of the computations have also been compared to predictions made with the mixing-length model[7] and with the Wilcox[2] k-ω model.

3.2 Numerical Considerations

Numerical Algorithm. The computations have been performed with a 3-D boundary layer program, EDDY3[8], which uses the Krauss[9] algorithm coupled with the Blottner[10] variable grid method. Additionally, the program uses the procedure devised by Wilcox[11] to permit large streamwise steps. To improve stability of the Krauss algorithm, the integration direction alternates from keel to waterline and vice versa as integration from bow to stern proceeds.

Boundary Conditions. Both computations use the Workshop supplied Douglas-Neumann inviscid velocity distribution. Computation is initiated from fully-turbulent boundary-layer profiles at x/L=.2 and x/L=.1 for the SSPA Model 720 and the HSVA Tanker, respectively, where L is hull length. The profiles used match the measured momentum thickness, shape factor and skin friction.

Finite Difference Grid. Computation is performed on a nonorthogonal grid which permits precise definition of hull shape

from keel to waterline. For the SSPA Model 720, the finite-difference mesh consists of approximately 75 steps in the streamwise direction, 21 equally-spaced points from keel to waterline, and an average of 40 points normal to the hull. The HSVA Tanker computations have a mesh with approximately 70 streamwise steps, 15 points from keel to waterline and an average of 50 points normal to the hull. Consistent with the Douglas-Neumann computation, both the keel and the waterline have been treated as symmetry planes.

Computing Time. Table 1 summarizes total computing time using our Definicon Motorola 68020/68881 based desk top microcomputer. By comparison, a comparable two-equation model computation for the SSPA Model 720 requires approximately 15 minutes on a UNIVAC 1108 mainframe computer.

Table 1. 3-D Boundary-Layer Computing Time

Ship Hull Model	Mixing Length	Two Equation	Multi-scale
SSPA 720	11 min	29 min	46 min
HSVA Tanker	8 min	28 min	30 min

3.3 Results

SSPA Model 720. Figure 1 compares computed and measured momentum thickness, θ, on three lines along the hull. Line A is the keel line. Line B is a line well below the waterline where the boundary layer is more-or-less of the classical "thin" variety. Line C is closer to the waterline and the boundary layer approaches the more complicated "thick" structure where terms such as $\partial p/\partial y$ become important.

Along Line A, the boundary layer is truly three dimensional as exhibited by its unusual behavior approaching the stern. Specifically, despite entering a region of adverse pressure gradient, the momentum thickness decreases. This behavior occurs because of large flow divergence near the stern. The multiscale and k-ω model predictions fall within experimental data scatter while the mixing-length prediction lies about 20% above measured values.

Along Line B, predictions of all three models are very close to one another, and all overshoot measured values of θ/L by between 25% and 30% approaching the stern. The most noticeable difference amongst the predictions is that the mixing-length boundary-layer separates earlier than that of the multiscale or k-ω models.

Along Line C, the multiscale and k-ω model predictions are both within 10% of measured values. By contrast, the mixing-length prediction is close to measured values up to x/L=.7; beyond this point the boundary layer separates much earlier than indicated by the data.

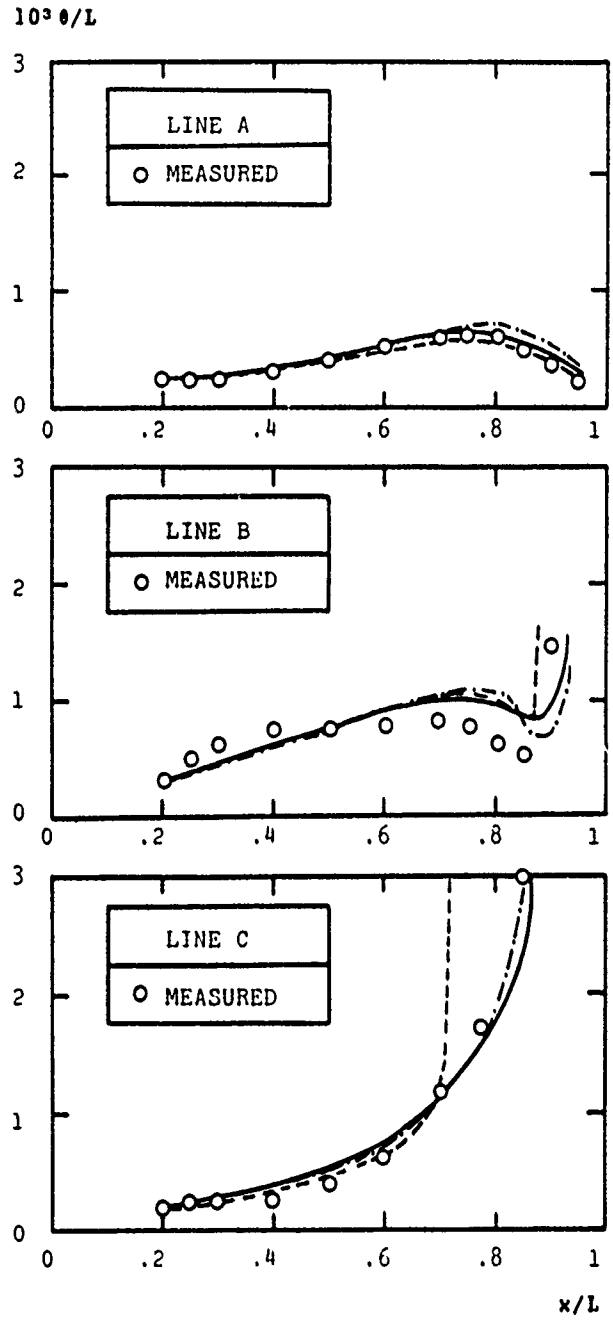

Figure 1. Comparison of computed and measured momentum thickness for the SSPA Model 720. --- Mixing Length, —·— k-ω, and —— Multiscale.

HSVA Tanker. Figure 2 compares computed and measured θ on three sections, viz, for x/L=.13, .65 and .75. Note that the abscissa, z, is the dimensionless girth with z=0 on the keel and z=1 on the waterline.

Inspection of Figure 2 shows that, for x/L=.13 and .65, computed values of θ for all three models are within 10% to 15% of corresponding measurements. On x/L=.75, the mixing-length model predicts boundary-layer separation over most of the section. By contrast, the multiscale and k-ω models follow the general trend of the data over most of the section.

While the mixing-length model's prediction of premature separation is a definite indication of its inadequacy for this flow, the 30% differences between computed and measured θ on x/L=.75 for the multiscale and k-ω models are unsurprising. That is, approaching the stern we expect the boundary layer to become "thick" so that classical thin-shear-layer approximations become suspect. Since EDDY3 is based upon these approximations, discrepancies should be expected this close to the stern. However, as shown by Wilcox[12], by accounting for $\partial p/\partial y$ with an integral-method approach coupled to the normal computational sequence, most of these discrepancies can be eliminated.

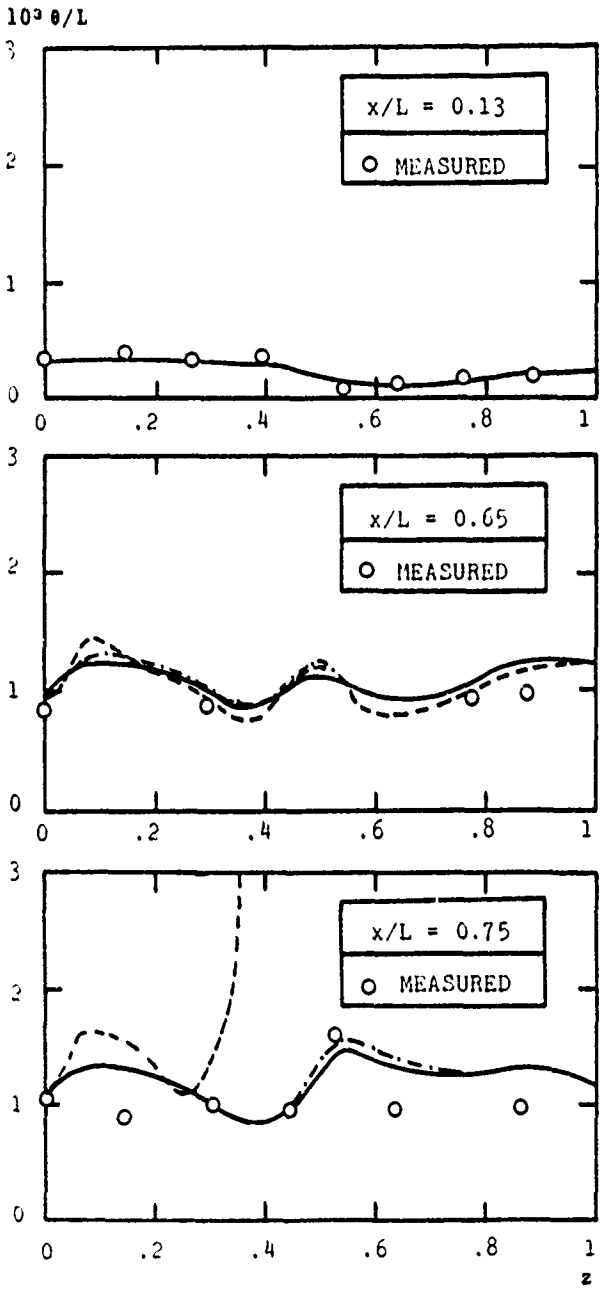

Figure 2. Comparison of computed and measured momentum thickness for the HSVA Tanker. --- Mixing Length, —·— k-ω, and —— Multiscale.

Summary. On the one hand, for both of the ship hulls considered, the multiscale model is clearly superior to mixing length. On the other hand, it offers little improvement over the k-ω model. Thus, our three-dimensional boundary-layer applications show no advantage in using the multiscale model. The reason for this may be that we have unknowingly selected flows in which anisotropic shear is absent. More tests will be needed to determine whether or not a model no more complex than the k-ω model is all that is needed to achieve accurate predictions for 3-D boundary layers.

4. Navier-Stokes Applications

The next round of applications is for Mach 3 turbulent boundary layers which undergo separation caused by reflection of an oblique shock wave from a flat plate. Such interactions pose an extremely difficult test for a turbulence model because of the sudden changes in mean strain rate attending separation and reattachment.

4.1 Cases Analyzed

Perhaps partly for sentimental reasons and certainly because of convenience (we still have the original graphs and experimental data), we have repeated two of the six cases done in 1974 by Wilcox[2] with somewhat coarse finite difference grids. In 1974, the Wilcox computations were the first of their kind using an advanced (two-equation) model of turbulence. Thus, repeating the computations with a more modern turbulence model, numerical procedure and computer provides an interesting historical perspective, if nothing else. Figure 3 schematically illustrates the simulated flowfield, viz, an oblique shock impinging on a flat plate.

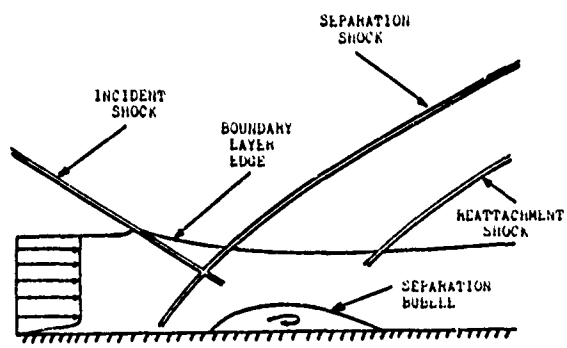

Figure 3. Schematic of the flowfield for reflection of an oblique shock wave from a flat plate in a viscous flow.

Freestream Mach number is 3 and Reynolds number based on thickness of the upstream boundary boundary layer is $2.5 \cdot 10^5$. We have done two cases with the new k-ω model, distinguished as follows.

Case 1. The incident shock deflects the freestream flow by $\theta = 9.87°$.

Case 2. The incident shock deflects the freestream flow by $\theta = 12.75°$.

Additionally, we have done the stronger shock computation (Case 2) using the multiscale model.

4.2 Numerical Considerations

Numerical Algorithm. The computations have been done with a two-dimensional Navier-Stokes program based on the implicit algorithm devised by MacCormack[14]. These computations demonstrate how numerically well-behaved the multiscale model appears to be. The same grid and timestep have been used for both the k-ω and multiscale models. In addition, both models have been integrated through the sublayer, with a viscous Courant number, $C_y = 2\nu\Delta t/(\Delta y)^2$, of about 40.

Boundary Conditions. Upstream boundary conditions for all computations have been obtained from our two-dimensional boundary layer program, EDDYBL[15].

Finite Difference Grid. The computational domain is $12.5\delta_0$ long by $6\delta_0$ high, where δ_0 is the thickness of the incident boundary layer. The finite difference grid is rectangular and consists of 32 equally-spaced points between upstream and downstream boundaries, while 36 points lie between the lower and upper boundaries. The first 20 grid points normal to the surface extend to $y=\delta_0$; grid-point spacing increases in a geometric progression with a 32% grading ratio. The remaining 16 points are equally spaced, covering the region from $y=\delta_0$ to $y=6\delta_0$.

Computing Time. Table 2 summarizes total computing time using our microcomputer. Steady flow conditions develop for the k-ω computations after a freestream fluid particle traverses the mesh five times. By comparison, adjusting for grid point number and total mesh lengths traveled by a freestream fluid particle, the 1974 computations for the weak and strong shock cases would have required 1.6 and 1.9 hours, respectively on a CDC 7600 mainframe computer. Note, of course, that had MacCormack's implicit algorithm been available in 1974, the computing times would have been reduced by at least a factor of 10. Nevertheless, these computing times show that two-dimensional Navier-Stokes computations are quite practical on a Motorola 68020/68881 based microcomputer.

Table 2. Navier-Stokes Computing Time

θ	Two Equation	Multiscale
9.87°	2.6 hrs	-
12.75°	3.5 hrs	8.8 hrs

4.3 Results

Weak Shock Results. Figure 4 compares results of the weak shock case with the 1974 computation. As shown, the new k-ω model predicts more upstream influence, a less gradual pressure rise, and a lower pressure plateau at separation, relative to the 1974 results. All of these features represent improvement in predictive accuracy. The predicted overall pressure rise is higher than measured because the finite difference grid is too coarse to accurately compute properties across the various shock waves, and no special shock-capturing procedure has been implemented in the program. Thus, the numerical shock is somewhat stronger than desired. Also, note that the Reynolds number for the experimental data is 10^6, so close agreement between experiment and theory should not be expected.

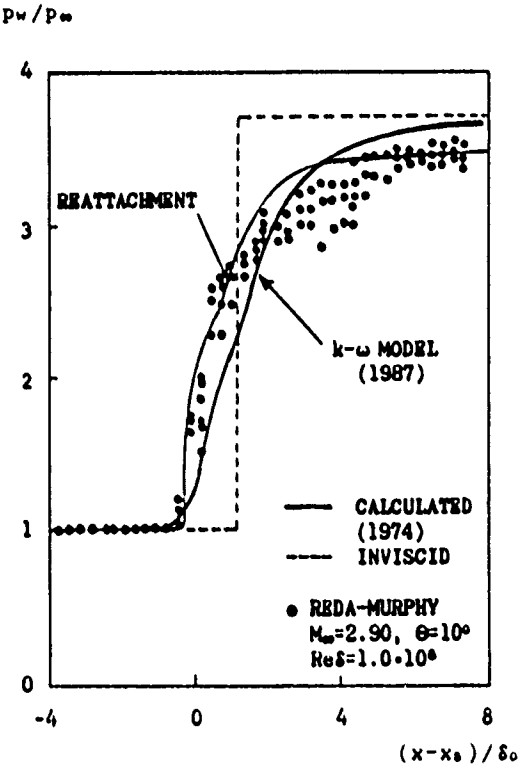

Figure 4. Comparison of calculated surface pressure distribution with experimental data for $M_\infty = 2.96$, $\theta = 9.87°$.

Strong Shock Results. Figure 5 compares results of the strong shock case with the 1974 computations. Results are included for both the k-ω model and the multiscale model. Again, for both models, more upstream influence is predicted, the pressure rise is more gradual and the pressure plateau at separation is reduced relative to the 1974 results. The major difference between the two computations is that, for the multiscale model, the separation bubble and its wake are unsteady. The latter feature is generally observed experimentally in this type of flow, thus suggesting that the multiscale model may

be simulating more of the physics of turbulence than the k-ω model. Note that, as in the weak shock case, Reynolds number for the experimental data is 10^6, so close correspondence between computed and measured pressures should not be expected.

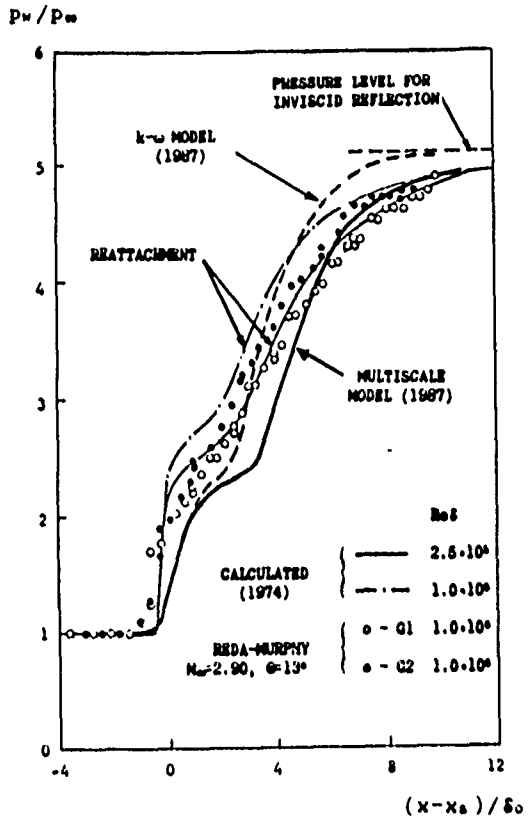

Figure 5. Comparison of calculated surface pressure distribution with experimental data for M_∞ = 2.96, Θ = 12.75°.

Summary. The fact that, consistent with experimental observations, the multiscale model predicts unsteadiness while the k-ω model does not may prove to be a profound development. More definitive applications such as the compression corner experiments of Settles, et al[17] and Brown[18] are needed to determine if this is true. Although the predicted trends are encouraging, there is little to be gained by continuing with these computations. Firstly, the finite-difference grid used is too coarse to provide error-free numerical results. Secondly, as with most data for two-dimensional shock-boundary-layer interactions, the experimental data[18] are of dubious quality, with strong three-dimensional effects known to be present.

5. Unsteady Boundary Layers

The final round of applications is for incompressible, unsteady turbulent boundary layers. These flows pose a difficult challenge to turbulence models because many complicated frequency dependent phenomena are generally present, including periodic separation and reattachment.

5.1 Cases Analyzed

To test the model equations for unsteady boundary layers, we have simulated the experiments performed by Jayaraman, Parikh and Reynolds.[19] In these experiments, a well developed steady turbulent boundary layer enters a test section which has been designed to have freestream velocity that varies according to (see Figure 6):

$$U_e = U_o[1-ax'[1-\cos(2\pi ft)]] \qquad (15)$$

The quantity x' is fractional distance through the test section defined by

$$x' = (x-x_0)/(x_1-x_0) \qquad (16)$$

where x_0 and x_1 are the values of streamwise distance, x, at the beginning and end of the test section, respectively.

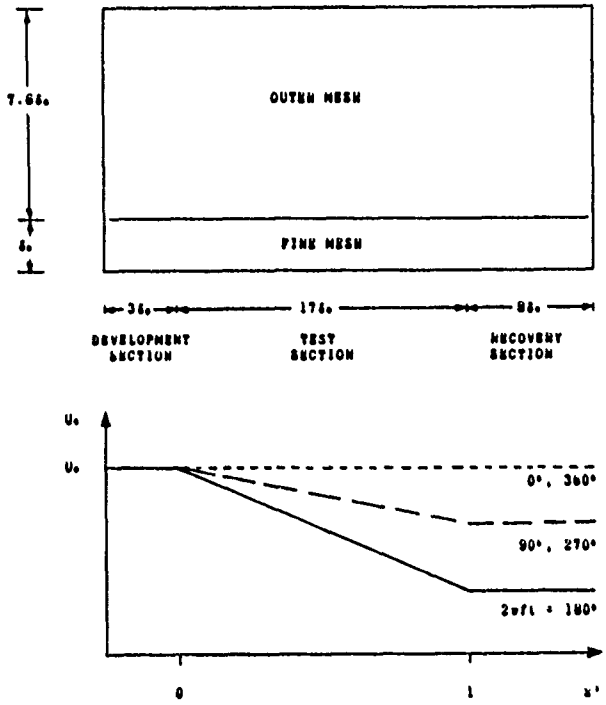

Figure 6. Schematics of the computational domain and freestream velocity distribution for the Jayaraman, Parikh and Reynolds experiments.

Thus, an initially steady equilibrium turbulent boundary layer is subjected to a sinusoidally varying adverse pressure gradient. The experiments were performed for "low" and "high" amplitude unsteadiness characterized by having a ≐ 0.05 and 0.25, respectively. For both amplitudes, experiments were conducted for five frequencies ranging from f = 0.1 hz to 2.0 hz. The computations simulate nine of the experiments, including all five of the low amplitude cases and all but the lowest frequency case for high amplitude. We will explain our reason for omitting this case in Subsection 5.3.

5.2 Numerical Considerations

Numerical Algorithm. The numerical algorithm used for our two-dimensional, unsteady boundary-layer computations is an unconditionally stable implicit marching method. The scheme is second-order accurate in the direction normal to the surface. For stability, particularly through separation, the computational procedure uses upwind differencing for the streamwise convection terms.

Although the algorithm is unconditionally stable, the presence of source terms in the turbulence model equations makes the equations sufficiently stiff to preclude using a streamwise Courant number, $C_x = U\Delta t/\Delta x$, in excess of approximately 0.6, a limitation comparable to that found in our Navier-Stokes applications. By contrast, the boundary-layer computations are stable with a viscous Courant number, $C_y = 2\nu\Delta t/(\Delta y)^2$, in excess of 600, significantly larger than the corresponding viscous Courant number of 40 in our Navier-Stokes applications.

Integration through separation is accomplished by computing the streamwise convective term in the momentum equation according to

$$u\partial u/\partial x = \max[0,u]\cdot\Delta u/\Delta x \qquad (17)$$

where $\Delta u/\Delta x$ is the finite difference approximation to $\partial u/\partial x$. In other words, on regions of reverse flow, we set the streamwise convective term to zero. This is the procedure first implemented by Reyhner and Flugge-Lotz.[20]

Boundary and Initial Conditions. The experiments did not realize the desired freestream velocity distribution given in Equation (15), especially for the high amplitude cases. The actual freestream velocity distribution achieved is presented graphically by Jayaraman, et al and can be fairly well represented in terms of five parameters a_0, a_1, a_2, a_3 and ϕ_0 as follows.

$$U_e = \bar{U}_e + A_{1,ue}\cos(2\pi ft+\phi) \qquad (18)$$

where

$$\bar{U}_e = \begin{cases} U_0(1 - a_0x') ; & 0 \le x' \le .38 \\ \lambda U_0(1 - a_1x') ; & .38 \le x' \le 1 \end{cases} \qquad (19)$$

$$A_{1,ue} = U_0 a_2 x' \qquad (20)$$

$$\phi(x') = \phi_0\exp(-a_3x') \qquad (21)$$

The parameter λ is chosen to insure continuity of the velocity, i.e., we require that $\lambda = (1-.38a_0)/(1-.38a_1)$. The data for the actual freestream velocity realized in the experiments are accurately represented using the values listed in Table 3 for the five parameters.

Table 3. Freestream Velocity Parameters

Amp	Frequency	a_0	a_1	a_2	a_3	ϕ_0
Low	0.1 hz	.0526	.0244	.05	2.5	-8°
Low*	0.2 hz	.0526	.0244	.05	3.7	-11°
Low	0.5 hz	.0526	.0244	.05	5.5	-15°
Low	1.0 hz	.0526	.0244	.05	4.0	-35°
Low	2.0 hz	.0526	.0244	.05	4.2	-65°
High	0.1 hz	.2200	.1500	.15	2.0	-26°
High	0.2 hz	.2200	.1650	.22	2.8	-35°
High	0.5 hz	.2250	.1850	.25	6.5	-40°
High	1.0 hz	.2500	.1700	.25	4.9	-65°
High	2.0 hz	.2500	.1700	.25	3.5	-100°

* No data given by Jayaraman, et al. Values inferred from interpolation between f=0.1 hz and f=0.5 hz.

Upstream boundary conditions for the computations have been established by using our steady two-dimensional boundary layer program, EDDYBL, to generate profiles which yield close matches to the measured skin friction ($3.22\cdot10^{-3}$), momentum-thickness Reynolds number (2790) and shape factor (1.42). For the computed profiles, we are able to match each of the three quantities to within 0.1% of the corresponding measured value. Because the finite-difference grid for the unsteady computations has its upstream boundary three initial boundary-layer thicknesses ($3\delta_0$) ahead of the test section, the EDDYBL profiles $3\delta_0$ ahead of the point where the experimental skin friction, etc. have been matched are used as upstream boundary conditions for the unsteady computations.

Initial conditions for all nine computations have been obtained by first setting all flow properties to the corresponding values at the upstream boundary and then running the program with the fluctuating velocity contribution set to zero. The solution is then advanced in time until temporal variations in flow properties vanish. The steady state solution obtained in this manner serves as the initial flowfield for the unsteady applications.

Finite Difference Grid. The computational domain, shown in Figure 6, covers the region from $x' = -0.18$ to $x' = 1.50$, and from $y' = 0$ to $y' = 0.50$, where $y' = y/(x_1-x_0)$. In terms of the boundary-layer thickness upstream of the test section, δ_0 = 35.5 mm (0.116 ft), the upstream and downstream boundaries are thus $28\delta_0$ distant from one another and the upper boundary lies $8.6\delta_0$ above the surface. The beginning of the test section, $x' = 0$, is located a distance $3\delta_0$ from the upstream boundary.

For all computations, the finite-difference mesh is rectangular. It has 34 equally-spaced points in the streamwise direction and 50 points normal to the surface. The normal mesh consists of a 35-point "fine" mesh between the surface

and $y \doteq \delta_o$, with the remaining 15 points placed in an "outer" mesh between the fine mesh and the upper boundary. In both regions, the distance between adjacent mesh points follows a geometric progression. The grading ratio is 1.21 for the fine mesh and 1.14 for the outer mesh. Numerical experimentation shows that doubling the number of grid points in each direction, i.e., using a 68 x 100 point mesh, has a negligible effect on solution accuracy.

Data Reduction. In order to compare computed and measured flow properties, we must decompose any flow property $y(\underline{x},t)$ in terms of three components, viz,

$$y(\underline{x},t) = \bar{y}(\underline{x}) + \tilde{y}(\underline{x},t) + y'(\underline{x},t) \qquad (22)$$

where $\bar{y}(\underline{x})$ is the long-time averaged value of $y(\underline{x},t)$, $\tilde{y}(\underline{x},t)$ is the organized response component due to the imposed unsteadiness, and $y'(\underline{x},t)$ is the turbulent fluctuation. In order to extract the quantities presented in graphical form by Jayaraman, et al, we first note that what our program computes is the phase averaged component, $\langle y(\underline{x},t)\rangle$, defined by

$$\langle y(\underline{x},t)\rangle = \bar{y}(\underline{x}) + \tilde{y}(\underline{x},t) \qquad (23)$$

Jayaraman, et al expand $\langle y(\underline{x},t)\rangle$ in a Fourier series according to

$$\langle y(\underline{x},t)\rangle = \bar{y}(\underline{x}) + \sum_{n=1}^{\infty} A_{n,y}(\underline{x})\cos[2n\pi ft+\phi_{n,y}(\underline{x})] \qquad (24)$$

Velocity profile data, for example, are presented by Jayaraman, et al in terms of $\bar{u}(\underline{x})$, $A_{1,u}(\underline{x})$ and $\phi_{1,u}(\underline{x})$. These quantities have been extracted from the boundary layer solution by the normal Fourier decomposition, viz, by computing the following integrals.

$$\bar{u}(\underline{x}) = f\int_0^{1/f} \langle u(\underline{x},t)\rangle dt \qquad (25)$$

$$A_{1,u}(\underline{x})\cos\phi_{1,u} = f\int_0^{1/f} \langle u(\underline{x},t)\rangle\cos(2\pi ft)dt \qquad (26)$$

$$A_{1,u}(\underline{x})\sin\phi_{1,u} = -f\int_0^{1/f} \langle u(\underline{x},t)\rangle\sin(2\pi ft)dt \qquad (27)$$

Computing Time. Table 4 lists the number of cycles and corresponding computing time required to achieve periodicity on our Motorola 68020/68881 based microcomputer. Execution times are approximately 30% longer than those which would be realized on a VAX 11-780 minicomputer.

5.3 Results

The Zero Frequency Limit. Before proceeding to the unsteady computations, we first test for consistency with a key observation made by Jayaraman, et al for the limit of zero frequency. On the one hand, they find that for the mean velocity given by Equation (15) with f = 0 and a = 0.25, massive separation occurs in the test section. On the other hand, even at the smallest frequency for which experiments were done, when f is not zero the observed flow is much more well behaved. On the average, the boundary layer remains attached although, at some frequencies for the high amplitude cases, periodic separation and reattachment occurs.

Table 4. Unsteady Boundary Layer Computing Time and Number of Cycles Needed to Achieve a Periodic Solution

Amp	Frequency	Cycles	k-ω	Multiscale
Low	0.1 hz	2	-	85 min
Low	0.2 hz	2	-	42 min
Low	0.5 hz	3	-	20 min
Low	1.0 hz	4	-	20 min
Low	2.0 hz	7	-	18 min
High	0.2 hz	2	25 min	42 min
High	0.5 hz	3	15 min	26 min
High	1.0 hz	5	15 min	25 min
High	2.0 hz	10	15 min	26 min

Part of the reason for this behavior is explained by Jayaraman, et al. When we set f = 0, the pressure gradient is given by

$$dp/dx' = \rho U_o^2 a(1 - ax') \quad \text{for } f = 0 \qquad (28)$$

However, because of the nonlinearity of the convective terms in the momentum equation, for any nonzero f, the mean (long-time average) pressure gradient is

$$d\bar{p}/dx' = \rho U_o^2 a(1 - {}^3/_2 ax') \quad \text{for } f \neq 0 \qquad (29)$$

The gradient for $f \neq 0$ is thus reduced (for adverse gradient, i.e., for $a > 0$), and is less likely to cause separation.

To test the model's consistency with this observation, two steady computations have been done, the first using the pressure gradient for f = 0 [Equation (28)] and the second for the gradient given in Equation (29). The computations were performed with our tried and proven steady boundary layer program, EDDYBL, and with the new unsteady program. This scheme, in addition to testing the model, also provides a test of the new program's accuracy relative to the established program.

Using a value for a of 0.25, our predictions match those described by Jayaraman, et al. Using the pressure gradient in Equation (28), the boundary layer separates at $x' = 0.87$. By contrast, when the pressure gradient of Equation (29) is used, the boundary layer remains attached throughout the test section.

Low Amplitude Cases. For each of the low amplitude cases, computation begins with the initial conditions and continues for at least five and as many as ten periods. This proves sufficient to achieve a periodic solution as determined by monitoring surface skin friction (see Table 4).

Figures 7 through 9 compare computed and measured velocity profiles at x' = 0.88 for the five low amplitude cases. As shown in Figure 7, computed mean velocity profiles differ from corresponding measured profiles by no more than 5% of scale. Comparison of computed and measured $A_{1,u}$ profiles shows that, consistent with measurements, unsteady effects are confined to the near wall Stokes layer at the higher frequencies (f > .5 hz). By contrast, at the two lowest frequencies, the entire boundary layer is affected with significant amplification of the organized component occurring away from the surface. Differences between the numerical and experimental $A_{1,u}$ profiles are less than 10%. Computed and measured phase, $\phi_{1,u}$, profiles are very similar with differences nowhere exceeding 5°.

High Amplitude Cases. The high amplitude cases have proven to be more difficult to simulate numerically. Although our unsteady boundary-layer program is stable using the measured freestream velocity (Table 3), the vertical velocity and hence, the thickness of the viscous region, is unreasonably large. This phenomenon is sometimes observed when the procedure of Reyhner and Flugge-Lotz is used to compute through separation with a parabolic marching scheme. Rather than predicting only modest periodic separation followed by reattachment, the program predicts catastrophic separation which extends to the end of the computational domain.

It is very likely that the difficulties encountered are due entirely to shortcomings of the boundary-layer approximations and not evidence of shortcomings in the turbulence model. In order to verify this claim, a full Navier-Stokes computation would be needed. Since we have no incompressible Navier-Stokes program suitable for such a computation, this point must be left as a matter of conjecture.

Further headway can be made with our unsteady boundary-layer program, however. We have found that by using a somewhat milder adverse pressure gradient, catastrophic separation can be avoided. If, at the peak of the cycle, the mean freestream velocity at x' = 1 decreases to 83% of its value at x' = 0 rather than the 80% realized in the experiments, only the highest frequency case shows any appreciable separation. Consistent with experimental observations, with the exception of

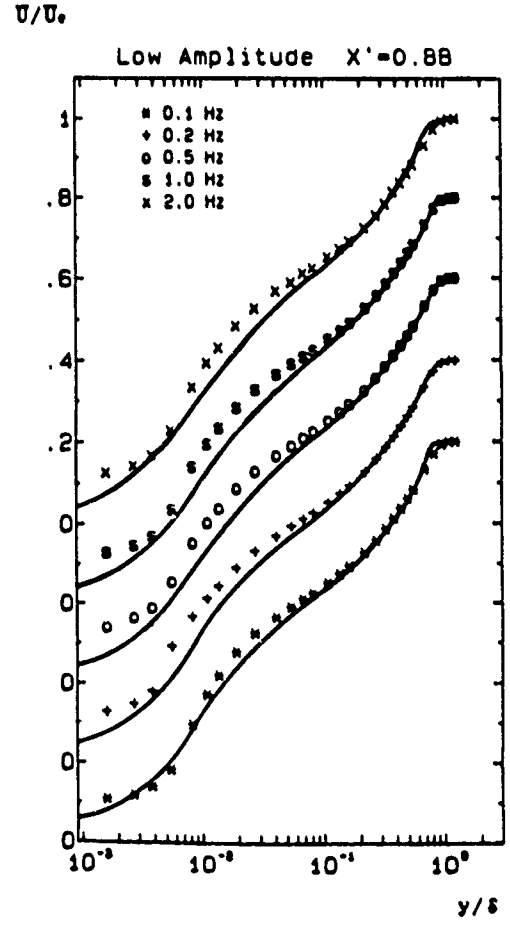

Figure 7. Comparison of computed and measured mean velocity profiles; low amplitude.

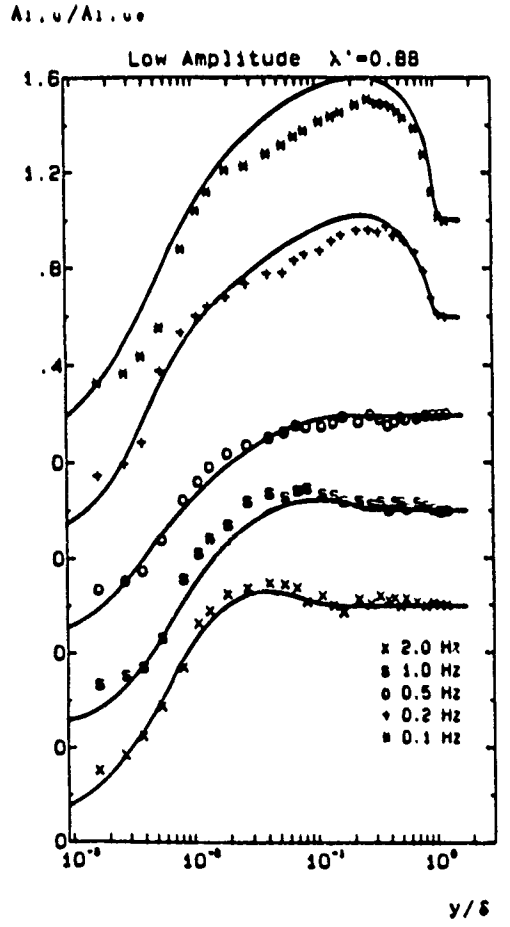

Figure 8. Comparison of computed and measured $A_{1,u}$ profiles; low amplitude.

the f = 0.1 hz case, the lower frequency cases are very close to, at most, incipient separation at some point during each cycle. We have been unable to find any combination of freestream parameters which yield a satisfactory solution for the f = 0.1 hz case.

Table 5 summarizes the altered freestream velocity parameters used in our computations. Note that only the parameters a_0 and a_1 have been altered, and that these parameters affect only the mean velocity component. In all cases, we have used the measured fluctuation amplitude.

Table 5. Modified Freestream Velocity Parameters

Amp	Frequency	a_0	a_1	a_2	a_3	ϕ_0
High	0.2 hz	.1650	.1650	.22	2.8	-35°
High	0.5 hz	.1700	.1700	.25	6.5	-40°
High	1.0 hz	.1700	.1700	.25	4.9	-65°
High	2.0 hz	.1700	.1700	.25	3.5	-100°

Figures 10 through 12 compare computed and measured velocity profiles at x' = 0.94. As with the low amplitude cases, computed and measured $\bar{u}(\underline{x})$ profiles lie within 5% of scale of each other. Similarly, the computed $A_{1,u}$ and $\phi_{1,u}$ profiles differ

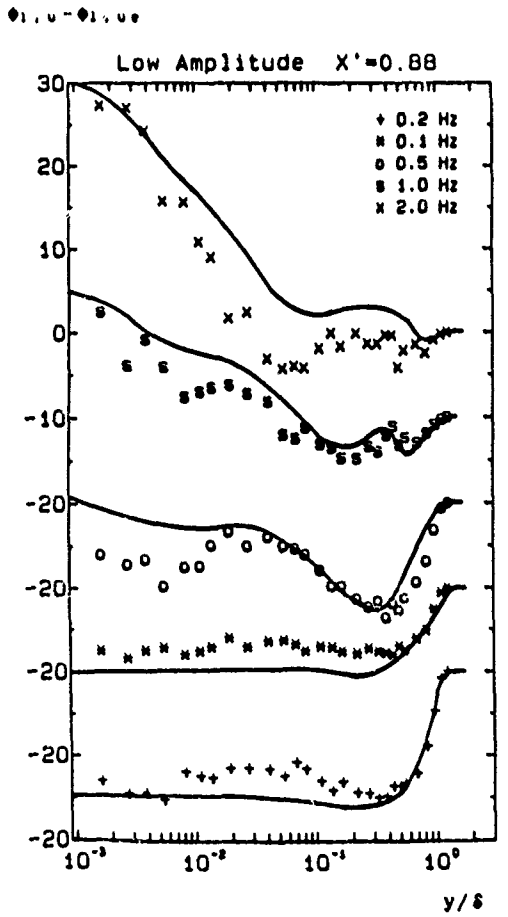

Figure 9. Comparison of computed and measured phase profiles; low amplitude.

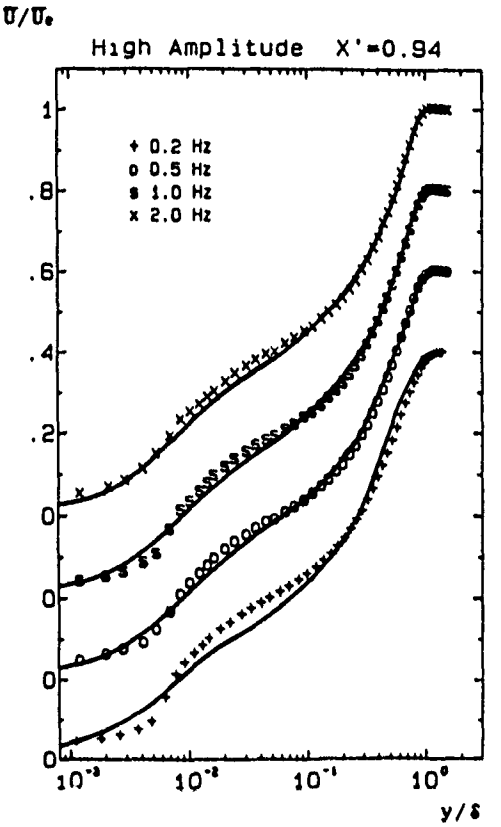

Figure 10. Comparison of computed and measured mean velocity profiles; high amplitude.

from the corresponding measured profiles by less than 10%. To provide a measure of how accurately temporal variations have been predicted, Figure 13 compares computed and measured shape factor through a complete cycle for all four frequencies. As shown, differences between computed and measured shape factors are less than 5%.

k-ω Model Predictions. The four high amplitude cases have also been computed using the k-ω model. Results are included in Figure 13 which shows that, as in our 3-D boundary layer computations, the k-ω and multiscale model predictions differ by only a few percent. Although it is possible the test cases are not as difficult as we expected, this seems unlikely in view of the wide Strouhal number range and the fact that periodic separation and reattachment are present. More likely, the k-ω model fares well because all of the cases have attached boundary layers through most of each cycle and in the mean.

6. Summary and Conclusions

Results of the three-dimensional boundary layer computations are inconclusive. The two cases considered apparently are sufficiently simple to permit accurate prediction with a two-equation turbulence model. To determine how much better the multiscale model is for 3-D boundary layers,

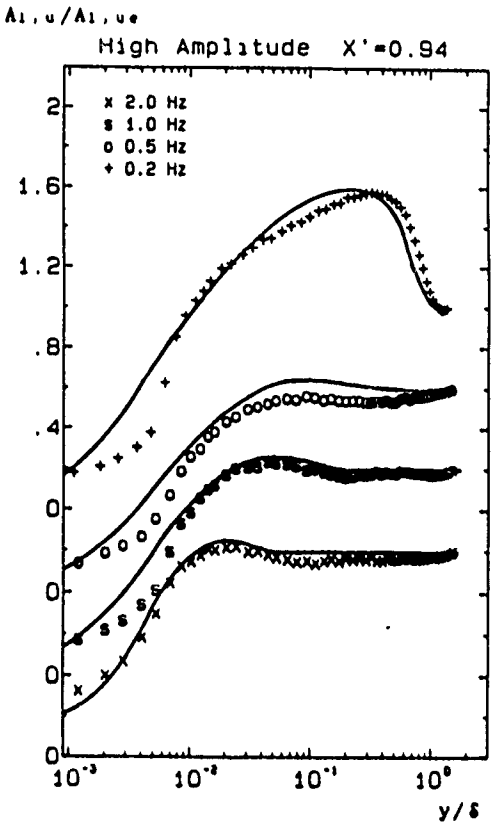

Figure 11. Comparison of computed and measured $A_{1,u}$ profiles; high amplitude.

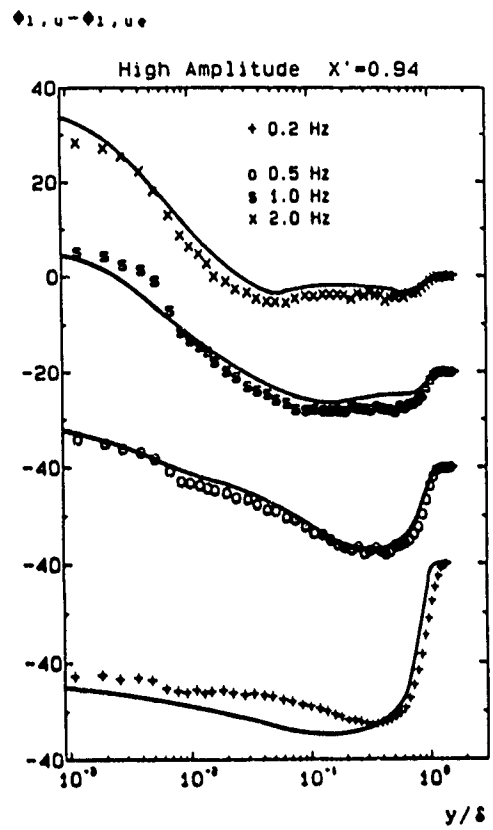

Figure 12. Comparison of computed and measured phase profiles; high amplitude.

more difficult tests involving anisotropic shear are needed.

Although only a cursory examination of model predictions for shock separated flows has been made, our Navier-Stokes computations indicate potentially profound results. While the k-ω model appears to improve somewhat upon the Wilcox[13] results of 1974, much more provocative things happen when the multiscale model is used. Consistent with most experimental observations, the flow within and in the wake of the separation bubble has been found to be inherently unsteady.

The unsteady boundary-layer computations offer the first definitive measure of how accurately the multiscale model simulates the physics of turbulent boundary layers. For a wide range of Strouhal numbers, the multiscale model more-or-less duplicates the structure of a turbulent boundary layer subjected to a sinusoidally varying adverse pressure gradient. As somewhat of a surprise, the two-equation model is just as accurate for these flows.

7. Acknowledgment

This research has been supported by the U.S. Army Research Office under Contract DAAG-29-83-C-0003.

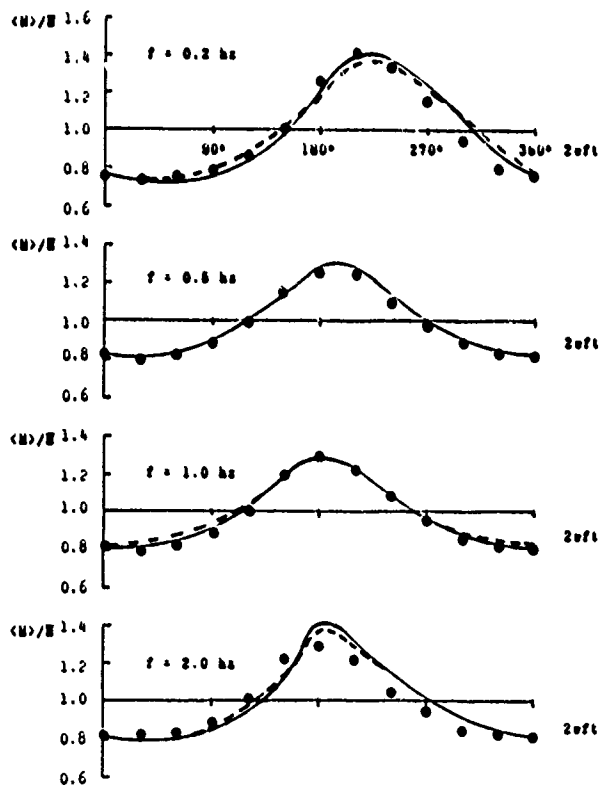

Figure 13. Comparison of computed and measured temporal variation of shape factor; high amplitude. --- k-ω Model, —— Multiscale Model.

References

1. Kline, S.J., Cantwell, B.J. & Lilley, G.M., 1980-81 AFOSR-HTTM-Stanford Conference on Complex Turbulent Flows, Stanford Univ (1981).

2. Wilcox, D.C., "A Complete Model of Turbulence Revisited," AIAA Paper 84-0176 (1984).

3. Wilcox, D.C., "Multiscale Model for Turbulent Flows," AIAA Paper 86-0029 (Jan 1986).

4. Marshall, T., Jones, C. and Kluger, S., "The Definicon 68020 Coprocessor," BYTE, pp 120-144 (Jul 1986).

5. Favre, A., "Equations des Gaz Turbulents Compressibles," J Mecan, Vol 4, No 3, pp 361-390 (1965).

6. Larsson, L., "SSPA-ITTC Workshop on Ship Boundary Layers," SSPA (1980).

7. Cebeci, T. and Smith, A.M.O., Analysis of Turbulent Boundary Layers, Ser in Appl Math & Mech, Vol XV, Academic Press (1974).

8. Wilcox, D.C., "Program EDDY3 User's Guide," DCW Industries, Inc. (Mar 1986).

9. Krauss, E., Comment on "Solution of a Three-Dimensional Boundary-Layer Flow with Separation," AIAA J, Vol 6, No 12, pp 575-576 (Mar 1969).

10. Blottner, F.G., "Variable Grid Scheme Applied to Turbulent Boundary Layers," Comput Meth Appl Mech & Eng, Vol 4, No 2, pp 179-194 (Sep 1974).

11. Wilcox, D.C., "Algorithm for Rapid Integration of Turbulence Model Equations on Parabolic Regions," AIAA Journal, Vol 19, No 2, pp 248-251 (Feb 1981).

12. Wilcox, D.C., "Boundary-Layer Development on Ship Hulls," DCW Industries Report No DCW-R-26-01 (1983).

13. Wilcox, D.C., "Numerical Study of Separated Turbulent Flows," AIAA Paper 74-584 (Jun 1974).

14. MacCormack, R.W., "A Numerical Method for Solving the Equations of Compressible Viscous Flow," AIAA Paper 81-0110 (1981).

15. Wilcox, D.C., "Program EDDYBL User's Guide," DCW Industries, Inc. (Feb 1986).

16. Reda, D.C. and Murphy, J.D., "Shock Wave-Turbulent Boundary Layer Interactions in Rectangular Channels, Part II: The Influence of Sidewall Boundary Layers on Incipient Separation and Scale of the Interaction," AIAA Paper 73-234 (1973).

17. Settles, G.S., Vas, I.E. and Bogdonov, S.M., "Details of a Shock Separated Turbulent Boundary Layer at a Compression Corner," AIAA Journal, Vol 14, pp 1709-1715 (Dec 1976).

18. Brown, J.D., "Two Component LDV Investigation of Shock Related Turbulent Boundary Layer Separation with Increasing Three Dimensionality," PhD Thesis, U.C. Berkeley (1986).

19. Jayaraman, R., Parikh, P. and Reynolds, W.C., "An Experimental Study of the Dynamics of an Unsteady Turbulent Boundary Layer," Technical Report No TF-18, Dept Mech Eng, Stanford Univ, CA (Dec 1982).

20. Reyhner, T.A. and Flugge-Lotz, I., "The Interaction of a Shock Wave With a Laminar Boundary Layer," International Journal of Non-Linear Mechanics, Vol 3, pp 173-199 (Jun 1968).

APPENDIX D: MULTISCALE MODEL BOUNDARY CONDITIONS

The paper reproduced in this appendix was presented at the AIAA 26th Aerospace Sciences Meeting, held in Reno, Nevada, January 11-14, 1988. The formal reference to this paper is as follows.

> Wilcox, D. C., "More Advanced Applications of the Multiscale Model for Turbulent Flows," AIAA Paper 88-0220, Jan. 1988.

This is a two-part paper, the first part focusing on further development of the Wilcox multiscale model and the second part focusing on shock-separated flows. The development part of the paper establishes multiscale-model boundary conditions for rough surfaces and for surface mass injection. The rough surface boundary conditions are tested for effects of roughness on boundary-layer skin friction. Applications also include a blown boundary layer, flow over convex surfaces, and the incompressible mixing layer. The shock separated applications were ultimately included in the paper reproduced in Appendix F.

AIAA'88

AIAA-88-0220

More Advanced Applications of the Multiscale Model for Turbulent Flows

D.C. Wilcox, DCW Industries, Inc.
La Cañada, California

AIAA 26th Aerospace Sciences Meeting
January 11-14, 1988/Reno, Nevada

For permission to copy or republish, contact the American Institute of Aeronautics and Astronautics
370 L'Enfant Promenade, S.W., Washington, D.C. 20024

MORE ADVANCED APPLICATIONS OF THE MULTISCALE MODEL FOR TURBULENT FLOWS

David C. Wilcox†
DCW Industries, Inc.
La Cañada, California

Abstract

The new "multiscale" model for turbulent flows developed by Wilcox has been subjected to a continuing series of rigorous applications, including shock-induced boundary-layer separation, to test its accuracy in simulating complex flow phenomena. While previous advanced applications presented by Wilcox have been inconclusive regarding superiority of the multiscale model over two-equation models, this paper demonstrates a marked improvement in predictive accuracy for flows which include boundary-layer separation. As speculated in the original development of the model, results obtained demonstrate that the model is superior because it accounts for disalignment of the Reynolds-stress-tensor and the mean-strain-rate-tensor principal axes. Effects of surface roughness, mass injection, streamline curvature and the mixing layer are also analyzed.

1. Introduction

This paper consists of two parts. The first part includes results of continued theoretical development of the Wilcox multiscale model[1,2]. Specifically, Part 1 includes analysis of: (a) model-predicted sublayer structure including surface roughness and mass injection; (b) streamline curvature effects; and (c) the mixing layer. The second part focuses upon application of the model to shock-separated flows. In all cases, detailed comparisons with experimental data are presented.

Although the original paper in which the multiscale model was formulated includes a perturbation analysis of the viscous sublayer, the focus was confined to perfectly smooth surfaces. This paper extends the analysis of the sublayer including surface roughness and mass injection in the same manner used in formulating the Wilcox k-ω model[3].

To demonstrate the model's ability to simulate flows with differing turbulence structure, boundary layers over curved surfaces and the mixing layer are investigated. Results of the analysis show that, unlike most two-equation models, the multiscale model appears to contain enough of the physics of turbulence to make accurate predictions for planar boundary layers, flow over curved surfaces and free shear flows without the need to adjust closure coefficients.

Part 2 presents the most important of all the applications to date, viz, shock-separated turbulent boundary layer computations. Flows considered include two planar Mach 3 compression-corner flows[4] and an axisymmetric Mach 3 compression corner flow[5]. The flows selected provide a definitive measure of differences attending use of the multiscale model as compared to the two-equation model.

†President; Associate Fellow AIAA.

Released to AIAA to publish in all forms.

To underscore the significance of the results obtained in this study, it is worthwhile to briefly review our own efforts over the past fourteen years in quest of an acceptable numerical solution for flow into a compression corner. The first solutions to the Reynolds-averaged Navier-Stokes equations, using an advanced turbulence model, for shock-induced separation of a turbulent boundary layer were done by Wilcox[6]. In this early computational fluid dynamics (CFD) study, Wilcox performed six computations, three for reflection of an oblique shock from a flat plate and three for flow into a compression corner. Results of the study indicated that, using a two-equation turbulence model, a reasonably accurate description of the flowfield can be obtained for reflection of an oblique shock from a flat plate. However, the numerical flowfields for the compression corner cases were significantly different from the experimentally observed flowfields, even though Mach and Reynolds numbers and shock strength were identical to those of the flat-plate cases. Thus, a seemingly simple change in flow geometry caused a major difference in predictive accuracy.

To put the Wilcox computations in proper perspective, note that the turbulence model used in the computations was the Saffman-Wilcox[7] k-ω[2] model with surface boundary conditions given by matching to the law of the wall, a procedure which has since come to be referred to as using wall functions. The numerical algorithm used was a first-order accurate explicit time-marching procedure. Since the Wilcox study, computational methods have improved dramatically thanks to the innovative work of many researchers, most notably, MacCormack[8], Beam and Warming[9] and Steger[10]. Today, it is possible to perform two-equation turbulence model computations for shock-separated flows without the aid of wall functions on a (relatively crude) 1200-point finite difference mesh using a fast desk top microcomputer[2]. However, until this study, little improvement in predictive accuracy relative to Wilcox's results of 1974 has been realized for compression corner flows.

The work of Horstman, et al[11,12] provides clear substantiation of this claim. They have applied many turbulence models to shock-separated flows with almost universal results, viz:

1. too little upstream influence as exhibited by pressure starting to rise at a point well downstream of the measured beginning of adverse pressure gradient;

2. surface pressure in excess of measured values above the separation bubble;

3. skin friction values higher than those measured downstream of reattachment;

4. velocity profiles downstream of reattachment which indicate flow deceleration in excess of corresponding measurements.

On the one hand, by using wall functions and the k-ε turbulence model[13], Viegas, Horstman and Rubesin[12] are able to remove item 3 from this list. On the other hand, they achieve only modest improvements in the other items. This lack of success on the compression-corner problem, which has persisted for more than a decade, is excellent testimony to the oft quoted statement that turbulence modeling is the pacing item in CFD.

One of the major conclusions of the study by Wilcox[6] is that the relatively poor performance of the two-equation model for the compression corner computations is caused by the model's use of the Boussinesq approximation which holds that the principal axes of the Reynolds stress tensor are parallel to those of the mean strain rate tensor. The physical reasoning is that, unlike the flow induced by an oblique shock reflecting from a flat plate, the mean strain rate tensor's principal axes abruptly rotate at the flat-plate/ramp junction. The Boussinesq approximation implies that the Reynolds stresses also change abruptly which, on physical grounds, would be a rather questionable event.

The excellent predictions made by Johnson[14,15] for transonic flow over a "bump" substantiate the notion that use of the Boussinesq approximation lies at the root of the two-equation model's inability to accurately simulate properties of separated flows. Using an approach in which a lag occurs between sudden changes in mean strain rate and the Reynolds shear stress, Johnson is able to duplicate measured flow properties to within engineering accuracy. His predictions are so much better than those obtained with the k-ε model that further applications with the latter seem pointless, especially since the k-ε model fares so poorly even for attached boundary layers in an adverse pressure gradient[3]. While Johnson offers significant improvement for transonic separated flows, the model has been demonstrated to be accurate for a limited range of Mach numbers and has been developed much in the spirit of mixing length, i.e., it is a very powerful "incomplete" model of turbulence.

The primary purpose of this research study has been to apply both the multiscale and k-ω models to the three well documented separated flows referenced above and to assess the differences. As will be shown, the differences are profound.

2. Equations of Motion

Most of the computations in this study have been done using both the k-ω model and the multiscale model. These models differ in the postulated constitutive relation between the Reynolds stress tensor and mean flow properties. The k-ω model implements the Boussinesq approximation in which Reynolds stress is assumed proportional to mean strain rate. By contrast, the multiscale model computes each component of the Reynolds stress tensor individually.

2.1 Mean Conservation Equations

For both models, we must solve the mass-averaged[16] equations for conservation of mass, momentum and energy, viz,

$$\partial\rho/\partial t + \partial/\partial x_j(\rho u_j) = 0 \qquad (1)$$

$$\partial/\partial t(\rho u_i) + \partial/\partial x_j(\rho u_i u_j) = -\partial p/\partial x_i + \partial\hat{\tau}_{ij}/\partial x_j \qquad (2)$$

$$\partial/\partial t(\rho E) + \partial/\partial x_j(\rho u_j H) = \partial/\partial x_j[u_i\hat{\tau}_{ij} - q_j + (\mu+\sigma^*\mu_T)\partial k/\partial x_j] \qquad (3)$$

where t is time, x_i is position vector, u_i is velocity vector, p is pressure, ρ is density, $\hat{\tau}_{ij}$ is the sum of molecular and Reynolds stress tensors and q_j is the sum of molecular and turbulent heat-flux vectors. In Equation (3), the quantities $E=e+k+u_iu_i/2$ and $H=h+k+u_iu_i/2$ are total energy and total enthalpy, respectively, with $h=e+p/\rho$; e and h denote internal energy and enthalpy. μ and μ_T are molecular and eddy viscosity, ρk is turbulent kinetic energy and σ^* is a closure coefficient.

2.2 Constitutive Relations

For both models, the heat flux vector is computed according to

$$q_j = -(\mu/Pr_L+\mu_T/Pr_T)\partial h/\partial x_j \qquad (4)$$

where Pr_L and Pr_T are laminar and turbulent Prandtl numbers.

The remaining step needed to close this system of equations is to postulate a relation between the total stress tensor, $\hat{\tau}_{ij}$, and mass-averaged flow properties. For both models, total stress is related to Reynolds stress, τ_{ij}, according to

$$\hat{\tau}_{ij} = 2\mu[S_{ij}-{}^1/_3\partial u_k/\partial x_k\delta_{ij}] + \tau_{ij} \qquad (5)$$

where $S_{ij}={}^1/_2(\partial u_i/\partial x_j+\partial u_j/\partial x_i)$ is the mean strain rate tensor.

On the one hand, the k-ω model uses the Boussinesq approximation that Reynolds stress is proportional to mean strain rate, viz,

$$\tau_{ij} = 2\mu_T[S_{ij}-{}^1/_3\partial u_k/\partial x_k\delta_{ij}] - {}^2/_3\rho k\delta_{ij} \qquad (6)$$

On the other hand, with the multiscale model, we introduce two energy scales corresponding to upper and lower partitions of the turbulent energy spectrum. The multiscale model computes τ_{ij} according to

$$\tau_{ij} = \rho T_{ij} - {}^2/_3\rho e\delta_{ij} \qquad (7)$$

where ρT_{ij} is the upper partition contribution to the Reynolds-stress tensor and ρe is the energy of the eddies in the lower partition.

2.3 Turbulent Kinetic Energy and Dissipation Rate

Both models determine turbulent energy and specific dissipation rate, ω, from the following two equations.

$$\partial/\partial t(\rho k) + \partial/\partial x_j(\rho u_j k) = \tau_{ij}\partial u_i/\partial x_j - \beta^*\rho\omega k + \partial/\partial x_j[(\mu+\sigma^*\mu_T)\partial k/\partial x_j] \qquad (8)$$

$$\partial/\partial t(\rho\omega) + \partial/\partial x_j(\rho u_j\omega) = (\gamma\omega/k)\tau_{ij}\partial u_i/\partial x_j - \beta\rho\omega^2 + \zeta\rho\omega[\sqrt{2\Omega_{mn}\Omega_{mn}}] + \partial/\partial x_j[(\mu+\sigma\mu_T)\partial\omega/\partial x_j)] \qquad (9)$$

where $\Omega_{mn}={}^1/_2(\partial u_m/\partial x_n-\partial u_n/\partial x_m)$ is the mean rotation tensor. The quantities β, β^*, γ, ζ, σ and σ^* are closure coefficients. Note also that the eddy

viscosity, μ_T, appearing in Equations (3, 4, 6, 8, and 9) is defined by

$$\mu_T = \rho k/\omega \tag{10}$$

2.4 Upper Partition Equations

For the multiscale model, the upper partition Reynolds stress equation is

$$\partial/\partial t(\rho T_{ij}) + \partial/\partial x_k(\rho u_k T_{ij}) = - P_{ij} + E_{ij} \tag{11}$$

where E_{ij} represents the exchange of energy amongst the mean, upper-partition and lower-partition energies, and is given by

$$E_{ij} = -C_1\beta^*\omega[\tau_{ij}+{}^2/_3\rho k\delta_{ij}] + \hat{\alpha}P_{ij} + \hat{\beta}D_{ij} + \hat{\gamma}\rho k[S_{ij}-{}^1/_3\partial u_k/\partial x_k\delta_{ij}] + {}^2/_3\beta^*\rho\omega k(1-e/k)^{3/2}\delta_{ij} \tag{12}$$

where C_1, $\hat{\alpha}$, $\hat{\beta}$ and $\hat{\gamma}$ are closure coefficients. The tensors P_{ij} and D_{ij} are defined by

$$P_{ij} = \tau_{im}\partial u_j/\partial x_m + \tau_{jm}\partial u_i/\partial x_m \tag{13}$$

$$D_{ij} = \tau_{im}\partial u_m/\partial x_j + \tau_{jm}\partial u_m/\partial x_i \tag{14}$$

Finally, it is instructive to contract Equation (11) which yields the following equation for upper-partition energy, $\rho(k-e) = -{}^1/_2\rho T_{kk}$.

$$\partial/\partial t[\rho(k-e)] + \partial/\partial x_j[\rho u_j(k-e)] = (1-\hat{\alpha}-\hat{\beta})\tau_{ij}\partial u_i/\partial x_j - \beta^*\rho\omega k(1-e/k)^{3/2} \tag{15}$$

This equation is normally used in place of one of the normal stress components of Equation (11).

2.5 Closure Coefficients

Finally, the ten closure coefficients appearing in Equations (1-15) have been established in the prior studies by Wilcox[1,3]. No changes in those coefficients have been made for any of the applications in this study. Their values are as follows.

Multiscale Model

$$\left.\begin{aligned} &\hat{\alpha} = 42/55, \quad \hat{\beta} = 6/55, \quad \hat{\gamma} = 1/4 \\ &\beta = 3/40, \quad \gamma = 4/5, \quad \sigma = 1/2 \\ &\beta^* = 9/100, \quad \zeta = 1, \quad \sigma^* = 1/2 \\ &C_1 = 1 + 4(1-e/k)^{3/2} \end{aligned}\right\} \tag{16}$$

k-ω Model

$$\left.\begin{aligned} &\beta = 3/40, \quad \gamma = 5/9, \quad \sigma = 1/2 \\ &\beta^* = 9/100, \quad \zeta = 0, \quad \sigma^* = 1/2 \end{aligned}\right\} \tag{17}$$

3. Part1: Model Development and Non-Separated Flows

In the first three subsections, we extend and test formulation of surface boundary conditions for the multiscale model to surfaces which include roughness elements or mass injection. Then, the model is tested for attached boundary layers on curved surfaces and for the mixing layer.

3.1 Surface Boundary Conditions

In formulating the multiscale model, Wilcox[1] used perturbation methods to analyze viscous sublayer structure predicted by the model. The analysis exactly paralleled that used for the k-ω model with perfectly smooth surfaces. For both models, the appropriate boundary conditions at a solid boundary follow from: (a) the no-slip boundary condition which means u_i and k vanish at the surface; and (b) the observation that the surface value of specific dissipation rate, ω_w, determines the value of the constant B in the law of the wall, i.e.,

$$u/u_\tau = \kappa^{-1}\ln(u_\tau y/\nu) + B \tag{18}$$

where u_τ is friction velocity, ν is kinematic viscosity, κ is Karman's constant, and y is distance from the surface. Perturbation analysis of the sublayer shows that the limit $\omega_w \to \infty$ corresponds to a perfectly smooth wall and the asymptotic behavior of ω approaching the surface for both models is

$$\omega \to 6\nu/(\beta y^2) \quad \text{as} \quad y \to 0 \quad \text{(Smooth Wall)} \tag{19}$$

In formulating the k-ω model, Wilcox[3] developed a correlation between the value of ω_w and roughness height and also surface mass injection rate which provides a simple and natural way to represent roughness and surface mass-injection effects. A corresponding analysis was not performed for the multiscale model because of numerical difficulties encountered in solving the multiscale equations in the sublayer.

To solve the sublayer equations, which are one-dimensional ordinary differential equations, the procedure used in previous studies has been to add unsteady terms and integrate in time until a steady solution is obtained (complete details are given by Wilcox[3]). The numerical algorithm has been a one-dimensional implicit time-marching method in which the various model equations are solved sequentially. In this study, the numerical difficulties have been resolved by implementing the coupled, Newton's iteration scheme recommended by MacCormack[17]. In addition to making solutions with finite surface values of ω possible, convergence rate for the perfectly smooth surface is dramatically improved. Steady solutions can be obtained in 40 timesteps as compared to nearly 300 timesteps with the uncoupled algorithm.

Using the revised sublayer program, correlations have been made between ω_w, roughness height, k_R, and surface mass-injection velocity, v_w. The resulting correlations are a little different from those appropriate for the k-ω model. The surface boundary conditions based on these correlations are as follows (k-ω model results are included for the sake of completeness). For rough surfaces,

$$\omega = u_\tau^2 S_R/\nu \quad \text{at} \quad y = 0 \quad \text{(Rough Wall)} \tag{20}$$

where the dimensionless coefficient S_R is defined in terms of $k_R^+ = u_\tau k_R/\nu$ by

Multiscale Model

$$S_R = \begin{cases} (50/k_R^+)^2 & ; \quad k_R^+ \le 25 \\ 500/(k_R^+)^{3/2} & ; \quad k_R^+ > 25 \end{cases} \tag{21}$$

k-ω Model

$$S_R = \begin{cases} (50/k_R^+)^2 & ; \quad k_R^+ \le 25 \\ 100/k_R^+ & ; \quad k_R^+ > 25 \end{cases} \tag{22}$$

For surfaces with mass injection,

$$\omega = u_\tau^2 S_B/\nu \quad \text{at} \quad y = 0 \qquad \text{(Mass Injection)} \quad (23)$$

where the dimensionless coefficient S_B is defined in terms of $v_w^+ = v_w/u_\tau$ by

Multiscale Model

$$S_B = 16/[v_w^+(1+4v_w^+)] \quad (24)$$

k-ω Model

$$S_B = 20/[v_w^+(1+5v_w^+)] \quad (25)$$

3.2 Surface Roughness Effects

As a test of the model and the rough-surface boundary condition, we have performed a series of flat-plate boundary layer computations in which both Mach number and surface roughness have been varied. The computations are designed to test consistency with the observation originally made by Goddard[18] that "the effect of surface roughness on skin-friction drag is localized deep within the boundary layer at the surface itself and is independent of the external flow, i.e., Mach number, per se, is eliminated as a variable."

The computations have been done with a compressible boundary layer program, EDDYBL[19], which is second-order accurate in streamwise and normal distance. The multiscale equations are solved in the same coupled manner used in the sublayer program discussed above. Computations have been done for Mach numbers of 0, 1 and 5 and roughness heights corresponding to k_R^+ ranging from zero to 100. For each Mach number, the reference smooth-wall skin friction coefficient, C_{f_o}, corresponds to a momentum-thickness Reynolds number, Re_θ, of 10,000.

Figure 1 compares computed skin friction with the data summarized by Reda, et al[20]. Computed skin friction falls well within experimental data scatter, and, consistent with Goddard's observation, Mach number has little effect on predicted C_f/C_{f_o}. Additionally, consistent with Reda's findings, computed skin friction departs noticeably from the smooth wall value for k_R^+ values near 4 to 5 as opposed to Goddard's correlation which indicates no effect for k_R^+ less than 10.

3.3 Surface Mass-Injection Effects

To test the multiscale model for mass injection effects, we consider an incompressible boundary layer with mass injection. The case considered is a flow analyzed by Andersen, et al[21], and has a surface mass injection rate, v_w, given by $.00375U_e$, where U_e is the (constant) boundary-layer edge velocity. Figure 2 compares computed and measured skin friction and and a velocity profile at the final station (2.3 m.). As shown, with the exception of the first three skin friction values for which differences are about 10%, computed and measured properties are within 4% of each other.

The k-ω model predicts effects of surface roughness and mass injection for the two applications considered here which virtually duplicate multiscale model predictions. This is unsurprising as the boundary conditions and, indeed, model-predicted sublayer structure are very similar for the two models.

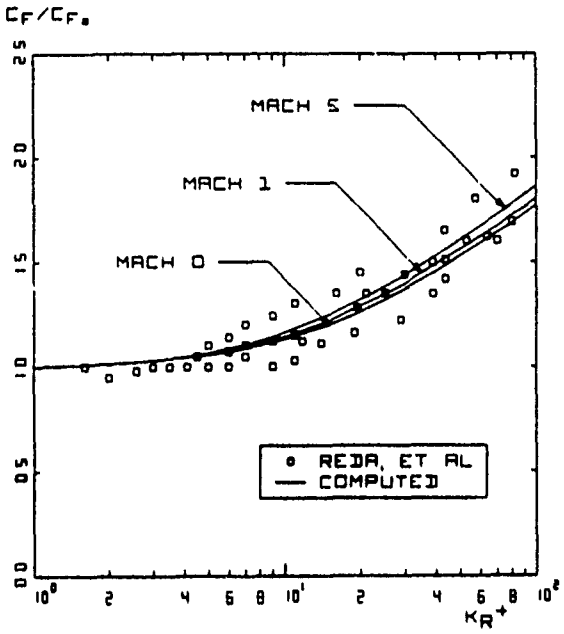

Figure 1. Comparison of computed and measured effect of Mach number on rough-to-smooth wall skin friction ratio.

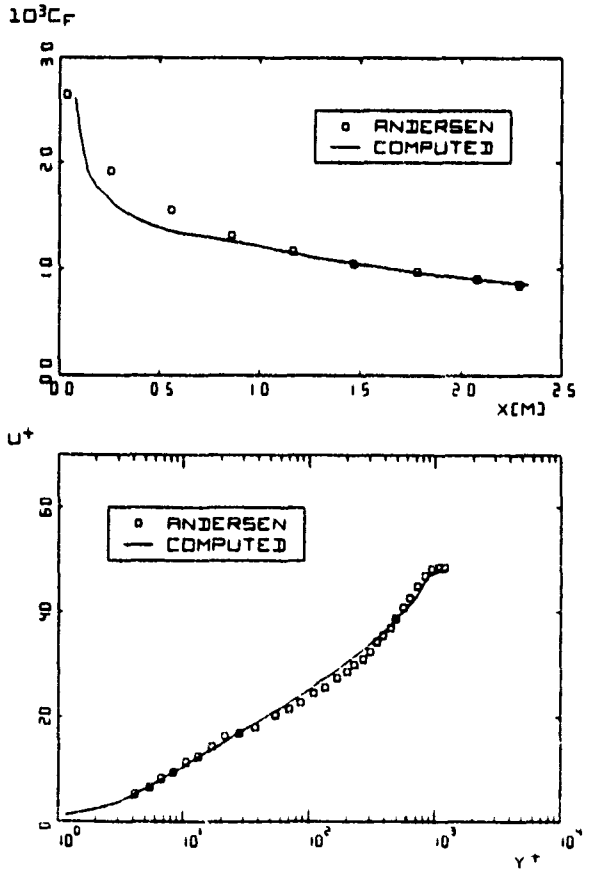

Figure 2. Comparison of computed and measured skin friction and velocity profile at x = 2.3 m. for an incompressible boundary layer with mass injection.

3.4 Streamline Curvature Effects

The centrifugal and Coriolis accelerations attending flow over curved surfaces are known to have a significant effect upon structural features of the turbulent boundary layer. Strictly speaking, such effects cannot be accurately predicted with a two-equation model as curvature has a trivial effect upon the turbulent kinetic energy equation. However, as shown by Wilcox and Chambers[22], if the quantity k is interpreted as being proportional to $\langle v'^2 \rangle$, it is possible to derive a rational modification to the equation for k which reproduces measured curved wall boundary layer properties reasonably well. The modified k equation is not easily generalized for general geometries though, and proves very difficult to implement in separated flow computations. In principle, the multiscale model should display none of these shortcomings. Thus, computing curved wall boundary layers poses an interesting test of the multiscale model.

Using program EDDYBL with terms included appropriate to flow over a curved surface (see Appendix), two computations have been done for flow over a convex surface. The two cases selected for testing the multiscale model are the constant pressure and adverse pressure gradient cases experimentally investigated by So and Mellor[23]. Figures 3 and 4 compare computed and measured skin friction and velocity profiles. To insure accurate starting conditions, the measured momentum and displacement thickness at x = 2 ft. have been matched to within 1%, a point well upstream of the beginning of the curved-wall portion of the run at x = 4 ft. For both computations, computed and measured flow properties differ by less than 6%.

3.5 The Mixing Layer

Another interesting test of the multiscale model is for free shear flows, i.e., flows not bounded by solid surfaces. Free shear flow turbulence has structural features different from wall-bounded flows and accurate predictions for both kinds of flow would imply some degree of universality of the model's closure approximations. For purposes of testing the model, we address the mixing layer, i.e., the mixing of two parallel streams of differing velocity. For the present purposes, one stream will be at rest.

Solutions have been obtained for both the k-ω model and the multiscale model. The model equations admit a similarity solution, valid in the far field, in which the independent variable is $\eta = y/x$. To solve the resulting equations, we have used the same time-marching procedure implemented in the sublayer analysis of Section 3.1. To assure numerically accurate solutions, mesh point number has been varied from 20 to 500. No more than 50 points are needed for grid independence.

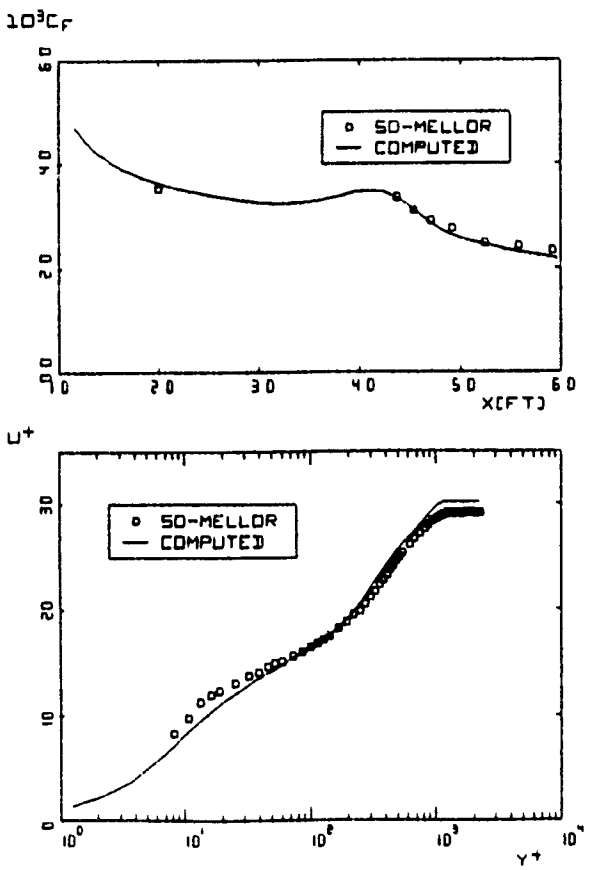

Figure 3. Comparison of computed and measured skin friction and velocity profile at x = 5.9 ft. for flow over a convex wall with constant freestream pressure.

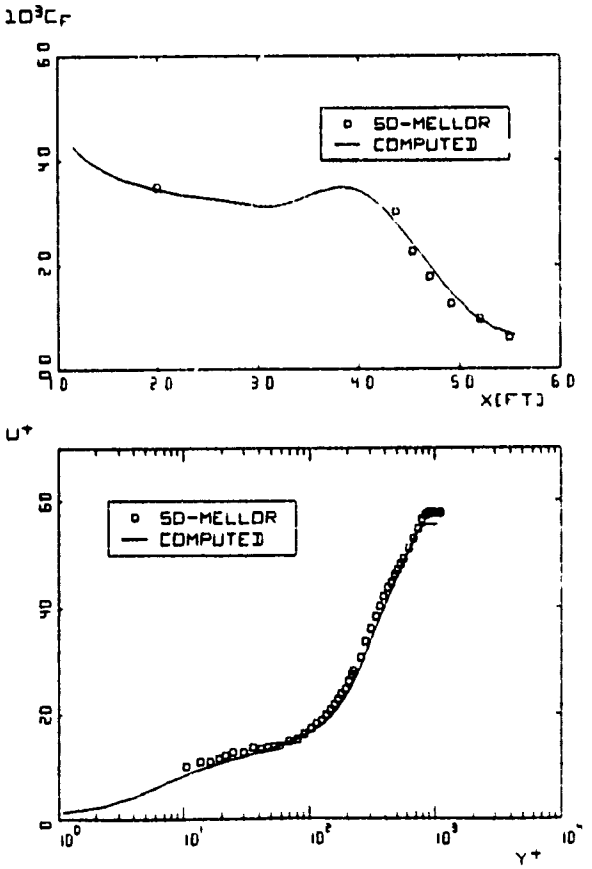

Figure 4. Comparison of computed and measured skin friction and velocity profile at x = 5.5 ft. for flow over a convex wall with adverse pressure gradient.

Table 1 summarizes computed and measured spreading rate. Birch's[24] definition has been used to define the spreading rate, viz, the difference in values of η at the points where $u/u_m = \sqrt{0.1}$ and $u/u_m = \sqrt{0.9}$. Predicted spreading rate is sensitive to the freestream values of k and ω so that a range of spreading rates are possible. In each case, the largest value quoted corresponds to the limiting case $\omega_\infty \to 0$, $k_\infty/\omega_\infty \to 0$, which implies zero freestream turbulence.

Table 1. Computed and Measured Mixing Layer Spreading Rates.

	Minimum	Maximum
k-ω Model	.100	.141
Multiscale Model	.094	.116
Measured	.115	

Figure 5 compares computed (for $\omega_\infty \to 0$, $k_\infty/\omega_\infty \to 0$) and measured[25] velocity profiles. Multiscale model predicted velocity is closer to measured velocity than that of the k-ω model.

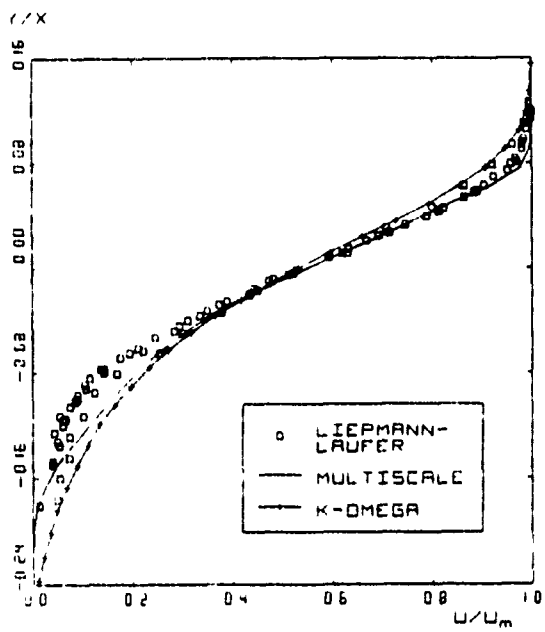

Figure 5. Comparison of computed and measured velocity profiles for the mixing layer.

4. Part 2: Separated Flows

We focus now on separated flows. The section begins with an overview of the numerical procedure, initial and boundary conditions, finite-difference grids used, and computing times required to achieve the solutions. Comparisons of computed and measured flow properties are given for each case.

4.1 Numerical Procedure

Algorithm. The numerical algorithm used in the computations was developed by MacCormack[8], and has been used for many compressible separated flow computations by Horstman, et al[11,12,14]. Because of its proven track record, we obtained the version of Horstman's program which uses the k-ε turbulence model to describe the turbulence. After purging the k-ε model and incorporating the multiscale and k-ω models, we find that the modified program requires about 30% more memory than the original, primarily because of the additional arrays needed for the Reynolds stress components.

Turbulence Models. All computations have been done using both the k-ω model and the multiscale model. The k-ω model is far less complex than the k-ε model, mainly because of all the special viscous modifications needed to integrate the k-ε model through the sublayer. As a consequence, a computation using the k-ω model requires only 75% as much CPU time per timestep as one using the k-ε model. The multiscale model requires approximately 50% more CPU time than the k-ω model. Thus, a computation using the multiscale model requires about 12% more CPU time per timestep than a corresponding computation using the k-ε model.

Finite Difference Grids. Dimensions of the computational domains for each case are listed in Table 2 in terms of the thickness of the incident boundary layer, δ_0. In all three computations, the finite difference grid consists of 80 equally-spaced points between upstream and downstream boundaries, while 45 points lie between the lower and upper boundaries. The first 30 grid points normal to the surface extend to $y=\delta_0$; grid-point spacing increases in a geometric progression with a grading ratio between 30% and 35%. The remaining 15 points are equally spaced, covering the region from $y=\delta_0$ to the top of the grid. The mesh point closest to the surface lies below $y^+ = 0.7$ throughout the grid in all three cases. Upstream of the ramp, finite difference cells are rectangular. Downstream of the ramp the cells are parallelograms aligned with the ramp.

Boundary and Initial Conditions. Upstream boundary conditions for the three computations have been obtained from the two-dimensional boundary layer program, EDDYBL. Using EDDYBL, we have been able to match the measured values of Re_θ and H for each case to within 1.0%. The upstream boundary-layer profiles have also been used as initial conditions throughout the computational domain.

Other Details. The equations of motion have been integrated through the sublayer, with a viscous Courant number, $C_y = 2\nu\Delta t/(\Delta y)^2$, ranging between 30 and 90 for most of the computation, and typically

Table 2. Primary Flow and Numerical Parameters

Parameter	20° Corner	24° Corner	30° Corner
Mach Number	2.79	2.84	2.85
Total Pressure (psf)	14,513	14,451	3,600
Total Temp. (°R)	464	472	513
Wall Temp. (°R)	493	497	487
B.L. Thickness, δ_0 (ft)	.082	.075	.033
Mom. Thickness, Re_θ	93,800	82,050	9,366
Shape Factor, H	5.08	5.08	4.00
Grid Length ($\Delta x/\delta_0$)	8	10	10
Grid Height ($\Delta y/\delta_0$)	6	6	5
k-ω Timesteps	7,000	24,000	12,000
k-ω CPU Time (min)	17	60	32
Multiscale Timesteps	7,000	40,000	12,000
Multiscale CPU (min)	25	138	45

half this value for the final 25% of the computation to eliminate any possibility of solution dependence on the timestep, a procedure recommended by MacCormack[8]. In every computation, a freestream fluid particle traversed the mesh at least 3 times, and as many as 18 times.

Table 2 summarizes freestream flow conditions, upstream boundary-layer properties, mesh dimensions, and computing time data on a Cray X-MP/48 computer for all three flows. Wilcox[26] gives additional details on the numerical procedure, including stability analysis and a study of solution sensitivity to grid-point number.

4.2 20° Compression Corner

The first of the three applications is for Mach 2.79 flow into a 20° compression corner. This flow has been experimentally investigated by Settles, Vas and Bogdonoff[4] and includes a small region over which separation of the incident turbulent boundary layer occurs. Figure 6 compares computed and measured surface pressure, p_w/p_∞, and skin friction, c_f. The multiscale model predicts more upstream influence, a lower pressure plateau at separation, and a more gradual increase in skin friction downstream of reattachment relative to the k-ω results. All of these features represent significant improvement in predictive accuracy.

Figure 7 compares computed and measured velocity profiles throughout the interaction region. Again, multiscale model predictions are much closer to measured properties than k-ω model predictions, especially near the separation point.

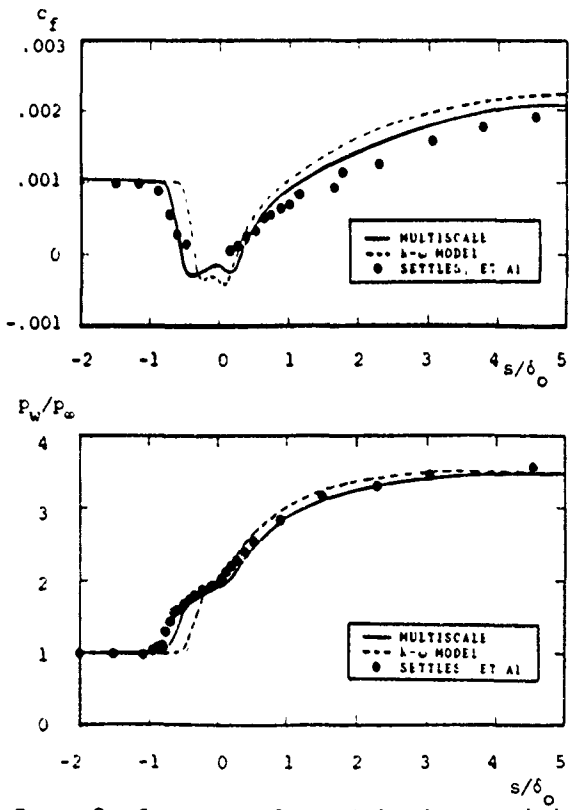

Figure 6. Comparison of computed and measured skin friction and surface pressure for Mach 2.79 flow into a 20° compression corner; s is tangential distance from corner.

Using the k-ε model and specially devised wall functions, Viegas, Rubesin and Horstman[12] are able to achieve similar accuracy for this flow.

4.3 24° Compression Corner

The second of the three applications is for Mach 2.84 flow into a 24° compression corner. This flow has also been experimentally investigated by Settles, Vas and Bogdonoff[4] and includes a larger region over which separation of the incident turbulent boundary layer occurs than in the 20° case of the preceding section. Figure 8 compares computed and measured surface pressure and skin friction. As in the 20° compression-corner computation, the multiscale model predicts much more upstream influence. Interestingly, the k-ω predicted pressure plateau at separation is very close to the measured level, and there is little difference between k-ω and multiscale predicted increase in skin friction downstream of reattachment.

Figure 9 compares computed and measured velocity profiles throughout the interaction region. Again, multiscale model predictions are closer to measured properties than k-ω model predictions, most notably near the separation point.

Note that, for this flow, Viegas, Rubesin and Horstman[12] predict pressure plateau values about 20% higher than measured, and are unable to simultaneously make accurate predictions for skin friction downstream of reattachment and the initial rise in surface pressure. That is, their solutions can match either skin friction or surface pressure, but not both.

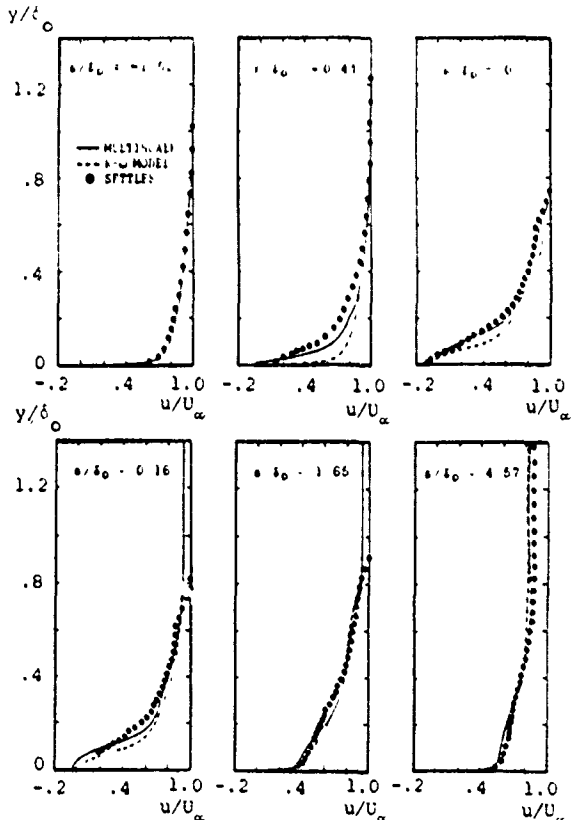

Figure 7. Comparison of computed and measured velocity profiles for Mach 2.79 flow into a 20° compression corner; y is distance normal to the surface.

4.4 Axisymmetric Compression Corner

Our third application is for Mach 2.85 flow into a 30° axisymmetric compression corner. This flow has been experimentally investigated by Brown[5] and includes a separation bubble of length comparable to the 24° planar compression corner discussed in the preceding subsection. Figure 10 compares computed and measured surface pressure. Computed skin friction is also shown. Once again we see that the multiscale model predicts much more upstream influence. For both models, the predicted pressure plateau at separation is about 10% higher the measured level, and there is little difference between k-ω and multiscale predicted increase in skin friction downstream of reattachment. The overall pressure rise is predicted by both models to be 4.7, while the measurements indicate a value of 4.0. The inviscid pressure rise for a 30° axisymmetric compression corner is 4.4, so that neither theory nor experiment appears to be completely consistent with the physics of this flow.

Figure 11 compares computed and measured velocity profiles throughout the interaction region. Multiscale model predictions are closer to measured properties than k-ω model predictions throughout the interaction region. Because of the stronger than measured overall pressure rise, the computed zero velocity line is more distant from the wall than measured, thus distorting the profiles somewhat.

In order to eliminate the possibility that the finite difference grid is too coarse to provide an accurate computation for the freestream, the k-ω computation has been repeated with an 80 x 60 grid. In the refined grid, the same spacing is used for the boundary layer while 30 equally spaced points cover the region from $y=\delta_o$ to $y=5\delta_o$. No significant changes in the solution result from this mesh refinement.

4.5 Data Analysis

Results presented in the preceding subsections indicate that, for the three compression-corner cases considered, the multiscale model provides a flowfield more consistent with experimental observations than does the k-ω model. The primary reason for the difference in the two model's predictions can be found by examining predicted behavior of the Reynolds shear stress near the separation point. Figure 12 shows the peak value of the Reynolds shear stress, τ_{max}, throughout the interaction region for the three compression-corner computations. As shown, the k-ω model predicts a more abrupt increase in τ_{max} at separation and a much larger maximum value than that predicted by the multiscale model. For the axisymmetric case, the figure includes experimental data for points ahead of the measured separation point. As shown, the multiscale model predicted τ_{max} falls within the scatter of the experimental data.

The physical implication of the pronounced difference in the rate of amplification of the Reynolds shear stress is clear. Using the Boussinesq approximation, the k-ω model makes a far more rapid adjustment to the rotation of the mean strain rate tensor's principal axes than the multiscale model.

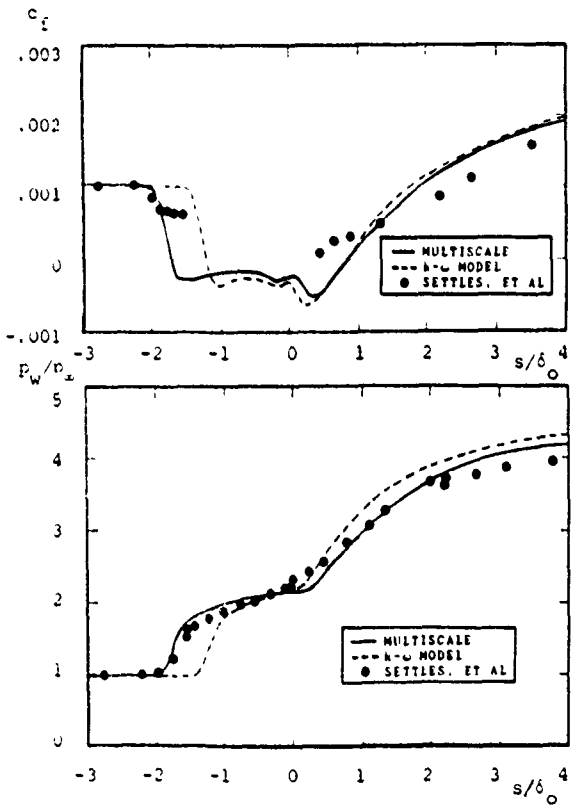

Figure 8. Comparison of computed and measured skin friction and surface pressure for Mach 2.84 flow into a 24° compression corner; s is tangential distance from corner.

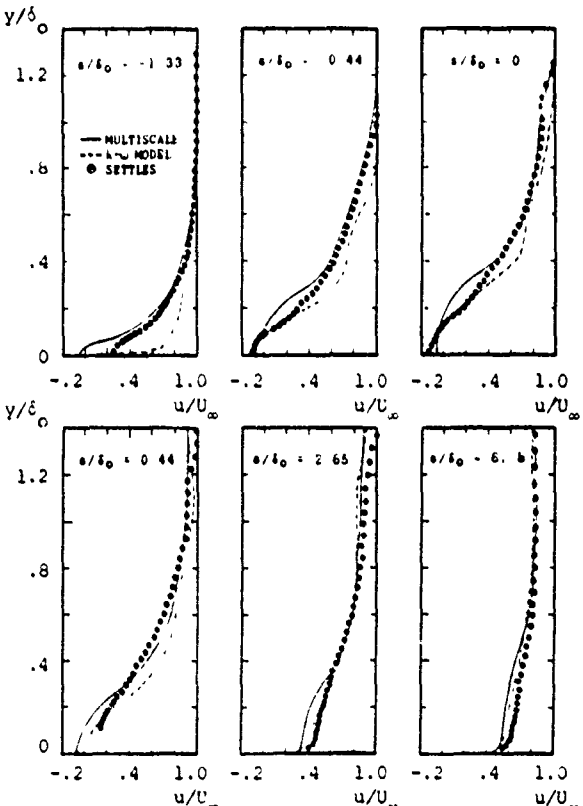

Figure 9. Comparison of computed and measured velocity profiles for Mach 2.84 flow into a 24° compression corner; y is distance normal to the surface.

Consequently, the predicted separation point and initial pressure rise lie closer to the corner with the k-ω model than measured. Predicting more physically realistic growth of the Reynolds stresses, the multiscale model predicts overall flow properties which are in much closer agreement with measurements.

It is interesting to note that for the multiscale model, although the pressure is in such close agreement with measurements, the numerical separation points are further upstream than indicated by oil flow measurements for all three compression corner cases. Table 3 summarizes computed and measured separation points. Careful examination of the numerical flowfields shows that: (a) the separation bubble is extremely thin near its leading edge; and, (b) reverse flow velocities are very small in this extremely thin region. This behavior is best exemplified in Figures 7 and 11. Specifically, the profile at $s/\delta_o = -0.44$ in Figure 7 and the profile at $s/\delta_o = -2.50$ in Figure 11 both show that the reverse flow portion of the numerical profile lies below the experimental data. Given the excellent agreement between computed and measured surface pressure which is strongly influenced by separation bubble shape, the computed separation points appear more physically realistic than those indicated by the oil flow measurements.

5. Summary and Conclusions

Part 1 of the paper shows that the multiscale model accurately predicts effects of surface roughness, mass injection and streamline curvature for attached boundary layers. Additionally, the model performs reasonably well for the mixing layer. As in past applications to non-separated flows, with the exception of streamline curvature effects for which two-equation models do not apply, no clear advantage is evident in using the multiscale model as the k-ω model is nearly as accurate.

Table 3. Computed and measured separation points

Case	Multiscale	k-ω	Measured
20°	-0.56	-0.38	-0.45
24°	-1.73	-1.23	-1.33
30°	-2.60	-1.70	-1.50

Part 2 of the paper addresses three separated flows, using the mass-averaged Navier-Stokes equations and both the k-ω and multiscale models. The multiscale model is clearly superior for supersonic compression corner flows, which is especially obvious in the vicinity of separation.

The multiscale model's superiority over the k-ω model appears to be due to a more physically realistic description of the Reynolds stress tensor. Unlike the k-ω model which uses the Boussinesq approximation that Reynolds stress is proportional to mean strain rate, the multiscale model predicts a gradual increase in Reynolds shear stress near separation. Because the flow's effective resistance to separation is thus reduced, the separation point, and hence the initial rise in pressure, lies farther from the corner. Multiscale

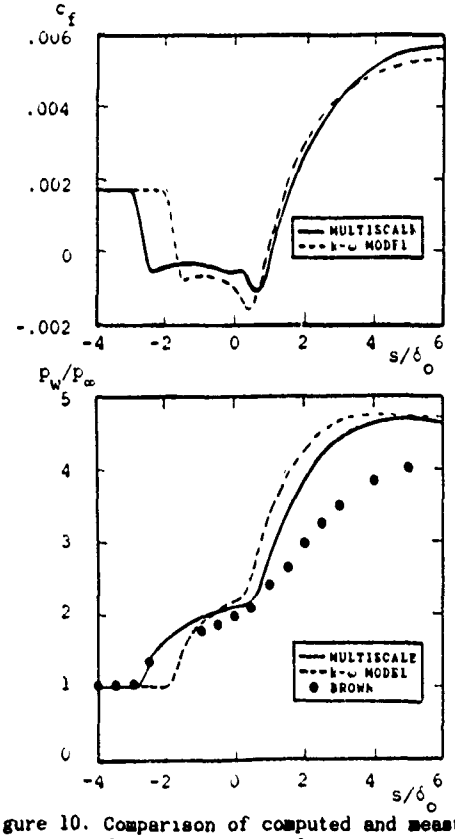

Figure 10. Comparison of computed and measured skin friction and surface pressure for Mach 2.85 flow into a 30° compression corner; s is tangential distance from corner.

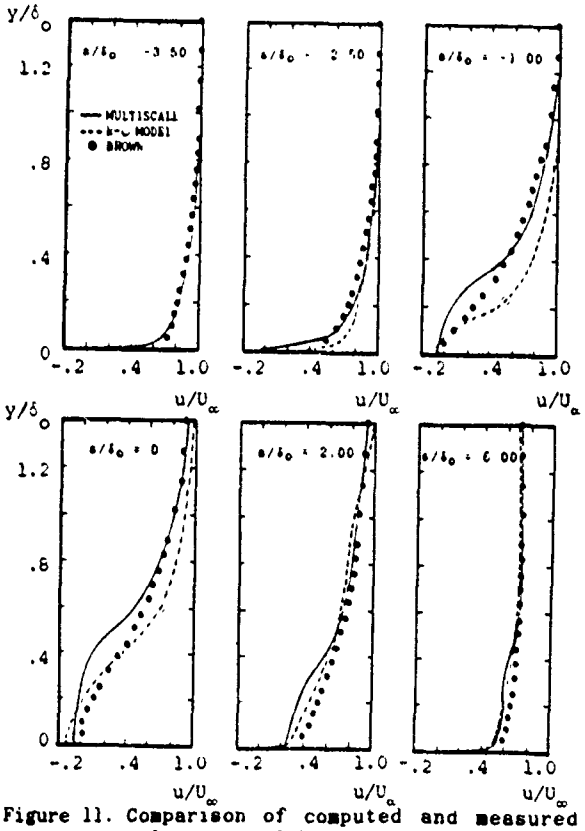

Figure 11. Comparison of computed and measured velocity profiles for Mach 2.85 flow into a 30° compression corner; y is distance normal to the axis of symmetry.

model predicted surface pressure is much closer to measurements than the corresponding k-ω model surface pressure. Close agreement with limited experimental Reynolds shear stress data for the axisymmetric compression corner flow adds further verification that the multiscale model's predictions are physically sound.

On balance, the results obtained indicate that an important advance in the state of the art of separated-flow numerical simulation has been made. These results leave little doubt that continued use of turbulence models based on the Boussinesq approximation holds scant promise for accurate predictions. By contrast, the multiscale model, with only a 50% computational penalty per timestep, brings numerical predictions into much closer agreement with the physics of separated flows.

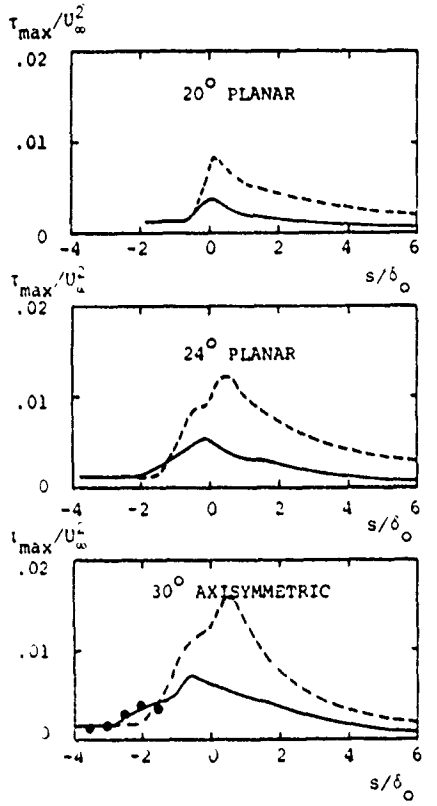

Figure 12. Variation of peak Reynolds shear stress through the interaction region for the compression-corner computations; --- k-ω model; —— multiscale model; ● Brown[5].

6. Acknowledgments

Research in Part 1 was supported by the U.S. Army Research Office under Contract DAAL03-87-C-0004 with Dr. Thomas Doligalski as Contract Monitor.

Funding for Part 2 of this study was provided by Dr. James Wilson of the Air Force Office of Scientific Research. Computing time was made available by Mr. Joseph Marvin of the NASA Ames Research Center. Dr. C. C. Horstman of the NASA Ames Research Center contributed invaluable assistance as well as the computer program which served as the foundation for this study.

Appendix: Curved-Wall Equations

For incompressible flow over a surface with radius of curvature R, the equations of motion are most conveniently written by following So and Mellor[23] who show that close to the surface the potential flow solution is $U_p(x,y) = U_{pw}(x)e^{-y/R}$. Thus, centrifugal and Coriolis acceleration terms can be absorbed in the convective terms by rewriting the equations in terms of $u=u_x e^{y/R}$ and $v=u_y e^{y/R}$, where u_x and u_y are the physical velocity components in the x and y directions, respectively. Hence, for an incompressible boundary layer on a curved surface, the multiscale model equations are

$$\partial u/\partial x + \partial v/\partial y = 0 \qquad (A1)$$

$$u\partial u/\partial x + v\partial u/\partial y = U_{pw}dU_{pw}/dx + \partial/\partial y[\nu\partial u/\partial y + \tau/\rho] \qquad (A2)$$

$$u\partial k/\partial x + v\partial k/\partial y = \tau(\partial u/\partial y - u/R) - \beta^*\omega k + \partial/\partial y[(\nu+\sigma^*\nu_T)\partial k/\partial y] \qquad (A3)$$

$$u\partial\omega/\partial x + v\partial\omega/\partial y = (\gamma\omega/k)\tau(\partial u/\partial y - u/R) - \beta\omega^2 - \beta|\omega|\partial u/\partial y + u/R| + \partial/\partial y[(\nu+\sigma\nu_T)\partial\omega/\partial y] \qquad (A4)$$

$$u\partial(k-e)/\partial x + v\partial(k-e)/\partial y = (1-\hat{\alpha}-\hat{\beta})\tau(\partial u/\partial y - u/R) - \beta^*\omega k(1-e/k)^{3/2} \qquad (A5)$$

$$u\partial\sigma_x/\partial x + v\partial\sigma_x/\partial y = {}^2/_3[2(1-\hat{\alpha})+\hat{\beta}]\tau(\partial u/\partial y - u/R) + 2(2-\hat{\alpha}+\hat{\beta})\tau u/R - \beta^* C_1\omega\sigma_x \qquad (A6)$$

$$u\partial\sigma_y/\partial x + v\partial\sigma_y/\partial y = -{}^2/_3[(1-\hat{\alpha})+2\hat{\beta}]\tau(\partial u/\partial y - u/R) - 2(2-\hat{\alpha}+\hat{\beta})\tau u/R - \beta^* C_1\omega\sigma_y \qquad (A7)$$

$$u\partial\tau/\partial x + v\partial\tau/\partial y = [-\hat{\beta}\sigma_x + (1-\hat{\alpha})\sigma_y + {}^2/_3(1-\hat{\alpha}-\hat{\beta}+3\gamma/4)k](\partial u/\partial y - u/R) + (2-\hat{\alpha}+\hat{\beta})(\sigma_y-\sigma_x)u/R - \beta^* C_1\omega\tau \qquad (A8)$$

where $\sigma_x \equiv \langle u'^2\rangle - {}^2/_3k$ and $\sigma_y \equiv \langle v'^2\rangle - {}^2/_3k$. Note that it makes little difference if (u,v) or (u_x,u_y) are used in Equations (A3-A8). Using (u,v) in the mean-flow equations is important, however, as it obviates the need to solve the normal component of the momentum equation.

References

1. Wilcox, D.C., "Multiscale Model for Turbulent Flows," AIAA Paper 86-0029 (Jan 1986).

2. Wilcox, D.C., "Advanced Applications of the Multiscale Model for Turbulent Flows," AIAA Paper 87-0290 (Jan 1987).

3. Wilcox, D.C., "A Complete Model of Turbulence Revisited," AIAA Paper 84-0176 (Jan 1984).

4. Settles, G.S., Vas, I.E. and Bogdonoff, S.M., "Details of a Shock Separated Turbulent Boundary Layer at a Compression Corner," AIAA J, Vol 14, pp 1709-1715 (Dec 1976).

5. Brown, J.D., "Two Component LDV Investigation of Shock Related Turbulent Boundary Layer Separation with Increasing Three Dimensionality," PhD Thesis, U.C. Berkeley (1986).

6. Wilcox, D.C., "Numerical Study of Separated Turbulent Flows," AIAA Paper 74-584 (Jun 1974).

7. Seffman, P.G. and Wilcox, D.C., "Turbulence-Model Predictions for Turbulent Boundary Layers," AIAA J, Vol 12, No 4, pp 541-546 (Apr 1974).

8. MacCormack, R.W., "A Numerical Method for Solving the Equations of Compressible Viscous Flow," AIAA J, Vol 20, pp 1275-1281 (Sep 1982).

9. Beam, R.M. and Warming, R.F., "An Implicit Finite-Difference Algorithm for Hyperbolic Systems in Conservation Law Form," Journal of Computational Physics, Vol 22, pp 87-110 (1976).

10. Steger, J. and Warming, R.F., "Flux Vector Splitting of the Inviscid Gasdynamics Equations with Application to Finite Difference Methods," NASA TM-78605 (1979).

11. Viegas, J.R. and Horstman, C.C., "Comparison of Multiequation Turbulence Models for Several Shock Boundary-Layer Interaction Flows," AIAA J, Vol 17, pp 811-820 (Aug 1979).

12. Viegas, J.R., Rubesin, M.W. and Horstman, C.C., "On the Use of Wall Functions as Boundary Conditions for Two-Dimensional Separated Compressible Flows," AIAA Paper 85-0180 (Jan 1985).

13. Jones, W.P. and Launder, B.E., "The Prediction of Laminarization with a Two-Equation Model of Turbulence," Int J of Heat and Mass Trans, Vol 15, pp 301-314 (1972).

14. Johnson, D.A., Horstman, C.C. and Bachalo, W.D., "Comparison Between Experiment and Prediction for a Transonic Turbulent Separated Flow," AIAA J, Vol 20, pp 737-744 (Jun 1982).

15. Johnson, D.A., "Transonic Separated Flow Predictions with an Eddy-Viscosity/Reynolds-Stress Closure Model," AIAA J, Vol 25, No 2, pp 252-259, (Feb 1987).

16. Favre, A., "Equations des Gaz Turbulents Compressibles," J Mecan, Vol 4, No 3, pp 361-390 (1965).

17. MacCormack, R.W., "Current Status of Numerical Solutions of the Navier-Stokes Equations," AIAA Paper 85-0032 (Jan 1985).

18. Goddard, F.E., Jr., "Effect of Uniformly Distributed Roughness on Turbulent Skin-Friction Drag at Supersonic Speeds," J Aero/Space Sciences, Vol 26, No 1, pp 1-15,24 (Jan 1959).

19. Wilcox, D.C., "Program EDDYBL User's Guide," DCW Industries Report No DCW-R-NC-04 (1987).

20. Reda, D.C., Ketter, F.C., Jr. and Fan, C., "Compressible Turbulent Skin Friction on Rough and Rough/Wavy Walls in Adiabatic Flow," AIAA Paper 74-574 (Jun 1974).

21. Andersen, P.S., Kays, W.M. & Moffat, R.J., "The Turbulent Boundary Layer on a Porous Plate: An Experimental Study of the Fluid Mechanics for Adverse Free-Stream Pressure Gradients," Report No HMT-15, Dept Mech Eng, Stanford Univ, CA (1972).

22. Wilcox, D.C. and Chambers, T.L., "Streamline Curvature Effects on Turbulent Boundary Layers," AIAA J, Vol 15, No 4, pp 574-580 (Apr 1977).

23. So, R.M.C and Mellor, G.L., "An Experimental Investigation of Turbulent Boundary Layers Along Curved Surfaces," NASA CR-1940 (Apr 1972).

24. Kline, S.J., Cantwell, B.J. & Lilley, G.M., 1980-81 AFOSR-HTTM-Stanford Conference on Complex Turbulent Flows, Stanford Univ (1981).

25. Liepmann, H.W. and Laufer, J., "Investigations of Free Turbulent Mixing," NACA TN 1257 (1947).

26. Wilcox, D.C., "Navier-Stokes Applications of the Multiscale Model for Turbulent Flows," DCW Industries Report No DCW-R-32-01 (Apr 1987).

APPENDIX E: AN ALTERNATIVE TO WALL FUNCTIONS

The paper reproduced in this appendix was presented at the AIAA 27th Aerospace Sciences Meeting, held in Reno, Nevada, January 9-12, 1989. The formal reference to this paper is as follows.

> Wilcox, D. C., "Wall Matching, A Rational Alternative to Wall Functions," AIAA Paper 89-0611, Jan. 1989.

This paper uses perturbation methods to develop a rational procedure for circumventing integration through the viscous sublayer. Applications include several shock-separated flows. The primary value of this approach would be for three-dimensional Reynolds-averaged Navier-Stokes computations.

AIAA'89

AIAA-89-0611

WALL MATCHING, A RATIONAL ALTERNATIVE TO WALL FUNCTIONS

D. C. Wilcox, DCW Industries, Inc.
La Cañada, California

27th Aerospace Sciences Meeting
January 9-12, 1989/Reno, Nevada

For permission to copy or republish, contact the American Institute of Aeronautics and Astronautics
370 L'Enfant Promenade, S.W., Washington, D.C. 20024

WALL MATCHING, A RATIONAL ALTERNATIVE TO WALL FUNCTIONS

by

David C. Wilcox†
DCW Industries, Inc.
La Cañada, California

Abstract

A methodology is presented which uniquely establishes surface boundary conditions, consistent with the law of the wall, for advanced turbulence models. This procedure is superior to the use of so-called "wall functions" as solutions demonstrably converge toward the corresponding solution obtained by integrating through the viscous sublayer in turbulent flows. Consistent with previous Navier-Stokes applications using wall functions, computing times for turbulent flows with boundary-layer separation are reduced dramatically as compared to computations which integrate through the sublayer.

I. Introduction

The conventional approach used to implement boundary conditions at a solid boundary for turbulence model computations is to postulate wall functions appropriate to the problem of interest. While the original intent of wall functions may have been to simply accommodate surface boundary conditions, their use has also accomplished the purpose of adding adjustable parameters to the turbulence model as a whole.

On the one hand, having additional adjustable parameters offers the possibility of being able to encompass a wider range of flow situations - a desirable end. On the other hand, as shown by Wilcox[1], using wall functions can actually mask inherent deficiencies of the turbulence model as a whole, most notably in the case of the widely-used k-ε model - an undesirable (and misleading) end. Numerical solutions are often very sensitive to boundary conditions and, correspondingly, wall functions are probab' the greatest cause of uncertainty in turbulent-flow computations[2].

The primary purpose of this paper is to use the method of singular perturbations to effect formal matching to the law of the wall, including effects of compressibility. Using this approach, the resulting boundary conditions are unique to the turbulence model to within a single additive constant. While analysis is confined to the Wilcox k-ω model[1] and the Wilcox multiscale model[3], the methodology is completely general and can be applied to any advanced turbulence model.

The analysis has been done with effects of compressibility included, following the approach first implemented by Saffman and Wilcox[4]. In contrast to the Saffman-Wilcox analysis, however, effects of pressure gradient have also been included. This proves to be very important in using wall functions.

Prior to this analysis, the wall function development of Viegas, Rubesin and Horstman[5] has been the most effective and physically acceptable for compressible flow applications. The primary advantage of their development is manifested in a tremendous reduction in computing time required for time-averaged Navier-Stokes computations. Their applications include boundary layer separation and they demonstrate quite convincingly that use of a logarithmic near-wall velocity profile yields satisfactory accuracy on separated regions.

Computations in this paper for three separated flows[6,7] add further substantiation to this claim. In fact, the case for using the law of the wall through separated regions is even more convincingly demonstrated in this paper since two of the computations have also been done with the equations of motion integrated through the sublayer. Differences attending the use of wall matching are shown to be unimportant.

The advantage of using the formal matching procedure becomes particularly evident when grid point spacing is varied. Computed skin friction and surface temperature/heat transfer vary by about 5% when the point nearest the surface lies at values of y^+ between 10 and 320. Most importantly, the computed values using wall matching are within 7% of values obtained by integrating through the viscous sublayer without the aid of wall matching. This stands in distinct contrast to results obtained with conventional wall functions such as those of Viegas, Rubesin and Horstman where corresponding differences would be 25% or more with no obvious convergence to a well defined limiting value as $y^+ \to 0$.

Not all of the improvement in grid insensitivity results from use of wall matching, however. Unlike the k-ω model, the k-ε model is very ill behaved approaching a solid boundary, and cannot be easily integrated through the viscous sublayer. This is the primary reason the Viegas, Rubesin and Horstman computations fail to produce convergence as $y^+ \to 0$.

To demonstrate the dramatic reduction in computing time, the paper includes results of a hypersonic (Mach 11.3) shock/boundary-layer interaction[7] computation. Without the aid of wall matching, the computation would require six hours of CPU time on a Cray XM-P/48. The computation presented has been done on a fast desk top microcomputer (80386/Weitek). This economy can have an important impact on the practicability of using numerical simulations in the design process for vehicles such as the National Aerospace Plane.

Section II discusses the theoretical foundation of wall matching and develops boundary conditions appropriate to both the Wilcox k-ω and multiscale models for compressible flows, including effects of

†President; Associate Fellow AIAA.

Copyright © American Institute of Aeronautics and Astronautics, Inc., 1989 All rights reserved

pressure gradient. Section III illustrates the way in which wall matching is implemented in a Navier-Stokes computation. Section IV presents results of compressible Navier-Stokes computations implementing wall matching. The concluding section summarizes results of the study. The Appendix includes the equations which constitute the Wilcox k-ω and multiscale models.

II. Theoretical Foundation of Wall Matching

Generally speaking, in order to solve the equations of motion for viscous flow over a solid surface, we must specify boundary conditions valid at the surface. Often, in turbulent flow computations, it is convenient to avoid integration through the sublayer. This can be done by assuming the law of the wall to be valid for the flow of interest so that, following Saffman and Wilcox[4], we write

$$u^*_2 = u_\tau[\kappa^{-1}\log(u_\tau y_2/\nu_w) + B] \qquad (1)$$

where $du^* = \sqrt{\rho/\rho_w}du$, u_τ is friction velocity, κ is Karman's constant, $B \doteq 5$ for smooth surfaces and ν_w is kinematic viscosity at the surface. The quantities u^*_2 and y_2 denote tangential velocity and normal distance from the surface at the first mesh point adjacent to the surface. Note that, in a strict mathematical sense, the boundary condition we are actually using when we invoke Equation (1) is:

$$u^* \to u_\tau[\kappa^{-1}\log(u_\tau y/\nu_w) + B] \quad \text{as} \quad y \to 0 \qquad (2)$$

We are thus idealizing the flow as having a zero thickness viscous sublayer (relative to the overall scale of the boundary layer).

A. The Origin of Wall Functions

When a turbulence model is used which involves partial differential equations describing evolution of turbulent field properties in addition to the mean flow conservation equations, more boundary conditions are needed. For example, using a two-equation k-ω turbulence model, we must specify appropriate boundary conditions for the turbulent energy, k, and specific dissipation rate, ω. Historically, this is the point at which so-called "wall functions" are introduced. These functions generally are deduced by examining the limiting form of the turbulence model equations as $y \to 0$. The equations simplify in this limit primarily through dropping of the convection terms. For example, using the method first outlined by Saffman and Wilcox[4] for a constant pressure compressible boundary layer, the Wilcox k-ω model equations (see Appendix) simplify to the following:

$$\mu_T du/dy = \rho_w u_\tau^2 \qquad (3)$$

$$\mu_T d(C_p T)/dy = Pr_T(q_w - \tau u) \qquad (4)$$

$$\mu_T(du/dy)^2 - \beta^*\rho\omega k + \sigma^* d/dy(\mu_T dk/dy) = 0 \qquad (5)$$

$$\gamma\rho(du/dy)^2 - \beta\rho\omega^2 + \sigma d/dy(\mu_T d\omega/dy) = 0 \qquad (6)$$

where ρ is density, T is temperature, τ is shear stress, and the eddy viscosity, μ_T, is defined by

$$\mu_T = \rho k/\omega \qquad (7)$$

In Equations (3-6), τ_w is surface shear stress, ρ_w is density at the surface, u_τ is friction velocity defined by $\tau_w = \rho_w u_\tau^2$, C_p is specific heat, and Pr_T is turbulent Prandtl number. The five closure coefficients, β, β^*, γ, σ and σ^* assume the following values.

$$\beta = 3/40, \quad \beta^* = 9/100, \quad \gamma = 5/9, \quad \sigma = \sigma^* = 1/2 \qquad (8)$$

One solution to Equations (3-8), which we shall denote as $k = k_w$ and $\omega = \omega_w$, is:

$$k_w = (\rho_w/\rho)u_\tau^2/\sqrt{\beta^*} \qquad (9)$$

$$\omega_w = \sqrt{\rho_w/\rho}\,|u_\tau|/(\sqrt{\beta^*}\kappa y) \qquad (10)$$

which is valid since the closure coefficients satisfy the condition $\gamma = \beta/\beta^* - 2\sigma\kappa^2/\sqrt{\beta^*}$. Equations (9) and (10) are used to define k_2 and ω_2 at $y = y_2$. As with the law-of-the-wall velocity boundary condition, the precise mathematical statement of the wall-function boundary conditions for k and ω is

$$k \to k_w \quad \text{and} \quad \omega \to \omega_w \quad \text{as} \quad y \to 0 \qquad (11)$$

Equations (2), (9) and (10) are valid for both the k-ω and multiscale models.

B. Non-Uniqueness of Wall Functions

Because the equations for k and ω are of second order, Equations (9) and (10) are not the only solutions of Equations (3-8). This point is most easily demonstrated for the limiting case of incompressible flow. By changing independent variables from y to u, the equation for k simplifies to

$$\sigma^* d^2K/dU^2 = \beta^* K^2 - 1 \qquad (12)$$

where $K = k/u_\tau^2$ and $U = u/u_\tau$. As above, one solution has $dK/dU = 0$ so that $K = 1/\sqrt{\beta^*}$. There are also solutions having $dK/dU \neq 0$ which can be obtained by multiplying both sides of Equation (12) by dK/dU and integrating twice to obtain

$$U = U_O \pm \sqrt{\frac{3\sigma^*}{2\beta^*}}\int_{K_O}^{K} \frac{dt}{\sqrt{t^3 - 3t/\beta^* + A}} \qquad (13)$$

where A is an integration constant and K_O, U_O denote reference values of K, U. Equation (13) is an elliptic integral whose properties vary widely with the value of the integration constant A. The primary goal here is not to examine in detail the behavior of K contained in Equation (13). Rather, the key point is to emphasize that more than one solution to the model equations exists and that, without careful analysis, we cannot be sure that all solutions necessarily are consistent with the law of the wall.

The latter observation underscores why arbitrarily deviating from Equations (9-11) by using some value other than β^* and/or κ for example may yield unexpected surprises, many of which may be lurking in the integrand of Equation (13). In essence, by selecting the wall functions defined in Equations (9-10) we are (a) demanding that our boundary conditions be consistent with the differential equations and (b) excluding any other asymptotic behavior (as $y \to 0$) which might be inconsistent with the law of the wall.

C. Effects of Pressure Gradient

All of the analysis above assumes constant pressure. As will be shown in this subsection, Equations (9-10) are inappropriate unless boundary conditions are applied much closer to the surface than is done in common practice. To see this, note that now Equation (3) must be replaced by

$$\mu_T du/dy = \rho_w u_\tau^2 + y(dp/dx) \tag{14}$$

where ρ is density and dp/dx is pressure gradient. Equations (4-6) remain as before. Letting $y^+ = u_\tau y/\nu_w$ we can rewrite Equation (14) as

$$\mu_T du/dy = \rho_w u_\tau^2(1 + \phi y^+) \tag{15}$$

where the dimensionless parameter ϕ is defined by

$$\phi = \nu_w(dp/dx)/(\rho u_\tau^3) \tag{16}$$

Order of magnitude estimates for boundary-layer flows in pressure gradient indicate ϕ is a small parameter except possibly in the immediate vicinity of separation. This suggests seeking a solution of the form:

$$k = (\rho_w/\rho)u_\tau^2/\sqrt{\beta^*}\,[1 + \phi k_1 y^+ + \ldots] \tag{17}$$

$$\omega = \sqrt{\rho_w/\rho}\,|u_\tau|/(\sqrt{\beta^*}\kappa y)[1 + \phi\omega_1 y^+ + \ldots] \tag{18}$$

$$du^+/dy = u_\tau/(\kappa y)\,[1 + \phi u_1 y^+ + \ldots] \tag{19}$$

Straightforward substitution of Equations (17-19) into Equations (4,5,6,14) yields the solution up to terms linear in ϕ as follows.

k-ω Model

$$k_1 = 1.16,\ \omega_1 = -0.32,\ u_1 = -0.48 \tag{20a}$$

Multiscale Model

$$k_1 = 1.04,\ \omega_1 = -0.86,\ u_1 = -1.11 \tag{20b}$$

To leading order of approximation, the mean energy equation and equation of state for a perfect gas integrate to

$$T = T_w - (Pr_T q_w/C_p\tau_w)u - (Pr_T/2C_p)u^2 \tag{21}$$

$$p = p_w \tag{22}$$

$$\rho = \rho_w(T_w/T) \tag{23}$$

Consequently, for flows with pressure gradient, Equation (2) must be replaced by

$$u^+ \to u_\tau[\kappa^{-1}\log(u_\tau y/\nu) + B + u_1(\phi/\kappa)u_\tau y/\nu_w]$$

$$\text{as} \quad y \to 0 \tag{24}$$

while, to this order of approximation, the wall functions k_w and ω_w defined in equations (9) and (10) must be replaced by

$$k_w = (\rho_w/\rho)u_\tau^2/\sqrt{\beta^*}\,[1 + k_1\phi u_\tau y/\nu_w] \tag{25}$$

$$\omega_w = \sqrt{\rho_w/\rho}\,|u_\tau|/(\sqrt{\beta^*}\kappa y)\,[1 + \omega_1\phi u_\tau y/\nu_w] \tag{26}$$

With the exception of the additive constant B in Equation (24), the asymptotic form of the solution is unique to the turbulence model of interest. The model equations must be integrated through the sublayer to determine B. For virtually all applications of the k-ω and multiscale models, the incompressible smooth wall value of B = 5 appears appropriate, and this is the recommended value.

For the multiscale model, the asymptotic values of the various Reynolds stress components must also be derived. The perturbation solution gives the following.

$$T_{xy} = \tau = \tau_w\,[1 + \phi u_\tau y/\nu_w] \tag{27}$$

$$T_{xx} = -.426(\rho_w/\rho)u_\tau^2/\sqrt{\beta^*}[1 + .85\phi u_\tau y/\nu_w] \tag{28}$$

$$T_{yy} = .032(\rho_w/\rho)u_\tau^2/\sqrt{\beta^*}[1 + .85\phi u_\tau y/\nu_w] \tag{29}$$

$$k\text{-}\varepsilon = .253(\rho_w/\rho)u_\tau^2/\sqrt{\beta^*}[1 + .85\phi u_\tau y/\nu_w] \tag{30}$$

To illustrate the importance of the order ϕ corrections on computational accuracy, Figure 1 shows results of an incompressible computation with the ε-ω model in which the order ϕ corrections have been omitted. The flow considered is the Bradshaw[8] "Flow C" adverse pressure gradient boundary layer. In the computation, surface boundary conditions have been applied at values of y^+ ranging between 12 and 20. The figure compares computed turbulent energy at x = 7 feet with Equation (25). At this x location, the value of y^+ for the mesh point nearest the surface is 12. As shown, the numerical solution rapidly approaches the analytical solution given by Equation (25) and the two solutions differ by less than 2% above $y^+ = 30$.

In a subsequent solution in which the order ϕ corrections to the law of the wall and the wall functions have been included, the numerical and analytical solutions are virtually identical up to about $y^+ = 100$. For larger values of y^+, terms of order ϕ^2 presumably become important.

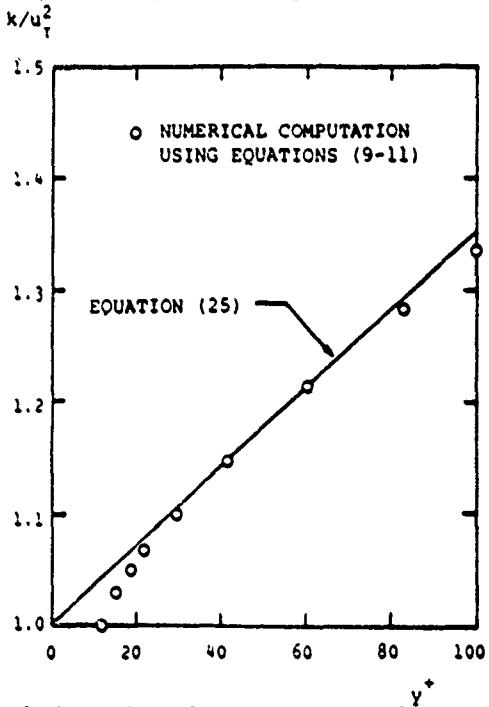

Figure 1. Deviation of computed turbulent energy from predicted near-wall behavior resulting from use of zeroth-order wall matching.

On the one hand, skin friction for the two numerical computations changes by less than 2% indicating neglect of the order ϕ corrections is not terribly important. On the other hand, note that in applying the boundary conditions at $y^+ = 12$ the error in κ is about 4%. Applying the boundary conditions at $y^+ = 40$, a value typical for those who use wall functions in their work, the error in k increases to 14% and yields a skin friction error of nearly 6%. By contrast, solutions are virtually independent of the point of application of the wall functions when the order ϕ corrections are included.

D. Additional Details

Two additional quantities are needed from the perturbation solution in order to implement wall matching in a Navier-Stokes computation. Specifically, the asymptotic value of the source term in the turbulence kinetic energy equation must be evaluated to insure numerical accuracy and an analytical relationship between u and u^s is required.

To leading order, production balances dissipation, which is consistent with one of the postulates of standard wall function formulations. From the perturbation solution, the difference is of order ϕ and is given by

$$(\tau_{ij}\partial u_i/\partial x_j - \beta^* \rho\omega k)/\rho k = C_k \phi \sqrt{\rho_w/\rho}\, \tau_w/\mu_w \qquad (31)$$

where

$$C_k = \begin{cases} 2\sqrt{\beta^*}(\kappa u_1 - \omega_1)/\kappa & ; \quad k\text{-}\omega \text{ Model} \\ \sqrt{\beta^*}(\kappa u_1 - \omega_1 + 1 - k_1)/\kappa; & \text{Multiscale Model} \end{cases} \qquad (32)$$

By definition, $du^s = \sqrt{\rho/\rho_w}\,du$, so that substituting for ρ/ρ_w from Equations (21) and (23) there follows

$$u^s = \frac{1}{a}\left\{ \sin^{-1}\left[\frac{2a^2u - b}{\sqrt{b^2+4a^2}}\right] + \sin^{-1}\left[\frac{b}{\sqrt{b^2+4a^2}}\right]\right\} \qquad (33)$$

where

$$a^2 = Pr_T/(C_p T_w), \quad b = -Pr_T q_w/(C_p T_w \tau_w) \qquad (34)$$

III. Implementation

Details regarding implementation of wall matching in a Navier-Stokes computation depend to some extent upon the numerical scheme used. In the present study, the computer program used is known as EDDY2C and is based upon MacCormack's[9] implicit method. The computational sequence in EDDY2C is as follows.

1. At the beginning of each timestep, Equation (21) is used to evaluate either T_w or q_w/τ_w from the known velocity parallel to the surface at the grid point nearest the surface, y_2.

2. ρ_w is computed from Equation (23) in terms of the known density and temperature at y_2.

3. The transformed velocity u^s_2 is computed in terms of the known velocity at y_2 from Equations (33) and (34).

4. Using the known values of u^s_2 and y_2, Equation (24) is solved for u_τ.

5. The surface flux vector, G_w, which represents the flux normal to the surface for mass, tangential momentum, normal momentum, total energy, turbulent kinetic energy, and specific dissipation rate, is specified according to

$$G_w = [\ 0 \quad -\tau_w \quad p_w \quad q_w \quad 0 \quad -G_2\ ]^T \qquad (35)$$

where $p_w = p_2$ according to Equation (22). The quantity G_2 is the flux from the top of the finite difference cell nearest the surface. Further comment on this feature will be made below.

6. Values of all parameters at the reflected point, $y_1 = -y_2$ are the same as those used for integration through the viscous sublayer, e.g.,

$$u_1 = -u_2, \quad v_1 = -v_2, \quad k_1 = -k_2 \qquad (36)$$

7. The source term for turbulent kinetic energy is specified according to Equations (31) and (32).

8. The source term for specific dissipation rate, ω, is replaced by $(\omega_w - \omega)$. Because ω is very large near the surface, this forces the solution algorithm to converge to $\omega_2 = \omega_w$.

9. The solution is advanced one timestep and program control returns to Step 1 until steady flow conditions are achieved.

This scheme provides minimum disruption of normal program operation. All nine steps could be accomplished in a single subroutine although, for clarity, two subroutines have been added to EDDY2C. The main reason for this minimal disruption is, as noted in Step 6, the boundary conditions used at the surface for all flow variables are identical to those used in a computation which integrates through the viscous sublayer. Wall matching affects the solution as follows. Equation (24) serves as the constitutive relation between surface shear stress and the mean velocity profile, while Equations (21-23) establish either surface temperature or surface heat flux in terms of the mean temperature and velocity profiles. Equations (31) and (32) set the net rate of production of turbulence in the finite difference cell adjacent to the surface. Finally, Step 8 forces the specific dissipation rate at the mesh point closest to the surface to assume the value given in Equation (26).

The surface flux for ω is infinite as is dissipation of ω which exactly balances the surface flux singularity. Consequently, the most direct way of enforcing $\omega_2 = \omega_w$ is to integrate the equation for ω beginning at the mesh point adjacent to the surface. In the procedure outlined above, this end is accomplished in an indirect manner by causing an exact cancellation of the diffusion term (see Step 5), and making the net production term in the equation for ω proportional to the difference between ω_w and the computed value of ω. Hence, in the finite difference cell adjacent to the surface, we are in effect replacing the equation for ω with

$$\partial(\rho\omega)/\partial t = (\omega_w - \omega)\rho\omega \qquad (37)$$

This indirect method of setting $\omega_2 = \omega_w$ has been used specifically to leave program logic unaltered.

Solution accuracy can be improved somewhat for unusually small values of $u_\tau y_2/\nu_w$ as follows. First, solve Equation (24) in the usual manner and call the solution $\tilde{u}_\tau$. Then, compute the friction velocity appropriate to a linear velocity profile, and call it $\hat{u}_\tau$. Finally, set $u_\tau = \max[\,\hat{u}_\tau\,,\,\tilde{u}_\tau\,]$.

As a final comment, unusual transient behavior such as that experienced early in a computation can lead to erratic behavior of the parameter ϕ. Potentially, such transients can even lead to instability and destruction of the solution. To suppress this undesirable effect, provision has been made in EDDY2C to limit the magnitude of ϕ. For all of the computations to date, no instability has been detected provided ϕ satisfies the following equation.

$$|\phi y_2^+| < 3/4 \qquad (38)$$

IV. Applications

To demonstrate how well the wall matching procedure works in numerical computations, three types of applications have been made, all using program EDDY2C, a compressible Navier-Stokes program implementing MacCormack's[9] method. The first computations are for a constant pressure Mach 3 boundary layer. Next, we simulate two cases of Mach 3 flow into a compression corner, including boundary-layer separation. Finally, a hypersonic shock/boundary-layer interaction is simulated. With the exception of the hypersonic case, all computations have been done using both the k-ω and multiscale models.

A. Flat Plate Boundary Layer

The first computations are for a Mach 3, adiabatic wall, constant pressure boundary layer. The purpose of these computations is to establish the accuracy of the wall matching procedure for an attached boundary layer. Most importantly, our goal is to determine solution sensitivity to the location of the grid point closest to the surface. A total of twenty mesh points are placed normal to the surface, and y_2^+ has been varied from 10 to 320. Figure 2 shows the percent error in skin friction relative to the value computed by integrating through the viscous sublayer (using $y_2^+ = 0.6$). The error for the k-ω model is everywhere less than 6%, while the error for the multiscale model is generally about 2% larger than the corresponding k-ω model error. Most importantly, for both models there is a monotonic decrease in the error as y_2^+ increases down to about 30. For smaller values of y_2^+, the error increases slightly.

B. Compression Corner Flows

Figures 3, 4, 5 and 6 compare wall matching solutions with corresponding solutions obtained by integrating through the sublayer, and with experimental data[6]. Two different ramp angles have been considered, viz, 20° (Figures 3 and 4) and 24° (Figures 5 and 6). The finite difference meshes for the 20° wedge consist of 25 mesh points normal to the surface, 15 of which lie in the boundary layer upstream of the interaction. For the 24° wedge, there are 30 points normal to the surface, with 15 in the boundary layer. By comparison, 25 mesh points are needed to resolve the sublayer.

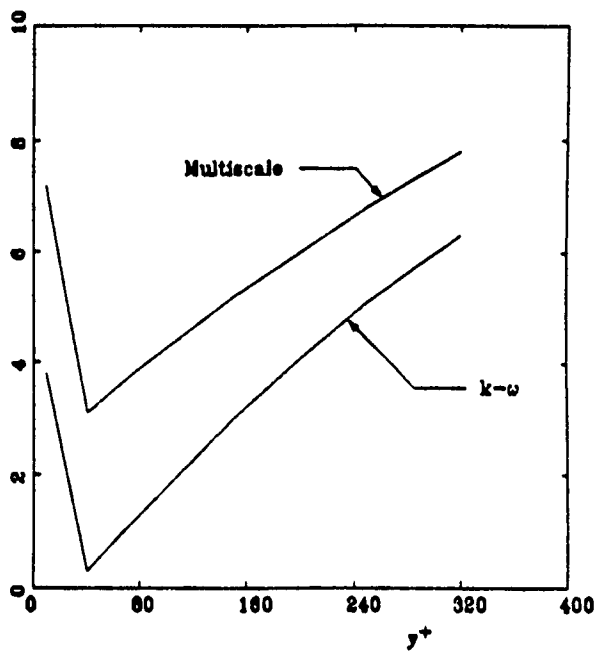

Figure 2. Percent error in skin friction as a function of mesh point placement adjacent to the surface for a Mach 3 flat plate boundary layer.

For the wall matching computation, the value of y_2^+ varies from 8 to 80 on the 20° wedge and from 8 to 90 on the 24° wedge. In both cases, y_2^+ is 30 for the boundary layer upstream of the interaction. Based on the analysis of Subsection IV-A, this value yields the minimum error when the boundary layer is attached. All computations have been done on a 16.7 megahertz 80386-based microcomputer with a Weitek math coprocessor. Table 1 summarizes computing times. Corresponding computing times for integration through the sublayer range from 15 to 35 hours.

Table 1. Computing Times for Compression Corners

Wedge Angle	k-ω	Multiscale
20°	4.0 hours	6.0 hours
24°	6.0 hours	10.5 hours

As shown in Figures 3 and 4, the surface pressure distributions for both models are almost unaffected on the 20° wedge. Unsurprisingly, for both models, skin friction differs most in the separation bubble, and the wall-matching bubbles are about 20% smaller. Skin friction differences of 10% or less persist downstream of reattachment because of the difference in separation bubble size.

Figures 5 and 6 demonstrate somewhat larger differences, primarily because the separation bubble is 30% smaller in the wall matching computations. Again, differences persist downstream of reattachment due to the difference in separation bubble size.

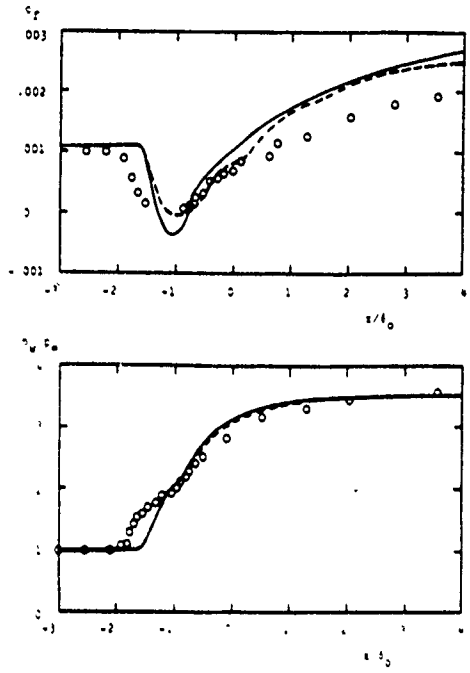

Figure 3. Comparison of computed and measured skin friction and surface pressure for Mach 3 flow into a 20° compression corner using the k-ω model. o Settles, et al; —— $y^+ \to 0$; ---- $y^+ = 30$.

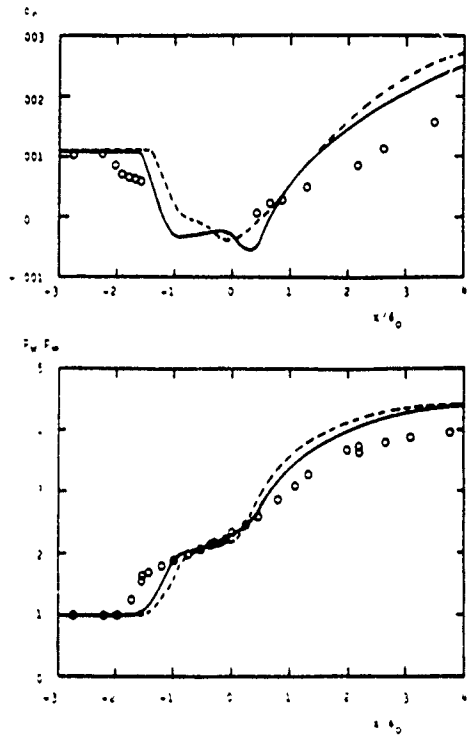

Figure 5. Comparison of computed and measured skin friction and surface pressure for Mach 3 flow into a 24° compression corner using the k-ω model. o Settles, et al; —— $y^+ \to 0$; ---- $y^+ = 30$.

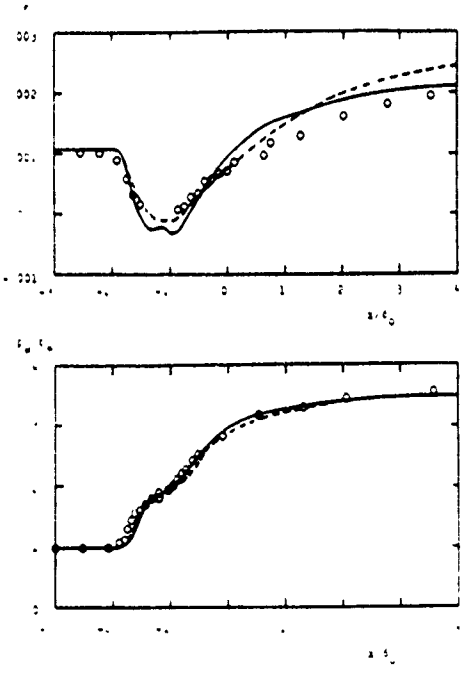

Figure 4. Comparison of computed and measured skin friction and surface pressure for Mach 3 flow into a 20° compression corner using the multiscale model. o Settles, et al; —— $y^+ \to 0$; ---- $y^+ = 30$.

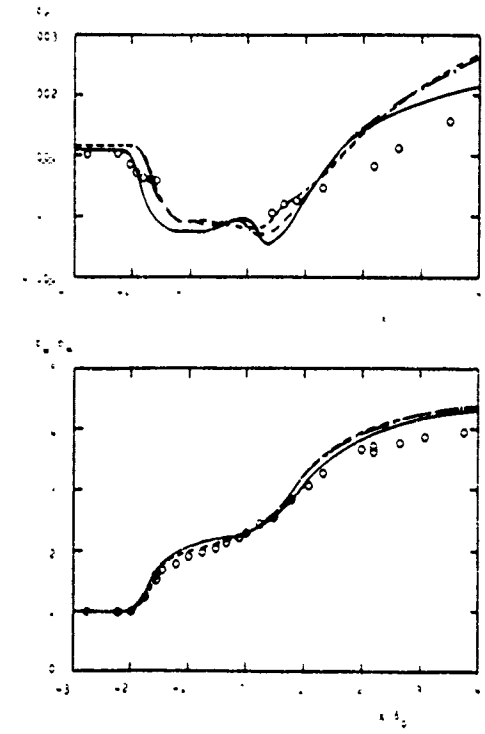

Figure 6. Comparison of computed and measured skin friction and surface pressure for Mach 3 flow into a 24° compression corner using the multiscale model. o Settles, et al; —— $y^+ \to 0$; —•— $y^+ = 15$; ---- $y^+ = 30$.

The multiscale 24° computation has also been done with y_2^+ halved (i.e., $y_2^+ = 15$ upstream of the interaction) to examine the hypothesis that wall matching solutions converge uniformly toward the solution obtained by integrating through the sublayer, at least away from separated regions. As shown, differences between the $y^+ = 15$ and $y^+ \to 0$ computations are smaller than those between the $y^+ = 30$ and $y^+ \to 0$ computations, thus confirming the hypothesis. Apparently, the wall matching solutions converge toward a separation bubble size smaller than the $y^+ \to 0$ solution which accounts for most of the differences.

C. Hypersonic Shock Boundary Layer Interaction

The final application is for the interaction of a hypersonic turbulent boundary layer with an oblique shock wave. The computation has been done using the multiscale model, with y_2^+ ranging between 5 and 400. Figure 7 compares computed and measured[7] surface pressure. Since no special compressibility modifications have been made to the multiscale model, close agreement between theory and experiment is not expected. This computation nevertheless demonstrates the efficiency of using wall matching. That is, the computation required 19 hours a 16.7 megahertz 80386/Weitek-based microcomputer as compared to 6 hours on a Cray XM-P/48 for a $y_2^+ \to 0$ computation.

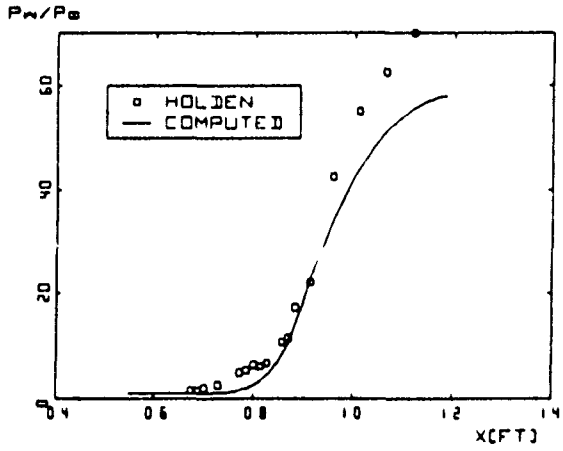

Figure 7. Comparison of computed and measured surface pressure for a Mach 11 shock boundary layer interaction; multiscale model.

V. Summary and Conclusions

Wall matching is an objective procedure for devising surface boundary conditions which can be used to obviate integration through the viscous sublayer. The approach differs in spirit from the conventional use of wall functions primarily in the avoidance of any attempt to enhance the turbulence model. There are four key points underscoring this difference in philosophy which can be stated as follows.

1. In matching to the law of the wall we are, in a strict mathematical sense, insisting upon specified asymptotic behavior of the velocity/surface-stress relationship in the limit $y/\delta \to 0$, where δ is a length characteristic of the overall scale of the boundary layer.

2. In using wall functions, we are likewise insisting upon specified asymptotic behavior of turbulence field properties in the limit $y/\delta \to 0$.

3. Wall functions are not unique. For a given turbulence model, there is generally more than one asymptotic solution as $y/\delta \to 0$ and only one of these solutions can usually be said with certainty to be consistent with the law of the wall.

4. In using wall functions for flows with pressure gradient, solution accuracy can be impaired if proper account is not taken of its effect on the wall functions and upon their point of application.

Results of the applications indicate the wall matching procedure is both computationally efficient and accurate. While, unlike the k-ε model, the k-ω and multiscale models do not require wall matching to achieve accurate solutions in general, there are applications where wall matching will be needed, most notably for three dimensional Navier-Stokes computations.

VI. Acknowledgement

Research was supported by the U. S. Army Research Office under Contract DAAL-87-C-0004 with Dr. Thomas Doligalski as Contract Monitor.

Appendix: Equations of Motion

This appendix summarizes the Wilcox k-ω and multiscale models. These models differ in the postulated constitutive relation between the Reynolds stress tensor and mean flow properties. The k-ω model implements the Boussinesq approximation in which Reynolds stress is assumed proportional to mean strain rate. By contrast, the multiscale model computes each component of the Reynolds stress tensor individually.

Mean Conservation Equations

For both models, we must solve the mass-averaged[10] equations for conservation of mass, momentum and energy, viz,

$$\partial\rho/\partial t + \partial/\partial x_j(\rho u_j) = 0 \qquad \text{(A1)}$$

$$\partial/\partial t(\rho u_i) + \partial/\partial x_j(\rho u_i u_j) = -\partial p/\partial x_i + \partial \hat{\tau}_{ij}/\partial x_j \qquad \text{(A2)}$$

$$\partial/\partial t(\rho E)+\partial/\partial x_j(\rho u_j H) = \partial/\partial x_j[u_i\hat{\tau}_{ij} - q_j + (\mu+\sigma^*\mu_T)\partial k/\partial x_j] \qquad \text{(A3)}$$

where t is time, x_i is position vector, u_i is velocity vector, p is pressure, ρ is density, $\hat{\tau}_{ij}$ is the sum of molecular and Reynolds stress tensors and q_j is the sum of molecular and turbulent heat-flux vectors. In Equation (A3), the quantities $E=e+k+u_iu_i/2$ and $H=h+k+u_iu_i/2$ are total energy and total enthalpy, respectively, with $h=e+p/\rho$; e and h denote internal energy and enthalpy. μ and μ_T are molecular and eddy viscosity, ρk is turbulent kinetic energy and σ^* is a closure coefficient.

Constitutive Relations

For both models, the heat flux vector is computed according to

$$q_j = -(\mu/Pr_L+\mu_T/Pr_T)\partial h/\partial x_j \qquad (A4)$$

where Pr_L and Pr_T are laminar and turbulent Prandtl numbers.

The remaining step needed to close this system of equations is to postulate a relation between the total stress tensor, $\hat{\tau}_{ij}$, and mass-averaged flow properties. For both models, total stress is related to Reynolds stress, τ_{ij}, according to

$$\hat{\tau}_{ij} = 2\mu[S_{ij}-(1/3)\partial u_k/\partial x_k\delta_{ij}] + \tau_{ij} \qquad (A5)$$

where $S_{ij}=(1/2)(\partial u_i/\partial x_j+\partial u_j/\partial x_i)$ is the mean strain rate tensor.

On the one hand, the k-ω model uses the Boussinesq approximation that Reynolds stress is proportional to mean strain rate, viz,

$$\tau_{ij} = 2\mu_T[S_{ij}-(1/3)\partial u_k/\partial x_k\delta_{ij}] - (2/3)\rho k\delta_{ij} \qquad (A6)$$

On the other hand, with the multiscale model, we introduce two energy scales corresponding to upper and lower partitions of the turbulent energy spectrum. The multiscale model computes τ_{ij} according to

$$\tau_{ij} = \rho T_{ij} - (2/3)\rho e\delta_{ij} \qquad (A7)$$

where ρT_{ij} is the upper partition contribution to the Reynolds-stress tensor and ρe is the energy of the eddies in the lower partition.

Turbulent Energy and Dissipation Rate

Both models determine turbulent energy and specific dissipation rate, ω, from the following two equations.

$$\partial/\partial t(\rho k) + \partial/\partial x_j(\rho u_j k) = \tau_{ij}\partial u_i/\partial x_j - \beta^*\rho\omega k + \partial/\partial x_j[(\mu+\sigma^*\mu_T)\partial k/\partial x_j] \qquad (A8)$$

$$\partial/\partial t(\rho\omega) + \partial/\partial x_j(\rho u_j\omega) = (\gamma\omega/k)\tau_{ij}\partial u_i/\partial x_j - \beta\rho\omega[\omega + \zeta\sqrt{2\Omega_{ij}\Omega_{ji}}] + \partial/\partial x_j[(\mu+\sigma\mu_T)\partial\omega/\partial x_j)] \qquad (A9)$$

where $\Omega_{ij}=(1/2)(\partial u_i/\partial x_j-\partial u_j/\partial x_i)$ is the mean rotation tensor. The quantities β, β^*, γ, ζ, σ and σ^* are closure coefficients. Note also that the eddy viscosity, μ_T, appearing in Equations (A3, A4, A6, A8, and A9) is defined by

$$\mu_T = \rho k/\omega \qquad (A10)$$

Upper Partition Equations

For the multiscale model, the upper partition Reynolds stress equation is

$$\partial/\partial t(\rho T_{ij}) + \partial/\partial x_k(\rho u_k T_{ij}) = - P_{ij} + E_{ij} \qquad (A11)$$

where E_{ij} represents the exchange of energy amongst the mean, upper-partition and lower-partition energies, and is given by

$$E_{ij} = -C_1\beta^*\omega[\tau_{ij}+(2/3)\rho k\delta_{ij}] + \hat{\alpha}P_{ij} + \hat{\beta}D_{ij} + \hat{\gamma}\rho k[S_{ij}-(1/3)\partial u_k/\partial x_k\delta_{ij}] + (2/3)\beta^*\rho\omega k(1-e/k)^{3/2}\delta_{ij} \qquad (A12)$$

where C_1, $\hat{\alpha}$, $\hat{\beta}$ and $\hat{\gamma}$ are closure coefficients. The tensors P_{ij} and D_{ij} are defined by

$$P_{ij} = \tau_{im}\partial u_j/\partial x_m+\tau_{jm}\partial u_i/\partial x_m \qquad (A13)$$

$$D_{ij} = \tau_{im}\partial u_m/\partial x_j+\tau_{jm}\partial u_m/\partial x_i \qquad (A14)$$

Finally, it is instructive to contract Equation (A11) which yields the following equation for upper-partition energy, $\rho(k-e) = -(1/2)\rho T_{kk}$.

$$\partial/\partial t[\rho(k-e)] + \partial/\partial x_j[\rho u_j(k-e)] = (1-\hat{\alpha}-\hat{\beta})\tau_{ij}\partial u_i/\partial x_j - \beta^*\rho\omega k(1-e/k)^{3/2} \qquad (A15)$$

This equation is normally used in place of one of the normal stress components of Equation (A11).

Closure Coefficients

Finally, the ten closure coefficients appearing in Equations (A1-A15) have been established in the prior studies by Wilcox[1,3]. No changes in those coefficients have been made for any of the applications in this study. Their values are as follows.

Multiscale Model

$$\left.\begin{array}{l} \hat{\alpha} = 42/55, \quad \hat{\beta} = 6/55, \quad \hat{\gamma} = 1/4 \\ \beta = 3/40, \quad \gamma = 4/5, \quad \sigma = 1/2 \\ \beta^* = 9/100, \quad \zeta = 1, \quad \sigma^* = 1/2 \\ C_1 = 1 + 4(1-e/k)^{3/2} \end{array}\right\} \qquad (A16)$$

k-ω Model

$$\left.\begin{array}{l} \beta = 3/40, \quad \gamma = 5/9, \quad \sigma = 1/2 \\ \beta^* = 9/100, \quad \zeta = 0, \quad \sigma^* = 1/2 \end{array}\right\} \qquad (A17)$$

References

[1]Wilcox, D. C., "Reassessment of the Scale Determining Equation for Advanced Turbulence Models," AIAA Journal, Vol 26, No 11, p 1299 (Nov 1988).

[2]Kline, S.J., Cantwell, B.J. & Lilley, G.M., "1980-81 AFOSR-HTTM-Stanford Conference on Complex Turbulent Flows," Stanford Univ (1981).

[3]Wilcox, D.C., "Multiscale Model for Turbulent Flows," AIAA Journal, Vol 26, No 11, p 1311 (Nov 1988).

[4]Saffman, P.G. and Wilcox, D.C., "Turbulence-Model Predictions for Turbulent Boundary Layers," AIAA J, Vol 12, No 4, pp 541- 546 (Apr 1974).

[5]Viegas, J.R., Rubesin, M.W. and Horstman, C.C., "On the Use of Wall Functions as Boundary Conditions for Two-Dimensional Separated Compressible Flows," AIAA Paper 85-0180 (Jan 1985).

[6]Settles, G.S., Vas, I.E. and Bogdonoff, S.M., "Details of a Shock Separated Turbulent Boundary Layer at a Compression Corner," AIAA Journal, Vol 14, pp 1709-1715 (Dec 1976).

[7]Holden, M.S., "Experimental Studies of Quasi-Two-Dimensional and Three-Dimensional Viscous Interaction Regions Induced by Skewed-Shock and Swept-Shock Boundary Layer Interaction," AIAA Paper 84-1677 (Jun 1984).

[8]Coles, D.E. and Hirst, E.A., Computation of Turbulent Boundary Layers-1968 AFOSR-IFP-Stanford Conference, Vol II, Stanford Univ (1969).

[9]MacCormack, R.W., "A Numerical Method for Solving the Equations of Compressible Viscous Flow," AIAA Journal, Vol 20, pp 1275-1281 (Sep 1982).

[10]Favre, A., "Equations des Gaz Turbulents Compressibles," J Mecan, Vol 4, No 3, pp 361-390 (1965).

APPENDIX F: SEPARATED FLOW APPLICATIONS

The paper reproduced in this appendix appears in the July, 1990 issue of the AIAA Journal. The formal reference to this paper is as follows.

> Wilcox, D. C., "Supersonic Compression-Corner Applications of a Multiscale Model for Turbulent Flows," *AIAA Journal*, Vol. 28, No. 7, Jul. 1990, pp. 1194-1198.

This paper applies the Wilcox k-ω and multiscale models to three Mach 3 compression corner flows including separation of a turbulent boundary layer. The paper demonstrates that the multiscale model is superior for such applications.

Supersonic Compression-Corner Applications of a Multiscale Model for Turbulent Flows

David C. Wilcox*
DCW Industries, Inc., La Cañada, California

The new "multiscale" model for turbulent flows developed by Wilcox has been subjected to a continuing series of rigorous applications, including shock-induced, boundary-layer separation, to test its accuracy in simulating complex flow phenomena. While previous applications have been inconclusive regarding superiority of the multiscale model over two-equation models, results obtained demonstrate a marked improvement in predictive accuracy for flows which include boundary-layer separation. As speculated in its original development, the model is superior because it accounts for disalignment of the Reynolds-stress-tensor and the mean-strain-rate-tensor principal axes.

I. Introduction

THIS paper includes results of three shock-separated turbulent boundary layer computations using both the multiscale and k-ω models developed by Wilcox.[1,2] In all cases, detailed comparisons with experimental data are presented. Flows considered include two planar Mach 3 compression-corner flows[3] and an axisymmetric Mach 3 compression corner flow.[4] The flows selected provide a definitive measure of differences attending use of the multiscale model compared to the k-ω model.

To underscore the significance of the results obtained in this study, it is worthwhile to briefly review our own efforts over the past 15 yr in quest of an acceptable numerical solution for flow into a compression corner. Wilcox[5] performed the first solutions to the Reynolds-averaged, Navier-Stokes equations using an advanced turbulence model for shock-induced separation of a turbulent boundary layer. This early computational fluid dynamics (CFD) study included six computations, three for reflection of an oblique shock from a flat plate and three for flow into a compression corner. Results of the study indicate that, using a two-equation turbulence model, a reasonably accurate description of the flowfield can be obtained for reflection of an oblique shock from a flat plate. However, the numerical flowfields for the compression corner cases differ significantly from the experimentally observed flowfields, even though Mach and Reynolds numbers and shock strength are identical to those of the flat-plate cases. Thus, a seemingly simple change in flow geometry causes a major difference in predictive accuracy.

To put these computations in proper perspective, note that the turbulence model used was the Saffman-Wilcox[6] k-ω^2 model with surface boundary conditions given by matching to the law of the wall, a procedure which has since come to be referred to as using wall functions. The numerical algorithm used was a first-order accurate, explicit, time-marching procedure. Since this study, computational methods have improved dramatically thanks to the innovative work of many researchers, most notably, MacCormack,[7] Beam and Warming,[8] and Steger[9]. Today, it is possible to perform two-equation turbulence model computations for shock-separated flows without the aid of wall functions on a (relatively crude) 1200-point finite difference mesh using a fast desk top microcomputer.[10] However, until this study, little improvement in predictive accuracy relative to our results of 1974 has been realized for compression corner flows.

The work of Horstman, et al.[11,12] provides clear substantiation of this claim. They have applied many turbulence models to shock-separated flows with almost universal results, viz 1) too little upstream influence as shown by pressure starting to rise well downstream of the measured beginning of adverse pressure gradient; 2) surface pressure in excess of measured values above the separation bubble; 3) skin friction higher than measured downstream of reattachment; and 4) velocity profiles downstream of reattachment which indicate flow deceleration in excess of corresponding measurements.

On the one hand, by using wall functions and the k-ϵ turbulence model,[13] Viegas, Rubesin and, Horstman[12] are able to remove item 3 from this list. On the other hand, they achieve only modest improvements in the other items. This lack of success on the compression-corner problem, which has persisted for more than a decade, is excellent testimony to the oft quoted statement that turbulence modeling is the pacing item in CFD.

Reference 5 conjectures that the relatively poor performance of the two-equation model for the compression corner computations is caused by the model's use of the Boussinesq approximation, which holds that the principal axes of the Reynolds stress tensor are parallel to those of the mean strain rate tensor. The physical reasoning is that, unlike the flow induced by an oblique shock reflecting from a flat plate, the mean strain rate tensor's principal axes abruptly rotate at the flat-plate/ramp junction. The Boussinesq approximation implies that the Reynolds stresses also change abruptly which, on physical grounds, would be a rather questionable event.

The excellent predictions made by Johnson[14,15] for transonic flow over a "bump" substantiate the notion that use of the Boussinesq approximation lies at the root of the two-equation model's inability to accurately simulate properties of separated flows. Using an approach in which a lag occurs between sudden changes in mean strain rate and the Reynolds shear stress, Johnson is able to duplicate measured flow properties to within engineering accuracy. His predictions are so much better than those obtained with the k-ϵ model that further applications with the latter seem pointless—especially since the k-ϵ model fares so poorly even for attached boundary layers in an adverse pressure gradient.[2] While Johnson offers significant improvement for transonic separated flows, the model has been demonstrated to be accurate for a limited range of Mach numbers and has been developed much in the spirit of mixing length, i.e., it is a very powerful "incomplete" model of turbulence.

Presented as Paper 88-0220 at AIAA 26th Aerospace Sciences Meeting, Reno, NV, Jan 11-14, 1988, received Feb 6, 1989 revision received July 11, 1989 Copyright © 1989 by American Institute of Aeronautics and Astronautics, Inc All rights reserved

*President. Associate Fellow AIAA.

The primary purpose of this research study has been to apply both the multiscale and k-ω models to the three well documened separated flows referenced above and to assess the differences. As will be shown, the differences are profound.

II. Equations of Motion

All of the computations in this study have been done using both the multiscale and k-ω models. These models differ in the postulated constitutive relation between the Reynolds stress-tensor and mean-flow properties. The k-ω model implements the Boussinesq approximation in which Reynolds stress is assumed proportional to mean-strain rate. By contrast, the multiscale model computes each component of the Reynolds stress tensor individually. Complete details of the turbulence model equations are given in Refs. 1 and 2.

III. Applications

A. Numerical Procedure

Algorithm

The numerical algorithm used in the computations was developed by MacCormack[7] and has been used for many compressible separated flow computations by Hortsman, et al.[11,12,14] Because of its proven track record, we obtained the version of Horstman's program, which uses the k-ϵ turbulence model to describe the turbulence. After purging the k-ϵ model and incorporating the multiscale and k-ω models, we find that the modified program requires about 30% more memory than the original, primarily because of the additional arrays needed for the Reynolds stress components.

Turbulence Models

All computations have been done using both the k-ω and multiscale models. The k-ω model is far less complex than the k-ϵ model, mainly because of all the special viscous modifications needed to integrate the k-ϵ model through the sublayer. As a consequence, a computation using the k-ω model requires only 75% as much CPU time per time step as one using the k-ϵ model. The multiscale model requires approximately 50% more CPU time than the k-ω model. Thus, a computation using the multiscale model requires about 12% more CPU time per time step than a corresponding computation using the k-ϵ model.

Finite-Difference Grids

Dimensions of the computational domains for each case are listed in Table 1 in terms of the thickness of the incident boundary layer, δ_0. In all three computations, the finite-difference grid consists of 80 equally-spaced points between upstream and downstream boundaries, and 45 points lie between the lower and upper boundaries. The first 30 grid points normal to the surface extend to $y = \delta_0$; grid-point spacing increases in a geometric progression with a grading ratio between 30% and 35%. The remaining 15 points are equally spaced, covering the region from $y = \delta_0$ to the top of the grid.

Table 1 Primary flow and numerical parameters

Parameter	20 deg corner	24 deg corner	30 deg corner
Mach number	2.79	2.84	2.85
Total pressure (psf)	14,513	14,451	3,600
Total temp. (deg R)	464	472	513
Wall temp. (deg R)	493	497	487
B. L. thickness, δ_0 (ft)	.082	.075	.033
Mom. thickness, Re_θ	93,800	82,050	9,366
Shape factor, H	5.08	5.08	4.00
Grid length ($\Delta x/\delta_0$)	8	10	10
Grid height ($\Delta y/\delta_0$)	6	6	5
k-ω time steps	7,000	24,000	12,000
k-ω CPU time (min)	17	60	32
Multiscale time steps	7,000	40,000	12,000
Multiscale CPU (min)	25	138	45

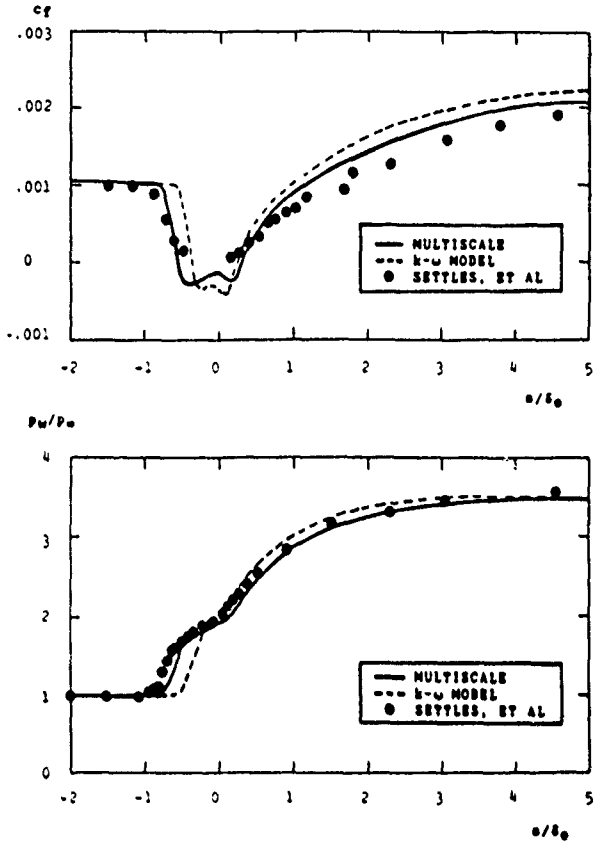

Fig. 1 Comparison of computed and measured skin friction and surface pressure for Mach 2.79 flow into a 20 deg compression corner; s is tangential distance from corner.

The mesh point closest to the surface lies below $y^+ = 0.7$ throughout the grid in all three cases. Upstream of the ramp, finite difference cells are rectangular. Downstream of the ramp, the cells are parallelograms aligned with the ramp.

Boundary and Initial Conditions

Upstream boundary conditions for the three computations have been obtained from a two-dimensional, boundary-layer program. We have been able to match the measured values of Re_θ and H for each case to within 1%. The upstream boundary-layer profiles have also been used as initial conditions throughout the computational domain.

Other Details

The equations of motion have been integrated through the sublayer with a viscous Courant number, $C_\nu = 2\nu\Delta t/(\Delta y)^2$ ranging between 30 and 90 for most of the computation and typically half this value for the final 25% of the computation to eliminate any possibility of solution dependence on the time step, a procedure recommended by MacCormack.[7] In every computation, a freestream fluid particle traverses the mesh at least 3 times and as many as 18 times. The relatively long run times are a direct consequence of having $y^+ < 1$, which was done to insure solution accuracy. Subsequent numerical experimentation has shown that having y^+ as large as 2 has little effect on solution accuracy with a significant reduction in CPU time.

IV. Applications

B. 20 deg Compression Corner

The first of the three applications is for Mach 2.79 flow into a 20 deg compression corner. This flow has been experimentally investigated by Settles, Vas and Bogdonoff[3] and includes a small region over which separation of the incident turbulent boundary layer occurs. Figure 1 compares computed and

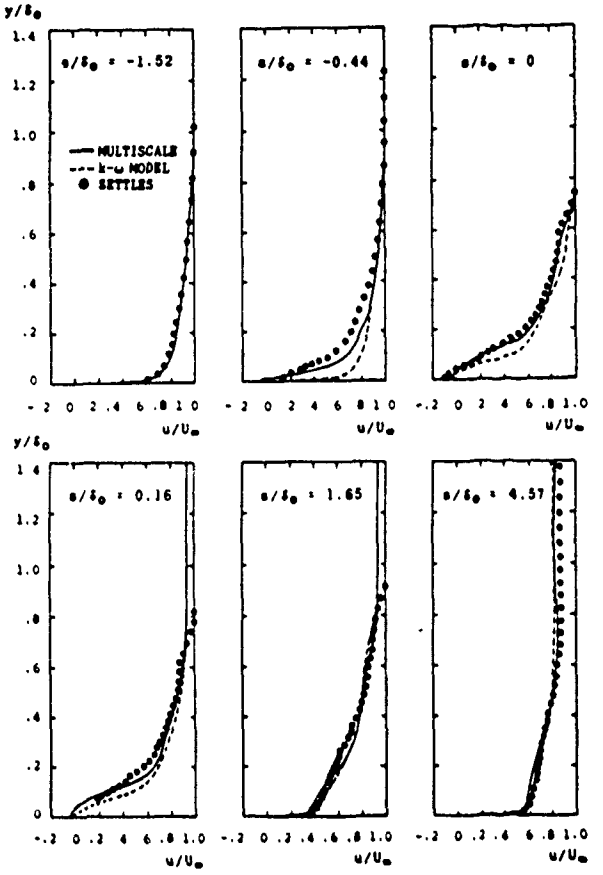

Fig. 2 Comparison of computed and measured velocity profiles for Mach 2.79 flow into a 20 deg compression corner; y is distance normal to the surface.

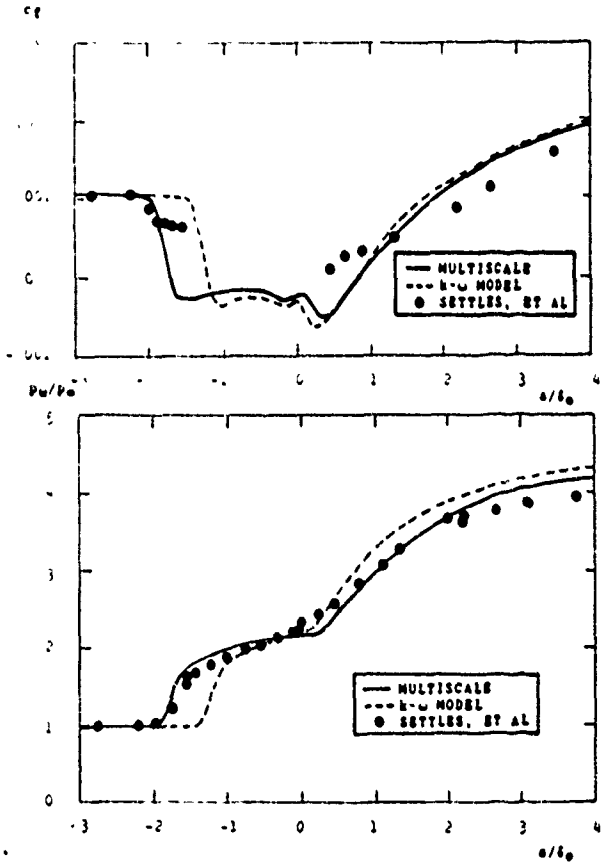

Fig. 3 Comparison of computed and measured skin friction and surface pressure for Mach 2.84 flow into a 24 deg compression corner; s is tangential distance from corner.

measured surface pressure p_w/p_∞ and skin friction, C_f. The multiscale model predicts more upstream influence, a lower pressure plateau at separation, and a more gradual increase in skin friction downstream of reattachment relative to the k-ω results. All of these features represent significant improvement in predictive accuracy. Figure 2 compares computed and measured velocity profiles throughout the interaction region. Multiscale model predictions are much closer to measured properties than k-ω model predictions—especially near the separation point. Using the k-ϵ model and specially devised wall functions, Viegas, Rubesin and Horstman[12] are able to achieve similar accuracy for this flow.

C. 24 deg Compression Corner

The second of the three applications is for Mach 2.84 flow into a 24 deg compression corner. This flow has also been experimentally investigated by Settles, Vas and Bogdonoff[3] and includes a larger region over which separation of the incident turbulent boundary layer occurs than in the 20 deg case of the preceding section. Figure 3 compares computed and measured surface pressure and skin friction. As in the 20 deg compression-corner computation, the multiscale model predicts much more upstream influence. Interestingly, the k-ω predicted pressure plateau at separation is very close to the measured level, and there is little difference between k-ω and multiscale predicted increase in skin friction downstream of reattachment. Figure 4 compares computed and measured velocity profiles throughout the interaction region. Again, multiscale model predictions are closer to measured properties than k-ω model predictions, most notably near the separation point.

Note that, for this flow, Viegas, Rubesin and Horstman[12] predict pressure plateau values about 20% higher than measured and are unable to simultaneously make accurate

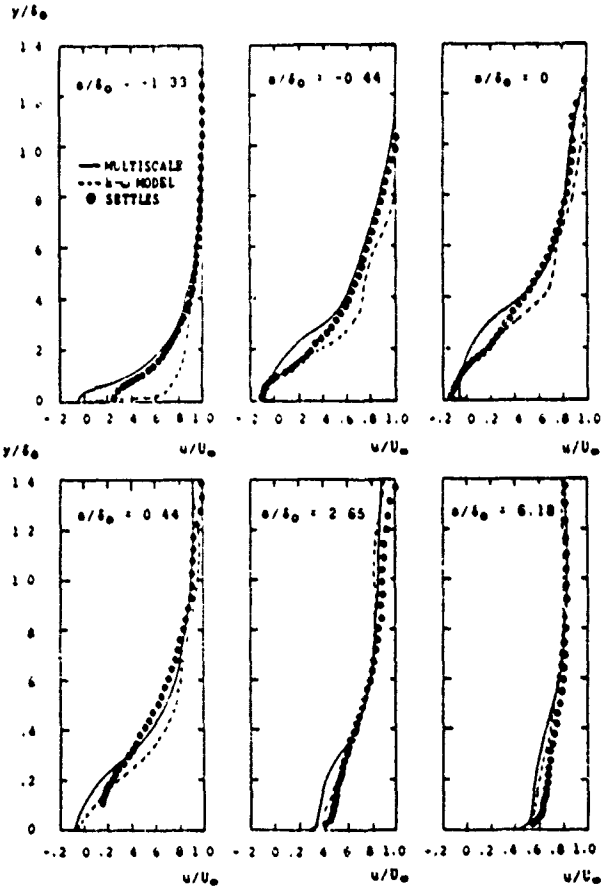

Fig. 4 Comparison of computed and measured velocity profiles for Mach 2.84 flow into a 24 deg compression corner; y is distance normal to the surface.

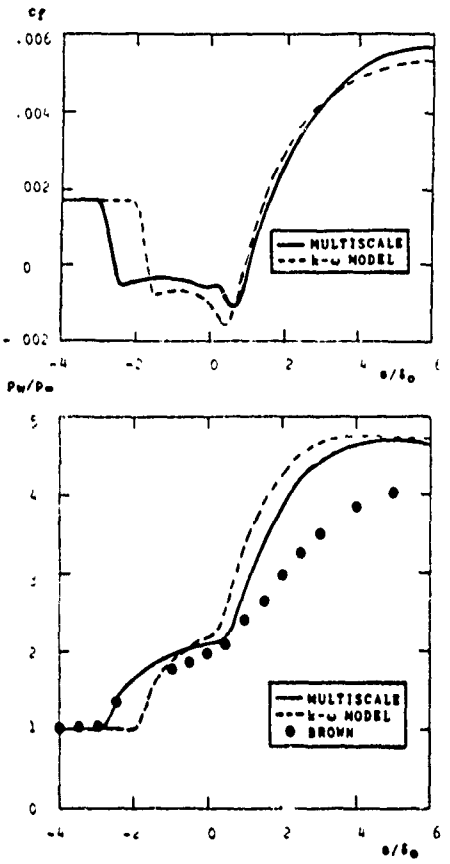

Fig. 5 Comparison of computed and measured skin friction and surface pressure for Mach 2.85 flow into a 30 deg compression corner; s is tangential distance from corner.

predictions for skin friction downstream of reattachment and the initial rise in surface pressure. That is, their solutions can match either skin friction or surface pressure, but not both.

D. Axisymmetric Compression Corner

Our third application is for Mach 2.85 flow into a 30 deg axisymmetric compression corner. This flow has been experimentally investigated by Brown[4] and includes a separation bubble of length comparable to the 24 deg planar compression corner. Figure 5 compares computed and measured surface pressure. Computed skin friction is also shown. Once again the multiscale model predicts much more upstream influence. For both models, the predicted pressure plateau at separation is about 10% higher the measured level, and there is little difference between k-ω and multiscale predicted increase in skin friction downstream of reattachment. The overall pressure rise is predicted by both models to be 4.7; whereas the measurements indicate a value of 4. The inviscid pressure rise for a 30 deg axisymmetric compression corner is 4.4 so that neither theory nor experiment appears to be completely consistent with the physics of this flow.

Figure 6 compares computed and measured velocity profiles throughout the interaction region. Multiscale model predictions are closer to measured properties than k-ω model predictions throughout the interaction region. Because of the stronger than measured overall pressure rise, the computed zero velocity line is more distant from the wall than measured and thus distorts the profiles somewhat.

In order to eliminate the possibility that the finite-difference grid is too coarse to provide an accurate computation for the freestream, the k-ω computation has been repeated with an 80×60 grid. In the refined grid, the same spacing is used for the boundary layer, and 30 equally spaced points cover the region from $y = \delta_0$ to $y = 5\delta_0$. No significant changes in the solution result from this mesh refinement.

E. Data Analysis

Results presented in the preceding subsections indicate that, for the three compression-corner cases considered, the multiscale model provides a flowfield more consistent with experimental observations than does the k-ω model. The primary reason for the difference in the two models' predictions can be found by examining predicted behavior of the Reynolds shear stress near the separation point. Figure 7 shows the maximum Reynolds shear stress τ_{max} throughout the interaction region for the three compression-corner computations. As shown, the k-ω model predicts a more abrupt increase in τ_{max} at separation and a much larger peak value than predicted by the multiscale model. For the axisymmetric case, the figure includes experimental data for points ahead of the measured separation point. As shown, the multiscale model τ_{max} falls within experimental data scatter.

The physical implication of the pronounced difference in the rate of amplification of the Reynolds shear stress is clear. Using the Boussinesq approximation, the k-ω model makes a far more rapid adjustment to the rotation of the mean strain rate tensor's principal axes than the multiscale model. Consequently, the predicted separation point and initial pressure rise lie closer to the corner with the k-ω model than measured. Predicting more physically realistic growth of the Reynolds stresses, the multiscale model predicts overall flow properties which are in much closer agreement with measurements.

It is interesting to note that for the multiscale model, although the pressure is in such close agreement with measurements, the numerical separation points are further upstream than indicated by oil flow measurements for all three compression corner cases. Table 2 summarizes computed and measured separation points. Careful examination of the numerical flowfields shows that a) the separation bubble is extremely thin near its leading edge and b) reverse flow velocities are very small in this extremely thin region. This behavior is best

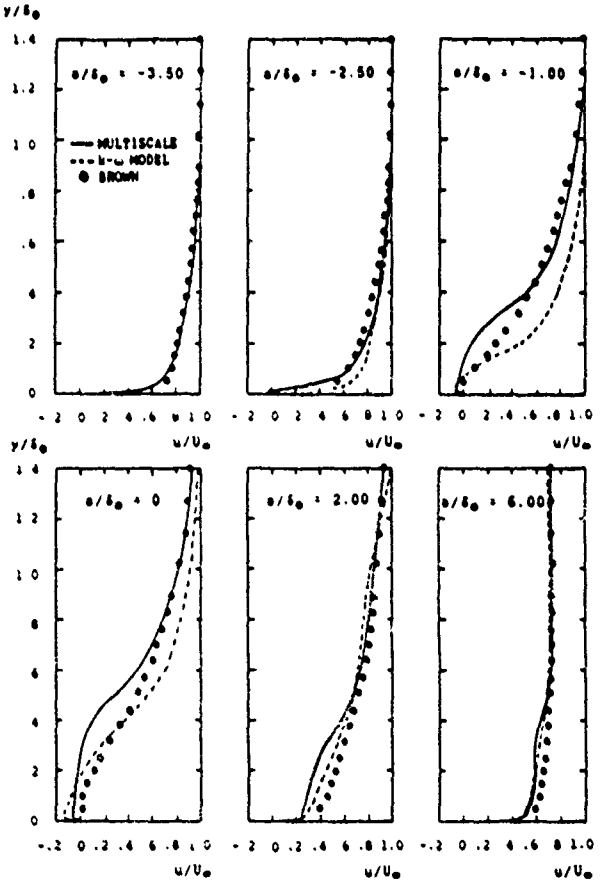

Fig. 6 Comparison of computed and measured velocity profiles for Mach 2.85 flow into a 30 deg compression corner; y is distance normal to the axis of symmetry.

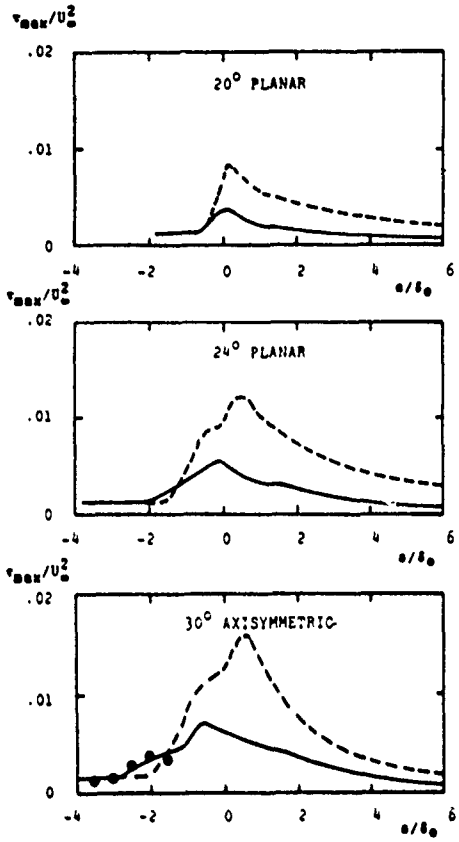

Fig. 7 Variation of peak Reynolds shear stress through the interaction region for the compression-corner computations; ——— k-ω model; ——— multiscale model; ● Brown.[4]

Table 2 Computed and measured separation points

Case	Multiscale	k-ω	Measured
20°	−0.56	−0.38	−0.45
24°	−1.73	−1.23	−1.33
30°	−2.60	−1.70	−1.50

exemplified in Figs. 2 and 6. Specifically, the profile at $s/\delta_0 = -0.44$ in Fig. 2, and the profile at $s/\delta_0 = -2.50$ in Fig. 6; both show that the reverse flow portion of the numerical profile lies below the experimental data. Given the excellent agreement between computed and measured surface pressure, which is strongly influenced by separation bubble shape, the computed separation points appear more physically realistic than those indicated by the oil-flow measurements.

V. Summary and Conclusions

Three shock-separated flows have been numerically simulated using the mass-averaged, Navier-Stokes equations and both the k-ω and multiscale models. The multiscale model is clearly superior for supersonic compression corner flows, which is especially obvious in the vicinity of separation.

The multiscale model's superiority over the k-ω model appears to be due to a more physically realistic description of the Reynolds stress tensor. Unlike the k-ω model, which uses the Boussinesq approximation that Reynolds stress is proportional to mean-strain rate, the multiscale model predicts a gradual increase in Reynolds shear stress near separation. Because the flow's effective resistance to separation is thus reduced, the separation point, and hence the initial rise in pressure, lies farther from the corner. Multiscale-model predicted surface pressure is much closer to measurements than the corresponding k-ω model surface pressure. Close agreement with limited experimental Reynolds shear stress data for the axisymmetric compression corner flow adds further verification that the multiscale model's predictions are physically sound.

On balance, the results obtained indicate that an important advance in the state of the art of separated-flow numerical simulation has been made. These results leave little doubt that continued use of turbulence models based on the Boussinesq approximation holds scant promise for accurate predictions. By contrast, the multiscale model, with only a 50% computational penalty per time step, brings numerical predictions into much closer agreement with the physics of separated flows.

Acknowledgments

Research was supported by the U.S. Army Research Office under Contract DAAL03-87-C-0004 with Thomas Doligalski as Contract Monitor. Partial funding for this study was also provided by James Wilson of the Air Force Office of Scientific Research. Computing time was made available by Joseph Marvin of the NASA Ames Research Center. C. C. Horstman of the NASA Ames Research Center contributed invaluable assistance as well as the computer program which served as the foundation for this study.

References

[1]Wilcox, D. C., "Multiscale Model for Turbulent Flows," *AIAA Journal*, Vol. 26, Nov. 1988, pp. 1311-1320.

[2]Wilcox, D. C., "Reassessment of the Scale Determining Equation for Advanced Turbulence Models," *AIAA Journal*, Vol. 26, Nov. 1988, pp. 1299-1310.

[3]Settles, G. S., Vas, I. E., and Bogdonoff, S. M., "Details of a Shock Separated Turbulent Boundary Layer at a Compression Corner," *AIAA Journal*, Vol. 14, 1976, pp. 1709-1715.

[4]Brown, J. D., "Two Component LDV Investigation of Shock Related Turbulent Boundary Layer Separation with Increasing Three Dimensionality," Ph.D. Thesis, University of California at Berkeley, 1986.

[5]Wilcox, D. C., "Numerical Study of Separated Turbulent Flows," AIAA Paper 74-584, 1974.

[6]Saffman, P. G., and Wilcox, D. C., "Turbulence-Model Predictions for Turbulent Boundary Layers," *AIAA Journal*, Vol. 12, April 1974, pp. 541-546.

[7]MacCormack, R. W., "A Numerical Method for Solving the Equations of Compressible Viscous Flow," *AIAA Journal*, Vol. 20, Sept. 1982, pp. 1275-1281.

[8]Beam, R. M., and Warming, R. F., "An Implicit Finite-Difference Algorithm for Hyperbolic Systems in Conservation Law Form," *Journal of Computational Physics*, Vol. 22, Sept. 1976, pp. 87-110.

[9]Steger, J., and Warming, R. F., "Flux Vector Splitting of the Inviscid Gasdynamics Equations with Application to Finite Difference Methods," NASA TM-78605, 1979.

[10]Wilcox, D. C., "Advanced Applications of the Multiscale Model for Turbulent Flows," AIAA Paper 87-0290, 1987.

[11]Viegas, J. R., and Horstman, C. C., "Comparison of Multiequation Turbulence Models for Several Shock Boundary-Layer Interaction Flows," *AIAA Journal*, Vol. 17, Aug. 1979, pp. 811-820.

[12]Viegas, J. R., Rubesin, M. W., and Horstman, C. C., "On the Use of Wall Functions as Boundary Conditions for Two-Dimensional Separated Compressible Flows," AIAA Paper 85-0180, 1985.

[13]Jones, W. P., and Launder, B. E., "The Prediction of Laminarization with a Two-Equation Model of Turbulence," *International Journal of Heat and Mass Transfer*, Vol. 15, 1972, pp. 301-314.

[14]Johnson, D. A., Horstman, C. C., and Bachalo, W. D., "Comparison Between Experiment and Prediction for a Transonic Turbulent Separated Flow," *AIAA Journal*, Vol. 20, June 1982, pp. 737-744.

[15]Johnson, D. A., "Transonic Separated Flow Predictions with an Eddy-Viscosity/Reynolds-Stress Closure Model," *AIAA Journal*, Vol. 25, Feb. 1987, pp. 252-259.

APPENDIX G: HISTORICAL OVERVIEW OF k-ω MODELS

The paper reproduced in this appendix was presented at the AIAA 29th Aerospace Sciences Meeting, held in Reno, Nevada, January 7-10, 1991. The formal reference to this paper is as follows.

> Wilcox, D. C., "A Half Century Historical Review of the k-ω Model," AIAA Paper 91-0615, Jan. 1991.

This paper, while reviewing the history of k-ω models, includes applications to free shear flows that have not been published elsewhere. The paper shows that, while k-ω model solutions are sensitive to the freestream value of ω, it is the only model capable of predicting a realistic spreading rate for all five of the free shear flows considered.

AIAA-91-0615

A HALF CENTURY HISTORICAL REVIEW OF THE k–ω MODEL

David C. Wilcox
DCW Industries, Inc.
La Cañada, CA

29th Aerospace Sciences Meeting
January 7-10, 1991/Reno, Nevada

For permission to copy or republish, contact the American Institute of Aeronautics and Astronautics
370 L'Enfant Promenade, S.W., Washington, D.C. 20024

A HALF CENTURY HISTORICAL REVIEW OF THE k-ω MODEL

by

David C. Wilcox*
DCW Industries, Inc.
La Cañada, California

Abstract

A brief historical review is presented tracing evolution of the k-ω two-equation turbulence model. The review compares the various k-ω models developed since 1942, and contrasts them to the well-known k-ϵ model. Straightforward results based on perturbation analysis illustrate advantages offered by k-ω models for flows with adverse pressure gradient and for integration through the sublayer. As part of the historical perspective, the paper shows that Kolmogorov did remarkably well in formulating his model without the aid of a computer.

I. Introduction

During the past twenty years, researchers have devoted a great deal of effort to formulation and testing of turbulence models. The aim of this research has been to devise an approximate set of constitutive equations suitable for accurately and efficiently predicting salient features of turbulent flows. By far the two most well-known models are the mixing-length model and the k-ϵ model.

The mixing-length model actually dates back to the early years of the twentieth century when Prandtl[1] first proposed the mixing-length hypothesis. Because of the nonlinearity introduced into the equations of motion, the model enjoyed limited success for simple flows but was not used for even the simplest boundary-layer computations prior to the advent of computers. As computers became available to scientists and engineers, refinements by Van Driest,[2] Cebeci and Smith[3] and others led to the modern day form of the model.

By contrast, the k-ϵ model is a product of the computer age. As noted by Launder and Spalding,[4] the model was first formulated in the late 1960's when mainframe computers were about as fast as today's 80386-based personal computers. Today the k-ϵ model is the most widely used (and modified) two-equation turbulence model in existence.

The k-ϵ model is not the only two-equation model and is, in fact, a relative newcomer on the turbulence modeling scene. Kolmogorov[5] formulated a two-equation turbulence model a quarter of a century earlier, viz, in 1942. As with most such models, Kolmogorov chose the kinetic energy of the turbulence as one of his turbulence parameters and modeled the differential equation governing its behavior. His second parameter was the dissipation per unit turbulence kinetic energy, ω. In his k-ω model, ω satisfies a differential equation similar to the equation for k. However, the model went with virtually no applications for the next quarter century because of the unavailability of computers to solve its nonlinear differential equations.

With no prior knowledge of Kolmogorov's work, Saffman[6] formulated a k-ω model which would prove superior to the Kolmogorov model. As part of the Imperial College efforts on two-equation models, Spalding[4] offered an improved version of the Kolmogorov model which removed some of its flaws. Shortly after formulation of Saffman's model and continuing to the present time, Wilcox, et al[7-11] have pursued further development and application of k-ω type turbulence models in earnest. As pointed out by Lakshminarayana[12], the k-ω models devised by Kolmogorov, Spalding, Saffman and Wilcox are the second most widely used class of turbulence models.

This paper traces evolution of the k-ω turbulence model during the past 49 years. Additionally this paper demonstrates some of the model's advantages over the k-ϵ model which are important in boundary layers with adverse pressure gradient and low Reynolds number applications. The paper also includes results for free shear flows and some of the most recent applications of the k-ω model, including some of the "Stanford Olympics III"[13] (aka "Collaborative Testing of Turbulence Models") results.

II. Historical Overview

As with all modern two-equation turbulence models, k-ω models invoke the Boussinesq approximation so that the Reynolds-stress tensor, $\langle -u_i' u_j' \rangle$, is proportional to the mean strain rate, i.e.,

$$\langle -u_i' u_j' \rangle = \nu_T \left[\partial u_i / \partial x_j + \partial u_j / \partial x_i \right] - \tfrac{2}{3} k \delta_{ij} \qquad (1)$$

The eddy viscosity, ν_T, is computed as the ratio of turbulence kinetic energy and ω so that

$$\nu_T = \gamma^* k / \omega \qquad (2)$$

where γ^* is a closure coefficient. Excepting Saffman's model, all of the k-ω models discussed in this section postulate that k satisfies the following differential equation.

$$dk/dt = \nu_T \left(\partial u_i / \partial x_j + \partial u_j / \partial x_i \right) \cdot \partial u_i / \partial x_j - \beta^* \omega k + \partial / \partial x_j \left[\sigma^* \nu_T \, \partial k / \partial x_j \right] \qquad (3)$$

where β^* and σ^* are additional closure coefficients. The derivative d/dt is the Eulerian derivative. The three terms on the right-hand side of Equation (3) are, respectively:

- Turbulence generation from the mean shear
- Turbulence dissipation due to self interaction
- Diffusion associated with triple correlation terms

Aside from the approximation introduced in Equation (1), the generation term is identical to the term appearing in the exact equation for turbulence energy defined as $\tfrac{1}{2}\langle u_i' u_j' \rangle$. The other two terms involve unknown correlations. The dissipation, ϵ, is modeled according to $\epsilon = \beta^* \omega k$, while the sum of the triple velocity correlation and pressure diffusion terms appearing in the exact equation for k are modeled as the last term in Equation (3).

A. Kolmogorov's Model

The very first two-equation turbulence model was formulated by Kolmogorov.[5] He referred to ω as "the rate of dissipation of energy in unit volume and time." To underscore its physical relation to the "'external scale' of turbulence, L" he also called it "some mean 'frequency' determined by $\omega = c k^{1/2}/L$, where c is a constant."

*President; Associate Fellow AIAA.

Copyright © 1990 American Institute of Aeronautics and Astronautics, Inc. All rights reserved

Inspection of Equations (2) and (3) shows why Kolmogorov chose to describe ω in two separate ways. On the one hand, the reciprocal of ω is the time scale on which dissipation of turbulence energy occurs. Hence, the variable is associated with dissipative processes. On the other hand, in analogy to laminar viscosity, we expect the eddy viscosity to be proportional to the product of a length scale and a velocity scale characteristic of fluctuations in the direction of shear, e.g., $k^{1/2}$. On dimensional grounds, we thus expect to have $\omega \propto k^{1/2}/L$.

The development of the Kolmogorov model in Reference 5 is quite brief and doesn't even establish values for all of the closure coefficients. Since little formal development of the equations is given, we can only speculate about how this great turbulence researcher may have arrived at his model equations. Since he makes no specific reference to any exact equations, it seems unlikely that he attempted to close the k and other moments of the Navier Stokes equations term by term. Rather, as a great believer in the power of dimensional analysis that he was, it is easy to imagine that Kolmogorov's original reasoning may have gone something like this.

(1) Since k already appears in the postulated constitutive relation [Equation (1)], it is plausible that $\nu_t \propto k$.

(2) The dimensions of ν_T are (length)^2/(time) while those of k are (length)^2/(time)^2.

(3) Consequently ν_t/k has dimensions (time).

(4) Turbulence dissipation $\epsilon = <\nu(\partial u_i/\partial x_j)'^2>$ has dimensions (length)^2/(time)^3.

(5) Consequently ϵ/k has dimensions 1/(time).

(6) We can close Equations (1) and (3) by introducing a variable with dimensions (time) or 1/(time).

Kolmogorov's postulated equation for ω (taking some notational liberties) is as follows.

$$d\omega/dt = -\beta\omega^2 + \partial/\partial x_j[\sigma\nu_T \partial\omega/\partial x_j] \qquad (4)$$

This equation has two particularly noteworthy features. ***First***, there is no analog to the k-equation's turbulence generation (production) term. The absence of a production term is consistent with Kolmogorov's notion that ω is associated with the smallest scales of the turbulence, and thus has no direct interaction with the mean motion. ***Second***, the equation is written in terms of ω rather than ω^2. As will be shown below, Kolmogorov's decision to write his equation in terms of ω was a somewhat prophetic choice.

Kolmogorov[5] establishes appropriate values only for the ratio of β to β^*. To establish values of the other closure coefficients, we can insist that the model agree with the law of the wall and that it predict $k \propto 0.3<-u'v'>$ approaching the sublayer from above. Also, we can use the fact that ω can be rescaled in such a way that γ^* is effectively set to unity. The resulting values for the closure coefficients are

$$\beta = .057, \quad \beta^* = .09, \quad \gamma^* = 1, \quad \sigma = \sigma^* = 1.14 \qquad (5)$$

Kolmogorov alludes to channel and pipe flow applications. He states that for channel flow, "the result is in agreement with the well-known results of von Karman."

B. Saffman's Model

Completely unaware of Kolmogorov's little known paper, Saffman[6] formulated a model using k and ω. Saffman described ω as "a frequency characteristic of the turbulence decay process under its self-interaction." He stated further that, "The rough idea is that ω^2 is the mean square vorticity of the 'energy containing eddies' and [k] is the kinetic energy of the motion induced by this vorticity." Saffman chose to write the equation for ω in terms of ω^2, and his equation was as follows.

$$d\omega^2/dt = \alpha\omega^2[(\partial u_i/\partial x_j)^2]^{1/2} - \beta\omega^3 + \partial/\partial x_j[\sigma\nu_T \partial\omega^2/\partial x_j] \qquad (6)$$

As shown in Equation (6), Saffman includes a production term in the ω equation. He also chose to represent the turbulence-energy production term in a manner similar to that used by Bradshaw.[14] That is, he approximated the k equation production term as $\alpha^* k[(\partial u_i/\partial x_j + \partial u_j/\partial x_i)^2]^{1/2}$.

The closure coefficients for the Saffman model are as follows.

$$.15 < \beta < .18, \quad \beta^* = .09, \quad \gamma^* = 1, \quad \sigma = \sigma^* = .50 \qquad (7)$$

Also, the coefficients α and α^* are given by $.15 < \alpha < .21$ and $\alpha^* = .30$.

Modeling the production terms in the manner he chose was dictated by a desire to capture the sharp turbulent-nonturbulent interface feature of turbulent shear layers. Saffman showed that his model has solutions at such an interface with simple algebraic asymptotic behavior that is consistent with measurements, provided also that the 'turbulent Prandtl numbers', σ and σ^* are equal to ½.

Saffman made an even more significant contribution in speculating as follows.

> "Effects of molecular viscosity have been neglected completely in the model equations. The molecular viscosity can be incorporated formally into the model equations in a simple and perhaps natural way by adding the molecular diffusivity ν to the turbulent diffusivity in the [diffusion terms]. The boundary condition at a rigid wall could then be applied on the wall itself, and appropriate conditions are easily shown to be
>
> $$u_i = 0, \quad k = 0, \quad \omega = (u_\tau^2/\nu)\Omega(u_\tau z_0/\nu) \qquad (8)$$
>
> where z_0 is the wall roughness and Ω is some (unknown) function depending on the nature of the wall."

Although he performed no computations with molecular viscosity included, he laid the foundation for one of the most convenient features of k-ω models, viz, the ease with which the equations can be integrated through the viscous sublayer.

C. Spalding's Model

As part of their extensive efforts in turbulence modeling, Launder and Spalding[4] developed a k-ω model. The equation for ω was again written in terms of ω^2 and is as follows.

$$d\omega^2/dt = \alpha\omega(\partial u_i/\partial x_j + \partial u_j/\partial x_i)^2 + \gamma\nu_t(\partial\zeta_i/\partial x_j)^2 - \beta\omega^3 + \partial/\partial x_j[\sigma\nu_T \partial\omega^2/\partial x_j] \qquad (9)$$

where ζ_i is the mean vorticity vector, $\alpha = 1.04\beta^*$, and $\gamma = 3.5\beta^*$. Closure coefficients for the Spalding model are

$$\beta = .17, \quad \beta^* = .09, \quad \gamma^* = 1, \quad \sigma = \sigma^* = .90 \qquad (10)$$

The form of the production term proportional to γ indicates that, similar to the later work of Wilcox and Alber,[7] Spalding identified ω as the RMS fluctuating vorticity.

D. Wilcox and Rubesin's Model

Building upon earlier efforts by Wilcox and Alber,[7] Saffman and Wilcox,[8] and Wilcox and Traci,[9] Wilcox and Rubesin[10] developed a k-ω model which has since been applied to a wide range of flows. Following Wilcox and Traci, Wilcox and Rubesin regard ω as being "related to" the ratio of dissipation, ϵ to k. For high-Reynolds-number turbulent flows, the equation for ω is

$$d\omega^2/dt = \gamma\omega(\partial u_i/\partial x_j + \partial u_j/\partial x_i)^2 - [\beta + 2\sigma(\partial \ell/\partial x_j)^2]\omega^3 + \partial/\partial x_j[\sigma\nu_T \partial\omega^2/\partial x_j] \quad (11)$$

where $\ell = k^{1/2}/\omega$ is the turbulent length scale and $\gamma = 10/9$. The other closure coefficients are as follows.

$$\beta = .15, \quad \beta^* = .09, \quad \gamma^* = 1, \quad \sigma = \sigma^* = .50 \quad (12)$$

The Wilcox-Rubesin model differs from Saffman's model in two ways. First, the production term in the k equation is as given in Equation (3), while the production term in the ω equation is γω/k times the k-equation production term. Second, addition of the term proportional to $(\partial \ell/\partial x_j)^2$ in Equation (11) limits the peak value of ℓ in the defect layer of a turbulent boundary layer. This eliminates what Saffman referred to as the "weak wake" defect-layer structure predicted by his model and greatly improves predictions for turbulent boundary layers.

E. Wilcox's Model

In the aftermath of Stanford Olympics II[16], Wilcox[11] made a key modification to the Wilcox-Rubesin model which greatly improves its predictive accuracy for adverse pressure gradient flows. Specifically, by simply writing the ω equation in terms of ω rather than ω^2, far more accurate predictions can be made for boundary layers subjected to an adverse pressure gradient. The equation for ω is

$$d\omega/dt = \gamma(\partial u_i/\partial x_j + \partial u_j/\partial x_i)^2 - \beta\omega^2 + \partial/\partial x_j[\sigma\nu_T \partial\omega/\partial x_j] \quad (13)$$

This equation differs from the original Kolmogorov equation (4) only by the addition of a production term. γ is 5/9 and the other closure coefficients are

$$\beta = .075, \quad \beta^* = .09, \quad \gamma^* = 1, \quad \sigma = \sigma^* = .50 \quad (14)$$

Wilcox specifically offers $\omega = \epsilon/(\beta^* k)$ as the definition of the turbulence property ω.

F. Speziale, Abid and Anderson's Model

Accepting Wilcox's definition of ω as the ratio of ϵ to k, Speziale, Abid and Anderson[17] have devised a k-ω model. Their approach was to begin with the classical k-ϵ model, make the formal change of dependent variables $\omega = \epsilon/k$, and transform the governing equations. The resulting ω equation for high-Reynolds-number turbulence is

$$d\omega/dt = \gamma(\partial u_i/\partial x_j + \partial u_j/\partial x_i)^2 - \beta\omega^2 + 2\sigma(\nu_T/k)\,\partial k/\partial x_i\,\partial\omega/\partial x_i + \partial/\partial x_j[\sigma\nu_T \partial\omega/\partial x_j] \quad (15)$$

with γ = 0.44 and

$$\beta = .075, \quad \beta^* = .09, \quad \gamma^* = 1, \quad \sigma = \sigma^* = .74 \quad (16)$$

The only significant difference between this model and the Wilcox[11] model is the addition of the 'cross-diffusion' term proportional to $\partial k/\partial x_i\,\partial\omega/\partial x_i$. Wilcox and Traci performed an identical analysis to arrive at a similar term to alleviate the Saffman model's "weak-wake" problem. Rather than use the precise cross-diffusion term which makes the ω equation extremely difficult to integrate (see Section IV-A), they introduced the term proportional to $(\partial \ell/\partial x_j)^2$ appearing in Wilcox and Rubesin's Equation (11). The choice was dictated by the relative ease with which the resulting ω equation can be integrated.

III. Effects of Pressure Gradient

As noted in the Introduction, the k-ϵ model is the most frequently used two-equation turbulence model. Almost every turbulence modeler bases his model upon an equation closely resembling the ϵ equation. While its near universality is indeed impressive, its degree of success in predicting relatively simple flows is not. As shown by Wilcox[11] and Rodi and Scheuerer[15], the k-ϵ model is very inaccurate for incompressible boundary layers in even the mildest of adverse pressure gradients. Furthermore, as shown by Wilcox[11], the blame for the poor predictions cannot be placed on use of "inappropriate wall functions," the usual explanation given by ϵ-equation advocates. Rather, the fault lies with the ϵ equation's intrinsic behavior approaching a solid boundary which can, to some extent, be mitigated by using wall functions.

Figure 1 (reproduced from Wilcox[11]) shows results of computations for incompressible boundary layers with pressure gradient. Velocity profiles are displayed in Figures 1(a) and 1(b) in terms of classical defect-layer coordinates, $(U_e-u)/u_\tau$ and y/Δ where $\Delta \equiv U_e\delta^*/u_\tau$. Figure 1(a) shows that differences amongst the Wilcox (k-ω), Wilcox-Rubesin (k-ω^2) and Launder (k-ϵ) models are barely noticeable for constant pressure. By contrast, Figure 1(b) shows that for adverse pressure gradient, computed velocity profiles are quite different amongst the three models.

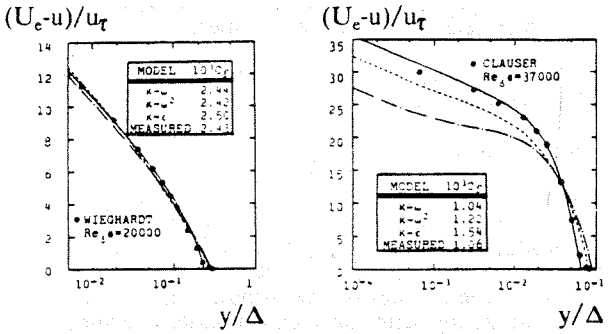

(a) Velocity profiles, $\beta_T = 0$ (b) Velocity profiles, $\beta_T = 8.7$

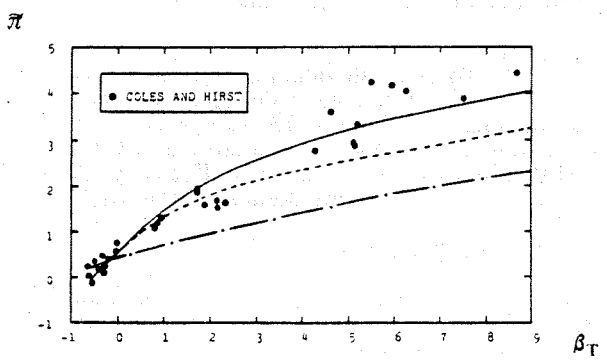

(c) Variation of wake strength with pressure gradient

Figure 1. Comparison of computed and measured defect-layer properties: —— Wilcox k-ω model; ----- Wilcox-Rubesin k-ω^2 model; —•— Launder k-ϵ model.

k-ω model results are closest to measured values, k-ϵ model results are farthest from measured values and k-ω² model results are about midway between. Figure 1(c) compares computed and measured values of Coles'[18] wake strength parameter, Π, as a function of dimensionless pressure gradient, β_1, defined by

$$\beta_\Gamma = \delta^*(dp/dx)/\tau_w \qquad (17)$$

where δ^* is displacement thickness, dp/dx is pressure gradient, and τ_w is surface shear stress. Again, it is clear that the k-ω model comes closest to matching measured values, k-ϵ is worst, and k-ω² is about midway between.

Using perturbation methods, Wilcox[11] demonstrates that approaching the surface on the scale of the defect layer, the velocity profile behaves asymptotically as

$$(U_e-u)/u_\tau \sim -\kappa^{-1}\log(y/\Delta) + A - C\beta_\Gamma(y/\Delta)\log(y/\Delta) \qquad (18)$$

The constant A is determined as part of the solution while the constant C follows directly from the analytically deducible limiting form of the solution as $y/\Delta \to 0$. Table 1 lists values of A, C and Π for four of the k-ω models discussed in Section II as well as the k-ϵ model. The numerical results for A and Π have been obtained with $\beta_\Gamma = 9$.

Table 1. Summary of computed defect-layer properties

Model	Type	A	C	Π
Wilcox	k-ω	13.1	1.18	4.05
Wilcox-Rubesin	k-ω²	9.8	2.60	3.26
Kolmogorov	k-ω	10.0	1.14	3.21
Launder	k-ϵ	5.2	6.09	2.27
Speziale	k-ω	5.1	4.96	2.23

Two conclusions can be drawn from Table 1. ***First***, inspection of the Π column shows that the Wilcox model predicts a value closest to the experimental value of between 4 and 5 [see Figure 1(c)], the Kolmogorov and Wilcox-Rubesin values are very similar, as are the Launder and Speziale values. ***Second***, the coefficient C is smallest for the Wilcox and Kolmogorov models, largest for the Launder and Speziale models, and about midway between for the Wilcox-Rubesin model. Inspection of Equation (18) and Figure 1(b) shows the consequence of having too large a value for C. Specifically, the velocity profile develops a curious (nonphysical) inflection approaching the surface for the Launder and Speziale models. By contrast, there is no inflection for the Wilcox model and the computed profile is very close to corresponding measured values.

Note that a large value of C causes velocity profile distortion to become more pronounced as β_1 increases in magnitude. By contrast, $\beta_\Gamma = 0$ for constant pressure and no distortion occurs as shown in Figure 1(a). This underscores the danger in relying strictly upon constant-pressure turbulence data for calibrating and testing a turbulence model.

While the Kolmogorov model does about as well as the Wilcox-Rubesin model for $\beta_\Gamma = 9$, its equations prove to be more difficult to integrate than any of the other models. The maximum timestep used in the one-dimensional time-marching solution to the defect-layer similarity equations is a tenth of the value which can be used for the other models.

As a final comment, the fact that the Speziale model has the same ill-behaved velocity profile for adverse pressure gradient is unsurprising as it has been derived from the k-ϵ model using a formal change of dependent variables. The only substantial difference between the models is in the values assigned to the turbulent Prandtl numbers σ and σ*

IV. Integration Through the Sublayer

Perhaps the strongest feature of the k-ω model is the ease with which the equations can be integrated through the viscous sublayer. This stands in complete contrast to the standard k-ϵ model which is notoriously difficult to integrate through the sublayer. This section first shows how the various models of Section II and the k-ϵ model fare in the sublayer without extensive viscous modifications. Next, the surface roughness function alluded to by Saffman [Equation (8)] is discussed. Finally, a particularly simple set of viscous modifications to the Wilcox k-ω model are presented which yield satisfactory prediction of subtle sublayer structure details such as $k \sim y^2$ as $y \to 0$, the sharp peak value of k near $y^+ = 20$, and accurate turbulence energy equation term balances.

A. Sublayer Behavior Without Viscous Damping

In order to integrate the turbulence model equations through the viscous sublayer we must, at a minimum, add molecular viscosity to the diffusion terms of the k, ω and mean-flow equations. Additional viscous damping functions generally are needed for the k-ϵ model to obtain satisfactory solutions, and many researchers have attempted to devise appropriate damping functions[19]. An interesting question is, "Does the same situation hold for the k-ω model?" The purpose of this subsection is to answer this question.

To facilitate our analysis, we simply add molecular diffusion terms to the k and ω equations for each of the six models discussed in Section II. In the case of the Speziale model, we also include molecular viscosity in the cross-diffusion term which is consistent with the Speziale, et al derivation. It is easy to demonstrate that the solution approaching y = 0 behaves as

$$k \sim y^n \quad \text{and} \quad \beta^* y^2\omega/\nu \sim \text{constant} \quad \text{as } y \to 0 \qquad (19)$$

Table 2 lists the values of n and the constant for the six models. As shown, none of the models predicts the exact theoretical values[17] of $n = \beta^* y^2\omega/\nu = 2$. This can only be accomplished with additional modification of the k and ω equations. Note that the asymptotic results for the Speziale model are independent of σ and σ* and are thus identical to the inherent behavior of Launder's k-ϵ model.

Table 2. Sublayer behavior without viscous damping

Model	Type	B	n	$\beta^* y^2\omega/\nu$
Wilcox-Rubesin	k-ω²	7.1	4.00	12.00
Saffman	k-ω²	6.0	3.7-4.0	12.00
Spalding	k-ω²	5.7	3.79	12.00
Wilcox	k-ω	5.1	3.23	7.20
Kolmogorov	k-ω	3.1	3.62	7.20
Speziale	k-ω	-2.2	1.39	0.53
Exact/Measured	-	5.0-5.7	2.00	2.00

It is interesting to take this analysis a step further by integrating the equations through the viscous sublayer. This is most conveniently done using perturbation methods.[8-11] In the perturbation solution, we apply no-slip boundary conditions at the surface, enforce the asymptotic behavior of ω dictated by Equation (19), and compute the constant in the law of the wall, B, from the following limit.

$$B = \lim_{y\to\infty} [u^+ - \kappa^{-1}\log y^+] \qquad (20)$$

where $y^+ = u_\tau y/\nu$ and $u^+ = u/u_\tau$ are conventional sublayer coordinates. Table 2 also lists the computed value of B for the six models. As shown, the Spalding and Wilcox models are sufficiently close to the generally accepted

value of between 5.0 and 5.7 to be used with no additional viscous modifications. The Speziale (and hence the k-ϵ) model is farthest from the generally accepted value for B.

The sublayer computations illustrate how difficult Speziale's cross-diffusion term is to handle numerically. The maximum timestep used in the one-dimensional time-marching solution to the sublayer equations is a tenth of the value which can be used for the other models. The only reason this problem did not appear in the defect-layer solution is because the computations were actually done in terms of k and ϵ with Speziale's closure coefficient values.

Figure 2 (reproduced from Wilcox[11]) shows just how well the Wilcox model does in the sublayer without additional viscous modifications. The excellent agreement between computed and measured sublayer properties has been achieved despite the fact that the model is not asymptotically correct as $y \to 0$. Since this model performs so well in flows with adverse pressure gradient, this author believes that current efforts by numerous researchers aimed at achieving asymptotically consistent solutions near $y = 0$ in the name of improving adverse pressure gradient predictions are unlikely to succeed. Inspection of the momentum-integral equation tells us that the skin friction is a function of the entire boundary-layer structure, not just localized near-surface turbulence details. Hence if a turbulence model does poorly in adverse pressure gradient, the most likely source of error is lurking in the defect layer, not in the sublayer.

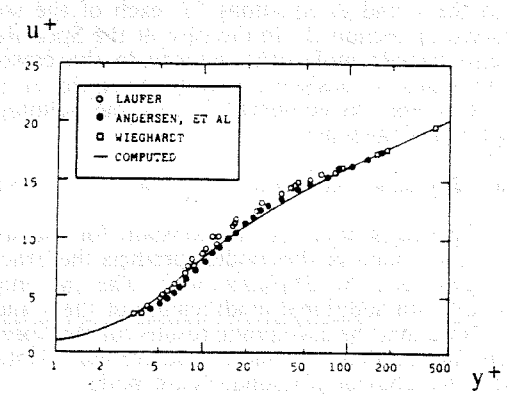

(a) Velocity profile

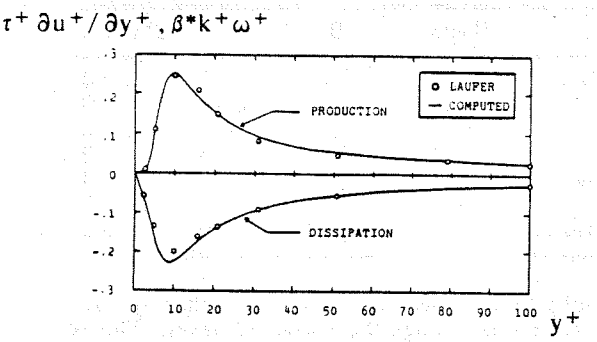

(b) Production and dissipation

Figure 2. Comparison of computed and measured sublayer properties for a perfectly smooth surface.

B. Surface Roughness

Wilcox and Traci were the first to confirm Saffman's postulated relationship [Equation (8)] between the surface value of ω and surface roughness, z_0. In addition to providing a straightforward way of representing surface roughness effects, Saffman's relationship yields an especially simple surface boundary condition which can be used for general flows over solid boundaries.

Following Chambers and Wilcox[20], we seek solutions to the model equations in which ω assumes a finite value at the surface, i.e., we expand in Taylor series. Thus, taking account of no-slip at $y = 0$, we have

$$\left.\begin{aligned} u &= u_1 y + \tfrac{1}{2}u_2 y^2 + \dots \\ k &= k_1 y + \tfrac{1}{2}k_2 y^2 + \dots \\ \omega &= \omega_0 + \omega_1 y + \dots \end{aligned}\right\} \qquad (21)$$

For all six of the models of Section II and for the k-ϵ model, the turbulence energy equation yields the following relation amongst k_2, k_1 and ω_0.

$$k_2 = -\sigma^* k_1^2/(\omega_0 \nu) \qquad (22)$$

For the various models, substitution of Equations (21) yields the following relationships.

Wilcox and Kolmogorov Models

$$\omega_2 = (\beta\omega_0^3 - \gamma\omega_0 u_1^2 - \sigma\omega_1 k_1)/(\nu\omega_0) \qquad (23a)$$

Saffman, Spalding and Wilcox-Rubesin Models

$$\omega_2 = (\beta\omega_0^3 - \alpha\omega_0^2 u_1 - 2\sigma\omega_1 k_1 - 2\nu\omega_1^2)/(2\nu\omega_0) \qquad (23b)$$

Speziale and Launder Models

$$[2\nu\omega_1 + (\sigma-\sigma^*)k_1]\omega_0 = 0 \qquad (23c)$$

Inspection of Equations (22) , (23a) and (23b) shows that four coefficients, viz, ω_0, ω_1, k_1 and u_1 are free in the Wilcox, Kolmogorov, Saffman, Spalding and Wilcox-Rubesin models. In practice, ω_0 can be assigned arbitrarily and the other three coefficients are determined by conditions far from the surface.

By contrast, Equation (23c) shows that the cross-diffusion term imposes an extra constraint on the solution. Consequently, for the Speziale and Launder models, either $\omega = 0$ or $2\nu\,\partial\omega/\partial y = (\sigma-\sigma^*)\,\partial k/\partial y$ at the surface. In either case, there are only three undetermined coefficients and the surface value of ω does not play as unique a role as it does with the other models.

This lack of flexibility with the Launder k-ϵ model is the basis of the ϵ equation's "stiffness" to which many authors allude. In Subsection IV-A, we found that one valid asymptotic solution to the equations is $\omega \sim y^{-2}$. The analysis above indicates the differential equations also support a solution in which $\omega \to 0$. This is analogous to having two exponential solutions with vastly different decay (growth) scales. Numerical solutions thus have a tendency to lock on to the undesirable infinite-ω solution which, as shown in Section IV-A, fails to approach the law of the wall with an acceptable value for B. By contrast, with the exception of the Speziale model, k-ω models have solutions for arbitrary surface values of ω varying continuously from 0 to ∞.

Figure 3 (reproduced from Wilcox[11]) illustrates the effect of varying the surface value of ω. The value of the constant B in the law of the wall varies continuously with Ω [see Equation (8)] as shown. Experimental measurements[21] indicate that B varies with surface roughness z_0. Based on these results, Wilcox[11] offers the following correlation.

$$\Omega = \begin{cases} (50\nu/u_\tau z_0)^2, & u_\tau z_0/\nu < 25 \\ (100\nu/u_\tau z_0), & u_\tau z_0/\nu \geq 25 \end{cases} \qquad (24)$$

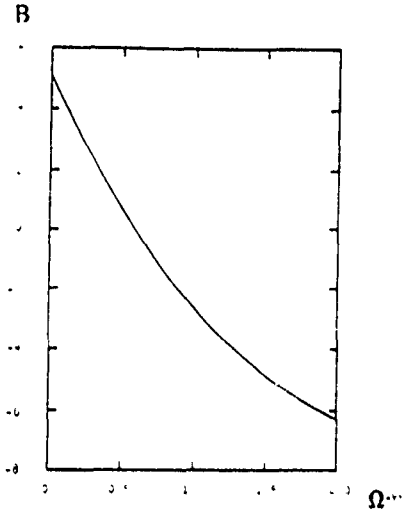

Figure 3. Computed variation of the constant in the law of the wall, B, as a function of the surface value of ω.

Notice that our solution asymptotes smoothly to the solution given in Equation (19) as $z_0 \to 0$. Consequently, we infer that Equation (19) in which ω is infinite approaching the surface corresponds to a perfectly smooth surface. In the limit $u_\tau z_0/\nu \to 0$, combining Equations (8) and (24) yields

$$\omega = 2500\nu/z_0^2 \quad \text{at} \quad y = 0 \tag{25}$$

In practice, Equation (25) should be used rather than Equation (19) even if a perfectly smooth surface is desired. The advantage in using Equation (25) is obvious for several reasons.

1. Local geometry (e.g., distance normal to the surface) does not appear so it can be applied even in three-dimensional geometries.

2. z_0 need only be small enough to have a hydraulically smooth surface which occurs when $u_\tau z_0/\nu < 5$. Resulting values for the surface value of ω are rarely ever large enough to cause numerical error provided a sensible finite-difference grid is used.

3. Experience has shown that Equation (25) works well for separated flows.

C. Viscous Modifications

As shown in Table 2, nearly all of the models discussed above require modification beyond simply adding molecular diffusion in order to facilitate integration through the sublayer. Achieving an acceptable value for B is just one consideration. For some applications, we require information about the point at which transition from laminar to turbulent flow occurs. All of the k-ω models and the k-ε model predict transition to turbulence at Reynolds numbers which are at least an order of magnitude too low for the Blasius boundary layer. In highly specialized applications such as the aerodynamic window, we require a realistic description of the experimentally-observed sharp near-surface peak in turbulent energy. All of the models fail to predict $k \sim y^2$ near a solid surface and, correspondingly, fail to predict this sharp peak.

To accommodate such applications, we must permit some of the closure coefficients to vary with Reynolds number. The most common parameter used is the turbulence Reynolds number, Re_T, defined by

$$Re_T = k/(\omega\nu) \tag{26}$$

This quantity is independent of flow geometry and thus preserves the universal nature of the model. Some authors also introduce the dimensionless distance $y^+ = u_\tau y/\nu$ in formulating viscous modifications. This has the disadvantage of reducing model universality and can be difficult to implement in complex geometries. The approach taken here is to cast all viscous modifications in terms of Re_T and to introduce the minimum amount of complexity.

As discussed by Speziale, et al[17], one long-standing problem faced by turbulence modelers is the ratio of β to β*. On the one hand, the ratio for all models is chosen to match the observed decay rate for homogeneous isotropic turbulence, which means we select $\beta^*/\beta = 6/5$. On the other hand, this ratio also controls the algebraic behavior of k as $y \to 0$.

One way to remove this deficiency with the addition of a single closure coefficient is to introduce a 'laminar Prandtl number' in the ω equation, viz, for the Wilcox model we modify Equation (13) as follows.

$$d\omega/dt = \gamma(\partial u_i/\partial x_j + \partial u_j/\partial x_i)^2 - \beta\omega^2 + \partial/\partial x_j[(\sigma_l\nu + \sigma\nu_T)\partial\omega/\partial x_j] \tag{27}$$

Equation (27) predicts $k \sim y^n$ and $\beta^* y^2\omega/\nu \sim 6\sigma_l\beta^*/\beta$ as $y \to 0$, where $n = \frac{1}{2}[1 + (1 + 24\sigma_l\beta^*/\beta)^{1/2}]$. Then if we set

$$\sigma_l = 5/18 \tag{28}$$

we have the desired solution, i.e., $n = \beta^* y^2\omega/\nu = 2$. Since diffusion terms vanish in homogeneous isotropic turbulence, we still have the desired decay rate.

While we now have the desired near-surface asymptotic behavior for k and ω, our sublayer solution has suffered a relapse. The model now predicts a constant in the law of the wall, B = 0.62, which is almost as bad as the k-ε model. We can simultaneously remedy this problem and facilitate accurate transition predictions by letting γ and γ* depend upon Re_T. The following functions are sufficient to accomplish our stated goals.

$$\gamma = {}^5/_9(\gamma_0 + Re_T/R_\omega)/(1 + Re_T/R_\omega) \tag{29}$$

$$\gamma^* = (\gamma_0^* + Re_T/R_k)/(1 + Re_T/R_k) \tag{30}$$

Equations (29) and (30) contain four new closure coefficients, viz, γ_0, γ_0^*, R_k and R_ω. The value for γ_0^* can be established using the procedure first presented by Wilcox.[32] To understand this procedure, we need an explanation of how we use the model equations to predict transition for the Blasius boundary layer. The following sequence of events occurs.

(1) The computation starts in a laminar region with k = 0 in the boundary layer and a small freestream value of k.

(2) Initially, dissipation of k exceeds production of k. Turbulence energy is entrained from the freestream and spreads through the boundary layer by molecular diffusion. It is not amplified and the boundary layer remains laminar.

(3) At a critical Reynolds number, Re_{x_c}, production catches dissipation. Downstream of x_c, k production exceeds k dissipation and turbulence energy is amplified.

(4) At some point downstream of x_c, k undergoes rapid growth and transition to turbulence occurs. The transition point is sensitive to the freestream values of both k and ω.

Using Equations (3), (27) and (30) along with the Blasius solution, the critical Reynolds number is

$$Re_{x_t} = 273\sigma_l^2/\gamma_0^* \qquad (31)$$

We can set the value of γ_0^* by requiring that Re_{x_t} match the minimum-critical Reynolds number of $9 \cdot 10^4$ predicted by linear stability theory for the Blasius boundary layer. The value of γ_0 controls the width of the transition region, and experience[9] has shown that experimental measurements are accurately reproduced by the model equations when we select $\gamma_0 = \gamma_0^*$. Hence, we conclude that

$$\gamma_0 = \gamma_0^* = \sigma_l^2/330 \qquad (32)$$

The values for R_k and R_ω are established by performing a series of sublayer computations.[9-11] For each value of R_k, there is a unique value of R_ω which yields a specified value of B. Table 3 shows results of a series of computations designed to yield B = 5.0. The table includes the peak value of dimensionless turbulence energy, $k_{max} = k/u_\tau^2$.

Table 3. Closure coefficients which yield B = 5.0

R_k	R_ω	k_{max}
1	0.22	3.33
2	0.78	3.33
5	2.75	3.50
10	6.47	3.81
20	14.65	4.24
30	23.50	4.55
40	32.90	4.78
50	42.70	4.98

Comparison between computed and measured sublayer, channel-flow and pipe-flow properties indicates that the optimum (R_k,R_ω) pair is (20,14.65). Figures 4 and 5 compare computed and measured sublayer and channel-flow properties for R_k = 20 and R_ω = 14.65. The low-Reynolds-number channel flow simulation data of Mansour, Kim and Moin[23] are included in both figures as well as the older, high-Reynolds-number pipe-flow measurements of Laufer[24]. Aside from the fact that dissipation has a nonzero value at the surface, the overall agreement between computed and measured sublayer properties is almost identical to that obtained with the unmodified Wilcox model (see Figure 2). On balance, computed production and dissipation for channel flow are closer to the Mansour, et al data than to the Laufer data.

The only way in which the viscous modifications proposed in Equations (27) through (32) fail to duplicate exact asymptotic behavior is for the shear stress, $<-u'v'>$. The modifications predict $<-u'v'> \sim y^4$ while the exact asymptotic variation should be y^3. The effect of this shortcoming on predicted flow properties is almost certainly negligible as the Reynolds stresses are of little consequence in the portion of the sublayer for which this asymptotic behavior holds.

In closing, note that the original Wilcox model has exactly five closure coefficients. The viscous modifications of this subsection double that number! Unless your application requires accurate transition prediction and/or detailed prediction of esoteric features such as the sharp peak in k near a solid boundary, the extra complexity just isn't worth it. There is virtually no difference in computed skin friction, mean velocity profiles, and even in the turbulence energy equation budget. Thus, for the majority of engineering applications, the Wilcox k-ω model is satisfactory without viscous modifications.

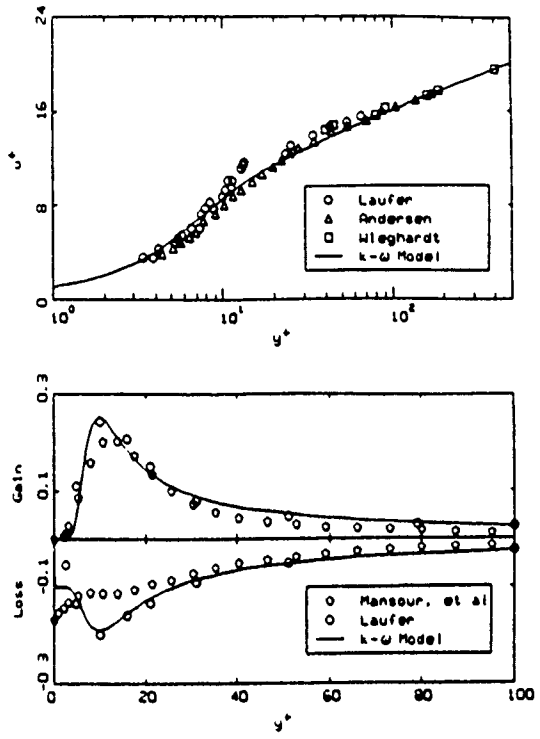

Figure 4. Comparison of computed and measured sublayer properties.

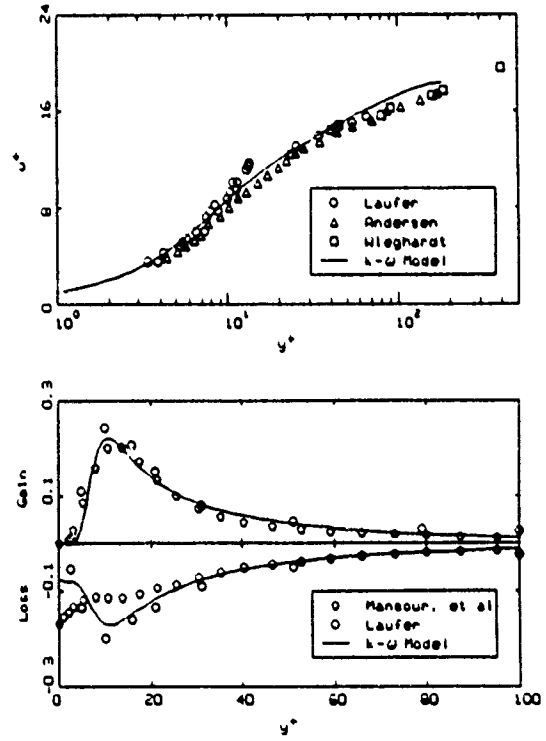

Figure 5. Comparison of computed and measured low-Reynolds-number channel-flow properties.

V. Free Shear Flows

One area in which further research is needed for the k-ω model is that of free shear flows. Table 4 presents computed spreading rates for the incompressible mixing layer, plane, round and radial jets, and the plane far wake.

Table 4. Spreading rates for free shear flows

Flow	Wilcox	Launder	Speziale	Measured
Mixing Layer	.100-.141	.099	.115	.116
Plane Jet	.090-.133	.108	.130	.100-.110
Round Jet	.115-.175	.120	.155	.086
Radial Jet	.088-.186	.095	.112	.096-.110
Plane Wake	.221-.498	.257	.285	.365

The Wilcox k-ω model solutions are very sensitive to the freestream value of ω. Consequently a range of spreading rates are possible. By contrast, the Launder k-ϵ model and Speziale's k-ω model show no sensitivity to freestream values. This is evidence that Speziale's 'cross-diffusion' terms remove the Wilcox model's sensitivity to freestream conditions.

Note that all three models suffer from the well-known "round-jet/plane-jet anomaly," i.e., in contrast to measurements, all models predict that the round jet spreads more rapidly than the plane jet.

VI. Stanford Olympics III Applications

A great deal of progress has been made with the k-ω model over the past 20 years, especially during the past decade. The Wilcox-Rubesin model was exercised in 60 of the Stanford Olympics II test cases, and the Wilcox model has been applied to all of the ongoing Stanford Olympics III cases. Two of the Wilcox model applications in the most recent Olympiad are of interest here.

The Samuel-Joubert boundary-layer case was the single flow which best exemplified the disappointing state of the art of two-equation turbulence models at the time of Stanford Olympics II.[16] This flow is an incompressible boundary layer in an increasingly adverse pressure gradient. No model made a satisfactory prediction of skin friction and velocity profiles for this flow, even though it was one of the "simple" entry cases. The same case has been included in Stanford Olympics III[13] to see if the state of the art has improved since 1981. Figure 6 compares predictions of the Wilcox k-ω model with experimental c_f for this flow. Computed c_f is within acceptable engineering accuracy.

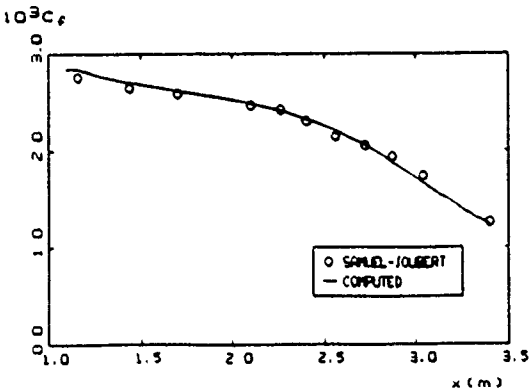

Figure 6. Computed and measured skin friction for Samuel and Joubert's boundary layer.

The other noteworthy result is for flow past a backward-facing step. Figure 7 compares computed and measured skin friction and surface pressure distributions. Computed reattachment length is approximately 5H, where H is the step height. Typical reattachment length for the unmodified k-ϵ model is 4H while the measured length is 6H. The most exciting result of this computation, performed by Salari[25], is the fact that peak values of the eddy viscosity are close to values inferred from measurements. By contrast, k-ϵ peak eddy viscosity values are typically twice the measured values.

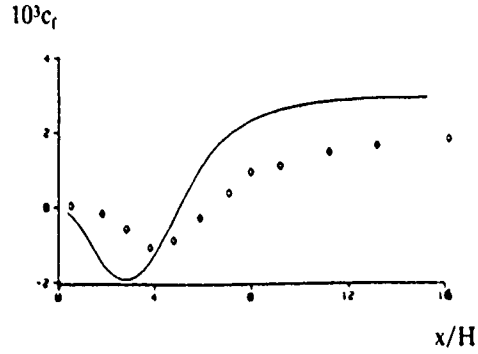

(a) Skin friction

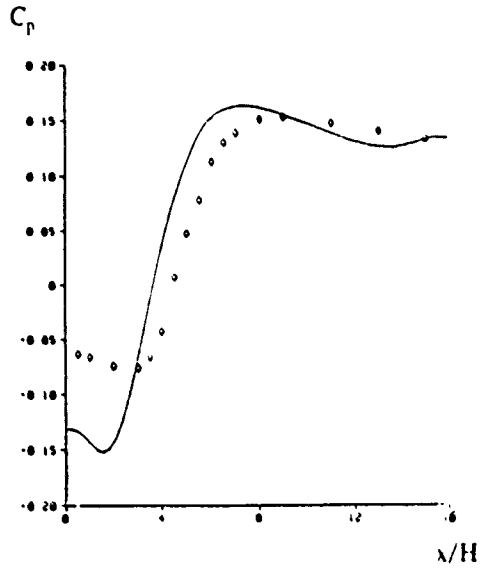

(b) Surface pressure

Figure 7. Computed and measured backward facing step flow properties.

VII. Summary and Conclusions

The k-ω two-equation turbulence model, although not as popular as the standard k-ϵ model, offers advantages for flows with adverse pressure gradient and for flows where integration through the sublayer is preferred. Kolmogorov's 1942 k-ω model was within a single term (production in the ω equation) of being as accurate as any two-equation turbulence model available today.

Results of Section IV show why the k-ω model is so easy to integrate through the sublayer. One of Saffman's most important contributions is his rough-wall boundary condition which has proven to be an especially useful feature of the k-ω model, a feature not shared by the k-ϵ model. The

viscous modifications devised permit accurate prediction of near-surface asymptotic behavior at the expense of doubling the number of closure coefficients. Nevertheless, the modified k-ω model can be used to predict boundary-layer transition and for low-Reynolds-number flows.

Additional research is needed to determine the cause of the k-ω model's sensitivity to the freestream value of ω.

The k-ω model has undergone a slow evolutionary process from the original work of Kolmogorov to the most recent work of Speziale, et al. Given its obvious strengths, perhaps the next decade will show increased interest from the turbulence community.

VIII. Acknowledgements

Research was supported by the U. S. Army Research Office and the NASA Langley Research Center under Contracts DAAL03-87-C-0004 and DAAL03-89-C-0032 with Dr. Thomas Doligalski and Dr. Julius Harris as Contract Monitors. Dr. Kambiz Salari and Dr. Patrick Roache of Ecodynamics Research Associates, Inc. were most helpful in making results of their backward-facing step computation available.

References

[1]Prandtl, L., "Bericht Über Untersuchungen zur ausgebildeten Turbulenz," ZAMM, Vol 5, p 136 (1925).

[2]Van Driest, E. R., "On Turbulent Flow Near a Wall," J Aero Sci, Vol 23, p 1007 (1956).

[3]Cebeci, T. and Smith, A. M. O., Analysis of Turbulent Boundary Layers, Ser in Appl Math & Mech, Vol XV, Academic Press (1974).

[4]Launder, B. E. and Spalding, D. B., Mathematical Models of Turbulence, Academic Press, London (1972).

[5]Kolmogorov, A. N., "Equations of Turbulent Motion of an Incompressible Fluid," Izvestia Academy of Sciences, USSR; Physics, Vol 6, Nos 1 and 2, pp 56-58 (1942).

[6]Saffman, P. G., "A Model for Inhomogeneous Turbulent Flow," Proc Roy Soc, Lond, Vol A317, pp 417-433 (1970).

[7]Wilcox, D. C. and Alber, I. E., "A Turbulence Model for High Speed Flows," Proc of the 1972 Heat Trans & Fluid Mech Inst, Stanford Univ Press, pp 231-252 (1972).

[8]Saffman, P. G. and Wilcox, D. C., "Turbulence-Model Predictions for Turbulent Boundary Layers," AIAA J, Vol 12, No 4, pp 541-546 (April 1974).

[9]Wilcox, D. C. and Traci, R. M., "A Complete Model of Turbulence," AIAA Paper 76-351 (1976).

[10]Wilcox, D. C. and Rubesin, M. W., "Progress in Turbulence Modeling for Complex Flow Fields Including Effects of Compressibility," NASA TP 1517 (1980).

[11]Wilcox, D. C., "Reassessment of the Scale Determining Equation for Advanced Turbulence Models," AIAA Journal, Vol 26, No 11, pp 1299-1310 (November 1988).

[12]Lakshminarayana, B., "Turbulence Modeling for Complex Shear Flows," AIAA Journal, Vol 24, pp 1900-1917, (December 1986).

[13]Bradshaw, P., Launder, B. E. and Lumley, J., "Collaborative Testing of Turbulence Models," AIAA Paper 91-0215 (January 1991).

[14]Bradshaw, P., Ferriss, D. H. and Atwell, N. P., "Calculation of Boundary Layer Development Using the Turbulent Energy Equation," JFM, Vol 28, Pt 3, pp 593-616 (1967).

[15]Rodi, W. and Scheuerer, G., "Scrutinizing the k-ϵ Turbulence Model Under Adverse Pressure Gradient Conditions," Transactions of the ASME, Vol 108, pp 174-179 (June 1986).

[16]Kline, S. J., Cantwell, B. J. & Lilley, G. M., 1980-81 AFOSR-HTTM-Stanford Conference on Complex Turbulent Flows, Stanford Univ (1981).

[17]Speziale, C. G., Abid, R. and Anderson, E. C., "A Critical Evaluation of Two-Equation Models for Near Wall Turbulence," AIAA Paper 90-1481 (June 1990).

[18]Coles, D. E. and Hirst, E. A., Computation of Turbulent Boundary Layers-1968 AFOSR-IFP-Stanford Conference, Vol II, Stanford Univ (1969).

[19]Patel, V. C., Rodi, W. and Scheuerer, G., "Turbulence Models for Near-Wall and Low Reynolds Number Flows: A Review," AIAA Journal, Vol 23, pp 1308-1319 (1985).

[20]Chambers, T. L. and Wilcox, D. C., "Critical Examination of Two-Equation Turbulence Closure Models for Boundary Layers," AIAA Journal, Vol 15, No 6, pp 821-828 (June 1977).

[21]Schlichting, H., Boundary Layer Theory, Fourth Ed, McGraw-Hill, New York, pp 519-527 (1960).

[22]Wilcox, D. C., "Turbulence-Model Transition Predictions," AIAA Journal, Vol 13, No 2, pp 241-243 (1975).

[23]Mansour, N. N., Kim, J. and Moin, P., "Reynolds Stress and Dissipation Rate Budgets in Turbulent Channel Flow," Journal of Fluid Mechanics, Vol 194, pp 15-44 (1988).

[24]Laufer, J., "The Structure of Turbulence in Fully Developed Pipe Flow," NACA 1174 (1952).

[25]Salari, K., personal communication (December 1991).

REFERENCES

1. Wilcox, D. C., "A Complete Model of Turbulence Revisited," AIAA Paper 84-0176, Jan. 1984.

2. Wilcox, D. C., "Multiscale Model for Turbulent Flows," AIAA Paper 86-0029, Jan. 1986.

3. Wilcox, D. C., "Advanced Applications of the Multiscale Model for Turbulent Flows," AIAA Paper 87-0290, Jan. 1987.

4. Wilcox, D. C., "More Advanced Applications of the Multiscale Model for Turbulent Flows," AIAA Paper 88-0220, Jan. 1988.

5. Wilcox, D. C., "Reassessment of the Scale Determining Equation for Advanced Turbulence Models," *AIAA Journal*, Vol. 26, No. 11, Nov. 1988, pp. 1299-1310.

6. Wilcox, D. C., "Multiscale Model for Turbulent Flows," *AIAA Journal*, Vol. 26, No. 11, Nov. 1988, pp. 1311-1320.

7. Wilcox, D. C., "Wall Matching, A Rational Alternative to Wall Functions," AIAA Paper 89-0611, Jan. 1989.

8. Wilcox, D. C., "Supersonic Compression-Corner Applications of a Multiscale Model for Turbulent Flows," *AIAA Journal*, Vol. 28, No. 7, Jul. 1990, pp. 1194-1198.

9. Wilcox, D. C., "A Half Century Historical Review of the k-ω Model," AIAA Paper 91-0615, Jan. 1991.

10. MacCormack, R. W., "Current Status of Numerical Solutions of the Navier-Stokes Equations," AIAA Paper 85-0032, Jan. 1985.

11. MacCormack, R. W., "A Numerical Method for Solving the Equations of Compressible Viscous Flow," *AIAA Journal*, Vol. 20, Sep. 1982, pp. 1275-1281.

12. Walters, R. W. and Thomas, J. L., "Advances in Upwind Relaxation Methods," State-of-the-Art Surveys on Computational Mechanics, pp 145-183.

13. Favre, A., "Equations des Gaz Turbulents Compressibles," J Mecan, Vol 4, No 3, pp 361-390 (1965).

14. Roe, P. L., "Approximate Riemann Solvers, Parameter Vectors, and Difference Schemes," Journal of Computational Physics, Vol 43, pp 357-372 (1981).

15. Van Leer, B., "Flux-Vector Splitting for the Euler Equations," ICASE Report 82-30 (September 1982).

16. Morrison, J., "Flux Difference Split Scheme for Turbulent Transport Equations," AIAA Paper 90-5251 (October 1990).